



NASA CR-134758
D180-18850-1

(NASA-CR-134758) FRACTURE CONTROL METHOD
FOR COMPOSITE TANKS WITH LOAD SHARING LINERS
Final Report, Jul. 1971 - Feb. 1975 (Boeing
Aerospace Co., Seattle, Wash.) 260 p HC
\$8.50

N75-29449

G3/38 32417
Unclas

FRACTURE CONTROL METHOD For COMPOSITE TANKS With LOAD SHARING LINERS

Final Report

by
W. D. Bixler



THE **BOEING AEROSPACE** COMPANY

Prepared For
NATIONAL AERONAUTICS AND SPACE ADMINISTRATION

NASA Lewis Research Center
CONTRACT NAS 3-14380

J. R. FADDOUL - Project Manager

1. Report No. NASA CR-134758		2. Government Accession No.		3. Recipient's Catalog No.	
4. Title and Subtitle Fracture Control Method for Composite Tanks With Load Sharing Liners (Final Report)				5. Report Date July 1975	
				6. Performing Organization Code	
7. Author(s) W. D. Bixler				8. Performing Organization Report No. D180-18850-1	
9. Performing Organization Name and Address Boeing Aerospace Company Research and Engineering Division Seattle, Washington 98124				10. Work Unit No.	
				11. Contract or Grant No. NAS 3-14380	
12. Sponsoring Agency Name and Address National Aeronautics and Space Administration 21000 Brookpark Rd., Lewis Research Center Cleveland, Ohio 44135				13. Type of Report and Period Covered Contract Report July 1971 through Feb. 1975	
				14. Sponsoring Agency Code	
15. Supplementary Notes Project Manager, J. R. Faddoul, Materials & Structures Div. NASA Lewis Research Center					
16. Abstract This experimental program was undertaken to establish a fracture control method for composite tanks with load sharing liners. The program was based on the premise that the plastic sizing cycle, which each pressure vessel is subjected to prior to operation, acts as an effective proof test of the liner; screening out all flaws or cracks larger than a critical size. In doing so, flaw growth potential is then available for cyclic operation at pressures less than the sizing pressure. Static fracture and cyclic life tests, involving laboratory type specimens and filament overwrapped tanks, were conducted on three liner materials: (1) 2219-T62 aluminum, (2) Inconel X750 STA and (3) cryoformed 301 stainless steel. Variables included material condition, thickness, flaw size, flaw shape, temperature, sizing stress level, operating stress level and minimum-to-maximum operating stress ratio. From the empirical data base obtained, a procedure was established by which the service life of composite tanks with load sharing liners could be guaranteed with a high degree of confidence.					
17. Key Words (Suggested by Author(s)) Fracture Control 2219-T62 Aluminum Composite Tanks Inconel X750 STA Load Sharing Liners Cryoformed 301 SS Surface Flaws Proof Testing Cyclic Crack Growth Rates				18. Distribution Statement Unclassified, Unlimited	
19. Security Classif. (of this report) Unclassified		20. Security Classif. (of this page) Unclassified		21. No. of Pages 244	
				22. Price*	

* For sale by the National Technical Information Service, Springfield, Virginia 22151

FOREWORD

This report describes the work performed by the Boeing Aerospace Company from July 1971 to February 1975, under Contract NAS 3-14380. The work was administered by Mr. James R. Faddoul of the NASA Lewis Research Center. Structural Composites Industries (SCI), acting in the capacity of an associate contractor, was primarily responsible for the design, analysis and fabrication of aluminum and Inconel lined composite tanks and the fabrication of related laboratory specimens. Ardé Inc. participated in the program as a subcontractor, supplying a design analysis for a cryoformed stainless steel lined composite tank and related laboratory specimens. Boeing, having overall program responsibility, conducted the experimental portion and performed the data analysis which resulted in the work presented herein.

Boeing personnel who conducted the investigation include J. N. Masters, project supervisor and W. D. Bixler, technical leader. Specimen testing support was provided by A. A. Ottlyk and H. Olden, and the technical illustration and art work was done by G. Beuhler. SCI personnel who contributed to the investigation include R. E. Landes, program supervisor and E. E. Morris, Vice-President. Ardé personnel who contributed to the investigation include A. Cozewith and D. Gleich.

The information contained in this report is also released as Boeing Document D180-18850-1.

TABLE OF CONTENTS

	<u>Page</u>
SUMMARY	1
1.0 INTRODUCTION	5
2.0 TECHNICAL APPROACH	7
2.1 Background	7
2.2 Brief Summary of the Interim Report	8
2.3 Testing Approach Since the Interim Report	9
2.3.1 Static Fracture Differences	10
2.3.2 Cyclic Life Differences	12
2.3.3 Establishing the Influence of Controlling Factors	14
2.3.4 Completion of the Overwrapped Tank Testing	14
3.0 MATERIALS AND PROCEDURES	15
3.1 Materials	15
3.2 Specimen Fabrication	16
3.2.1 Uniaxial Specimens	16
3.2.2 Open-Ended Cylinder Specimens	17
3.2.3 Spherical Cap Specimens	17
3.2.4 301 SS Tank Specimens	18
3.3 Specimen Test Procedures	19
3.3.1 Uniaxial Static Fracture Tests	19
3.3.2 Uniaxial Cyclic Life Tests	20
3.3.3 Open-Ended Cylinder Tests	21
3.3.4 Spherical Cap Tests	21
3.3.5 301 Stainless Steel Tank Tests	21
3.4 Cyclic Crack Growth Rate Analysis	22
4.0 STATIC FRACTURE AND BURST TEST RESULTS	25
4.1 Static Fracture in a Uniaxial Stress Field	25

TABLE OF CONTENTS (Cont.)

	<u>Page</u>
4.1.1 Crack Shape Effects	26
4.1.2 Failure Loci Definition	28
4.1.3 Extrapolation to Other Materials	29
4.1.4 Failure Prediction Limitations	30
4.1.5 Curvature Effects	31
4.2 Static Fracture in a Biaxial Stress Field	32
4.2.1 Spherical Cap Results	33
4.2.2 Cylindrical Tank Results	33
4.3 Correlation of Static Fracture Results	34
4.4 Crack Growth Occurring During Sizing	36
5.0 CYCLIC CRACK GROWTH TEST RESULTS	39
5.1 Baseline Uniaxial Cyclic Rate Data	39
5.1.1 Cyclic Stress Effects	41
5.1.2 Sizing Stress Effects	42
5.1.3 Crack Shape Effects	44
5.1.4 Thickness Effects	44
5.1.5 Temperature Effects	45
5.1.6 Comparison of BM and WM Rates	45
5.1.7 Analytical Description of Baseline Cyclic Crack Growth Rates	45
5.2 Effect of R Ratio in a Uniaxial Stress Field	46
5.3 Correlation of Uniaxial Cyclic Crack Growth Rates With Tank Test Results	48
5.4 Mode of Failure During Cyclic Tests	48
6.0 OBSERVATIONS AND CONCLUSIONS	51

TABLE OF CONTENTS (Cont.)

	<u>Page</u>
7.0 APPLICATIONS	55
7.1 Materials	56
7.2 Crack Size Screened During Sizing	56
7.3 Cyclic Life Determination	58
7.4 Storage Life Considerations	63
7.5 Parametric Life Analysis	64
7.6 Limitations	65
REFERENCES	67
APPENDIX A DESIGN AND STRESS ANALYSIS OF SPHERICAL CAP SPECIMENS	221
APPENDIX B EXAMPLE OF SERVICE LIFE CALCULATION	237
APPENDIX C SYMBOLS	243

LIST OF ILLUSTRATIONS

<u>Figure</u>		<u>Page</u>
1	Stress/Strain Schematic for Composite Tanks with Load Sharing Liners	69
2	Fracture Mechanics Approach to Guaranteeing Service Life of Metal Liner in Overwrapped Tanks	70
3	Biaxial Loading of a Surface Crack	71
4	Flat Uniaxial Specimen Configurations	72
5	Open-Ended Cylinders Made of 2219-T62 Aluminum	73
6	Test Fixture for Producing Uniaxial Stress Field in a Pressurized Cylinder	74
7	Spherical Cap Specimen Configurations	75
8	Spherical Cap Specimen Test Setups	76
9	301 Stainless Steel Liner	77
10	Pressure Cups Used for Flaw Breakthrough Detection on Uniaxial Specimens	78
11	2219-T62 Aluminum Static Fracture Specimen with Flaw Anti-Deflection Bars	79
12	Compression/Tension Setup for Testing Uniaxial Specimens	80
13	Tension/Compression Specimen in Test	81
14	Typical Stress/Strain for 2219-T62 Aluminum When Loaded in Compression After a Plastic Sizing Cycle in Tension	82
15	Spherical Cap Test Arrangement	83
16	Shape Parameter Curves for Surface Flaws	84
17	Deep Flaw Magnification Curves	85
18	Failure Loci for 2.29 mm (0.090 Inch) Thick 2219-T62 Aluminum Base Metal as a Function of Crack Depth	86

LIST OF ILLUSTRATIONS (Cont.)

<u>Figure</u>		<u>Page</u>
19	Failure Loci for 4.57 mm (0.180 inch) Thick 2219-T62 Aluminum Base Metal as a Function of Crack Depth	87
20	Failure Loci for 7.62 mm (0.300 inch) Thick 2219-T62 Aluminum as a Function of Crack Depth	88
21	Failure Loci for 2219-T62 Aluminum Base Metal as a Function of a/Q .	89
22	Failure Loci for 2219-T62 Aluminum Base Metal at 78K (-320°F) as a Function of a/Q .	90
23	Failure Loci for 2219-T62 Aluminum Weld Metal as a Function of a/Q .	91
24	Failure Loci for 2219-T62 Aluminum Weld Metal at 78K (-320°F) as a Function of a/Q .	92
25	Failure Loci for Inconel X750 STA Base Metal as a Function of a/Q .	93
26	Failure Loci for Inconel X750 STA Base Metal at 78K (-320°F) as a Function of a/Q .	94
27	Failure Loci for Inconel X750 STA Weld Metal as a Function of a/Q .	95
28	Failure Loci for Inconel X750 STA Weld Metal at 78K (-320°F) as a Function of a/Q .	96
29	Failure Loci for Cryostretched 301 Stainless Steel Base Metal at 78K (-320°F) as a Function of a/Q .	97
30	Failure Loci for Cryostretched 301 Stainless Steel Weld Metal at 78K (-320°F) as a Function of a/Q .	98
31	Relationship Between S and t .	99
32	Failure Loci for 2219-T87 Aluminum Base Metal as a Function of a/Q .	100

LIST OF ILLUSTRATIONS (Cont.)

<u>Figure</u>		<u>Page</u>
33	Failure Loci for 7075-T651 Aluminum Base Metal as a Function of a/Q .	101
34	Failure Loci for 6Al-4V STA Titanium Base Metal as a Function of a/Q .	102
35	Relationship Between S and t for Various Materials.	103
36	Comparison of Static Fracture Data Developed With and Without Flaw Restraint Plates - 2.29 mm (0.090 inch) Thick 2219-T62 Aluminum BM at 295K (72°F).	104
37	Comparison of Static Fracture Data Developed Using Flat and Curved Specimens Made of 2.29 mm (0.090 inch) Thick 2219-T62 Aluminum at 295K (72°F).	105
38	Failure Loci for Equal Biaxially Loaded (Spherical Cap Specimens) 2219-T62 Aluminum BM as a Function of a/Q .	106
39	Failure Loci for Equal Biaxially Loaded (Spherical Cap Specimens) Inconel X750 STA BM as a Function of a/Q .	107
40	Failure Loci of 2.29 mm (0.090 inch) 2219-T62 Aluminum Cylindrical Tank Specimens (Non-Overwrapped and Over-wrapped) as a Function of a/Q .	108
41	Failure Loci of 2.29 mm (0.090 inch) 2219-T62 Aluminum Cylindrical Tank Specimens (Overwrapped) as a Function of a/Q at 78K (-320°F).	109
42	Failure Loci of 1.02 mm (0.040 inch) Inconel X750 STA Cylindrical Tank Specimens (Non-Overwrapped and Over-wrapped) as a Function of a/Q .	110
43	Failure Loci of 1.02 mm (0.040 inch) Inconel X750 STA Cylindrical Tank Specimens (Overwrapped) as a Function of a/Q at 78K (-320°F).	111
44	Failure Loci of 0.89 mm (0.035 inch) Cryoformed 301 Stainless Steel Tank Specimens (Non-Overwrapped and Overwrapped) as a Function of a/Q at 78K (-320°F).	112

LIST OF ILLUSTRATIONS (Cont.)

<u>Figure</u>		<u>Page</u>
45	Relationship Between S and t for Uniaxial and Biaxial Static Fracture Results.	113
46	Crack Growth-on-Loading for 2.29 mm (0.090 inch) Thick 2219-T62 Aluminum Base Metal.	114
47	No Growth Loci for 2.29 mm (0.090 inch) Thick 2219-T62 Aluminum Base Metal.	115
48	Crack Growth Occuring During Sizing for 2.29 mm (0.090 inch) Thick 2219-T62 Aluminum Base Metal, $(a/2c_i) = 0.1$.	116
49	Distribution of Cracks in a Typical Structure	117
50	Baseline Cyclic Crack Growth Rates for 2.29 mm (0.090 inch) Thick 2219-T62 Aluminum BM at 295K (72°F) and $R = 0$.	118
51	Baseline Cyclic Crack Growth Rates for 2.29 mm (0.090 inch) Thick 2219-T62 Aluminum BM at 78K (-320°F) and $R = 0$.	119
52	Baseline Cyclic Crack Growth Rates for 2.29 mm (0.090 inch) Thick 2219-T62 Aluminum WM at 295K (72°F) and 78K (-320°F) and $R = 0$.	120
53	Baseline Cyclic Crack Growth Rates for 4.57 mm (0.180 inch) Thick 2219-T62 Aluminum BM at 295K (72°F) and $R = 0$.	121
54	Baseline Cyclic Crack Growth Rates for 4.57 mm (0.180 inch) Thick 2219-T62 Aluminum BM at 78K (-320°F) and $R = 0$.	122
55	Baseline Cyclic Crack Growth Rates for 4.57 mm (0.180 inch) Thick 2219-T62 Aluminum WM at 295K (72°F) and 78K (-320°F) and $R = 0$.	123
56	Baseline Cyclic Crack Growth Rates for 7.62 mm (0.300 inch) Thick 2219-T62 Aluminum BM at 295K (72°F) and $R = 0$.	124
57	Baseline Cyclic Crack Growth Rates for 1.02 mm (0.040 inch) Thick Inconel X750 STA BM at 295K (72°F) and $R = 0$.	125
58	Baseline Cyclic Crack Growth Rates for 1.02 mm (0.040 inch) Thick Inconel X750 STA BM at 78K (-320°F) and $R = 0$.	126

LIST OF ILLUSTRATIONS (Cont.)

<u>Figure</u>		<u>Page</u>
59	Baseline Cyclic Crack Growth Rates for 1.02 mm (0.040 inch) Thick Inconel X750 STA WM at 295K (72°F) and 78K (-320°F) and R = 0.	127
60	Baseline Cyclic Crack Growth Rates for 3.30 mm (0.130 inch) Thick Inconel X750 STA BM at 295K (72°F) and R = 0.	128
61	Baseline Cyclic Crack Growth Rates for 3.30 mm (0.130 inch) Thick Inconel X750 STA BM at 78K (-320°F) and R = 0.	129
62	Baseline Cyclic Crack Growth Rates for 3.30 mm (0.130 inch) Thick Inconel X750 STA WM at 295K (72°F), and 78K (-320°F) and R = 0.	130
63	Baseline Cyclic Crack Growth Rates for 0.71 mm (0.028 inch) Thick Cryostretched 301 Stainless Steel BM at 295K (72°F) and 78K (-320°F) and R = 0.	131
64	Baseline Cyclic Crack Growth Rates for 0.71 mm (0.028 inch) Thick Cryostretched 301 Stainless Steel WM at 295K (72°F) and 78K (-320°F) and R = 0.	132
65	Baseline Cyclic Crack Growth Rates for 2.54 mm (0.100 inch) Thick Cryostretched 301 Stainless Steel BM at 295K (72°F) and 78K (-320°F) and R = 0.	133
66	Baseline Cyclic Crack Growth Rates for 2.54 mm (0.100 inch) Thick Cryostretched 301 Stainless Steel WM at 295K (72°F) and 78K (-320°F) and R = 0.	134
67	Comparison of Cyclic Crack Growth Rates With and Without Sizing Cycle for 2.29 mm (0.090 inch) Thick 2219-T62 Aluminum BM at 295K (72°F).	135
68	Comparison of Cyclic Crack Growth Rates With and Without Sizing Cycle for 4.57 mm (0.180 inch) Thick 2219-T62 Aluminum BM at 295K (72°F).	136
69	Comparison of Cyclic Crack Growth Rates With and Without Sizing Cycle for 7.62 mm (0.300 inch) Thick 2219-T62 Aluminum BM at 295K (72°F).	137

LIST OF ILLUSTRATIONS (Cont.)

<u>Figure</u>		<u>Page</u>
70	Cyclic Crack Growth Rate Constants for 2219-T62 Aluminum ($R = 0$).	138
71	Cyclic Crack Growth Rate Constants for Inconel X750 STA ($R = 0$).	139
72	Cyclic Crack Growth Rate Constants for Cryostretched 301 Stainless Steel BM and WM ($R = 0$).	140
73	Cyclic Crack Growth Rates for 2.29 mm (0.090 inch) Thick 2219-T62 Aluminum BM at 295K (72°F) and Various R Ratios.	141
74	Cyclic Crack Growth Rates for 4.57 mm (0.180 inch) Thick 2219-T62 Aluminum BM at 295K (72°F) and Various R Ratios.	142
75	Cyclic Crack Growth Rates for 7.62 mm (0.300 inch) Thick 2219-T62 Aluminum BM at 295K (72°F) and Various R Ratios.	143
76	Cyclic Crack Growth Rates for 1.02 mm (0.040 inch) Thick Inconel X750 STA BM at 295K (72°F) and Various R Ratios.	144
77	Cyclic Crack Growth Rates for 3.30 mm (0.130 inch) Thick Inconel X750 STA BM at 295K (72°F) and Various R Ratios.	145
78	Cyclic Crack Growth Rates for 0.71 mm (0.028 inch) Thick Cryostretched 301 Stainless Steel BM at 295K (72°F) and Various R Ratios.	146
79	Cyclic Crack Growth Rates for 2.54 mm (0.100 inch) Thick Cryostretched 301 Stainless Steel BM at 295K (72°F) and Various R Ratios.	147
80	Influence of R Ratio on Cyclic Crack Growth Rates for 2.29 mm (0.090 inch) Thick 2219-T62 Aluminum BM at 295K (72°F).	148
81	Influence of R Ratio on Cyclic Crack Growth Rates for 4.57 mm (0.180 inch) Thick 2219-T62 Aluminum BM at 295K (72°F).	148
82	Influence of R Ratio on Cyclic Crack Growth Rates for 7.62 mm (0.300 inch) Thick 2219-T62 Aluminum BM at 295K (72°F).	149

LIST OF ILLUSTRATIONS (Cont.)

<u>Figure</u>		<u>Page</u>
83	Influence of R Ratio on Cyclic Crack Growth Rates for 1.02 mm (0.040 inch) Thick Inconel X750 STA BM at 295K (72°F).	149
84	Influence of R Ratio on Cyclic Crack Growth Rates for 3.30 mm (0.130 inch) Thick Inconel X750 STA BM at 295K (72°F).	150
85	Influence of R Ratio on Cyclic Crack Growth Rates for 0.71 mm (0.028 inch) Thick Cryostretched Steel BM at 295K (72°F).	150
86	Influence of R Ratio on Cyclic Crack Growth Rates for 2.54 mm (0.100 inch) Thick cryostretched 301 Stainless Steel BM at 295K (72°F).	151
87	Comparison of Uniaxial and Tank Test Cyclic Crack Growth Rates for 2.29 mm (0.090 inch) Thick 2219-T62 Aluminum BM at 295K (72°F).	152
88	Comparison of Uniaxial and Tank Test Cyclic Crack Growth Rates for 2.29 mm (0.090 inch) Thick 2219-T62 Aluminum BM at 78K (-320°F).	153
89	Comparison of Uniaxial and Tank Test Cyclic Crack Growth Rates for 2.29 mm (0.090 inch) Thick 2219-T62 Aluminum WM at 295K (72°F).	154
90	Comparison of Uniaxial and Tank Test Cyclic Crack Growth Rates for 2.29 mm (0.090 inch) Thick 2219-T62 Aluminum WM at 78K (-320°F).	155
91	Comparison of Uniaxial and Tank Test Cyclic Crack Growth Rates for 1.02 mm (0.040 inch) Thick Inconel X750 STA BM at 295K (72°F).	156
92	Comparison of Uniaxial and Tank Test Cyclic Crack Growth Rates for 1.02 mm (0.040 inch) Thick Inconel X750 STA BM at 78K (-320°F).	157
93	Comparison of Uniaxial and Tank Test Cyclic Crack Growth Rates for 1.02 mm (0.040 inch) Thick Inconel X750 STA WM at 295K (72°F).	158

LIST OF ILLUSTRATIONS (Cont.)

<u>Figure</u>		<u>Page</u>
94	Comparison of Uniaxial and Tank Test Cyclic Crack Growth Rates for 1.02 mm (0.040 inch) Thick Inconel X750 STA WM at 78K (320°F).	159
95	Influence of Assumed Initial Crack Shape on Cyclic Life for 4.57 mm (0.18 inch) 2219-T62 Aluminum BM.	160
96	Service Life for 2219-T62 Aluminum Liners (BM) at RT - Initial Flaw Shape of 0.10.	161
97	Service Life for 2219-T62 Aluminum Liners (BM) at RT - Initial Flaw Shape of 0.030.	162
98	Service Life for 2219-T62 Aluminum Liners (BM) at RT - Initial Flaw Shape of 0.050.	163
99	Service Life for 2219-T62 Aluminum Liners (WM) at RT - Initial Flaw Shape of 0.10.	164
100	Service Life for 2219-T62 Aluminum Liners (WM) at RT - Initial Flaw Shape of 0.3.	165
101	Service Life for 2219-T62 Aluminum Liners (WM) at RT - Initial Flaw Shape of 0.5.	166
102	Service Life for Inconel X750 STA Liners (BM) at RT - Initial Flaw Shape of 0.10.	167
103	Service Life for Inconel X750 STA Liners (BM) at RT - Initial Flaw Shape of 0.30.	168
104	Service Life for Inconel X750 STA Liners (BM) at RT - Initial Flaw Shape of 0.50.	169
105	Service Life for Inconel X750 STA Liners (WM) at RT - Initial Flaw Shape of 0.10.	170
106	Service Life for Inconel X750 STA Liners (WM) at RT - Initial Flaw Shape of 0.3.	171
107	Service Life for Inconel X750 STA Liners (WM) at RT - Initial Flaw Shape of 0.50.	172

LIST OF ILLUSTRATIONS (Cont.)

<u>Figure</u>		<u>Page</u>
108	Service Life for Cryoformed 301 Stainless Steel Liners (BM) at RT - Initial Flaw Shape of 0.1.	173
109	Service Life for Cryoformed 301 Stainless Steel Liners (BM) at RT - Initial Flaw Shape of 0.3.	174
110	Service Life for Cryoformed 301 Stainless Steel Liners (BM) at RT - Initial Flaw Shape of 0.5.	175
111	Service Life for Cryoformed 301 Stainless Steel Liners (WM) at RT - Initial Flaw Shape of 0.1.	176
112	Service Life for Cryoformed 301 Stainless Steel Liners (WM) at RT - Initial Flaw Shape of 0.3.	177
113	Service Life for Cryoformed 301 Stainless Steel Liners (WM) at RT - Initial Flaw Shape of 0.5.	178
A1	Aluminum Failure Stress Relationship Between Curved and Flat Panels Containing a Surface Flaw.	229
A2	Comparison of Experimental and Analytical Stresses for 2.29 mm (0.090 inch) Thick 2219-T62 Aluminum Cap Specimen.	230
A3	Analytical Stresses for 4.57 mm (0.18 inch) Thick 2219-T62 Aluminum Cap Specimen	231
A4	Analytical Stresses for 7.62 mm (0.30 inch) Thick 2219-T62 Aluminum Cap Specimen.	232
A5	Analytical Stresses for 2.01 mm (0.080 inch) Thick Inconel X750 STA Cap Specimen.	233
A6	Strain Gage Results for 2.29 mm (0.090 inch) Thick 2219-T62 Aluminum Cap Specimen	234
A7	Effective Stress vs. Effective Strain for 2.29 mm (0.090 inch) Thick 2219-T62 Aluminum	235

LIST OF TABLES

<u>Table</u>		<u>Page</u>
1	Uniaxial Static Fracture Test Matrix	179
2	Equal Biaxial Static Fracture Test Matrix	180
3	Tank Burst Test Matrix	181
4	Uniaxial Cyclic Life Test Matrix	182
5	Tank Cyclic Life Test Matrix	183
6	Summary of Mechanical Properties of the Liner Materials	184
7	Material/Specimen Utilization	185
8	Heat Treatment of Liner Materials	186
9	Mechanical Properties of 7.62 mm (0.300 inch) 2219-T62 Aluminum at 295K (72°F)	187
10	Uniaxial Static Fracture Tests of 2219-T62 Aluminum	188
11	Uniaxial Cylinder Burst Tests of 2219-T62 Aluminum	189
12	Equal Biaxial Static Fracture Tests of 2219-T62 Aluminum Spherical Cap Specimens	190
13	Equal Biaxial Static Fracture Tests of Inconel X750 STA Spherical Cap Specimens	192
14	Burst Tests of Tanks with Cryoformed 301 Stainless Steel Liners at 78K (-320°F).	193
15	Uniaxial Cyclic Tests of 2.29 mm (0.090 inch) 2219-T62 Aluminum	194
16	Uniaxial Cyclic Tests of 4.57 mm (0.180 inch) 2219-T62 Aluminum	199
17	Uniaxial Cyclic Tests of 7.62 mm (0.300 inch) 2219-T62 Aluminum	204

LIST OF TABLES (Cont.)

<u>Table</u>		<u>Page</u>
18	Uniaxial Cyclic Tests of 1.02 mm (0.040 inch) Inconel X750 STA	208
19	Uniaxial Cyclic Tests of 3.30 mm (0.130 inch) Inconel X750 STA	212
20	Uniaxial Cyclic Tests of 0.71 mm (0.028 inch) Cryostretched Stainless Steel BM	214
21	Uniaxial Cyclic Tests of 2.54 mm (0.100 inch) Cryostretched 301 Stainless Steel BM	216
22	Uniaxial Cyclic Tests of 2219-T62 Aluminum Without Sizing Cycle	218
23	Illustration of Numeric Integration Procedure to Determine Cyclic Life	220
B1	Cyclic Life Calculation for Example ($R = 0$)	242

SUMMARY

This experimental program was undertaken to establish a fracture control method for composite tanks with load sharing liners. The tanks under consideration here have metallic liners which are filament overwrapped. After fabrication the tanks are subjected to a pressure cycle (called sizing) which plastically deforms the liner. Subsequent pressurization of the tank stresses the metallic liner from residual compression to tension while the filament overwrap material is stressed from residual tension to tension. The tanks are generally designed so that the metallic liner carries about 1/2 the membrane load at maximum operating pressure.

The establishment of a fracture control method for these tanks is based on the premise that the plastic sizing cycle acts as an effective proof test of the metallic liner, screening out all flaws larger than a critical size. In doing so, flaw growth potential is available to allow cyclic operation at pressure levels less than the sizing pressure. To that end, tests were conducted with specimens made of candidate liner materials containing precracked semi-elliptical surface flaws. The type of specimens utilized were (1) flat uniaxial specimens, (2) spherical cap specimens, (3) glass filament overwrapped cylinders, and (4) all-metal cylinders made of 2219-T62 aluminum, Inconel X750 STA and cryoformed 301 stainless steel. Base metal and weld metal tests were conducted. The tests were divided into two areas: Those dealing with (1) static fracture (what size flaw is screened by the sizing cycle) and (2) cyclic life (at what rate did flaws grow when subjected to the operating environment after experiencing a sizing cycle). The variables investigated in the static fracture testing included temperature, material thickness, flaw depth, flaw shape, and stress field. In the cyclic life testing the variables were temperature, material thickness, flaw depth, flaw shape, sizing stress level, minimum and maximum operating stress level, and stress field.

The uniaxial static fracture testing demonstrated that the failure stress of surface flawed specimens is related to flaw size by the equation $\sigma = \sigma_{ult} - A/t^m (a/Q)_i$

where the parameter A is material strength related and the parameter m is constant. The relationship is valid above a stress of $0.90 \sigma_{ys}$ and there is a limiting material thickness (t_c) above which value the failure loci is defined by the above equation with $t = t_c$, where $t_c \approx 0.6 (K_{IE}/\sigma_{ys})^2$. Equal biaxial static fracture testing also demonstrated that the relationship above described the failure loci and was the same for the uniaxial tests of Inconel and 301 stainless steel materials. Only the aluminum material exhibited a stress field dependency, where the failure stress in a biaxial stress field was higher than that developed in a uniaxial stress field. The failure relationship was still described by the above equation, but the values of A and m took on different values than those developed in a uniaxial stress field. This difference between the uniaxial and biaxial static fracture results decreased as the specimen thickness increased. The failure of over-wrapped tanks could be described by the uniaxial static fracture results for Inconel and 301 stainless liners and by equal biaxial static fracture results for the aluminum liners. The reason for this biaxial dependency of static fracture results in aluminum and not in Inconel or 301 stainless steel is unknown. Stable crack growth can occur during sizing, but it was shown that if an overwrapped tank successfully passes the sizing cycle without leaking or failing, the subsequent cyclic operation at a reduced pressure can be assured with a relatively high confidence level by assuming that the final crack size existing after the sizing cycle is equal to the critical flaw size based on initial flaw size static fracture data.

The cyclic life testing demonstrated that the crack growth rates for the liner materials tested at a $\sigma_{min}/\sigma_{max}$ (R) ratio of zero in a uniaxial stress field can be adequately described by the equation $da/dN = C K_{max}^n$ where C and n are empirically defined parameters. Stress level, flaw size and flaw shape parameters are accounted for in the calculation of stress intensity (K). The crack growth rates were found to increase for negative R ratios compared to data developed at $R = 0$ and the same maximum cyclic stress level (σ_{max}). This effect of R ratio, both positive and negative, could be accounted for in the crack growth rate equation presented above by the inclusion of the parameter B such that $da/dN = C B K_{max}^n$. The

value of B was found to be dependent upon the material, thickness, maximum stress level and R ratio. Uniaxial cyclic crack growth rates which incorporate negative R ratio effects correlated extremely well with those developed from overwrapped tanks that were cyclic tested. It was concluded from the testing accomplished that the service life of overwrapped tanks could be determined using crack growth rate data developed in a uniaxial stress field and stress range of the liner under investigation.

An applications section describing how to use the data developed on the program is presented along with a life analysis for parametric studies.

1.0 INTRODUCTION

This document presents the results of a program designed to establish a fracture control method which would guarantee the service life of composite tanks with load sharing liners. The type of tanks being considered have filament overwrapped (OW) metal liners which are pressurized on the first cycle until the metallic liner yields a predetermined amount and then the pressure is released. The filament overwrap material remains elastic throughout this pressure or sizing cycle. Upon releasing the pressure, the filament and liner stresses decrease and reach a condition of force and displacement equilibrium. In this state, the liner is in compression and the filaments are in tension. The stress range for the metal liner on subsequent operating cycles is from compression at zero tank pressure to tension (always less than the liner stress at the sizing pressure) at tank operating pressure. The liner, as well as the filament overwrap, is assumed to operate elastically during an operating pressure cycle. The sizing operation and subsequent operating cycles are schematically illustrated in Figure 1.

In general, the service life of all-metal tanks can be guaranteed by an effective proof test based on the application of linear elastic fracture mechanics. The proof stress cycle screens out all flaws or defects above the critical size and thereby provides assurance of a certain amount of flaw growth potential available for cyclic operation at reduced stresses (less than proof value) before tank failure can occur. It was anticipated that as with a proof test of an all-metal tank, the sizing cycle of a composite tank with load sharing liner acts as an effective proof test, thereby screening out flaws above a specific size in the metallic liner. Contrary to the case of the all-metal tank where proof and operating stresses are below the material's yield strength and linear elastic fracture mechanic principles apply, the sizing stress cycle for the type of composite tanks under consideration here takes place well above the material's yield strength. Linear elastic fracture mechanics principles do not apply in this regime and therefore it was necessary to develop an empirical data base with which to assess these types of composite tanks. The approach to assessing the allowable service life of composite tank liners is schematically illustrated in Figure 2.

The basic approach was to establish correlation between surface flawed uniaxial and biaxial static fracture and cyclic life specimens so that uniaxial specimen tests could be used to generate the large amounts of data required. The biaxial specimens were primarily overwrapped tanks with surface flawed liners and it would not be economically feasible to generate this fracture data using this type specimen. Once the correlation was established between overwrapped tanks and uniaxial specimens, uniaxial specimens could then be used to assess the influence of pertinent variables on the service life of overwrapped tanks. This empirical approach was basically divided into two areas; (1) static fracture and (2) cyclic life behavior. The static fracture tests dealt with determining the stress versus flaw size failure locus so that at a given sizing stress, the critical flaw size could be established. The cyclic life tests dealt with determining the cyclic crack growth rates and the pertinent parameters influencing those rates so that the number of operating cycles to grow a flaw from the critical size screened by the sizing cycle to the point of leakage or fracture could be predicted. The candidate liner materials tested were 2219-T62 aluminum, Inconel X750 STA, and cryostretched 301 stainless steel; base metal (BM) and weld metal (WM).

This program was conducted over a period extending from July 1971 to February 1975. The efforts of the first year and one-half were published as an Interim Report (Reference 1). The detailed results of the tests conducted since the publication of the Interim Report are contained herein along with a complete summary of the data generated over the entire program and final conclusions.

2.0 TECHNICAL APPROACH

2.1 Background

At the beginning of this contract a parametric design study was conducted by Structural Composites Industries to aid designers in selecting weight optimum glass fiber composite tanks with load sharing liners for specific design conditions. This work was published as a Design Guide (Reference 2). Given the overwrap tank operating pressure, required volume, available tank space, metal shell material, and an assumed operating to sizing metal shell stress ratio, the necessary equations and design curves are presented in Reference 2 to completely establish the tank design. First, the vessel shape is established using the volume relationships presented in Reference 2, along with the volume and envelope requirements. Once the shape has been selected, the liner and composite thicknesses and stresses, burst strength, performance factor and vessel weight can be determined. No attempt is made in the Design Guide to establish the service life of these overwrapped tanks. To that end a fracture program was initiated to (1) verify the basic assumption that the sizing cycle acts as an effective proof test, thereby providing assurance of subsequent safe operation and (2) provide an adequate data base to perform life assessments for a wide range of overwrapped tanks and operating conditions. It was not economically feasible to use flawed overwrapped tanks to develop the large data base desired, so it was decided that a limited number of tank tests would be conducted and the results compared to the results of similar tests of uniaxial specimens. If correlation was not obtained, the pertinent parameters affecting the differences would then be established and appropriate changes in the testing would be initiated.

The first phase of the fracture testing program was completed in March 1973, and the results at that time were published as an Interim Report (Reference 1). This testing centered around the testing of surface flawed uniaxial specimens and tanks (primarily hoop overwrapped) with surface flawed liners. Differences were observed in comparing these results and, therefore, additional testing was initiated to resolve these differences. The following paragraphs summarize the work presented in the Interim Report

and describes the testing approach taken since the publication of that report. The overall test program is presented in Tables 1 through 5.

2.2 Brief Summary of the Interim Report

From the Design Guide, tank designs which incorporated hoop glass overwrapped cylinders with hemispherical ends were established for three liner materials; (1) 2219-T62 aluminum, (2) Inconel X750 STA and (3) cryoformed 301 stainless steel. Based on these designs, uniaxial and biaxial (tank) specimens containing artificially induced surface flaws were fabricated and tested at 295K (72°F) and 78K (-320°F). Uniaxial specimens for each liner material investigated were either pulled to failure or cycled to leakage at a $\sigma_{\min}/\sigma_{\max}$ ratio (R) of zero. Tank specimens with 2219-T62 aluminum and Inconel X750 STA liners were either burst or cyclic tested. The material thicknesses investigated in the Interim Report for the various materials are presented below:

Liner Material	Specimen Type	
	Uniaxial	Tank
2219-T62 Aluminum	2.29 mm (0.090 inch) 4.57 mm (0.180 inch)	2.29 mm (0.090 inch)
Inconel X750 STA	1.02 mm (0.040 inch) 3.30 mm (0.130 inch)	1.02 mm (0.040 inch)
Cryoformed 301 Stainless Steel	0.71 mm (0.028 inch) 2.54 mm (0.100 inch)	Not Tested

The static fracture and cyclic life results obtained from the uniaxial and tank specimens were compared to determine the extent that the uniaxial results could be used to predict the overwrapped tank fracture behavior. The comparisons resulted in the following observations:

- (1) Uniaxial surface flawed static fracture results can be used to predict burst test failures for hoop overwrapped Inconel X750 STA tanks with surface flawed liners having thicknesses of about 1.02 mm (0.040 inch).
- (2) Uniaxial surface flawed static fracture results underestimate the burst strength of hoop overwrapped 2219-T62 aluminum tanks with surface flawed liners having thicknesses of about 2.29 mm (0.090 inch). This difference ranged from about 10 to 35% in the thickness tested.
- (3) The cyclic life of both hoop overwrapped Inconel and aluminum tanks containing surface flawed liners are overestimated by uniaxial surface flawed specimens, with tank specimens exhibiting as much as a factor of six increase in crack growth rates.

2.3 Testing Approach Since the Interim Report

Testing since publication of the Interim Report was primarily directed at:

- (1) Resolving the differences observed between the uniaxial static fracture and tank burst test results; particularly for the 2.29 mm (0.090 inch) thick 2219-T62 aluminum liner material,
- (2) Resolving the differences observed between the uniaxial cyclic life and tank service life test results; for both the 2219-T62 aluminum and Inconel X750 STA liner materials,
- (3) Establishing the influence of controlling parameters on the static fracture and cyclic life behavior of the candidate liner materials. These parameters included flaw size, flaw shape, material thickness and stress level,
- (4) Further evaluation of cryoformed 301 stainless steel as a liner material by burst testing hoop overwrapped cylinders.

2.3.1 Static Fracture Differences

The problem of increased static fracture strength for the aluminum lined tanks compared to the uniaxial specimens posed a puzzle since the Inconel lined tank results agreed very favorably with the uniaxial specimen results. It should be remembered that only one thickness of each liner material was investigated by performing tank burst tests; the liner thicknesses were 2.29 mm (0.090 inch) for the 2219-T62 aluminum and 1.02 mm (0.040 inch) for the Inconel X750 STA. The parameters which possibly could have influenced these results were reviewed. From this review the parameters most likely to be causing the differences observed were selected, which were;

- (1) liner curvature and shell stiffness, and
- (2) biaxial stresses.

In reference to liner curvature effects, it was speculated that with the flat uniaxial specimen, the presence of the surface flaw offsets the neutral axis in the immediate vicinity of the crack causing a local bending moment and giving rise to an additional tension stress at the flaw tip and a reduction in the back surface stress directly behind the crack. This idea is in agreement with the experimental results presented in Reference 3 which demonstrated that the rear surface directly behind the flaw can actually go into compression depending upon the applied tension stress and flaw depth-to-thickness ratio. This local bending moment might be eliminated in the case of a curved shell where the stiffness due to curvature, tank material and thickness effectively react it and the result would be essentially a pure tension field over the remaining ligament below the crack. In the flat uniaxial specimen, the material is essentially free to deflect laterally and, therefore reacts the bending with the material beneath the crack. Also, the uniaxial specimens were visually observed during loading to deflect laterally in the immediate vicinity of the flaw, giving more credibility to the idea. An effectively higher tensile stress at the crack tip for a given applied stress would cause the uniaxial specimens to fail at a lower load than one in a curved specimen. In addition, this idea could

also explain why the Inconel tank results agreed with the uniaxial results while the aluminum tank results did not. The Inconel liner which was tested had a lower shell stiffness and, therefore, would not effectively react the local bending moment at the flaw tip.

Tests were conducted to prove or disprove the idea that the curvature was the primary factor in the observed phenomena. Two types of tests were conducted. The first tests involved the positioning of anti-deflection bars or plates on the front and back side of uniaxial aluminum specimens; thereby reducing the lateral movement of the flaw while loading to failure. The results of these tests agreed with the non-restrained tests conducted earlier. To further evaluate the curvature effect hypothesis, burst tests were conducted using surface flawed cylindrical sections in which the longitudinal pressure load was not carried by the cylinder, but by end plates and connecting bolts. This basically subjects a surface flaw in a curved shell to a uniaxial stress field. These results also agreed with the standard uniaxial static fracture tests conducted earlier. These two types of tests conclusively demonstrated that the tank curvature had no effect on the static fracture results and therefore it was deduced that the differences observed in the static fracture results between the uniaxial specimens and tank tests were due to the differences in stress field.

Other investigators have either observed similar phenomena or predicted it. Work by Kibler and Roberts (Reference 4) showed that the apparent plane stress fracture toughness is elevated due to biaxial stresses when failures occur at or near the material yield strength. Recent theoretical analysis by Hilton (Reference 5) involving large scale yielding for cracked plates subjected to biaxial loading (see Figure 3) indicates that as the stress parallel to the crack increases the failure stress perpendicular to the crack also increases. Previous testing of preflawed uniaxial and tank specimens in the elastic range (Reference 6) does not show this dependence of failure stress at a given flaw size or fracture toughness on biaxial stresses.

Based on the information gained from the static fracture tests conducted and briefly discussed in the preceding paragraphs, it was decided that it was necessary to develop static data in an equal biaxial stress field for various thicknesses of liner materials. Spherical cap specimens were designed which accomplished this. In addition to determining the effects of thickness upon the static fracture results in an equal biaxial stress field, the influence of flaw shape was also investigated with these specimens.

The results of these tests showed that for the aluminum material investigated, the biaxial stress field had a definite effect on the static fracture results; increasing the failure stress at a given crack size compared with uniaxial results. The effect also increased as the material thickness decreased for the aluminum. These equal biaxial results agreed very well with the corresponding cylindrical tank results for the same thickness of material; 2.29 mm (0.090 inch); thereby verifying that the differences observed and reported in Reference 1 were indeed biaxial stress field effects. As pointed out in Paragraph 2.2, uniaxial surface flawed static fracture results for 1.02 mm (0.040 inch) Inconel agreed with the corresponding cylindrical tank results, thereby indicating that biaxial stresses had no influence for this material at that thickness. This conclusion was further substantiated by spherical cap Inconel specimen tests.

Cylindrical tanks (overwrapped and non-overwrapped) of cryoformed 301 stainless steel were burst tested and the results of these tests agreed with the uniaxial static fracture results as did the Inconel material. The reason for the biaxial dependency of static fracture results in aluminum and not in Inconel or 301 stainless steel is presently not known.

2.3.2 Cyclic Life Differences

The problem of significantly decreased cyclic life of overwrapped tank tests compared to uniaxial specimen tests, as reported in the Interim Report, was evaluated as follows. The uniaxial data used in this comparison was developed at an R ratio of zero, whereas the overwrapped tank data was developed at R values ranging

from +0.20 to -0.86; with the majority at negative R values. As pointed out in the introduction, with the type of tanks being considered herein, the liner normally operates from a compressive stress at zero operating pressure to a tensile stress at maximum operating pressure. This condition produces a negative stress ratio.

The first and final step in improving the correlation of uniaxial and overwrapped cyclic life data was to include the compressive portion of the operational stress cycle in the surface flawed uniaxial cyclic testing. Loading of uniaxial specimens in compression was accomplished by fitting side plates to a standard flat specimen which effectively increased the column stability. With the inclusion of this portion of the stress cycle, excellent agreement was obtained between uniaxial and overwrapped tank cyclic life results.

Various investigators have conducted fatigue crack growth tests utilizing compression/tension loading. Hudson/Scardina (Reference 7), Illg/McEvily (Reference 8) and Donaldson/Andersen (Reference 9) have developed fatigue crack growth rate data for 2024-T3 and 7075-T6 aluminum incorporating the compression portion of the loading cycle. These investigators have observed only a very slight effect, if any, of compression/tension testing compared to zero/tension testing. This data was developed using through-the-thickness crack specimens. Crooker (Reference 10) investigated negative R ratio effects on 9Ni-4Co-0.20C steel, HY-80 steel and 6Al-4V titanium using 22.9 mm (0.90 inch) thick surface flawed specimens. At R values of -1.0, Crooker showed that a 50% increase in fatigue crack growth rates was obtained. The negative R effects uncovered during the testing reported herein was found to be significant and a function of both the maximum tensile stress and material thickness at a constant R value. As the maximum tensile stress increased, the cyclic crack growth rates increased, whereas as the material thickness increased the rates generally decreased. In Crooker's testing of steels and titanium, the applied cyclic stresses were relatively low (approx. $0.50 \sigma_{ys}$) and the material thickness was relatively thick [($t = 22.9$ mm (0.90 inch))]. Both conditions would tend to reduce the effects of the compression portion of the loading cycle on the cyclic crack growth rates.

From the results presented herein and, at least in part, substantiated by other investigators, it appears that the effects of crack growth rates of compression/tension testing as compared to zero/tension can be significant for thin surface flawed materials subjected to moderate-to-high stresses.

2.3.3 Establishing the Influence of Controlling Factors

Considerable testing of the liner materials was accomplished to determine how the stress and flaw parameters affected service life. Specifically, the flaw size, flaw shape and material thickness were investigated with uniaxial static fracture tests. Initial flaw shapes ranged from 0.1 to 0.4 and in addition to the thicknesses previously tested (as reported in the Interim Report) one more thickness of 2219-T62 aluminum was added; 7.62 mm (0.300 inch). Flaw sizes were selected such that failure would occur at stresses generally above the material's yield strength.

Other testing was also accomplished which included cyclic life testing of uniaxial specimens to determine the influence of flaw shape, material thickness, sizing stress, maximum cyclic stress and R ratio on the cyclic crack growth rates. Again, initial flaw shapes ranged from 0.1 to 0.4 and as indicated for the static fracture testing, one more thickness of 2219-T62 aluminum was added. Tests were generally conducted at one specific sizing stress, except several tests which were conducted without having a sizing cycle prior to performing the cyclic test. Maximum cyclic stress levels ranged from 38 to 85% of the sizing stress level with R ratios ranging from +0.5 to -2.0.

2.3.4 Completion of the Overwrapped Tank Testing

During the Interim Report period, uniaxial specimens made of aluminum, Inconel and 301 stainless steel were fracture tested along with overwrapped tanks made of aluminum and Inconel. To complete this testing, overwrapped tanks having 301 stainless steel liners were burst tested. Again, the object was to compare these results and, if correlation was established, the uniaxial data could then be used to assess the service life of overwrapped tanks.

3.0 MATERIALS AND PROCEDURES

3.1 Materials

The three liner materials investigated in this experimental program were 2219-T62 aluminum, Inconel X750 STA and cryostretched 301 stainless steel. S-glass with epoxy resin was used as the overwrap material for the composite tanks. A summary of all the metallic mechanical properties developed for these materials is presented in Table 6. These are average values and were obtained parallel to the rolling direction. The properties for the aluminum and Inconel were developed by loading tensile specimens directly to failure at the test temperature while the properties of the stainless steel were obtained in a different manner as discussed below.

Considerable straining at liquid nitrogen temperature is required to obtain the desired strength level of cryoformed 301 stainless steel for use as an overwrapped tank liner. This straining is accomplished in two steps. First, the all-metal liner is plastically stretched (pressurized) at 78K (-320°F); this stress cycle is hereafter referred to as prestressing. Next, the liner is overwrapped, subjected to a thermal cycle to cure the overwrap and then subjected to a sizing cycle at 78K (-320°F). The sizing cycle is a continuation of the cryogenic plastic stretching process which strengthens the 301 material. This cryogenic stretching process, called cryoforming, causes the material to change from an austenitic to a martensitic structure. The 301 mechanical properties at 78K (-320°F) were obtained with specimens that were subjected to a cryogenic prestress (σ_{ps}) cycle of 932 MN/m^2 (135 ksi) and then loaded to failure at the same temperature. The properties shown in Table 6 are the result of the second cryogenic stretch. The 301 mechanical properties at 295K (72°F) were obtained with specimens that were subjected to (1) a cryogenic prestress cycle of 932 MN/m^2 (135 ksi), (2) a simulated resin cure cycle of 340K (150°F) for 3 hours followed by 420K (300°F) for 5 hours, (3) a cryogenic sizing cycle to 1442 MN/m^2 (209.2 ksi) and (4) finally pulled to failure at room temperature. Because of the excessive deformation that takes place during the

prestress cycle, all mechanical properties for the 301 material are based on the specimen dimensions at the beginning of the second cryostretch.

The material specifications and thicknesses used to fabricate the various specimens reported in this report are presented in Table 7. The 2219 aluminum thicknesses of 3.18 mm (0.125 inch) and 6.35 mm (0.250 inch) were purchased in the T87 temper and then fully annealed prior to final heat treatment. The aluminum thicknesses of 12.7 mm (0.500 inch) and 29.4 mm (1.156 inch) were purchased in the O temper and then final heat treated. The Inconel and 301 stainless steel materials were purchased in the annealed condition and all materials were heat treated per Table 8.

Detailed mechanical property tests were conducted for the 7.62 mm (0.300 inch) thick uniaxial aluminum specimens tested herein and the results of these tests are presented in Table 9. Mechanical property test results for Inconel, 301 stainless steel and other thicknesses of aluminum tested previously are contained in Reference 1.

3.2 Specimen Fabrication

Uniaxial, open-ended cylinders, spherical cap, all-metal cylinders and hoop overwrapped cylinders were fabricated for the testing reported herein. The specimens used for tests reported in the Interim Report are contained in that report. Detailed descriptions of the specimens used to develop data for this report are presented below.

3.2.1 Uniaxial Specimens

All flat uniaxial specimens used for the testing reported herein were fabricated per Figure 4. The only welded specimens tested were made from the 12.7 mm (0.50 inch) 2219-T62 aluminum material. These specimens were electron beam welded and then machined down to a test section thickness of 7.62 mm (0.300 inch). To introduce surface flaws into the uniaxial specimens a starter notch with a terminating radius of less than 0.076 mm (0.003 inch) was electric discharge

machined (EDM) into the specimen. The EDM starter notch was then extended using low stress/high cycle fatigue; periodic examinations were conducted, using a microscope, to determine when a fatigue crack had been initiated around the entire periphery of the EDM notch. Precracking stresses for the aluminum, Inconel and stainless steel materials were as high as 138 (20), 483 (70), and 345 (50) MN/m^2 (ksi), respectively, depending upon the starter notch sharpness and depth relative to the specimen thickness. Precracking operations were done in air at room temperature at a frequency of 30 Hz (1800 cpm). All uniaxial specimens were subjected to a simulated resin cure cycle after precracking of 340K (150°F) for 3 hours followed by 420K (300°F) for 5 hours. The 301 uniaxial specimens were first flawed, then subjected to a cryogenic prestress cycle of 932 MN/m^2 (135 ksi) followed by the simulated resin cure cycle described previously. The results of subsequent tests of the 301 specimens were based on the physical dimensions of the specimen after the prestress cycle. Considerable straining takes place during the prestressing operation resulting in a thinning of about 6%. If the specimens original dimensions were used to calculate stresses throughout testing, significant errors would result. Thinning of all three materials tested as a result of the sizing cycle is about 1%, thus engineering stress/strain closely approximates true stress/strain if the specimen dimensions prior to sizing are used.

3.2.2 Open-Ended Cylinder Specimens

Open-ended cylindrical 2219-T62 aluminum sections as illustrated in Figure 5 were fabricated by roll forming, seam welding, heat treating and machining to thickness. Surface cracks were introduced as previously described, but precracking was accomplished by internally pressurizing the cylinders in a test setup as shown in Figure 6. Precracking operations were done in lab air at a frequency of 1 Hz (60 cpm).

3.2.3 Spherical Cap Specimens

The spherical cap specimens tested are illustrated in Figure 7. Pre-cut material in the fully annealed state was draw-formed into a dome, heat treated and then

machined to the desired dimensions. The heat treatments of the 2219 aluminum and Inconel X750 materials were accomplished per Table 8. Two basic configurations were established; one of 178 mm (7.0 inch) radius and another of 254 mm (10.0 inch) radius. This was done primarily to minimize the effects of the radius of curvature. The design and stress details for these spherical cap specimens are presented in Appendix A. Surface cracks were introduced as previously described for uniaxial specimens while precracking was done by internally pressurizing the spherical cap specimens as shown in Figure 8. The stresses required to precrack the spherical cap specimens were as high as 276 MN/m^2 (40 ksi) for the aluminum and 524 MN/m^2 (76 ksi) for the Inconel. Precracking operations were done in lab air at a frequency of 1 Hz (60 cpm).

3.2.4 301 SS Tank Specimens

The 301 stainless steel liners that were tested were supplied by NASA/Lewis and conformed to the sketch presented in Figure 9. These cylindrical tanks were fabricated by Ardé, Inc. to drawing E-3793. Both hoop overwrapped and non-overwrapped 301 tanks were fabricated and tested. A design analysis was performed by Ardé, Inc. to establish the S-glass hoop overwrapped thickness, prestress and sizing stress levels utilizing these 301 liners. Prior to introducing the surface flaws, the liners were subjected to a pressure cycle at room temperature (RT) to develop a hoop stress of 344 MN/m^2 (50 ksi). After the RT pressure cycle, a surface crack starter notch was introduced and precracked by internal pressure. This procedure was arrived at after several premature leaks at the weld fusion line occurred during precracking of the starter notches when introduced prior to the tank being subjected to a pressure cycle. Applying a pressure cycle prior to introducing the starter notch, reduced the number of cycles required to obtain a fully precracked flaw. The precracking operation was performed at room temperature at a hoop stress of 310 MN/m^2 (45 ksi) and at a frequency of 1Hz (60 cpm). After flawing, the tanks were cleaned per Ardé specification AES 253D, annealed per AES 251A, pickled per AES 250D and passivated per AES 254C. Once these

processes were completed, the tanks were cryogenically prestressed at 78K (-320°F) in a stretch die to a pressure of 13.8 MN/m^2 (2000 psi). This stretch die was cylindrical in shape with a 145 mm (5.70 inch) inside diameter. The pressure required to stretch the tank or liner to equal the inside diameter of the stretch die was 10.6 MN/m^2 (1540 psi). An overpressurization to 13.8 MN/m^2 (2000 psi) was used to bring the cylinder-to-head intersection out to the die. This prestress cycle subjected the tank to a nominal hoop stress of 711 MN/m^2 (103 ksi) at 78K (-320°F). The liners to be tested as hoop overwrapped cylinders were wound with S-glass and epoxy resin per SCI specification procedure 1269430 and cured. All 301 stainless steel liners that were tested as all-metal tanks were subjected to a simulated resin cure cycle of 340K (150°F) for 3 hours followed by 420K (300°F) for 5 hours.

3.3 Specimen Test Procedures

Uniaxial, open-ended cylinders, spherical cap, all-metal cylinders and hoop overwrapped cylinders were tested to determine the static fracture behavior of the liner materials under investigation. The specimens used to develop the cyclic data were the same ones used to develop the static fracture data with the exception of the spherical cap specimens which were used only for static fracture data. The test procedures used for the tests reported herein are presented in the following paragraphs. Test procedures used for tests reported in the Interim Report are contained in that report.

3.3.1 Uniaxial Static Fracture Tests

Uniaxial specimens used to determine the static fracture behavior of the liner materials were all surface flawed and instrumented with pressure cups, as depicted in Figure 10. Low pressure, 3.45 kN/m^2 (5 psi), gaseous helium was supplied to the pressure cup opposite the surface flaw during specimen test. The non-pressurized pressure cup transducer output was observed as a function of uniaxial specimen load on an x-y plotter during the test to determine if and at what load the surface flaw

broke through-the-thickness. Specimens were tested at a loading rate such that failure occurred in about one minute after initial load application.

Uniaxial specimens with flaw restraint plates positioned over the flaw during loading were also static fracture tested. This test arrangement is illustrated in Figure 11. Procedures used were identical to those employed for the uniaxial specimens without restraint plates.

3.3.2 Uniaxial Cyclic Life Tests

Uniaxial specimens used to determine the cyclic life behavior of the liner materials were all surface flawed and instrumented with pressure cups as described for the uniaxial static fracture specimens.

The majority of the cyclic life specimens tested were instrumented to measure the crack opening displacement (COD) on the surface as the flaw grew due to cyclic loading. The change in flaw opening displacement can be related to the change in flaw size and instantaneous flaw growth rates can be calculated per the analysis outlined in Paragraph 3.4.

The aluminum and Inconel cyclic life specimens were sized to stresses of 332 (48.2) and 850 (123.3) MN/m^2 (ksi) at RT prior to being cycled at the selected operating stress levels. The cryostretched 301 stainless steel specimens were sized at 1442 MN/m^2 (209.2 ksi) at 78K (-320°F) then proof tested to 1234 MN/m^2 (179.0 ksi) at RT followed by cyclic testing at RT.

A majority of the uniaxial specimens tested and reported herein received a simulated sizing stress cycle and then were cycled from tension to compression until crack breakthrough occurred. To prevent the thin, flat specimens from buckling under the compressive load, side plates were employed as depicted in Figure 12. A photograph of a tension/compression specimen in test is shown in Figure 13. Teflon tape, 0.127 mm (0.005 inch) thick, was applied to the side plates in order to reduce the sliding friction between the plates and the specimen. A checkout specimen

(unflawed) was strain gaged to determine the amount of load transfer between the plates and specimen. The results of this test showed that no load was transferred between the two. A typical stress/strain plot for an aluminum specimen subjected to a compression load after receiving a simulated sizing cycle is presented in Figure 14. This plot shows a significant amount of Bauschinger effect. The design of overwrapped metallic liners assumes that the liner remains elastic during pressure unloading. As shown in Figure 14, tank designs having high residual compressive stresses (at zero tank pressure) do not behave elastically and for the particular case shown an additional 50% increase in strain results.

All cyclic testing was accomplished using sinusoidal loading at 0.8 Hz (50 cpm).

3.3.3 Open-Ended Cylinder Tests

Open-ended cylindrical sections were burst tested in a uniaxial stress field in a test setup as shown in Figure 6. When internally pressurized with hydraulic fluid, the longitudinal load is not carried by the test specimen but by the bolt arrangement that structurally transfers the load between the end restraint plates. These specimens were pressurized at a rate to cause failure in from one to two minutes after pressure initiation.

3.3.4 Spherical Cap Tests

Spherical cap specimens were burst tested in a test setup as pictorially shown in Figure 15. The detailed description of the two test setups utilized is presented in Figure 8. These specimens were also pressurized with hydraulic fluid at a rate to cause failure or leakage in about one to two minutes after pressure initiation.

3.3.5 301 Stainless Steel Tank Tests

Burst tests were conducted with hoop overwrapped and non-overwrapped cryoformed 301 stainless steel liners at 78K (-320°F) using liquid nitrogen. Flaw leak detection and hoop deflection measurement devices, as described in Interim Report,

were used in testing these tanks when required. These tanks were also pressurized at a rate to cause failure or leakage in about one to two minutes.

3.4 Cyclic Crack Growth Rate Analysis

In general, the cyclic crack growth rates were determined by the expression:

$$\frac{da}{dN} = \frac{\Delta a}{\Delta N} \quad (1)$$


where: $\frac{da}{dN}$ = cyclic crack growth rate
 Δa = change in crack depth
 ΔN = number of load cycles which propagated the crack depth an amount Δa .

The majority of cyclic specimens were instrumented with a crack opening displacement (COD) device so that the crack depth as a function of applied cycles could be determined and consequently instantaneous crack growth rates. The COD for a surface flaw can be approximated by the expression: (Details are presented in Reference 1)

$$\delta = \alpha \frac{\sigma a}{\sqrt{Q}} \quad (2)$$

where δ = crack opening displacement ($\delta_{max} - \delta_{min}$)
 α = constant
 σ = applied stress
 a = crack depth
 Q = crack shape parameter, $f(a/2c, \sigma/\sigma_{ys})$ (see Figure 16)

The value of α can be determined at test initiation and termination from knowledge of the stress level, initial and final flaw sizes, and the corresponding COD as indicated below:

 For specimens which were sized prior to cycling, the sizing stress was substituted for σ_{ys} in the determination of Q .

$$\alpha_i = \frac{\delta_i}{\sigma} \left(\frac{\sqrt{Q}}{a} \right)_i; \alpha_f = \frac{\delta_f}{\sigma} \left(\frac{\sqrt{Q}}{a} \right)_f \quad (3)$$

where the subscripts *i* and *f* refer to initial and final conditions, respectively.

The value of α tends to increase with increasing crack size, rather than remain constant. Crack growth rate calculations in this report were based on an assumed linear variation in α between the known initial and final values.

In order to relate the flaw parameter (a/\sqrt{Q}) to δ for values of (a/\sqrt{Q}) between the initial and final values an assumption must be made as to the manner in which the flaw shape changes from test initiation to termination. It was assumed that the percentage of flaw depth (*a*) growth relative to the total change in flaw depth is equal to the percentage of flaw length (*2c*) growth relative to the total change in flaw length. This relationship is presented in the following equation:

$$\frac{a - a_i}{a_f - a_i} = \frac{2c - 2c_i}{2c_f - 2c_i} \quad (4)$$

The flaw shape parameter (*Q*) can now be determined as a function of flaw depth and, in turn, can be related to COD using Equation 2. The number of cycles (*N*) corresponding to each selected flaw depth value can be determined from the test record and, consequently the ΔN for each increment of flaw depth is known. A series of da/dN data points are then derived from a single specimen where COD measurements are made and analyzed per the above discussion, as opposed to a single data point for a non-instrumented test specimen. Consequently, fewer instrumented specimens are required to adequately define the fatigue crack growth rates as a function of stress intensity.

For specimens which were not instrumented with a COD device, an average cyclic crack growth rate was determined by the expression:

$$\frac{da}{dN} = \frac{a_f - a_i}{N} \quad (5)$$

where: a_i = initial crack depth
 a_f = final crack depth
 N = total number of cycles

The cyclic crack growth rates were plotted herein as a function of the maximum stress intensity (K_{max}). The K_{max} was calculated using the equation:

$$K_{max} = 1.1 \sigma_{max} \left(\frac{\pi a}{Q} \right)^{1/2} M_{km} \quad (6)$$

where: K_{max} = max. stress intensity
 σ_{max} = max. applied stress
 M_{km} = deep flaw magnification factor from Reference 11
 $f(a/2c, a/t)$ (see Figure 17)

The result of plotting the cyclic crack growth rates as a function of the maximum stress intensity was a linear relationship on log-log paper which can be represented by the equation:

$$\frac{da}{dN} = CB K_{max}^n \quad (7)$$


where: C = empirical constant based on $R = 0$ baseline data
 B = empirical constant which accounts for R ratio effects
 n = empirical constant

4.0 STATIC FRACTURE AND BURST TEST RESULTS

Static fracture and burst tests were conducted to determine the load carrying capability of the liner materials containing semi-elliptical surface cracks. The tests were conducted using (1) flat specimens loaded in a uniaxial stress field ($\sigma_x/\sigma_y = 0$), (2) open-ended cylinders subjected to internal pressure (uniaxial stress field with $\sigma_x/\sigma_y = 0$), (3) spherically shaped domes subjected to internal pressure (an equal biaxial stress field with $\sigma_x/\sigma_y = 1.0$), (4) cylindrical tanks subjected to internal pressure (a biaxial stress field with $\sigma_x/\sigma_y = 0.5$), or (5) hoop overwrapped cylinders subjected to internal pressure (a biaxial stress field with $\sigma_x/\sigma_y \approx 1.0$). The following paragraphs describe and compare the static fracture behavior in uniaxial and biaxial stress fields for the liner materials considered. In addition, a discussion of the crack growth that can occur during sizing is presented.

4.1 Static Fracture in a Uniaxial Stress Field

Flat specimens made of 2219-T62 aluminum, Inconel X750 STA and cryostretched 301 stainless steel containing surface cracks were loaded to failure to develop the relationship between the failure stress and crack size in a uniaxial stress field. The majority of these tests were conducted to obtain failure data above the material's yield strength. These specimens were instrumented to detect if crack breakthrough occurred during loading and, if so, at what stress level. All of the uniaxial flat specimen static fracture data developed on this program are analyzed in this section. The test results obtained prior to the Interim Report are contained in that report, while the test results obtained since are contained in Table 10.

Initially, static fracture results were analyzed as a function of failure or leakage stress and initial  crack depth. Typical results presented in this manner are:

 The reference to "initial" refers to the conditions prior to specimen loading.

shown in Figures 18, 19 and 20 for the three thicknesses of 2219-T62 aluminum base metal (BM) tested at 295K (72°F). These results show a significant effect of crack shape; the crack depth screened by a given sizing stress decreases as the crack shape ratio decreases (i.e., as $a/2c$ goes from 0.4 to 0.1). All results shown in Figures 18, 19 and 20 had a fail mode-of-failure (MOF) with the exception of two specimens shown in Figure 18. One specimen with a crack shape of 0.2, exhibited a leak MOF followed by a fail MOF with just a fractional increase in stress. The other specimen, with a crack shape of 0.4, had an initial crack depth essentially equal to the material thickness and the specimen leaked at a gross stress of 75% of the failure stress, and was not representative of the tests conducted in this program. The other static fracture specimens either failed prior to leakage or leaked and subsequently failed with less than a 5% increase in stress.

4.1.1 Crack Shape Effects

To normalize the crack shape effects, the results of the static fracture tests were plotted as a function of failure stress and the initial crack size parameter, $(a/Q)_i$ (where a_i is the initial crack depth and Q_i is the initial crack shape parameter defined in Fig. 16). This approach works extremely well for the data developed and is graphically illustrated in Figure 21. For a given material thickness, the failure loci for the 2219-T62 aluminum base metal can be described as a single straight line when plotted as a function of a/Q . This relationship can be described using the equation:

$$\sigma = \sigma_{ult} - S(a/Q)_i \quad (8)$$

where





- σ = failure stress
- σ_{ult} = ultimate material strength (typical values)
- S = slope of the failure loci
- a = flaw depth
- Q = flaw shape parameter
- i = refers to initial conditions

1 Abrupt fracture.

2 When $\sigma/\sigma_{ys} > 1.0$, a value of $\sigma/\sigma_{ys} = 1.0$ is used to determine Q .

It is also evident from Figure 21 that for a given flaw size, the failure stress increases as the material thickness increases.

To further develop this representation of the failure of uniaxially loaded surface flawed specimens, all of the uniaxial static fracture data presented in Reference 1 were re-analyzed. These results are presented in Figures 22 through 30 as a function of failure or leakage stress versus the initial crack size $(a/Q)_i$. These figures cover 2219-T62 aluminum, Inconel X750 STA and cryostretched 301 stainless steel as presented below:

UNIAXIAL STATIC FRACTURE RESULTS				
Material		Test Temp. K (° F)	Material Thicknesses Tested mm (Inch)	Ref. Figure
2219-T62 Aluminum	BM	295 (72)	2.29 (0.090), 4.57 (0.180), 7.62 (0.300)	21
		78 (-320) 	2.29 (0.090), 4.57 (0.180)	22
	WM	295 (72)	2.29 (0.090), 4.57 (0.180), 7.62 (0.300)	23
		78 (-320) 	2.29 (0.090), 4.57 (0.180)	24
Inconel X750 STA	BM	295 (72)	1.02 (0.040), 3.30 (0.130)	25
		78 (-320) 		26
	WM	295 (72)		27
		78 (-320) 		28
Cryostretched 301 SS	BM	78	0.71 (0.028), 2.54 (0.100)	29
	WM	(-320)		30

 Sized at RT prior to being loaded to failure at test temperature.

The results of this analysis paralleled those obtained for the 2219-T62 aluminum base metal at 295K (72°F); exhibiting a linear failure loci for a given material thickness when plotted as a function of $(a/Q)_i$. The data for the 2219-T62 aluminum and Inconel X750 STA was generated at or above the material yield strength (σ_{ys}), whereas the data developed for the 301 stainless steel material were obtained at stress levels ranging from 25% of the material's ultimate strength (σ_{ult}) up to σ_{ult} at 78K (-320°F). This stress range for the 301 material includes the area where the structural transformation takes place (from an austenitic to martensitic). The results shown in Figures 29 and 30 for the 301 material indicate several specimens which failed somewhat above the proposed failure loci. It is believed that these specimens were not fully precracked and consequently exhibited a higher failure stress than a specimen with a fully precracked flaw. The combination of extremely small flaws of around 0.25 mm (0.010 inch) deep and a very ductile material made precracking exceptionally difficult in the 301 material. The starter notches in some cases would appear to crack somewhat and then stop, even though additional load cycles were applied. Based on this, it was decided that the linear representation of the failure loci shown in Figures 29 and 30 adequately describe the failure results for the 301 material at 78K (-320°F).

4.1.2 Failure Loci Definition

As pointed out in the previous discussion, the failure loci for a given material appeared to increase as the material thickness increased. The manner in which the failure loci varied with thickness was investigated by plotting the slope of the failure loci (S) versus material thickness on log-log graph paper for each of the material/temperature combinations tested. The result was a straight line for each material as shown in Figure 31, which indicates the relationship between the failure loci slope (S) and the material thickness (t) is of the form:

$$S = \frac{A}{t^m} \quad (9)$$

where: t = material thickness
 A, m = constants

Therefore, Equation (9) can be substituted into Equation (8) to yield:

$$\sigma = \sigma_{ult} - \frac{A}{t^m} (a/Q)_i \quad (10)$$

The parameter, A, appears to be material dependent; increasing as the material strength increases as shown in Figure 31. The value of the parameter m appears relatively constant, varying between 0.59 and 0.87, with most of the data being represented by an m value of 0.74.


4.1.3 Extrapolation to Other Materials

Can the failure loci of other materials at or above their yield strength be described in a like manner as presented in Paragraph 4.1.2? The room temperature failure loci for 2219-T87 aluminum (Reference 12), 7075-T651 aluminum (Reference 13 and 6Al-4V STA titanium (Reference 3) are shown in Figures 32, 33 and 34. Again the results were basically the same; exhibiting a linear relationship between failure stress and initial crack size $(a/Q)_i$. The slopes of these failure loci along with additional data developed for 7075-T6 aluminum, 2219-T87 aluminum and 6Al-4V STA titanium are presented as a function of material thickness in Figure 35. The results are very consistent with the test results developed herein and presented in Figure 31. The slope (S) in Equation 8 appears to be limited to a value equal to the slope tangent to the critical fracture toughness (K_{IE}) curve, as illustrated in Figures 33 and 34. This essentially means that above a critical material thickness (t_c) the slope (S) remains constant in Equation 8. The value of t_c can be determined if the fracture toughness and the ultimate strength of the material are known or can be estimated. Therefore, it appears that for failures occurring above $0.90 \sigma_{ys}$, the failure loci in a uniaxial stress field can be described for most materials using Equation 8 or 10 with the limiting condition described above. Where failures occur below $0.90 \sigma_{ys}$, linear elastic fracture mechanic methods can be used to describe the failure. It also appears that the value of t_c is equal to $0.60 (K_{IE}/\sigma_{ys})^2$ for the materials investigated.

The fact that the 2219-T62 aluminum and Inconel X750 STA static fracture results are described by Equation 10 indicates that these tests were performed on material thicknesses that are less than those required to yield linear elastic fracture results (where $\sigma \geq 0.90 \sigma_{ys}$). This might be expected since these are very tough materials, exhibiting fracture toughnesses probably greater than $55 \text{ MN/m}^{3/2}$ ($50 \text{ ksi}\sqrt{\text{in}}$) for the 2219-T62 aluminum, and $110 \text{ MN/m}^{3/2}$ ($100 \text{ ksi}\sqrt{\text{in}}$) for the Inconel X750 STA.


4.1.4 Failure Prediction Limitations

The failure relationship of Equation 10 is a useful tool in describing the plastic failure behavior of uniaxially stressed structures containing surface defects or cracks. By knowing the material's thickness, ultimate strength, crack size, parameter A (dependent upon the ultimate strength of the material) and the parameter m (only slightly material dependent), the failure stress can be predicted for failures which occur at or above the material's yield strength. The following limitations should be observed when using Equation 10 to describe the fracture behavior of metals:

1. uniaxial stress field
2. $\sigma \geq 0.90 \sigma_{ys}$
3. failure stress occurs within 5% of the flaw breakthrough stress 
4. when $t \geq t_c \approx 0.60 (K_{IE}/\sigma_{ys})^2$, t_c should be used in Equation 10
5. applicable to moderate to high ductility materials

It should be pointed out that some work in this area was recently done by Bonesteel (Reference 13) where the failure stress was presented as a function of $\frac{a}{t^{1/2} \phi^2}$

where $\phi^2 = Q + 0.212 (\sigma/\sigma_{ys})^2$ and a linear relationship was obtained primarily for thin sections of aluminum. For failures at or above the material yield

 The data analyzed herein either exhibited a fail MOF or leak MOF followed by a fail MOF with less than a 5% increase in applied stress.

strength, the value of $\phi^2 = Q + 0.212$ and the relationship used by Bonesteel becomes $\frac{a}{t^{1/2} (Q + 0.212)}$. This expression is very similar to the normalizing relationship arrived at in the work completed herein; $\frac{a}{t^m Q}$, where m takes on a value of about 0.74.

4.1.5 Curvature Effects

During the course of the program several special tests were conducted in an attempt to separate the curvature effects from the biaxial stress effects with regard to the static fracture data. Substantial differences were observed between flat uniaxial and cylindrical tank (non-overwrapped and hoop overwrapped) aluminum liner material static fracture results. The differences are discussed in detail in Paragraph 4.3, but it suffices at this point to indicate that the failure stress for the tanks was higher than that of the flat uniaxial specimens for the same crack size. It was initially speculated that with the flat uniaxial specimen the presence of the surface flaw offsets the neutral axis in the immediate vicinity of the crack causing a bending moment and giving rise to an additional tension stress at the flaw tip. The crack located in a cylindrical tank is also stressed in a similar manner except that the stiffness due to curvature, tank material and thickness effectively react the local bending moment across the crack front and the result is essentially a pure tension field over the remaining ligament below the crack. In the flat uniaxial specimen, the material is essentially free to deflect laterally and, therefore, reacts the bending with the material beneath the crack. These types of differences could account for the high apparent static fracture strength of the tank specimens over flat uniaxial specimens.

In order to prove or disprove the possible explanation, a simple test was conducted using two flat uniaxial specimens. Flat restraint plates were fitted over the flaw as depicted in Figure 11 and the retaining fasteners torqued until the plates were snug against the flat fracture specimen. The intent of the restraint plates was to prevent the specimen material in the flaw area to displace perpendicular to the plane of the

specimen. This displacement was readily observable when loading unrestrained flat uniaxial specimens and is a necessary condition if local bending is taking place. By eliminating this lateral movement it was speculated that the local bending would be eliminated. The results of these two tests are presented in Figure 36 along with the unrestrained flat specimen results. The failures were within the scatterband of the unrestrained data. From these tests it appeared that the effects observed in the static fracture results between flat uniaxial specimens and tanks cannot be accounted for by the tank curvature.

To further evaluate if the tank curvature was affecting the static fracture results, additional tests were conducted. These tests involved the use of flawed cylindrical sections in which the longitudinal pressure load was not carried by the cylinder, but by end plates and connecting bolts. A sketch of the test setup is presented in Figure 6. By eliminating the longitudinal stress in the cylinder, the surface crack was subjected only to a uniaxial stress field. By comparing curved and flat uniaxial static fracture data the effects of curvature can be directly assessed. The results of these curved uniaxial static fracture tests are presented in Figure 37 for both the base metal (BM) and weld metal (WM) material. The detailed results are contained in Table 11. As the figure indicates, the curved uniaxial results fell within the scatterband of the flat uniaxial results and thereby conclusively illustrated that the tank curvature had no effect on the static fracture results. From these tests it was deduced that the differences observed in the static fracture results between the uniaxial specimens and tank tests were due to the differences in stress field (uniaxial versus biaxial).

4.2 Static Fracture in a Biaxial Stress Field

Spherical cap specimens, all-metal cylindrical tanks and overwrapped cylindrical tanks containing surface flaws were burst tested. The spherical cap specimens developed an equal biaxial stress field ($\sigma_x/\sigma_y = 1.0$), while the cylindrical tank specimens developed biaxial stress fields ($\sigma_x/\sigma_y = 0.5, \approx 1.0$) dependent upon whether or not the cylinders were hoop overwrapped or not. The results of the static fracture (burst) tests conducted using these various specimen configurations are presented in the following paragraphs.

4.2.1 Spherical Cap Results

Spherical cap specimens, as indicated in Figure 7, were surface flawed at the apex and pressurized internally until either leakage or rupture occurred. Caps made of 2219-T62 aluminum and Inconel X750 STA were tested at room temperature. The aluminum thicknesses tested were 2.29 (0.090), 4.57 (0.180), and 7.62 (0.300) mm (inch), while the Inconel thickness tested was 2.07 mm (0.082 inch). All test specimens were of base metal (BM) material. The results of these tests are presented in Figures 38 and 39 for the 2219-T62 aluminum and Inconel X750 STA materials, respectively; while the detailed data for each specimen tested are presented in Tables 12 and 13. The results of these tests were very consistent and, as with the uniaxial static fracture data developed, a linear relationship of stress and crack size (a/Q), prevailed.

The aluminum results shown in Figure 38 demonstrated that the failure stress increases as the material thickness increases for a given crack size. The slope (S) of the failure loci for a given material thickness is, in general, less for the equal biaxial static fracture results than the uniaxial results. This is the same observation reported in the Interim Report. More on this subject is discussed in Paragraph 4.3 dealing with the correlation of static fracture results in various stress fields.

4.2.2 Cylindrical Tank Results

Cylindrical liners made of 2219-T62 aluminum, Inconel X750 STA and cryoformed 301 stainless steel were burst tested as all-metal tanks and hoop overwrapped tanks at room temperature and 78K (-320°F). Surface flaws were located in both the BM and WM. The liner thicknesses tested were 2.29mm (0.090 inch) for the aluminum, 1.02mm (0.040 inch) for the Inconel and 0.89mm (0.035 inch) for the stainless steel. The results of these burst tests are presented in Figures 40 through 44. The detailed data for each specimen are contained in Reference 1 for the aluminum and Inconel, and in Table 14 for the 301 stainless steel. Several tanks did not fail at the artificially induced surface flaws and are identified by an arrow attached

to the data point in the figures, indicating that failure at the flaw would have occurred at a higher stress level. In general, the all-metal tank static fracture results agreed with the OW tank results. The correlation of this data with the data developed using uniaxial and equal biaxial specimens are discussed in the following paragraph.

4.3 Correlation of Static Fracture Results

The static fracture results obtained from uniaxial specimens ($\sigma_x/\sigma_y = 0$), spherical cap specimens ($\sigma_x/\sigma_y = 1.0$), all-metal cylindrical tank specimens ($\sigma_x/\sigma_y = 0.5$) and hoop overwrapped cylindrical tank specimens ($\sigma_x/\sigma_y = 0.81-1.69$) are compared in this paragraph.

Figure 40 shows the effect of a biaxial stress field on the static fracture results of the 2.29 mm (0.090 inch) 2219-T62 aluminum BM and WM tested at room temperature. The uniaxial static fracture results for this material/thickness underestimate the failure stress for a given crack size in an overwrapped (OW) tank, whereas the equal biaxial results either agreed with the OW tank results or were slightly conservative. Apparently, in this thin gage of aluminum the biaxial stress field has a definite effect on the failure stress of surface flawed structure above the material's yield strength. Figure 40 does illustrate that the OW tank results appear to approach the uniaxial results as deeper flaws are introduced and gross failure stresses approach about $0.90 \sigma_{ys}$. Figure 41 shows the effect of a biaxial stress field for the same thickness of aluminum tested at 78K (-320°F). At this temperature the BM uniaxial and OW tank specimen results agree while the WM uniaxial results underestimate the failure stress for a given flaw size compared to the OW tank WM results.

The fact that the uniaxial static fracture results, in general, underestimate the failure stress for this thin gage of aluminum compared to OW tank results is important because if uniaxial data was used to estimate the flaw size screened by the sizing cycle, a smaller flaw size would be obtained than would be actually screened by an OW tank. This would result in an apparent flaw growth potential available


for cyclic operation greater than would actually exist and, consequently, a longer operational life would be calculated. This result would be unconservative for OW tanks having thin gage aluminum liners. Using the static fracture results obtained in an equal biaxial stress field to predict the flaw size screened by the sizing cycle would yield a result that closely approximates the OW tank behavior for 2219-T62 aluminum liner thicknesses less than 6.60 mm (0.260 inch). For thicknesses greater than 6.60 mm (0.260 inch) the uniaxial results should be used.


Figure 42 shows the effect of a biaxial stress field on the static fracture results of 1.02 mm (0.040 inch) Inconel X750 STA BM and WM tested at room temperature. The uniaxial static fracture results for this material/thickness agree very well with the OW tank results. Apparently, in this gage of Inconel, the biaxial stress field has no effect on the failure stress. Additional evidence of no biaxial stress field influence for this material is shown in Figure 39 where 2.08 mm (0.082 inch) Inconel spherical cap specimen static fracture data is shown. The failure loci obtained for this thickness would have been predicted based on the uniaxial results discussed in Paragraph 4.1.2. Figure 43 shows the effect of a biaxial stress field for a liner thickness of 1.02 mm (0.040 inch) tested at 78K (-320°F). At this temperature the uniaxial static fracture results slightly overestimate the failure stress of the OW tank results for a given flaw size. Thus, for Inconel X750 STA use of the static fracture results obtained in a uniaxial stress field to predict the flaw size screened by the sizing cycle yields a result that closely approximates the OW tank behavior.

Figure 44 shows the effect of a biaxial stress field on the static fracture results of 0.89 mm (0.035 inch) cryoformed 301 stainless steel BM tested at 78K (-320°F). Uniaxial data was obtained for this material using thicknesses of 0.71 mm (0.028 inch) and 2.54 mm (0.100 inch), and the OW tank results were only slightly above the 0.71 mm (0.028 inch) thick uniaxial results, indicating that the biaxial stress field had no effect on the failure stress as with the Inconel material. Therefore, using the static results obtained in a uniaxial stress field to predict the flaw size screened by the sizing cycle would yield a result that closely approximates the OW tank behavior if cryoformed 301 stainless steel liners were used.

A summary of the static fracture results is presented in Figure 45, which relates the failure loci slope (S) to the material thickness for the liner materials investigated as was done for the uniaxial static fracture results discussed in Paragraph 4.1. The failure stress for a given flaw size can be determined using Equation 8 if the appropriate value of S is used. As was uncovered in the testing performed herein, the value of S is independent of the stress field for the Inconel and 301 stainless steel material and thicknesses investigated, but was dependent in the case of the aluminum. Figure 45 shows that the value of S is significantly less for a biaxial stress field ($\sigma_x/\sigma_y = 0.5 \rightarrow 1.0$) than a uniaxial one and that the difference decreases as the material thickness increases until a thickness of 6.60 mm (0.260 inch) is reached. It is assumed that above this thickness the failure slope is adequately defined by the uniaxial value.

4.4 Crack Growth Occurring During Sizing

From uniaxial specimens which were subjected to a simulated sizing cycle and then cycled to leakage, crack extension during the sizing cycle was observed. Typical growth-on-loading (GOL) data is shown in Figure 46 for 2.29 mm (0.090 inch) thick 2219-T62 aluminum base metal. This data was obtained from specimens which were loaded to 332 MN/m^2 (48.2 ksi) and then unloaded. Figure 46 shows what final crack size can be anticipated for a given initial crack size for a family of different crack shapes. The initial crack size which causes failure at a sizing stress of 332 MN/m^2 (48.2 ksi) is 1.02 mm (0.040 inch) and is independent of crack shape . Figure 46 illustrates that for a given initial crack size, more crack growth occurs for specimens with a crack shape of 0.1 compared to one of 0.4. Figure 46 also shows that crack growth does not occur until a specific initial crack size is exceeded. The value at which this crack growth is initiated is also crack shape dependent. To illustrate this point more clearly, a failure versus initial crack size curve is shown in Figure 47 for the 2.29 mm (0.090 inch) thick 2219-T62 aluminum. The GOL data presented in Figure 46 was used to establish lines of no-growth for a family of crack shapes. If specimens containing initial cracks are

 The crack shape parameter (Q) normalizes the static fracture data with respect to crack shape as discussed in Paragraph 4.1.1.

stressed above the corresponding no-growth lines, crack extension takes place. This crack extension occurs primarily in the depth direction.

Since considerable crack growth can occur during sizing, how can one be sure of what crack size exists after the sizing cycle? Figure 46 illustrates that the amount of crack growth is asymptotic to the critical initial crack size. It is possible then for a crack to grow to the point of almost failure or leakage and then be unloaded; and upon applying the first operational stress cycle the pressure vessel would fail. With this type of crack growth occurring, how can the sizing cycle act as an effective proof test? The answer to this question lies in the manner in which the crack growth takes place. To illustrate this point, refer to Figure 48 where the crack growth and failure loci are shown for 2.29 mm (0.090 inch) 2219-T62 aluminum base metal having cracks with initial crack shapes of 0.1.

Figure 48 shows what happens to various size cracks present prior to being subjected to a sizing cycle of 322 MN/m^2 (48.2 ksi). This growth data was obtained from the GOL data developed in Figure 46. Initial crack size ① would not grow during sizing, whereas crack ② would grow only a slight amount. Initial crack size ③ would grow to a value ③ equal to the critical initial crack size $[(a/Q)_i^{cr} = ⑥]$ which would cause failure at σ_s . Initial crack size ⑥ which is equal to $(a/Q)_i^{cr}$ would grow to failure along the path described in Figure 48. For initial crack sizes existing between ③ and ⑥ say ④ and ⑤, crack growth would take place with the final crack size being greater than $(a/Q)_i^{cr}$, but less than the final crack size which causes failure or leakage. These crack growth paths for different size initial cracks define 3 distinct regions as indicated below:

- If $(a/Q)_i > (a/Q)_i^{cr} = ⑥$, then the pressure vessel fails or leaks during sizing—(Region III).
- If $(a/Q)_i \leq ③$, then assuming that $(a/Q)_i^{cr}$ was the crack size after sizing would yield a conservative estimate of crack growth potential available and thereby guarantee the cyclic life operation of the pressure vessel based on cyclic crack growth rate data—(Region I).

- If $(a/Q)_i > \textcircled{3}$, but $< (a/Q)_i^{cr} = \textcircled{6}$, then the service life could not be guaranteed by the sizing cycle, because one would not know the final crack size after sizing and the crack size could be of such proportions to cause failure or leakage on the subsequent operational cycle-(Region II).

The initial crack sizes defined by Region II is a very narrow band for the aluminum material when compared to the specimen thickness. A worst case situation is presented in Figure 48 where the initial crack shape was assumed to be 0.1. This Region II defines a crack depth band equal to about 8% of the thickness. Only if the initial crack size is within this narrow band, the sizing cycle does not guarantee the service life of the pressure vessel. This region reduces to about 5% of the thickness if an initial crack shape of 0.2 or greater is assumed.

The question arises "How effective is a proof test or sizing cycle in screening flaws that is based on the approach outlined in the preceding paragraphs?". For sure, if the tank leaks or fails the proof test was 100% effective, but if the pressure vessel passes the proof test, how effective was it? To pursue this further, a schematic representation of the distribution of crack sizes in a fabricated structure is illustrated in Figure 49. The Region II area of flaw sizes or depths is small when compared to the total area, but for the case of a tank which successfully passed a proof test, the Region II area must be compared to the summation of the Regions I and II areas. In the illustration, the Region II area is a small percentage of the total defined by crack sizes less than a_i^{cr} . This is believed to be the general case for the materials investigated.

Based on the above observations, if a pressure vessel successfully passes the sizing cycle without failing or leaking, the subsequent cyclic service life can, in general, be assured with a high confidence level by assuming that the final crack size existing after the sizing cycle is equal to $(a/Q)_i^{cr}$.

5.0 CYCLIC CRACK GROWTH TEST RESULTS

For the liner materials under investigation, 2219-T62 aluminum, Inconel X750 STA and cryostretched 301 stainless steel, cyclic life tests were conducted using pre-cracked surface flawed specimens. Two types of specimens were utilized, flat uniaxial specimens and cylindrical tanks which were either all-metal or hoop over-wrapped. The variables investigated include material (BM and WM), thickness (t), sizing stress level (σ_s), maximum operating stress level (σ_o), minimum-to-maximum operating stress level ratio (R), flaw shape (a/2c), and test temperature (T). Except where noted, these cyclic tests were conducted after subjecting the specimens to simulated resin cure, sizing and proof cycles as applicable. The 2219-T62 aluminum and Inconel X750 STA specimens cycled at a test temperature of 295K (72°F) were first subjected to a 295K (72°F) sizing cycle; whereas, the specimens cycled at a test temperature of 78K (-320°F) were first subjected to a 295K (72°F) sizing cycle, followed by a 78K (-320°F) proof test. The cryostretched 301 stainless steel specimens cycled at a test temperature of 78K (-320°F) were first subjected to a 78K (-320°F) sizing cycle; whereas the specimens cycled at a test temperature of 295K (72°F) were first subjected to a 78K (-320°F) sizing cycle followed by a 295K (72°F) proof test.

The approach used in analyzing these test results was to present the data in terms of cyclic crack growth rate (da/dN) versus the maximum stress intensity (K_{max}), both of which are defined in Paragraph 3.4. This procedure is one used extensively in the analysis of cyclic crack growth rate data developed under linear elastic conditions. Because of the many variables investigated it was decided to establish a baseline set of cyclic crack growth rate data with which to compare data developed by varying specific variables. A baseline was developed for each material, thickness and test temperature with uniaxial specimens subjected to a sizing stress cycle and then cycled at a minimum-to-maximum stress ratio (R) of zero.

5.1 Baseline Uniaxial Cyclic Rate Data

The vast majority of cyclic tests conducted involved uniaxial specimens cycled at an

R ratio of zero and having initial flaw shapes of 0.20. A table summarizing the materials, thicknesses and test temperatures investigated at an R = 0 is presented below:

BASELINE UNIAXIAL CYCLIC RATE TEST PROGRAM (R = 0)				
Material		Test Temp. K (°F)	Material Thicknesses Tested mm (Inch)	Ref. Fig.
2219-T62 Aluminum	BM	295 (72)	2.29 (0.090), 4.57 (0.180), 7.62 (0.300)	50, 53, 56
		78 (-320)	2.29 (0.090), 4.57 (0.180)	51, 54
	WM	295 (72)		52, 55
		78 (-320)		52, 55
Inconel X750 STA	BM	295 (72)	1.02 (0.040), 3.30 (0.130)	57, 60
		78 (-320)		58, 61
	WM	295 (72)		59, 62
		78 (-320)		59, 62
Cryostretched 301 Stainless Steel	BM	295 (72)	0.71 (0.028), 2.54 (0.100)	63, 65
		78 (-320)		63, 65
	WM	295 (72)		64, 66
		78 (-320)		64, 66

The table above also indicates the figures in which the various data results can be found. The details for each specimen tested are presented either in Reference 1 or Tables 15 through 21. These specimens were cycled at a frequency of 0.8 Hz (30 cpm).

Within each baseline set of data, the influence of sizing stress, maximum cyclic stress and flaw shape is incorporated. What effect, if any, the maximum cyclic stress level, sizing stress, crack shape, thickness, temperature and material condition (BM and WM) had on the cyclic crack growth rates are discussed in the following paragraphs.

5.1.1 Cyclic Stress Effects

In general, all of the baseline ($R = 0$) crack growth rate data developed varied linearly with the maximum stress intensity (K_{max}) when plotted on log-log graph paper. The linear relationship indicates that da/dN can be adequately described by the expression given below:

$$\frac{da}{dN} = C K_{max}^n \quad (11)$$

where C and n are empirically defined constants. The cyclic crack growth rate data used to establish each baseline covered a wide range of maximum cyclic stress levels. As with the analysis of surface flawed cyclic crack growth rates under linear elastic conditions, the representation of the rates as a function of stress intensity incorporates the stress level influences. This is done through the calculation of stress intensity which includes both the stress level and flaw size effects.

It is important to note that this linearization of cyclic crack growth rates with the maximum stress intensity for various stress levels only occurs if the deep flaw magnification factor indicated in Equation 6 is incorporated. A layering of the rates as a function of cyclic stress level will occur if this magnification factor is assumed to be unity. For constant specimen thickness, critical crack depth in specimens subjected to high stresses are a smaller percentage of the specimen thickness than in specimens subjected to lower stresses. Hence, stress intensity factors in high stress specimens are not elevated by deep flaw effects as much as in low stress specimens. As a result, cyclic crack growth rates in low stress specimens are increased by deep flaw effects more than for high stress specimens, and, if deep flaw effects are not

accounted for in calculating stress intensity, it would appear that crack growth rates are faster in the low stress specimens than in the high stress specimens at a constant stress intensity. This phenomena was first observed and discussed in Reference 14.

Where instantaneous cyclic crack growth rates were not obtained from COD instrumentation, average rates were calculated based on initial flaw size, final flaw size and number of cycles, and the result plotted at the arithmetic stress intensity average. This approach is satisfactory in defining a crack growth rate curve if the test specimens are not cycled over a very large stress intensity range (approximately a factor of two). As the stress intensity range gets larger, the average rate yields values that are considerably slower than actually experienced. For the cyclic testing of aluminum, Inconel, and the 0.71 mm (0.028 inch) thick 301, the stress intensity range was relatively small and consequently average flaw growth rates adequately described the behavior. The 2.54 mm (0.100 inch) thick 301 material tested was cycled to a final stress intensity that was about three times the initial value. Error would result if the growth rate curve was selected based on the average plotted values. It should be pointed out that this phenomena is not specifically a 301 material related problem, but an analysis problem and could have occurred with Inconel or aluminum specimens.

Since all cyclic flaw growth rate data generated in this program were adequately described by Equation 11, it was decided to generate cyclic life curves using various values of C and n for the thick 301 and to select the constants which best described the cyclic life results. Key specimens were selected which were not cycled over large stress intensity ranges; the actual growth rate curve must pass through those data points. With this as a baseline, values of C and n were selected which best described the cyclic life behavior. As Figure 66 shows, the estimated flaw growth rate curve represents a faster rate than the average rate values would indicate.

5.1.2 Sizing Stress Effects

Where instantaneous cyclic crack growth rates were obtained using COD instrumentation, retardation in those rates was generally observed immediately following the

application of the sizing cycle for specimens cycled at $R = 0$. This phenomena was observed for the 2219-T62 aluminum and Inconel X750 STA, but not for the limited amount of cryostretched 301 stainless steel data obtained. Figures 50, 53, 54, 55, 56, 57 and 60 most readily show this effect. As the ratio of maximum cyclic stress to sizing stress (σ_o/σ_s) decreases, the amount of initial retardation increases. Initial retardation in rates of an order of magnitude were observed for $\sigma_o/\sigma_s = 0.38$, while at $\sigma_o/\sigma_s = 0.75$ the effects were almost nil. Apparently, the zone ahead of the crack is affected by the sizing cycle and at low σ_o/σ_s ratios a significant increase in the number of cycles is required to propagate the crack through this zone. As will be discussed in Paragraph 5.2, dealing with the influence of R ratio on the cyclic crack growth rates, the initial retardation in rates after sizing was only present sporadically and was not a phenomena that could be assured of happening. The fact that the initial retardation was (1) present in some materials only sporadically, (2) not present in all materials cyclic tested at $R = 0$, and (3) not present for all operating stress levels of interest, lead the investigator to basically ignore the phenomena in calculating the service life of overwrapped tanks. This is a conservative approach which becomes more conservative as the maximum cyclic stress level decreases.

The effect of the magnitude of the sizing stress on the cyclic crack growth rates was investigated at 295K (72°F) using 2219-T62 aluminum BM. Specimens were cycled at a σ_o of 249 MN/m^2 (36.1 ksi) without receiving a prior sizing cycle using three thicknesses of aluminum. Both $R = 0$ and negative R values were investigated, and the detail data for these tests are presented in Table 22. The results of these tests are presented in Figures 67, 68 and 69, along with the corresponding results generated with similar specimens subjected to a sizing cycle. For all practical purposes the data generated with specimens not experiencing the sizing cycle fell within the scatter bands of the data generated using specimens which did experience the sizing cycle. It was thus concluded from these tests that the magnitude of the sizing cycle has no influence on the resulting cyclic crack growth rates when cycled at a $\sigma_o = 249 \text{ MN/m}^2$ (36.1 ksi). It is believed that cyclic crack growth rate

data developed at lower cyclic stress levels would be independent of sizing stress level, if the initial retardation was ignored as was the case for the growth rate relationships established herein.

5.1.3 Crack Shape Effects

The influence of crack shape ($a/2c$) on the cyclic crack growth rates was investigated at 295K (72°F) using 2219-T62 aluminum BM. Specimens with initial crack shapes ranging from 0.1 to 0.4 were tested at 249 MN/m² (36.1 ksi) using three thicknesses of aluminum. The results of these tests are presented in Figures 50, 53 and 56. No discernible influence of crack shape was observed within the normal scatter of cyclic data. Apparently, the inclusion of the shape factor (Q) in the calculation of stress intensity (Equation 6) was enough to account for this variable.

It is interesting to note that the flaw shape changed as the flaw propagated. In general, if the initial flaw shape was either 0.1 to 0.2 the final flaw shape at test termination (point at which the flaw penetrated the thickness) was about 0.35 for the aluminum and Inconel and 0.42 for the 301 stainless steel. For specimens having an initial flaw shape of 0.40, the shape remained about constant as the flaw propagated.

5.1.4 Thickness Effects

The influence the material thickness has on the cyclic crack growth rates can most readily be observed in Figures 70, 71 and 72, which present the two empirical constants (C, n) used in Equation 11, which describes the rate behavior of $R = 0$ data. The cyclic crack growth rates are directly proportional to these constants. A consistent trend was not established for all materials investigated, but specific observations were made. The 2219-T62 aluminum rates decrease with increasing thickness with one exception as shown in Figure 70. The weld metal (WM) material tested at 78K (-320°F) showed an increase in cyclic crack growth rates with increasing material thickness. Aluminum thicknesses from 2.29 (0.090) to 7.62 (0.300) mm (inch) were investigated. The Inconel X750 STA rates remained constant for the

base metal (BM), but appeared to decrease with increasing thickness for the WM as shown in Figure 71. Within the range of stress intensities investigated with the 301 stainless steel material, the cyclic crack growth rates decrease with increasing thickness. At stress intensities lower than about $22\text{MN}/\text{m}^{3/2}$ ($20\text{ ksi } \sqrt{\text{in}}$) the opposite is true. The rate curves actually crossed for the two thicknesses of 301 material investigated which were 0.71 (0.028) and 2.54 (0.100) mm (inch). This phenomena can be observed by comparing Figure 63 with 65 and Figure 64 with 66.

5.1.5 Temperature Effects

Cyclic crack growth rates were determined at two temperatures, 295K (72°F) and 78K (-320°F) for the materials tested. In general, as the test temperature decreased the cyclic crack growth rates decreased. Only the 4.57 mm (0.180 inch) thick 2219-T62 aluminum WM (see Figure 55) deviated from this trend, where the influence of temperature was negligible.

5.1.6 Comparison of BM and WM Rates

Again, no general trend was observed in comparing the BM and WM cyclic crack growth rates which were developed. The aluminum WM rates were in all instances higher than the BM rates for the thicknesses of material tested. The Inconel WM rates were higher than the BM rates at the thinnest thickness tested while the opposite was true at thickest thickness tested. With the 301 stainless steel material, the WM and BM rates were equal.

5.1.7 Analytical Description of Baseline Cyclic Crack Growth Rates

As pointed out in Paragraph 5.1.1, the baseline $R = 0$ cyclic crack growth rates can be adequately described by Equation 11 which involves two empirical constants; C and n . For the materials investigated, these constants are defined in Figures 70, 71 and 72 as a function of material condition (BM and WM), thickness and test temperature.

5.2 Effect of R Ratio in a Uniaxial Stress Field

The effect of R ratio on the cyclic crack growth rates was investigated for the liner materials under consideration using flat uniaxial specimens. This effort was primarily directed at the effects of negative R ratios since this is the condition most prevalent in the type of tanks being considered herein. A table summarizing the materials, thicknesses and test temperature investigated is presented below:

EFFECT OF R RATIO TEST PROGRAM				
Material		Test Temp. K (°F)	Material Thicknesses Tested mm (Inch)	Ref. Fig.
2219-T62 Aluminum	BM	295 (72)	2.29 (0.090), 4.57 (0.180), 7.62 (0.300)	73 74 75
Inconel X750 STA	BM	295 (72)	1.02 (0.040), 3.30 (0.130)	76 77
Cryostretched 301 SS	BM	295 (72)	0.71 (0.028), 2.54 (0.100)	78 79

The table above also indicates the figures in which the various data results can be found. The test details for each specimen are presented in Table 15 through 21. All specimens were cycled at a frequency of 0.8 Hz (50 cpm).

These tests showed a significant influence of R ratio; increasing the crack growth rates at negative R values and decreasing the crack growth rates at positive R values relative to the baseline $R = 0$ data. As with the baseline data, the relationship between da/dN and K_{max} was linear when plotted on log-log graph paper, thus indicating the cyclic crack growth rates can be expressed by Equation 7 which is a modified form of Equation 11, where $da/dN = C B K_{max}^n$. The parameter B accounts for R ratio effects. The data presented in Figures 73 through 79 were used to establish values of the parameter B as a function of material, thickness, maximum cyclic stress level and R ratio. These results are presented in Figure 80

through 86; where the parameter B is plotted against the parameter $1-R$. When $R = 0$ the value of B equals unity and Equation 7 reduces to Equation 11; the $R = 0$ baseline growth rate equation. The results presented in Figures 80 through 86 are very consistent, illustrating (1) as R ratio increases (positive R values) the value of B decreases, (2) as R ratio decreases (negative R values) the value of B increases, (3) at negative R values, the value of B increased as the maximum cyclic stress level (σ_o) increases, and (4) at positive R values, the value of B decreases as σ_o increases. From the data generated, there also appears to be material thickness effect on the value of B .

An initial retardation in growth rates was observed immediately following the application of the sizing cycle for some of the tests conducted at negative R values; especially at low maximum operating stresses. This initial retardation was observed for most of the tests conducted at $R = 0$ and discussed in Paragraph 5.1.2. It appears that the presence of compressive stresses tend to negate or reduce the effects of a prior overload. This phenomena was also reported in Reference 15. Since the initial retardation cannot be relied upon to occur especially in the presence of compressive loads (which is the general case in overwrap tank liners), the phenomena was ignored in establishing the parameter B , the factor accounting for R ratio effects in the cyclic crack growth rate equation.

The influence of crack shape was also investigated at negative R values at 295K (72°F) using 2219-T62 aluminum BM. Specimens with initial crack shapes ranging from 0.1 to 0.4 were tested at a σ_o of 249 MN/m³ (36.1 ksi) using three thicknesses of aluminum. The results of these tests are presented in Figures 73, 74 and 75. In Figures 73 [$t = 2.29$ mm (0.090 inch)] and 75 [$t = 7.62$ mm (0.300 inch)] no discernible influence of crack shape was observed within the normal scatter of cyclic data. The data in Figure 74 [$t = 4.57$ mm (0.180 inch)] showed a larger than normal scatter in data. The rates developed with an initial crack shape of 0.4 are considerably faster or higher than those developed at the other crack shapes. This effect was not observed in testing the other two thicknesses of material and therefore it does not seem feasible for there to be a shape effect for only this one

thickness of material. Material differences in the specimens or undetected test machine malfunctions are then the only possible explanations for the phenomena observed.

5.3 Correlation of Uniaxial Cyclic Crack Growth Rates With Tank Test Results

The cyclic test results of the all-metal cylindrical tanks and hoop overwrapped cylindrical tanks reported in Reference 1 were compared to the uniaxial cyclic results presented in the preceding paragraphs. This comparison is made using the cyclic crack growth rates. Only 2219-T62 aluminum and Inconel X750 STA materials were analyzed since no 301 stainless steel tanks were cyclic tested. These results are presented in Figures 87 through 94. The correlation was excellent; with the tank data at each test R value agreeing with the uniaxially developed data within the normal scatter of cyclic data. From this comparison, it appears that uniaxial cyclic specimen results, which incorporate the entire stress environment from positive to negative values, can be used to predict overwrapped tank liner behavior.

5.4 Mode of Failure During Cyclic Tests

For specimens cyclically tested in this program the majority failed by leakage. If this occurred with a liner of an overwrapped tank, pressurant and pressure would be lost. The only specimens which failed before leaking during test either were overloaded or failed in the grips due to tension/compression fatigue.

The leak mode-of-failure (MOF) during cyclic operation could have been anticipated for the combinations of materials, stresses and thicknesses tested. As pointed out in Paragraph 5.1.3, the flaw shape at flaw breakthrough approached steady-state values regardless of the initial flaw shapes. These steady-state flaw shape values were only slightly material dependent, ranging around 0.4 for the materials and flaw orientations tested. When this flaw shape with a depth equal to the thickness is used in calculating the maximum stress intensity obtained during cyclic testing, the results are values which are less than the fracture toughness (K_{IE}). The fracture toughness

is believed greater than $55 \text{ MN/m}^{3/2}$ ($50 \text{ ksi} \sqrt{\text{in}}$) for the 2219-T62 aluminum and $110 \text{ MN/m}^{3/2}$ ($100 \text{ ksi} \sqrt{\text{in}}$) for the Inconel X750 STA and cryoformed 301 stainless steel at room temperature. Catastrophic failure (fast rupture) would be anticipated if the maximum attained stress intensity during cycling equalled the fracture toughness.

6.0 OBSERVATIONS AND CONCLUSIONS

The following major observations were made while testing surface flawed specimens fabricated of 2219-T62 aluminum, Inconel X750 STA and cryoformed 301 stainless steel.

Static Fracture Testing

- (1) The failure stress in a uniaxial stress field ($\sigma_x/\sigma_y = 0$) is related to the surface flaw size by the relationship $\sigma = \sigma_{ult} - A/t^m (a/Q)_i$, where the parameter A appears to be material strength related and the parameter m is constant. The relationship holds only for failures occurring above $0.90 \sigma_{ys}$; for failures below this value, linear elastic fracture mechanic principles should be employed. There appears to be a maximum material thickness (t_c) above which value the failure loci is defined by the above equation with $t = t_c$, where $t_c \approx 0.6 \sqrt{K_{IC}/\sigma_{ys}}$.
- (2) In an equal biaxial stress field ($\sigma_x/\sigma_y = 1.0$), the relationship and parameters developed in a uniaxial stress field presented above holds for the Inconel and 301 stainless steel tested but for the aluminum material, the relationship holds but the parameters A and m take on values different than those developed in a uniaxial stress field. The failure relationship for the aluminum material tested showed that the failure stress in a biaxial stress field was higher than that developed in a uniaxial stress field for the same flaw size. This difference decreased as the material thickness increased until a thickness of 6.60 mm (0.260 inch) was reached, at which point the static fracture data developed in a biaxial stress field was less than in a uniaxial stress field.
- (3) Stable crack growth does occur during loading to failure for the materials investigated.

It was concluded from the observations above that the flaw size screened in the metal liner by the sizing cycle of a OW tank can be determined if the liner material, thickness, sizing stress and biaxiality effects are known. It was also concluded that if an OW tank successfully passes the sizing cycle without leaking or failing, the cyclic operation can be assured with a relatively high confidence level by assuming that the final crack size existing after the sizing cycle is equal to $(a/Q)^{cr}$ based on initial flaw size static fracture data.

Cyclic Life Testing

- (1) For cyclic loading the crack growth rates for the liner materials tested at an R ratio equal to zero in a uniaxial stress field can be adequately described by the equation, $da/dN = CK_{max}^n$, where C and n are empirically defined parameters. The stress intensity parameter in the equation when calculated with a deep flaw magnification factor accounts for stress level, flaw size and flaw shape differences.
- (2) The crack growth rates were found to increase for negative R ratios compared to data developed at $R = 0$ and the same maximum cyclic stress level. This effect, as well as positive values of R , could be accounted for by modifying the crack growth rate equation presented above by the inclusion of the parameter B to yield the equation, $da/dN = CBK_{max}^n$. The value of B was found to be dependent upon the material, thickness, maximum stress level and R ratio.
- (3) Some of the materials exhibited cyclic crack growth retardation immediately following the application of a sizing stress cycle. This retardation decreased as the flaw grew until it was out of the influence of the zone formed by the overload cycle; at which time the growth rates equalled those obtained from non-overloaded specimens. The amount of retardation was related to the cyclic stress/sizing stress ratio; the lower the ratio the more initial retardation.

- (4) The cyclic crack growth rates were found to be material, thickness and temperature dependent.
- (5) Uniaxial cyclic crack growth rates which incorporated negative R ratio effects correlated extremely well with those developed from OW tanks that were cyclic tested.
- (6) A leak mode-of-failure was observed for all the cyclic testing performed.

It was concluded from the observations above that the cyclic life of the metal liner of an OW tank could be determined using crack growth rate data developed in a uniaxial stress field which accounted for the stress range of the liner under investigation.

7.0 APPLICATIONS

in order to utilize the data presented in the previous sections of this report to determine the service life of an overwrapped tank with a load sharing liner, a specific design must first be established. This will necessitate using the Reference 2 Design Guide or equivalent approach to establish the physical parameters associated with the liner; these include material, thickness, sizing stress, maximum operating stress, minimum operating stress and operating temperature. The service life of the composite tank is based on determining the service life of the metallic liner; i.e., how many operating pressure cycles can the liner withstand without failing, either by leakage or catastrophically? No attempt is made in this report to do a life analysis of the filament overwrap material; which should be done if a complete pressure vessel analysis is undertaken. The approach presented herein is assumed to be dependent on the metal liner stress state and thus independent of the type of overwrap material and the pressure vessel shape.

It was concluded in Section 6 that liner life can be guaranteed by the plastic sizing cycle the overwrapped tank is subjected to during fabrication. This sizing cycle, in stressing the liner, will cause it to either leak or fail if any flaws greater than a certain critical size are present. The subsequent cyclic operational life of the liner can then be analytically determined based upon the operational stress environment.

The liner life analysis should establish the area of the liner which yields the least cyclic life. This will necessitate performing a life analysis for different flaw orientations (relative to the liner stress fields) in both the base metal (BM) and weld metal (WM) material. It is conceivable that a lower stressed flaw orientation could yield a lower service life than a higher stressed orientation depending upon the thicknesses involved. The following paragraphs deal specifically with, (1) the liner materials to which the results can be applied, (2) the flaw size screened during sizing, (3) the cyclic life available after sizing, (4) the tank storage life, (5) trade study curves based on a cyclic life analysis and (5) limitations of the approach. Appendix B presents a specific example of how to determine the service life of an overwrapped tank.

7.1 Materials

Three liner materials were investigated during the experimental effort of this program. These were; (1) 2219-T62 aluminum, (2) Inconel X750 STA and (3) crycstretched 301 stainless steel. The parent or base metal and weld metal were variables in most of the tests conducted. The test results presented in previous sections of this report can be used directly in the analysis of these materials as discussed in the following paragraphs. To obtain ball park estimates for other liner materials these same results can be used providing the correct assumptions and adjustments are made as discussed in the following paragraphs.

7.2 Crack Size Screened During Sizing

The crack size that is screened during the sizing operation can be determined using Equation 8 which is repeated below:

$$\sigma = \sigma_{ult} - S(a/Q)_i$$

The stress (σ) in the above equation is set equal to the sizing stress (σ_s) and by substituting the appropriate values of ultimate material strength (typical value) and the empirically defined parameter S the critical flaw size $(a/Q)_i^{cr}$ screened during sizing can be determined. Figure 45 presents the value of S for the liner materials investigated as a function of material thickness and biaxiality (σ_x/σ_y defined in Figure 3) present in the liner.

Once the critical flaw size at the sizing stress level has been established, the corresponding flaw depth (a_i^{cr}) can be determined by knowing the flaw shape parameter (Q). This flaw shape parameter is dependent on the flaw shape ($a/2c$) and the sizing stress-to-yield strength ratio (σ_s/σ_{ys}). A flaw shape must be assumed and this quantity ranges from 0.1 to 0.5. The sizing stress-to-yield strength ratio will always be greater than unity and therefore to utilize the Q chart shown in Figure 16 a value of unity is assumed. Since the value of Q increases with increasing flaw shape, the value of the critical flaw depth also increases. Therefore, the usable amount of flaw growth potential available for cyclic operation is less if

a numerically higher value flaw shape is assumed. This does not necessarily mean that the least operational cyclic life is obtained by assuming the higher value initial flaw shape, since the cyclic crack growth rate is generally slower for higher value flaw shapes than lower value ones. This is primarily because the stress intensity which controls the cyclic crack growth rate, is lower for high values of the flaw shape parameter (Q) as evident in Equation 6. It therefore becomes necessary to analyze various assumed initial flaw shapes to determine the most critical value. Additional discussion on this subject is presented in Paragraph 7.3 in dealing with the determination of the operational cyclic life.

How the static fracture data presented herein applies to other materials is discussed briefly. As pointed out in Paragraph 4.1.3, the general relationship describing failure of the liner materials loaded uniaxially ($\sigma_x/\sigma_y = 0$) is presented as Equation 10, which is repeated below:

$$\sigma = \sigma_{ult} - \frac{A}{t^m} (a/Q)_i$$

The constant A appears to be dependent upon the ultimate strength of the material as illustrated in Figure 35 ($S = A/t^m$). In general, this figure shows the value of the constant A increasing with increasing ultimate material strength. An estimate could be made based on this information. The value of parameter m is relatively constant with an average value of 0.74. Armed with estimates of the constants A and m, the flaw size screened by the sizing stress in a uniaxial stress field could be estimated for materials other than those tested. From the analysis conducted in Paragraph 4.1.3, there is a critical material thickness (t_c) above which the failure loci is defined by substituting t_c into the above equation. The value of t_c appears to be equal to $0.6 (K_{IE}/\sigma_{ys})^2$.

As pointed out in Paragraph 4.3, the biaxiality present in the liner can affect the static fracture results and thereby the value of the flaw size screened during sizing.

The only liner material that was influenced by the biaxiality was the 2219-T62 aluminum and the effect appeared to decrease with increasing material thickness. This effect is illustrated in Figure 45 in terms of the failure loci slope (S) where S is related to thickness by Equation 9 which is repeated below:

$$S = \frac{A}{t^m}$$

It appears that for biaxiality ratios of 0.5—1.0 for the aluminum, the value of A is higher than that indicated for a uniaxial stress field failure and the value of m is lower (about 0.27). How this information relates to other aluminums and, in general, other materials not tested is not known. It appears safe to assume that for thick sections of aluminum the uniaxial static fracture results can be used, but for thin gages biaxiality should be accounted for.

To establish the response for materials not tested herein to a biaxial stress field when static fractured, it would be necessary to conduct tests unless the materials were metallurgically and strength-wise similar to those reported herein.

7.3 Cyclic Life Determination

Once the flaw depth (a_i^{cr}) that is screened by the sizing cycle (stress) is established, the next step is to determine how many operational pressure cycles the pressure vessel can withstand without leaking or failing catastrophically. In other words, how many operational cycles does it take to grow a flaw from the depth screened by the sizing cycle to the point of catastrophic failure or leakage (flaw penetrating the liner thickness), whichever occurs first.

The liner physical parameters affecting the cyclic life must first be established. These are:

- (1) material
- (2) thickness, t
- (3) operating temperature, T
- (4) maximum operating stress, σ_o
- (5) minimum to maximum stress ratio, R

The next step involves a numerical integration procedure to determine the number of cycles required to grow the flaw from a_i^{cr} to the point of leakage where $a_f =$ liner thickness (t). The flaw growth potential $[t - a_i^{cr}]$ is divided into a sufficient number of increments to ensure a close approximation to the cyclic life. Normally, ten increments will suffice. Table 23 illustrates the numeric integration involved. The same initial flaw shape as assumed when determining the flaw depth screened by the sizing stress should be used. An assumption must be made which describes the manner in which the flaw shape changes from its initial value until the flaw penetrates the liner thickness. The crack growth rates developed in this program assumed both the flaw depth and length growth, simultaneously reach the same percentage of their respective total growth from initial to final values. This relationship is described by Equation 4 which is repeated below:

$$\frac{a - a_i}{a_f - a_i} = \frac{2c - 2c_i}{2c_f - 2c_i}$$

For analysis consistency, the same relationship should be used. The testing conducted herein demonstrated that regardless of the flaw shape when cycling started, the flaw shape always attempted to approach a material dependent steady-state value which was approximately 0.35 for the 2219-T62 aluminum and Inconel X750 STA, and 0.42 for the cryostretched 301 stainless steel. This limiting condition is due to differences in cyclic crack growth rates in the flaw depth and width directions. For cases where the liner thickness is too thin to develop the steady-state flaw shape for a given initial flaw shape, it should be assumed that the flaw length $(2c)_i$ does not change; flaw growth occurs only in the depth direction.

By knowing the various flaw shape values and the maximum operating stress-to-sizing stress ratio (σ_o/σ_s), the corresponding values of Q can be determined. The deep flaw magnification factor can also be calculated since the flaw depth-to-thickness ratio (a/t) is known. The stress intensity based on the maximum cyclic stress for each selected value of flaw depth can be determined using Equation 6 which is repeated below:

$$K_{\max} = 1.1 \sigma_{\max} \left(\frac{\pi a}{Q} \right)^{1/2} M_{km}$$

where: σ_{\max} = maximum operational stress
 a = flaw or crack depth
 Q = flaw shape parameter (see Figure 16)
 M_{km} = deep flaw magnification factor (see Figure 17)

The average stress intensity ($\frac{K_{\max i} + K_{\max j}}{2}$) for each increment of flaw growth can now be determined. The cyclic crack growth rate for each increment can be calculated from Equation 7 using the average stress intensity for that increment. Equation 7 is repeated below:

$$\frac{da}{dN} = C B (K_{\max}^n)_{av}$$

where: $\frac{da}{dN}$ = cyclic crack growth rate
 $(K_{\max})_{av}$ = average stress intensity based on maximum stress level
 C, B, n = empirical constants

The empirical constants, C and n are defined in Figures 70, 71 and 72 for the three candidate liner materials. These constants describe the crack growth rate behavior when $R = 0$. The constant, B , which accounts for stress ratios other than zero is defined in Figures 80 through 86. The number of cycles required to grow the flaw each increment is determined by dividing the crack growth increment by

the corresponding crack growth rate. The total cyclic life to flow breakthrough is the summation of these incremental cycles.

Although the cyclic life tests conducted in this program demonstrated flow leakage for the thicknesses tested, it is extremely likely that with thicker specimens catastrophic failure would occur prior to the flow propagating through-the-thickness.

In actual overwrapped liners leakage might result rather than catastrophic failure because of the additional restraint offered by the overwrap material. In the case of linear elastic fracture mechanics, cyclic failure is assumed to occur when the critical stress intensity (K_{IE}) is reached. The maximum stress intensities attained at 295K (72°F) for the maximum thickness of materials tested are presented below:

Material		K_{max} $MN/m^{3/2}$ (ksi \sqrt{in})
2219-T62 Aluminum	BM	55.0 (50.0)
	WM	44.6 (40.6)
Inconel X750 STA	BM	98.3 (89.4)
	WM	99.9 (90.9)
Cryostretched 301 SS	BM	128.0 (116.5)
	WM	101.4 (92.3)

These values were calculated using Equation 6 and are based on the flaw size at breakthrough and the maximum stress at which the specimens were cycled. The maximum stress intensities cited above are believed to be less than the K_{IE} values for these materials.

In performing the cyclic life analysis presented in this section it should be assumed that catastrophic failure will occur when K_{IE} is reached. In other words, when a value of K_{IE} is attained in performing the numeric integration outlined in Table 23,

the cyclic life should be those cycles required to grow the flaw from its initial conditions to the point where K_{IE} is reached. In lieu of actual K_{IE} values for the materials investigated herein, the preceding table of maximum stress intensities attained during cycling testing should be used. If K_{IE} is not reached prior to the flaw penetrating the liner thickness, then leakage is the mode-of-failure.

Because of the amount of data scatter normally observed in cyclic crack growth rates it is necessary to apply a scatter factor to the life determined to arrive at a guaranteed value. In most instances, experimentally determined rates vary by a factor of about three (3) at a given stress intensity level. The values of the cyclic crack growth rate parameters (B, C and n) presented herein were, in general, selected to yield average rates. The above facts coupled with the fact that initial retardation in the rates normally occurs after experiencing a sizing cycle, prompted the investigator to suggest that the cyclic life determined in the preceding paragraphs be reduced by a factor of two (2). This reduction should account for any data scatter that might occur.

The selection of the initial flaw shape as pointed out in Paragraph 7.2 is an important part of the life analysis. How important it is, is graphically illustrated in Figure 95 where various initial flaw shapes were assumed for 4.57 mm (0.180 inch) thick 2219-T62 aluminum base metal. In this case the flaw shape yielding the least life is 0.50. For the aluminum and Inconel materials investigated herein, this is generally the case; an initial flaw shape of 0.50 will yield the least cyclic life. Cyclic life analysis of the 301 stainless steel material indicates the answer is not as clear cut, being highly dependent upon the thickness of material under consideration. For this material, especially, various initial flaw shapes need be considered and the one yielding the least cyclic life should be used.

How the cyclic life data presented herein applies to other materials is discussed briefly. As concluded in Paragraph 5.1.2, the sizing stress level did not have any influence on the cyclic crack growth rates except for an initial retardation. This retardation is caused by the sizing stress overload and the magnitude of the retardation is a

function of the maximum operating stress-to-sizing stress ratio; the lower this value the more retardation experienced. The growth rate analysis presented herein ignores this retardation since it was not a consistent phenomena observed throughout the testing. The subsequent rates, after the flaw has propagated to the point when the influence of the sizing stress has vanished, are equal to rates obtained without any prior sizing stress. This suggests that baseline crack growth rate data for other materials could be obtained from surface flawed cyclic tests developed for linear elastic fracture mechanic analysis. To use this data it would be necessary that this rate data be presented as a function of K_{\max} as defined by Equation 6, which incorporates a deep flaw magnification factor. It should be remembered that this baseline data must be developed at a stress ratio of zero.

To establish the response of the materials other than those tested herein to R ratios other than zero (specifically negative values) it would be necessary to conduct tests to ascertain this influence. The effect of R ratio is handled by the constant B in Equation 7 and, as pointed out earlier, B is also dependent upon the material, liner thickness and the maximum operating stress level.

7.4 Storage Life Considerations

The life analysis presented in the previous paragraphs is based solely on how many operational pressure cycles the liner can withstand without failing. This analysis assumes the pressurant to be compatible with the liner material from a stress corrosion standpoint. Stress corrosion exists when flaws propagate under sustained stress when exposed to the pressurant. If this condition did exist, the operational life of the liner would be severely reduced.

The question of flaw growth under sustained stress was not addressed in this experimental program and therefore for material/environment combinations other than those tested herein (which were compatible) serious consideration should be given to this aspect of the life analysis. Ultimately, the answer of stress corrosion compatibility should be obtained by performing sustained load tests of the liner material

(and thickness) containing surface flaws which are exposed to the pressurant. Tests of this type would be able to define the stress/flaw size combinations in which the flaws propagate and those in which they do not. At no time during the cyclic operation of the liner would the stress/flaw size combination be permitted to exceed this stress corrosion threshold. This would essentially reduce the flaw growth potential available for cyclic operation.

7.5 Parametric Life Analysis

A parametric service life analysis is presented as an aide in performing trade studies involving overwrapped tanks with load sharing liners. This analysis is generally somewhat conservative; yielding the least cyclic life for the conditions stated. Where a more accurate life analysis is required, the procedures outlined in Paragraphs 7.2 and 7.3 should be followed.

Nomographs for liner materials, 2219-T62 aluminum, Inconel X750 STA and cryo-stretched 301 stainless steel (base metal and weld metal) are presented in Figures 96 through 113. By knowing the material, liner thickness, sizing stress, maximum operating stress (determined using the Reference 2 Design Guide), and an assumed initial flaw shape the operational cyclic life for $R = 0$ (minimum-to-maximum operational stress ratio) can be found directly from these nomographs. These figures are presented for various assumed initial flaw shapes for two reasons; (1) the cyclic life can be highly dependent on the assumed initial flaw shape and (2) in some cases, the sizing cycle does not screen a flaw if a high value of flaw shape is assumed and it is desirable to know the cyclic life capability of the liner for those flaw shapes that are screened. To obtain cyclic life values at cyclic stress levels other than those presented, the following expression should be used:

$$\frac{N_{\sigma}}{N_{\sigma=X}} = \left(\frac{\sigma_x}{\sigma} \right)^n \quad (12)$$

where: N_{σ} = cyclic life at a stress level
 $N_{\sigma=x}$ = cyclic life at a stress level of $\sigma = x$
 n = flaw growth rate exponent for the liner material
under consideration (Figures 70, 71 and 72)

These nomographs are presented in terms of cycles to leakage and this is the general failure mode for the materials, operating stress levels and thicknesses tested. If higher operating stresses are employed, a check on whether or not the material's K_{IE} is exceeded during cycling should be made as outlined in Paragraph 7.3. The cyclic life of a liner is defined by either the crack propagating through the thickness of the liner (causing leakage) or the crack reaching critical proportions (causing catastrophic failure), whichever occurs first.

To adjust the life for R ratios other than zero, the following expression should be used:

$$\frac{N_{R=0}}{B_{R=X}} = N_{R=X} \quad (13)$$

The value of B is found in Figures 80 through 86 and is based on the material, liner thickness and the maximum operating stress level. The cyclic lives do not reflect any factor to account for data scatter (refer to Paragraph 7.3 for a discussion of this important point).

7.6 Limitations

When applying Equation 10 in determining the crack size screened by the sizing cycle, there is a maximum material thickness (t_c) above which the failure loci is defined by t_c , where $t_c \approx 0.6 (K_{IE}/\sigma_{ys})^2$. The use of Equation 10 is also

limited to failure stresses which occur above $0.90 \sigma_{ys}$. These limitations are discussed in more detail in Paragraph 4.1.4.

In addition, care should be exercised in using the data presented as applying to other materials, temperatures, thicknesses and stresses. Extrapolations could be dangerous, especially for the materials where only two thicknesses were investigated.

REFERENCES

1. W. D. Bixler, "Development of a Fracture Control Method for Composite Tanks with Load Sharing Liners", (Interim Report), NASA CR-120918, Boeing Aerospace Company, March 1973.
2. R. E. Landes, "Glass Fiber Reinforced Metal Pressure Vessel Design Guide", NASA CR-120917, Structural Composites Industries, July 1972.
3. J. N. Masters, W. D. Bixler and R. W. Finger, "Fracture Characteristics of Structural Aerospace Alloys Containing Deep Surface Flaws", NASA CR-134587, Boeing Aerospace Company, December 1973.
4. J. J. Kibler and R. Roberts, "The Effect of Biaxial Stresses on Fatigue and Fracture", Trans. of the ASME, Journal of Engineering for Industry, November 1970.
5. P. D. Hilton, "Plastic Intensity Factors for Cracked Plates Subjected to Biaxial Loading", International Journal of Fracture, Vol. 9, No. 2, June 1973.
6. C. F. Tiffany, P. M. Lorenz and L. R. Hall, "Investigation of Plane-Strain Flaw Growth in Thick-Walled Tanks", NASA CR-54837, The Boeing Company, February 1966.
7. C. M. Hudson and J. T. Scardina, "Effect of Stress Ratio on Fatigue-Crack Growth in 7075-T6 Aluminum-Alloy Sheet", Engineering Fracture Mechanics, Vol. 1, No. 3, April 1969.
8. W. Illg and A. J. McEvily Jr., "The Rate of Fatigue-Crack Propagation for Two Aluminum Alloys Under Completely Reversed Loading", NASA Technical Note D-52, Langley Research Center, October 1959.
9. D. R. Donaldson and W. E. Andersen, "Crack Propagation Behavior of Some Airframe Materials", Crack Propagation Symposium Proceedings - Cranfield, England, Vol. 2, September 1961.

10. T. W. Crooker, "Effect of Tension - Compression Cycling on Fatigue Crack Growth in High-Strength Alloys", NRL Report 7220, Naval Research Laboratory, January 1971.
11. J. N. Masters, W. P. Haese and R. W. Finger, "Investigation of Deep Flaws in Thin Walled Tanks", NASA CR-72606, The Boeing Company, December 1969.
12. J. N. Masters, W. L. Engstrom and W. D. Bixler, "Deep Flaw in Weldments of Aluminum and Titanium", NASA CR-134649, Boeing Aerospace Company, April 1974.
13. R. M. Bonesteel, "Fracture of Thin Sections Containing Surface Cracks", Engineering Fracture Mechanics, Vol. 5, No. 3, September 1973.
14. L. R. Hall and W. D. Bixler, "Subcritical Crack Growth of Selected Aerospace Pressure Vessel Materials", NASA CR-120834, The Boeing Company, December 1972.
15. L. R. Hall, R. C. Shah and W. L. Engstrom, "Fracture and Fatigue Crack Growth Behavior of Surface Flaws and Flaws Originating at Fastener Holes", AFFDL-TR-74-47, Boeing Aerospace Company, May 1974.

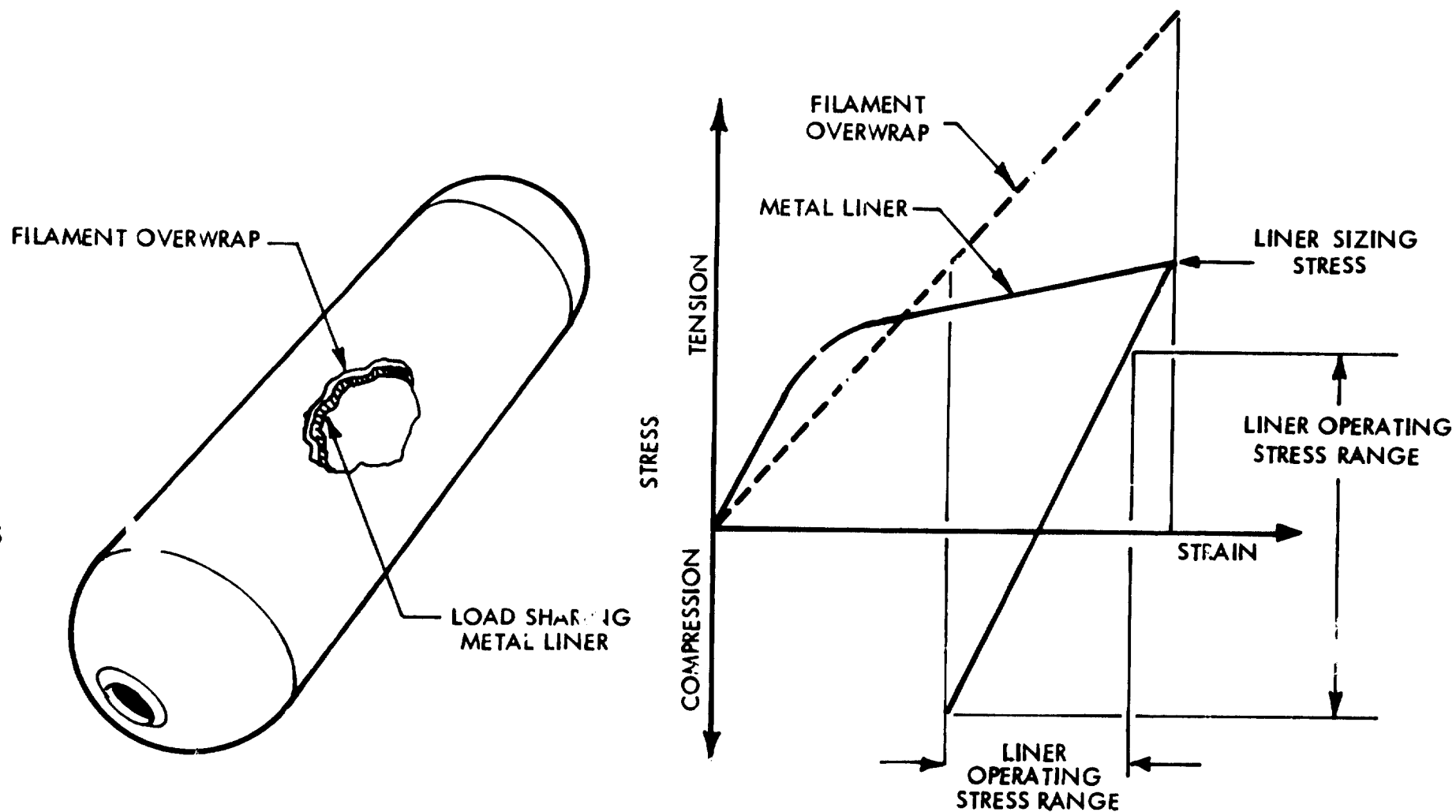


FIGURE 1: STRESS/STRAIN SCHEMATIC FOR COMPOSITE TANKS WITH LOAD SHARING LINERS

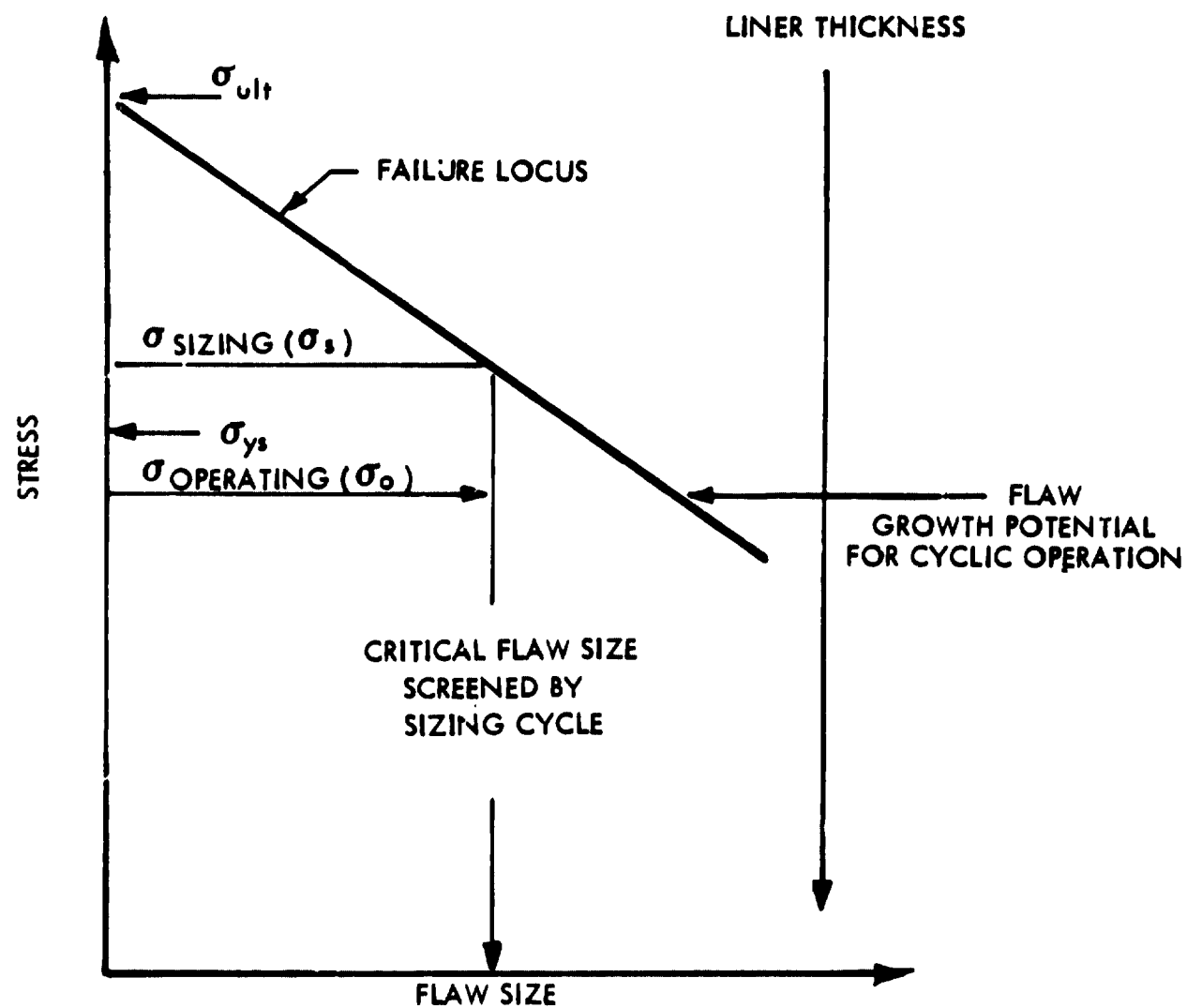


FIGURE 2: FRACTURE MECHANICS APPROACH TO GUARANTEEING SERVICE LIFE OF METAL LINER IN OVERWRAPPED TANKS

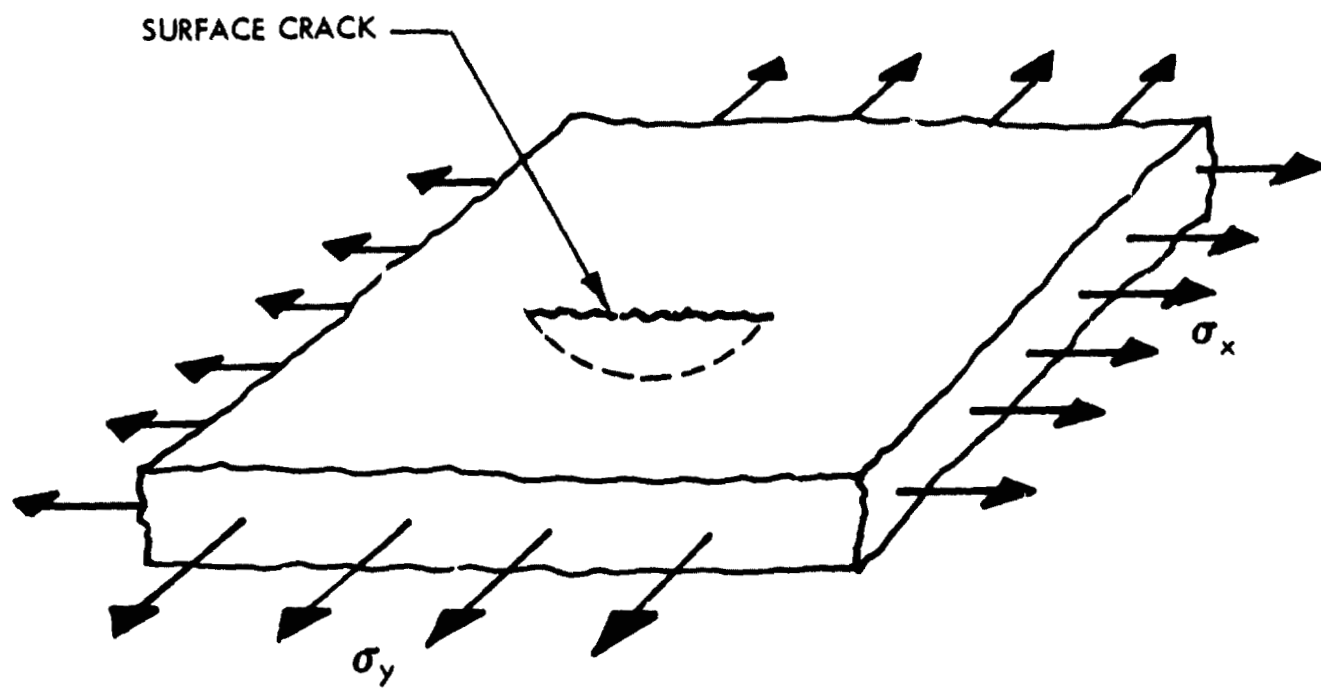
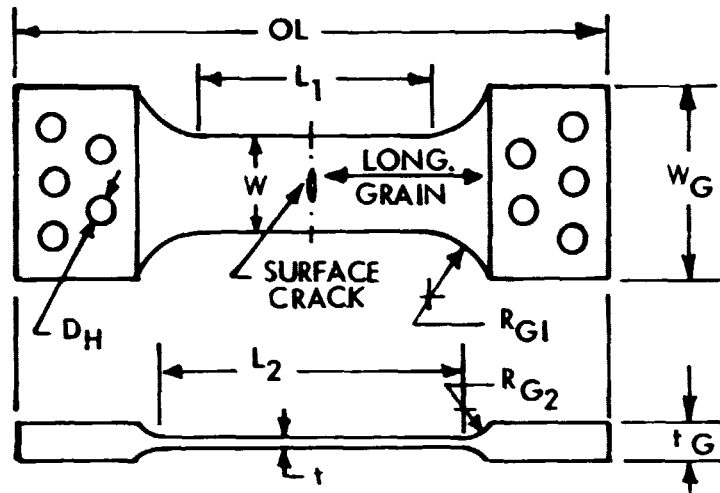


FIGURE 3: BIAXIAL LOADING OF A SURFACE CRACK



MATERIAL	SPECIMEN CODE	THICKNESS, t mm (INCH)	WIDTH, W mm (INCH)	LENGTH, L_1 mm (INCH)	LENGTH, L_2 mm (INCH)	OVERALL LENGTH, OL mm (INCH)	GRIP THICKNESS, t_G mm (INCH)	GRIP WIDTH, W_G mm (INCH)	GRIP RADIUS, R_{G1} mm (INCH)	GRIP RADIUS, R_{G2} mm (INCH)	GRIP HOLE DIAM , D_H mm (INCH)	NUMBER OF GRIP HOLES PER END
2219-T62 ALUMINUM	IATC	2.29 (0.090)	45.7 (1.80)	45.7 (1.80)	-	254.0 (10.00)	2.29 (0.090)	101.6 (4.00)	38.1 (1.50)	-	12.7 (0.50)	5
	IAX		63.5 (2.50)	63.5 (2.50)								
	IAM		50.8 (2.00)	50.8 (2.00)								
	IAW		63.5 (2.50)	101.6 (4.00)		101.6 (4.00)						
	2ATC	4.57 (0.180)	63.5 (2.50)	101.6 (4.00)	-	368.3 (14.50)	4.57 (0.180)	139.7 (5.50)	50.8 (2.00)	-	16.0 (0.63)	5
	2AX		69.9 (2.75)	69.9 (2.75)								
	2AAX		88.9 (3.50)	101.6 (4.00)					38.1 (1.50)			
	24M		127.0 (5.00)	-					177.8 (7.00)			
	3AX	7.62 (0.300)	127.0 (5.00)	127.0 (5.00)	-	609.6 (24.00)	7.62 (0.300)	228.6 (9.00)	63.5 (2.50)	-	25.4 (1.00)	5
	3AWX											
INCO X750 STA	1BTC	1.02 (0.040)	25.4 (1.00)	3.81 (1.50)	-	215.9 (8.50)	1.02 (0.040)	63.5 (2.50)	50.8 (2.00)	-	12.7 (0.50)	3
	2BTC	3.30 (0.130)	57.2 (2.25)	57.2 (2.25)	-	355.6 (14.00)	3.30 (0.130)	139.7 (5.50)	50.8 (2.00)	-	16.0 (0.63)	5
CRYO 301 SS	1CTC	0.71 (0.028)	12.7 (0.50)	20.3 (0.80)	-	203.2 (8.00)	0.71 (0.028)	63.5 (2.50)	61.7 (2.43)	-	12.7 (0.50)	3
	2CTC	2.54 (0.100)	34.3 (1.35)	50.8 (2.00)	-	345.4 (13.60)	2.54 (0.100)	139.7 (5.50)	61.7 (2.43)	-	16.0 (0.63)	5

FIGURE 4: FLAT UNIAXIAL SPECIMEN CONFIGURATIONS

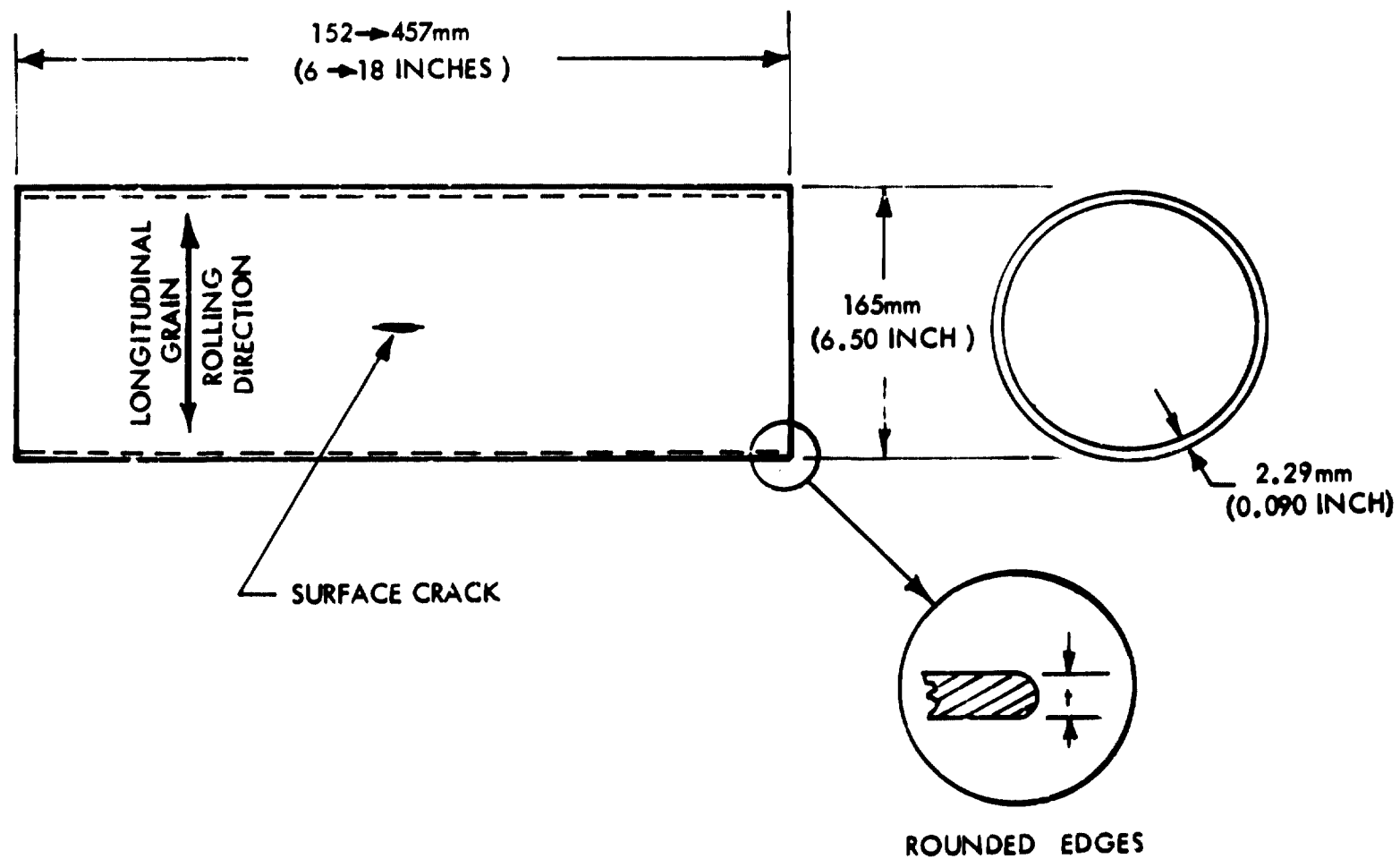


FIGURE 5: OPEN-ENDED CYLINDERS MADE OF 2219-T62 ALUMINUM

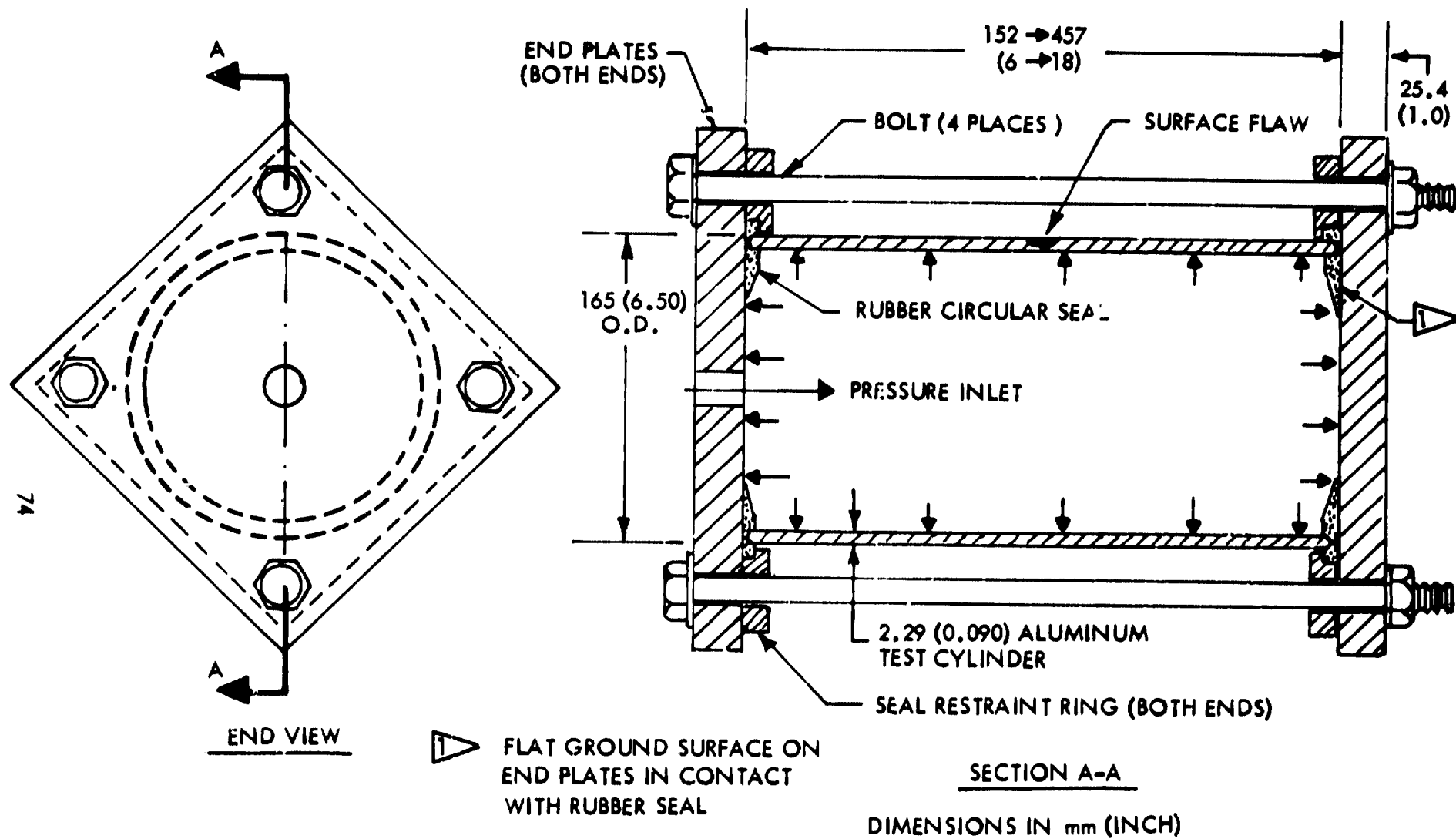
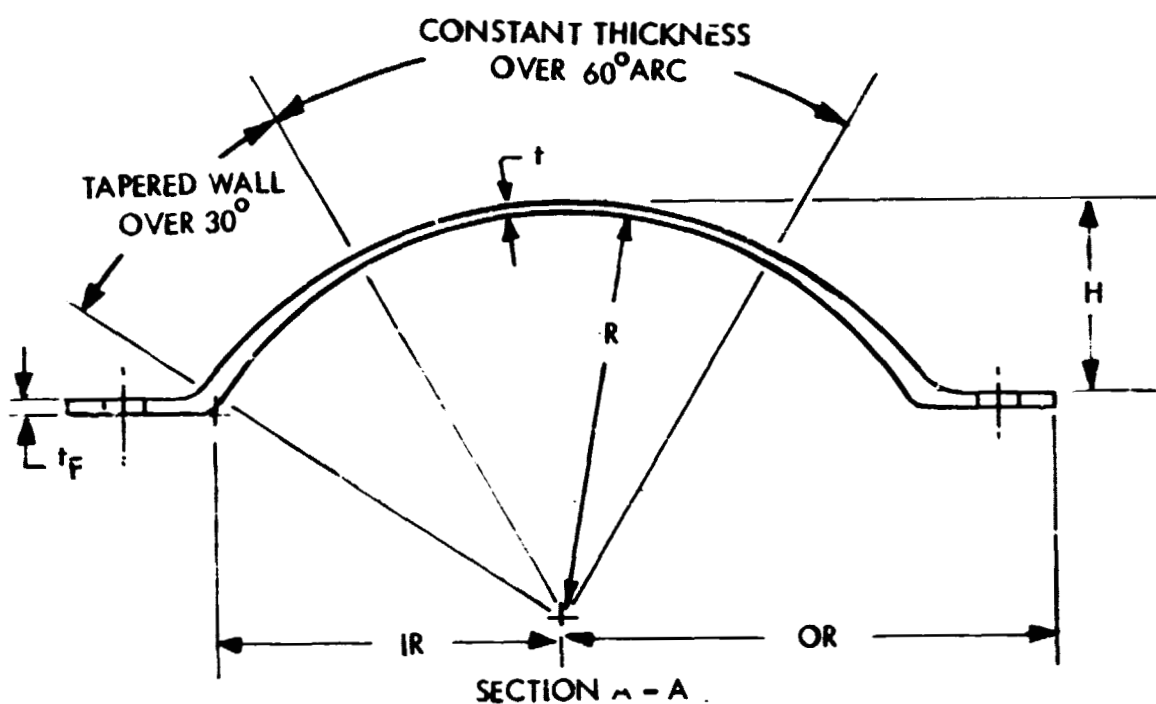
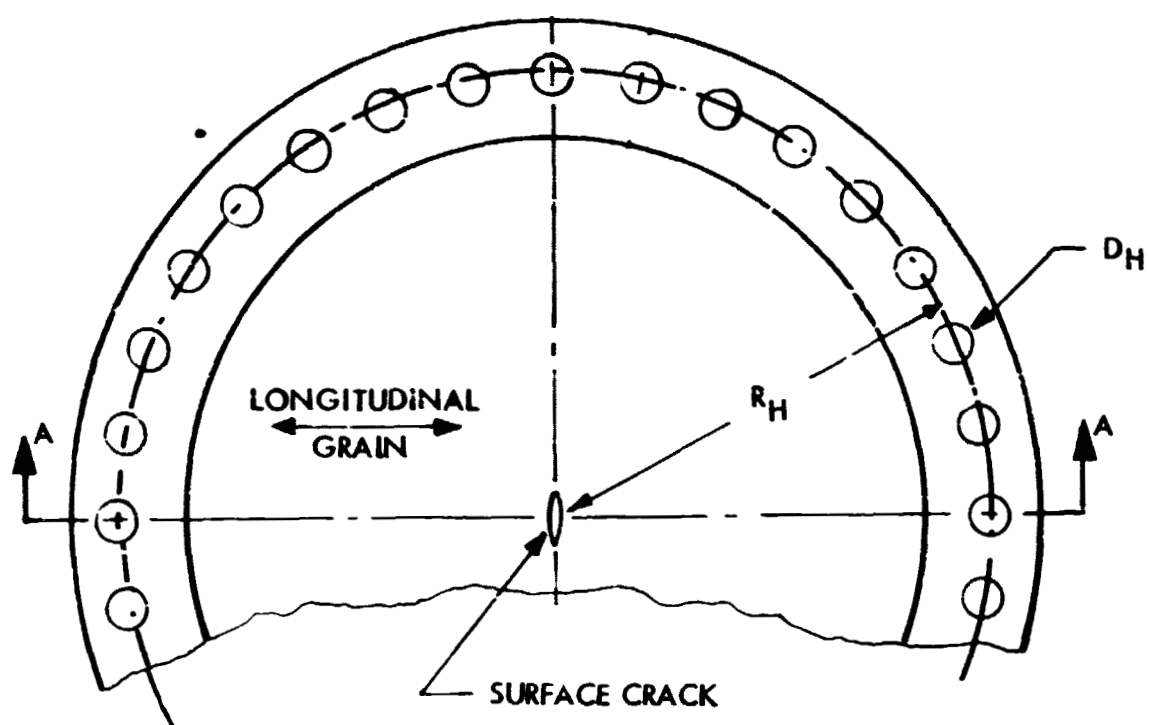
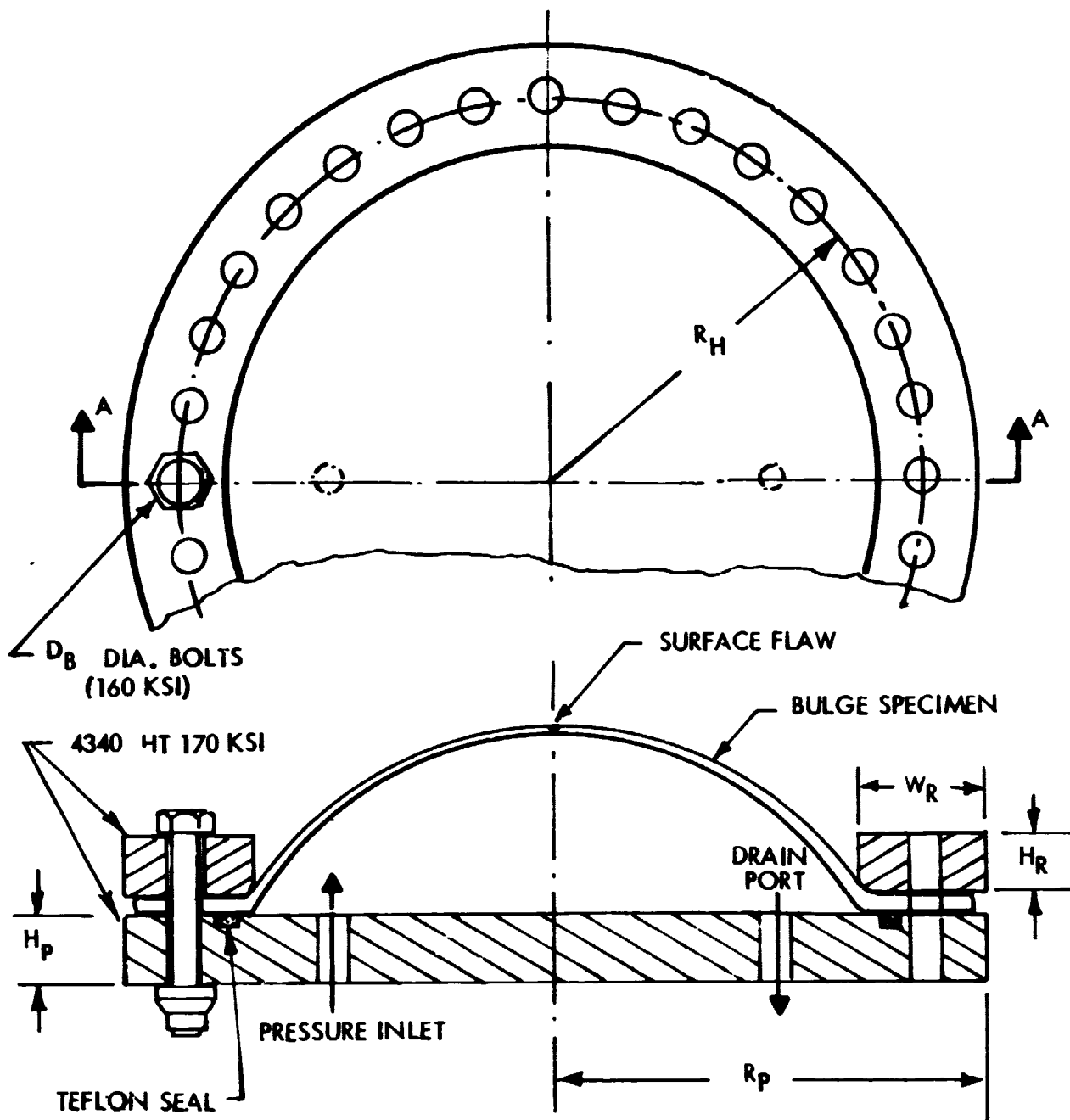


FIGURE 6: TEST FIXTURE FOR PRODUCING UNIAXIAL STRESS FIELD IN A PRESSURIZED CYLINDER



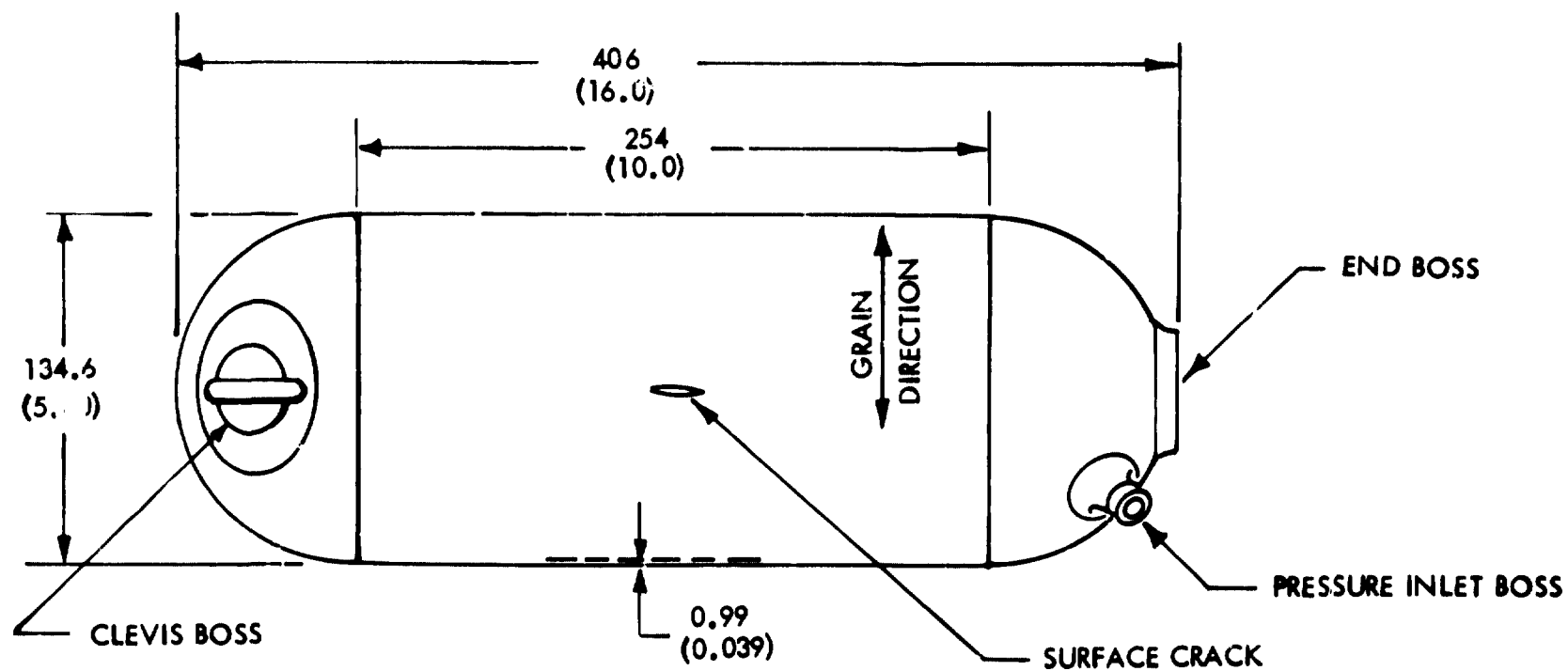
MATERIAL	DIMENSIONS, mm (INCH)								NO. OF HOLES	SPEC. I.D.
	t	R	t _F	IR	OR	H	R _H	D _H		
2219-T ₀₂ ALUMINUM	2.29 (0.090)	177.8 (7.00)	6.35 (0.25)	153.9 (6.06)	215.9 (8.50)	82.6 (3.25)	190.5 (7.50)	16.00 (0.63)	32	1AB-
	4.57 (0.180)	177.8 (7.00)	12.70 (0.50)	150.9 (5.94)	222.3 (8.75)	71.1 (2.80)	190.5 (7.50)	16.00 (0.63)	32	2AB-
	7.62 (0.300)	254.0 (10.00)	17.78 (0.70)	219.9 (8.66)	317.5 (12.50)	108.0 (4.25)	279.4 (11.00)	22.35 (0.88)	32	3AB-
INCONEL X750 STA	2.03 (0.080)	177.8 (7.00)	4.83 (0.19)	154.9 (6.10)	215.9 (8.50)	84.8 (3.34)	190.5 (7.50)	16.00 (0.63)	32	28B-

FIGURE 7 : SPHERICAL CAP SPECIMEN CONFIGURATIONS



TEST SETUP	TEST SPEC. I.D.	DIMENSIONS, mm (INCH)						NO OF BOLTS
		H_p	R_p	H_R	W_R	R_H	D_B	
1	1AB 2AB 28B	38.1 (1.50)	222.3 (8.75)	31.75 (1.25)	167.4 (6.59)	190.5 (7.50)	16.00 (0.63)	32
2	3AB	63.5 (2.50)	317.5 (12.50)	50.80 (2.00)	250.2 (9.85)	279.4 (11.00)	22.35 (0.88)	40

FIGURE 8: SPHERICAL CAP SPECIMEN TEST SETUPS



DIMENSIONS IN mm (INCH)

FIGURE 9: 301 STAINLESS STEEL LINER

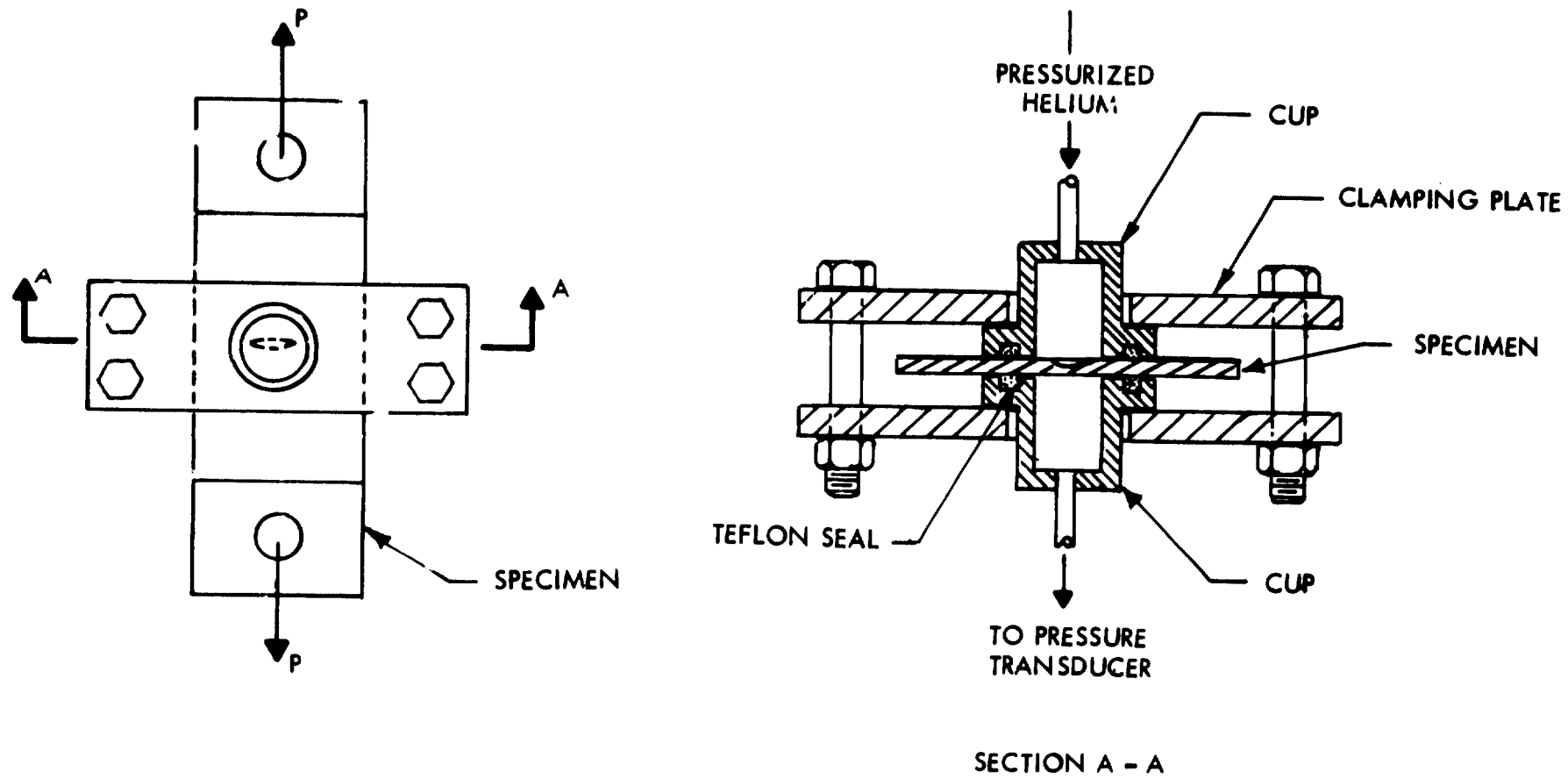


FIGURE 10: PRESSURE CUPS USED FOR FLAW BREAKTHROUGH DETECTION ON UNIAXIAL SPECIMENS

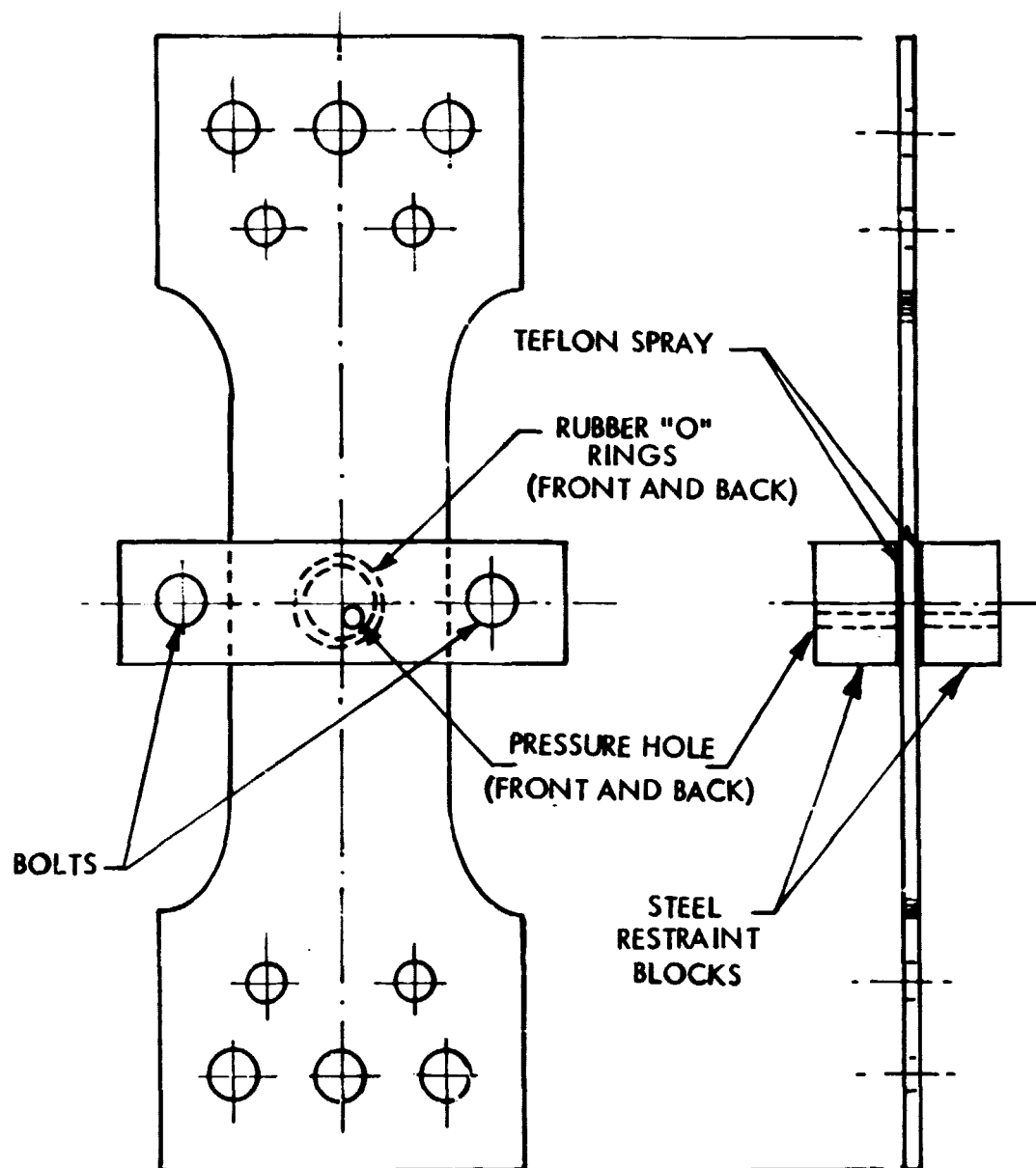
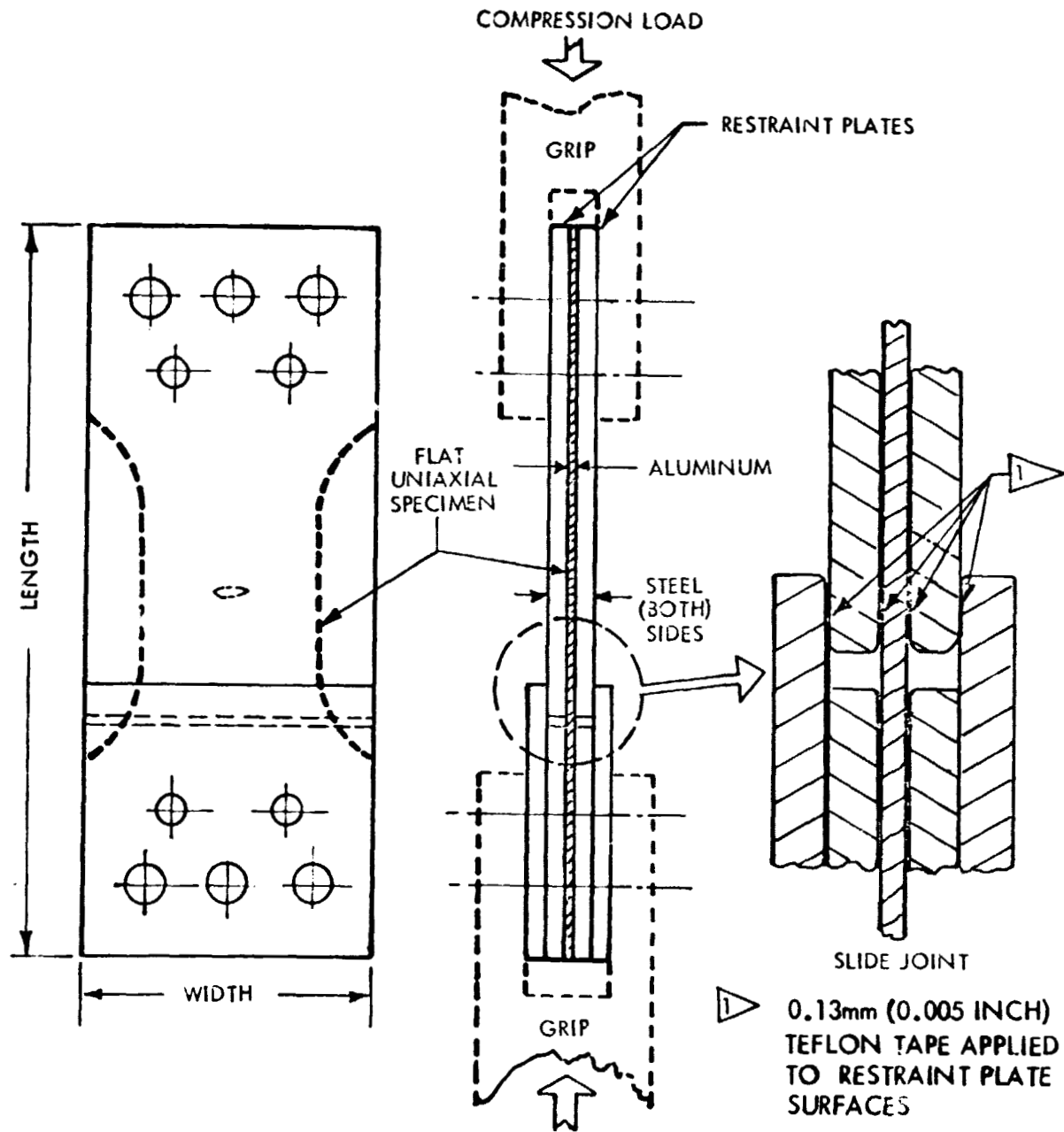


FIGURE 11: 2219-T62 ALUMINUM STATIC FRACTURE SPECIMEN WITH FLAW ANTI-DEFLECTION BARS



SPECIMEN I.D.	PLATE DIM'S. mm (INCH)		
	WIDTH	LENGTH	THICKNESS
1BTC, 1CTC	101.6 (4.00)	215.9 (8.50)	4.78 (0.188)
1ATC, 1AX	101.6 (4.00)	254.0 (10.00)	6.35 (0.250)
2ATC, 2AX, 2BTC, 2CTC	101.6 (4.00)	368.3 (14.50)	9.53 (0.375)
3AX	203.2 (8.00)	609.6 (24.00)	12.7 (0.500)

FIGURE 12: COMPRESSION/TENSION SETUP FOR TESTING UNIAXIAL SPECIMENS

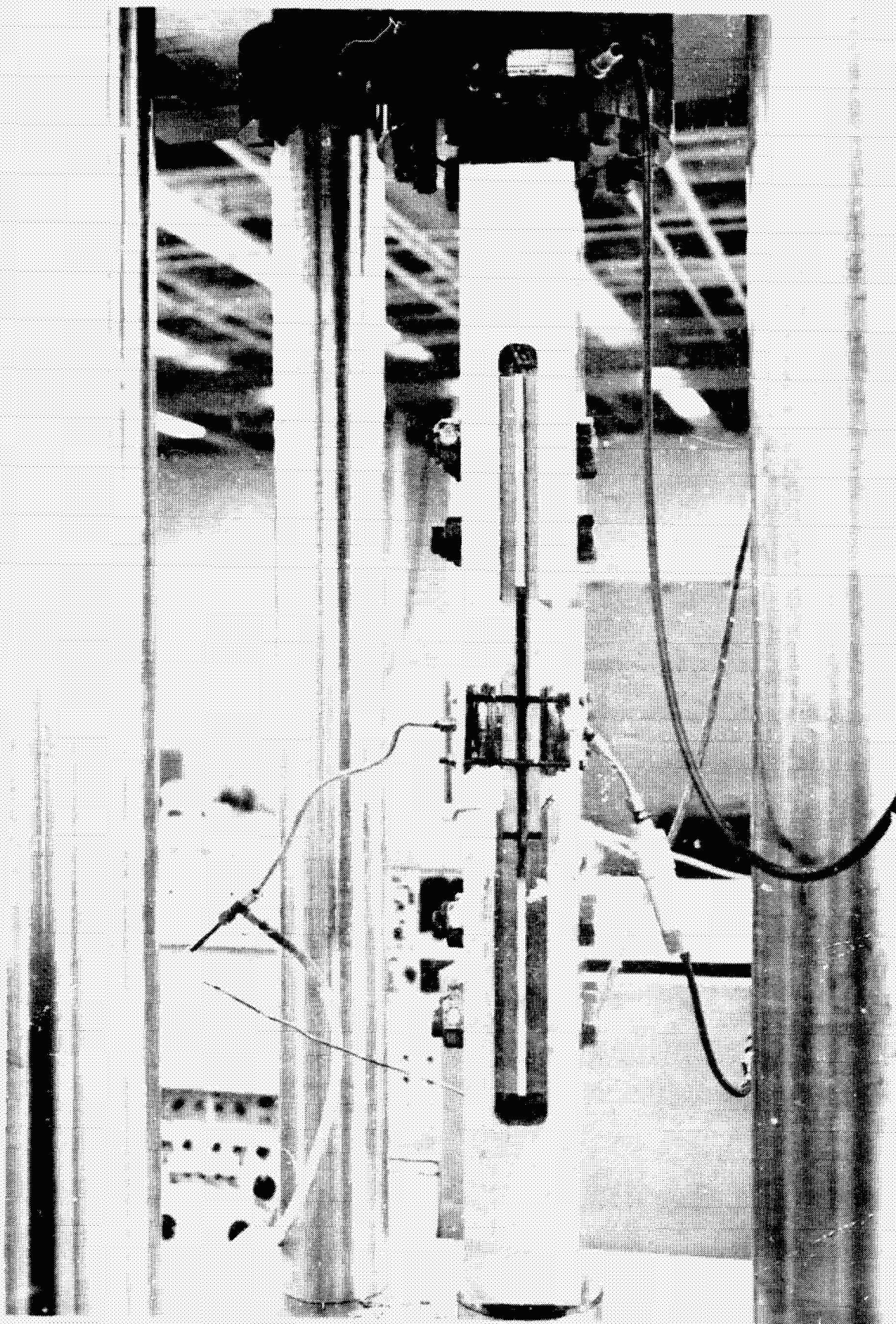


FIGURE 13: TENSION/COMPRESSION SPECIMEN IN TEST

ORIGINAL PAGE IS
OF POOR QUALITY

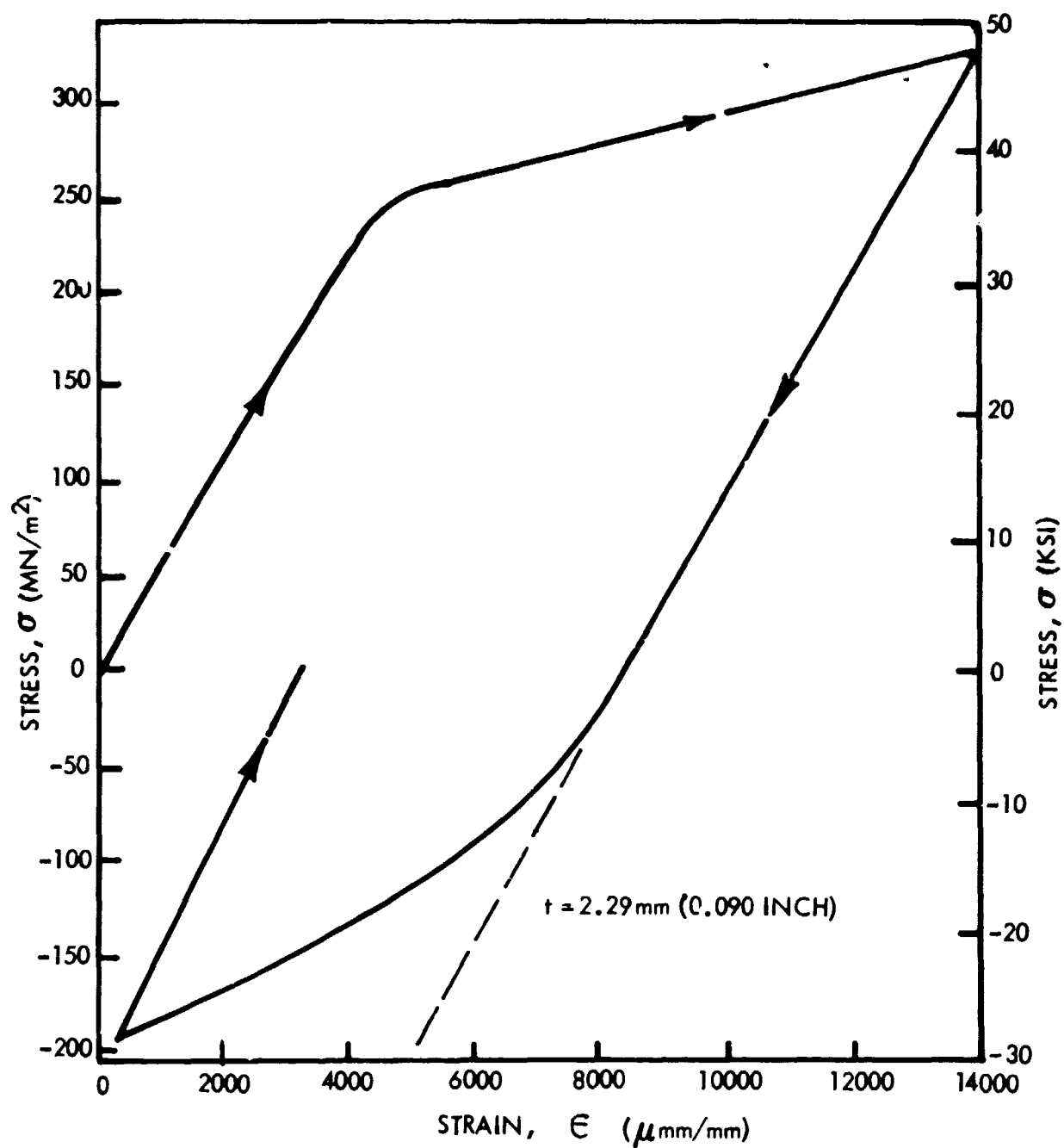


FIGURE 14: TYPICAL STRESS/STRAIN FOR 2219-T62 ALUMINUM WHEN LOADED IN COMPRESSION AFTER A PLASTIC SIZING CYCLE IN TENSION.

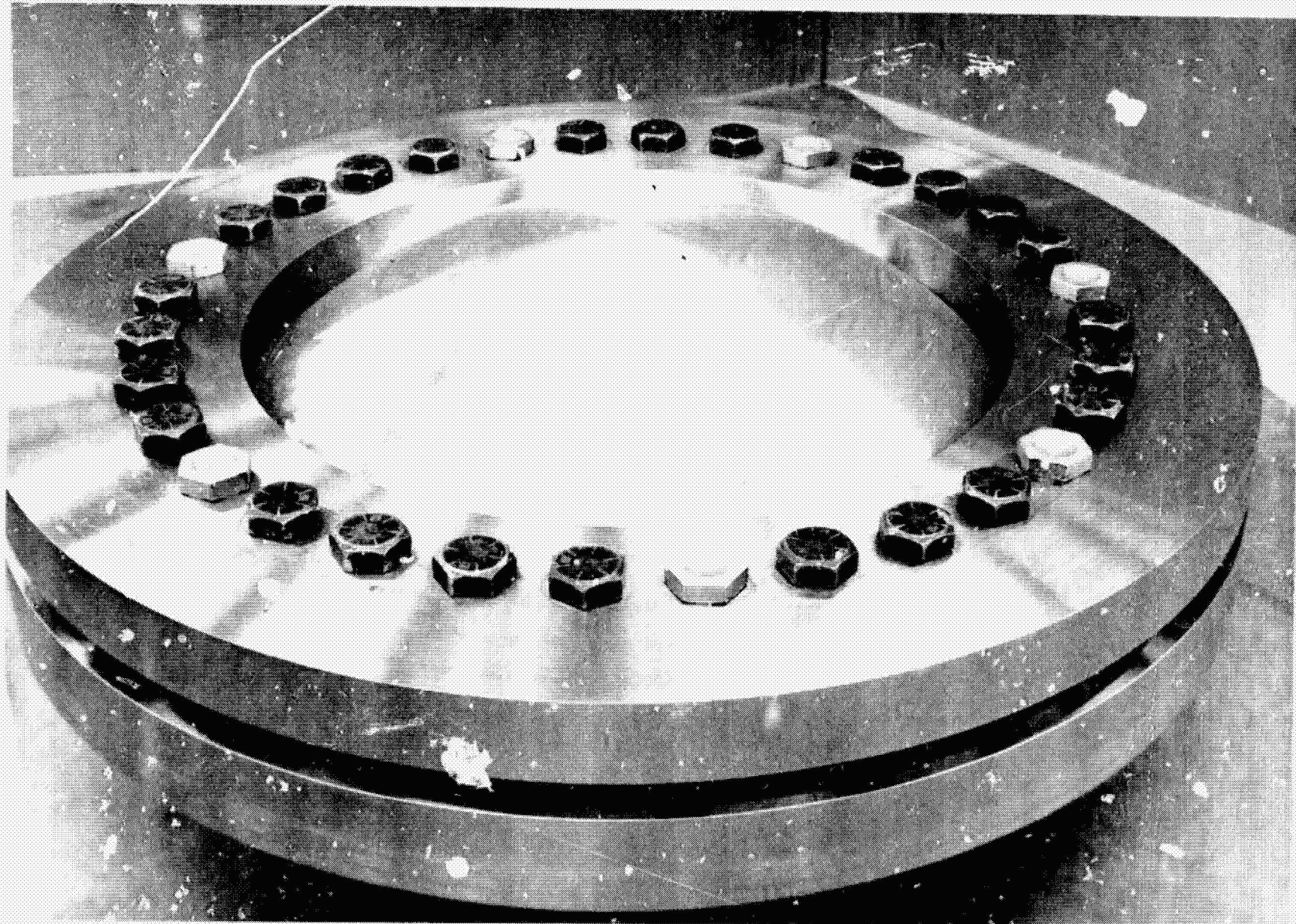


FIGURE 15: SPHERICAL CAP TEST ARRANGEMENT

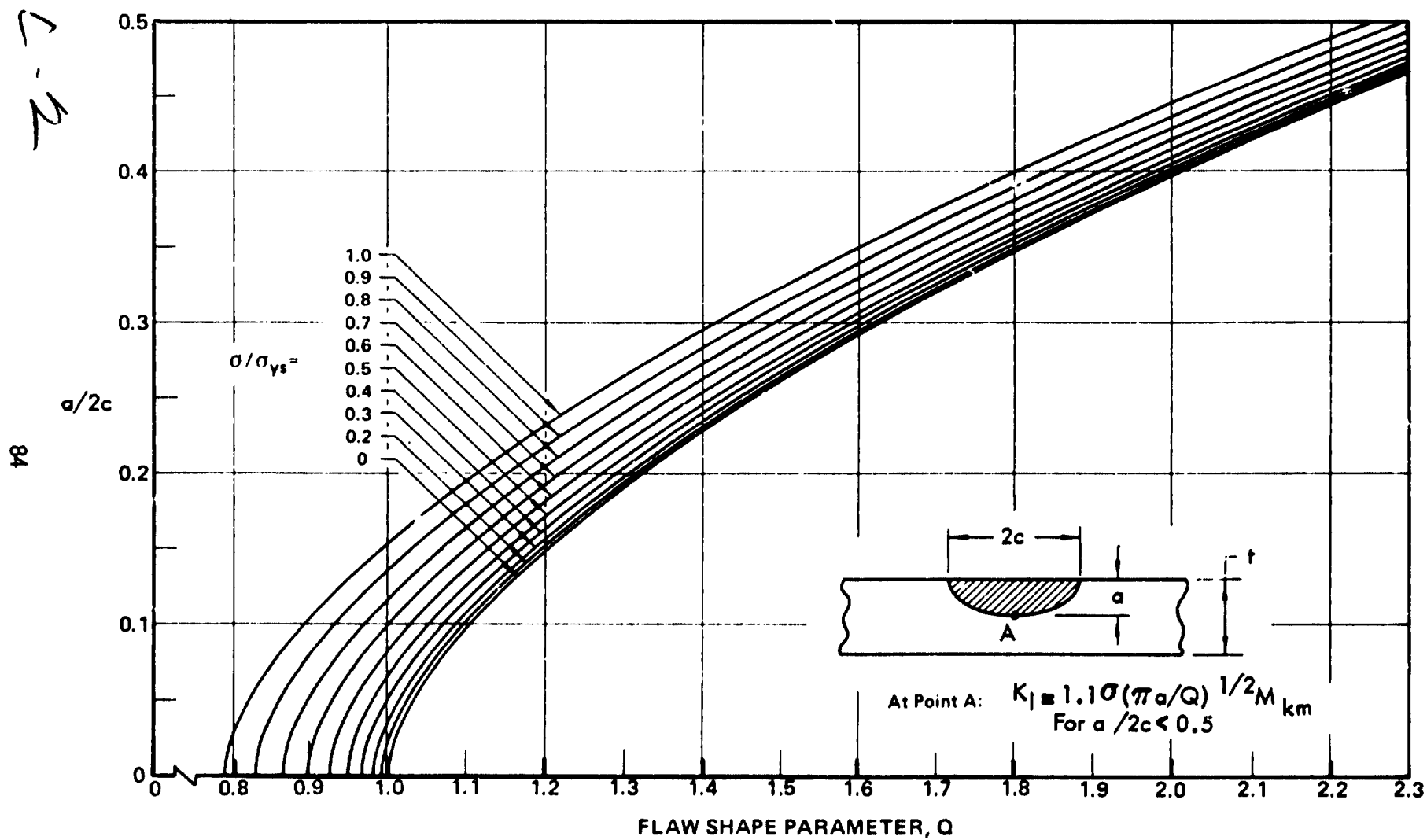


FIGURE 16: SHAPE PARAMETER CURVES FOR SURFACE FLAWS

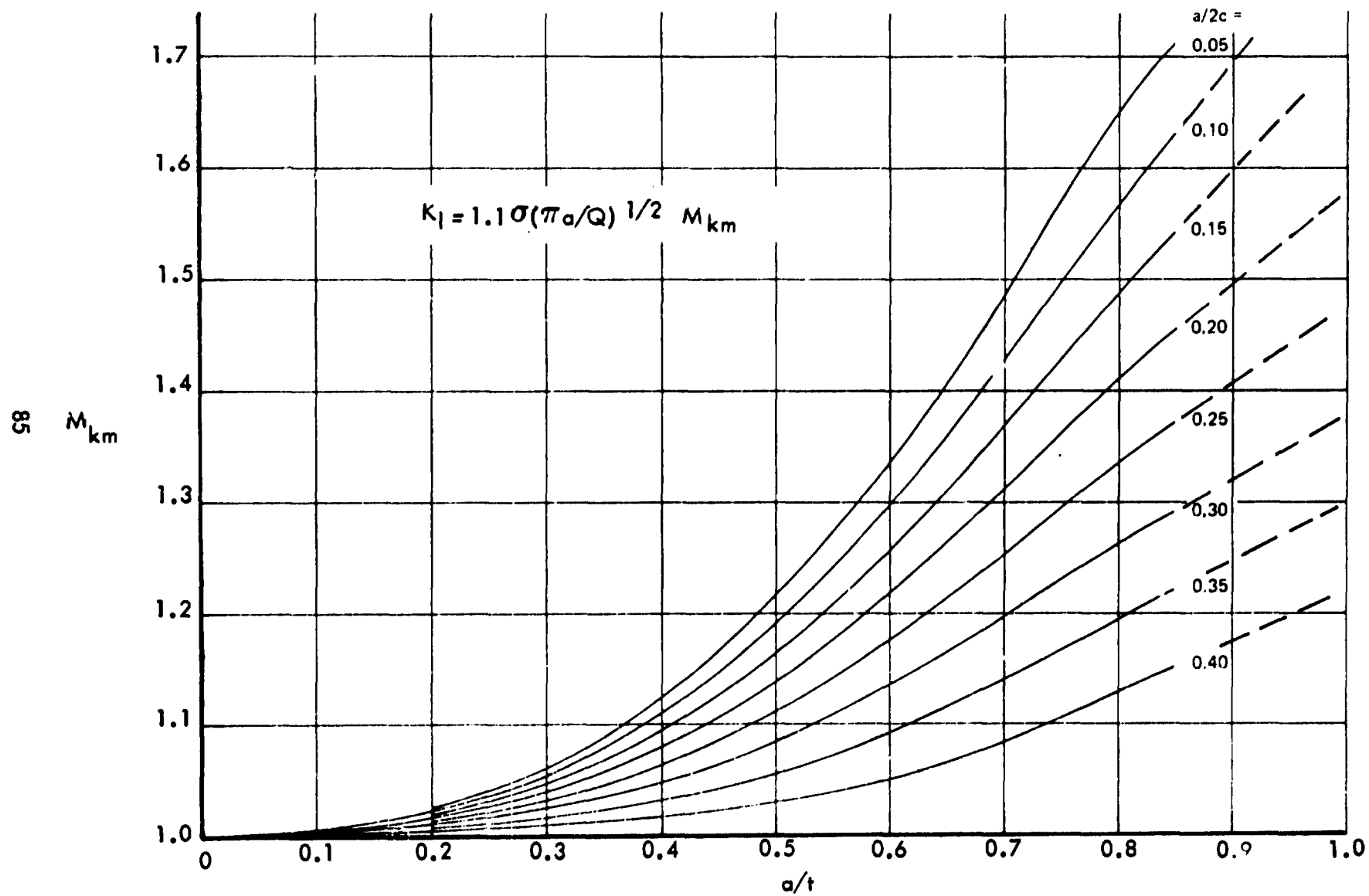


FIGURE 17: DEEP FLAW MAGNIFICATION CURVES (Reference 11)

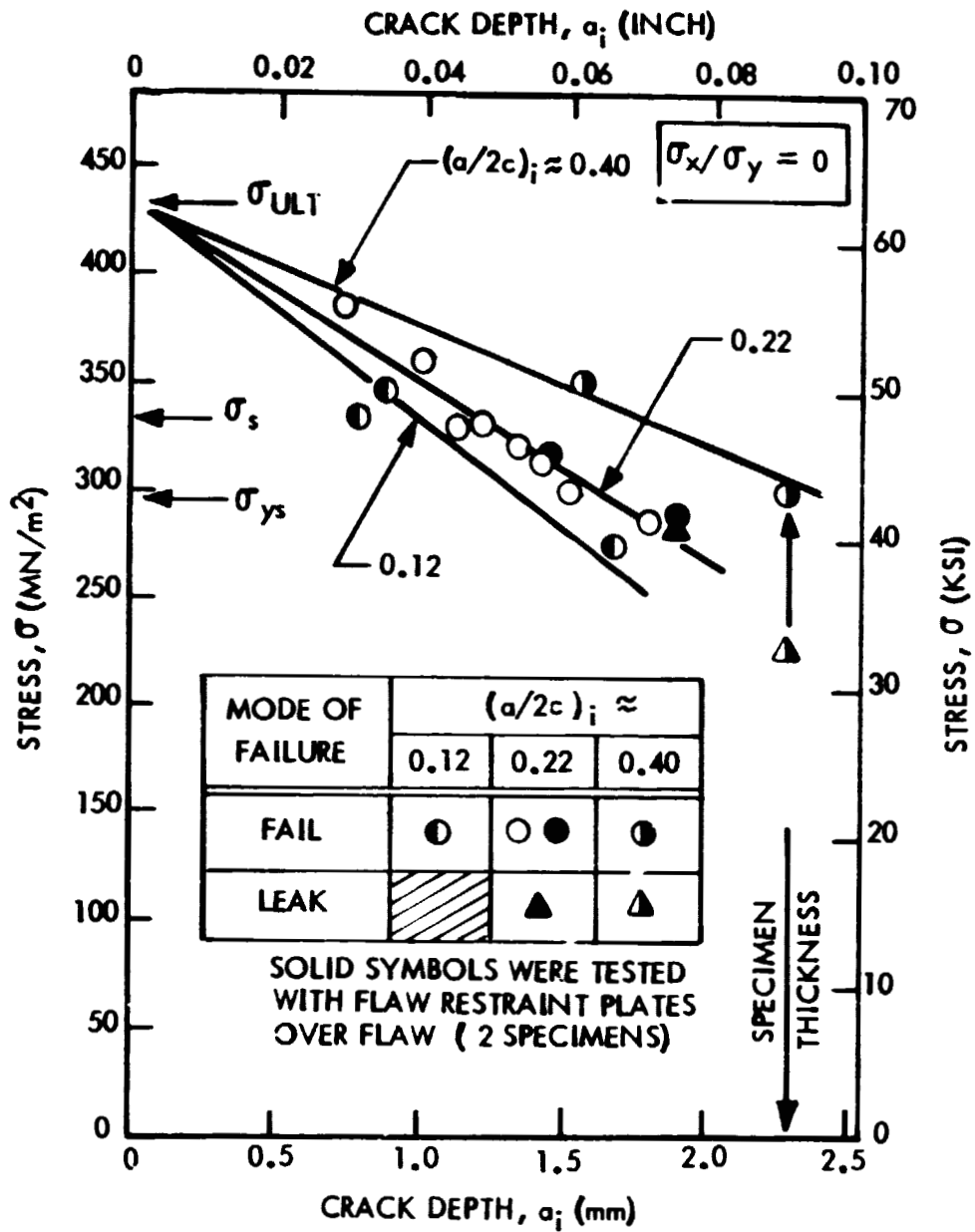


FIGURE 18: FAILURE LOCI FOR 2.29 mm (0.090 INCH) THICK 2219-T62 ALUMINUM BASE METAL AS A FUNCTION OF CRACK DEPTH

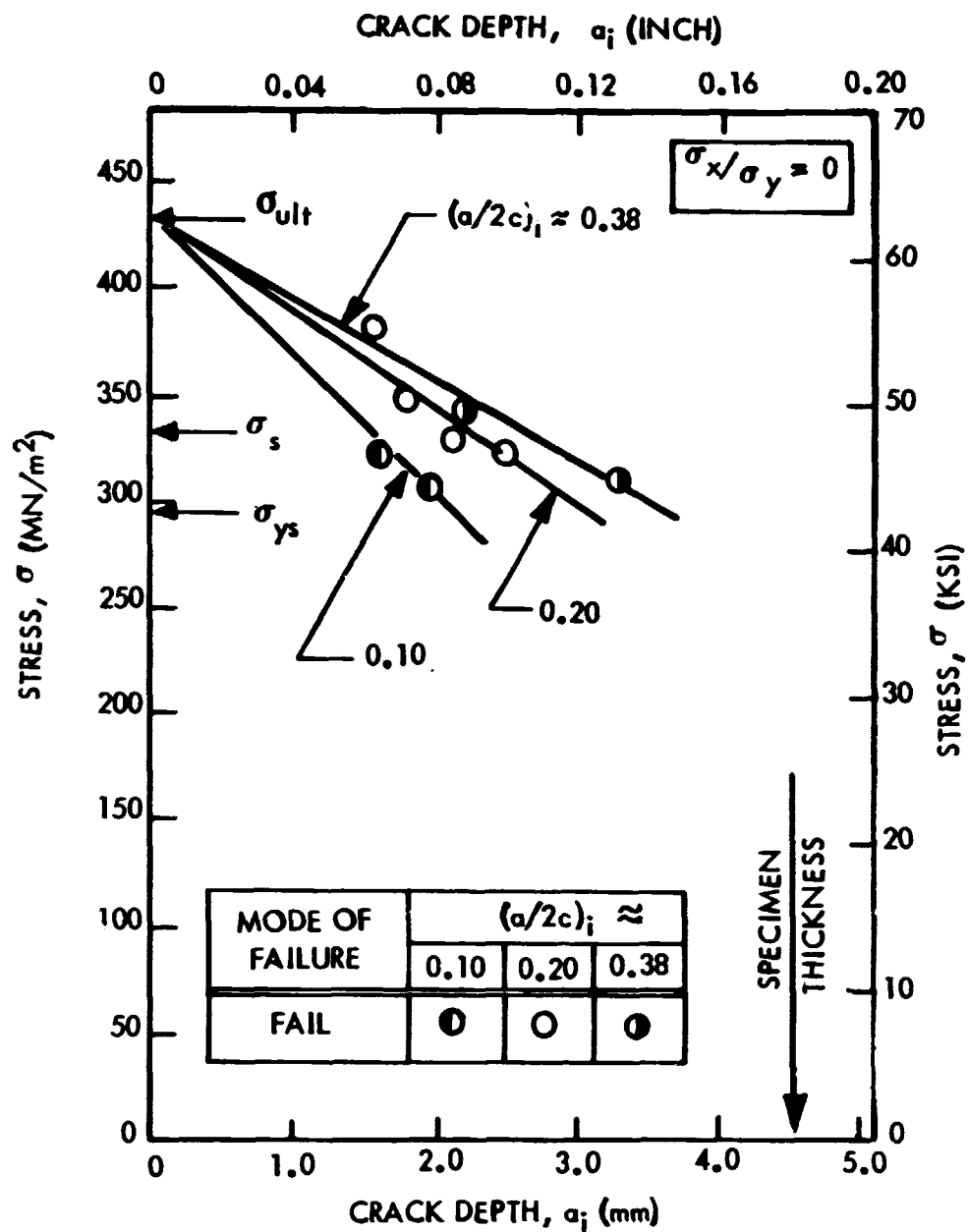


FIGURE 19: FAILURE LOCI FOR 4.57 mm (0.180 INCH) THICK 2219-T62 ALUMINUM BASE METAL AS A FUNCTION OF CRACK DEPTH

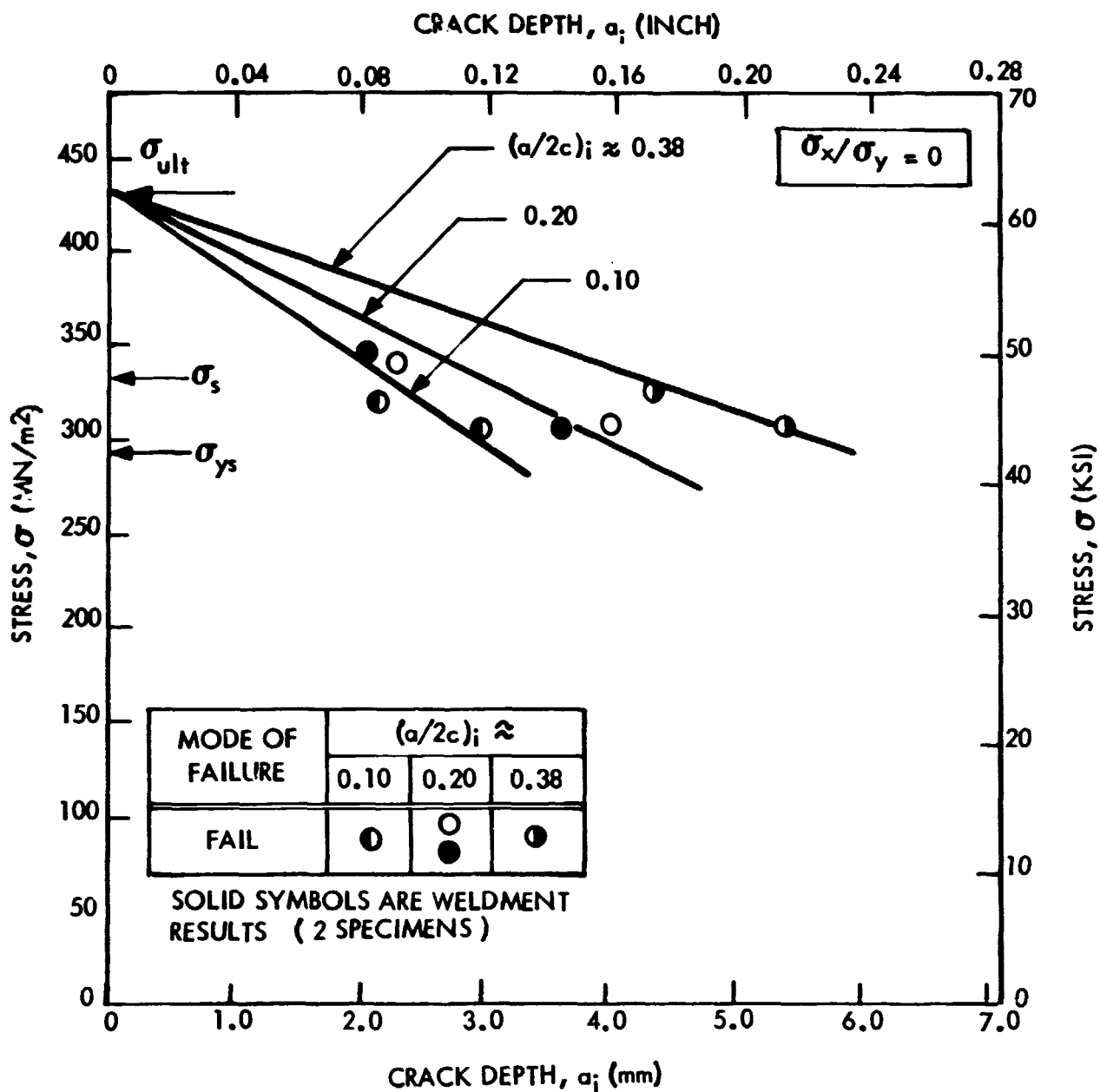


FIGURE 20: FAILURE LOCI FOR 7.62 mm (0.300 INCH) THICK 2219-T62 ALUMINUM AS A FUNCTION OF CRACK DEPTH

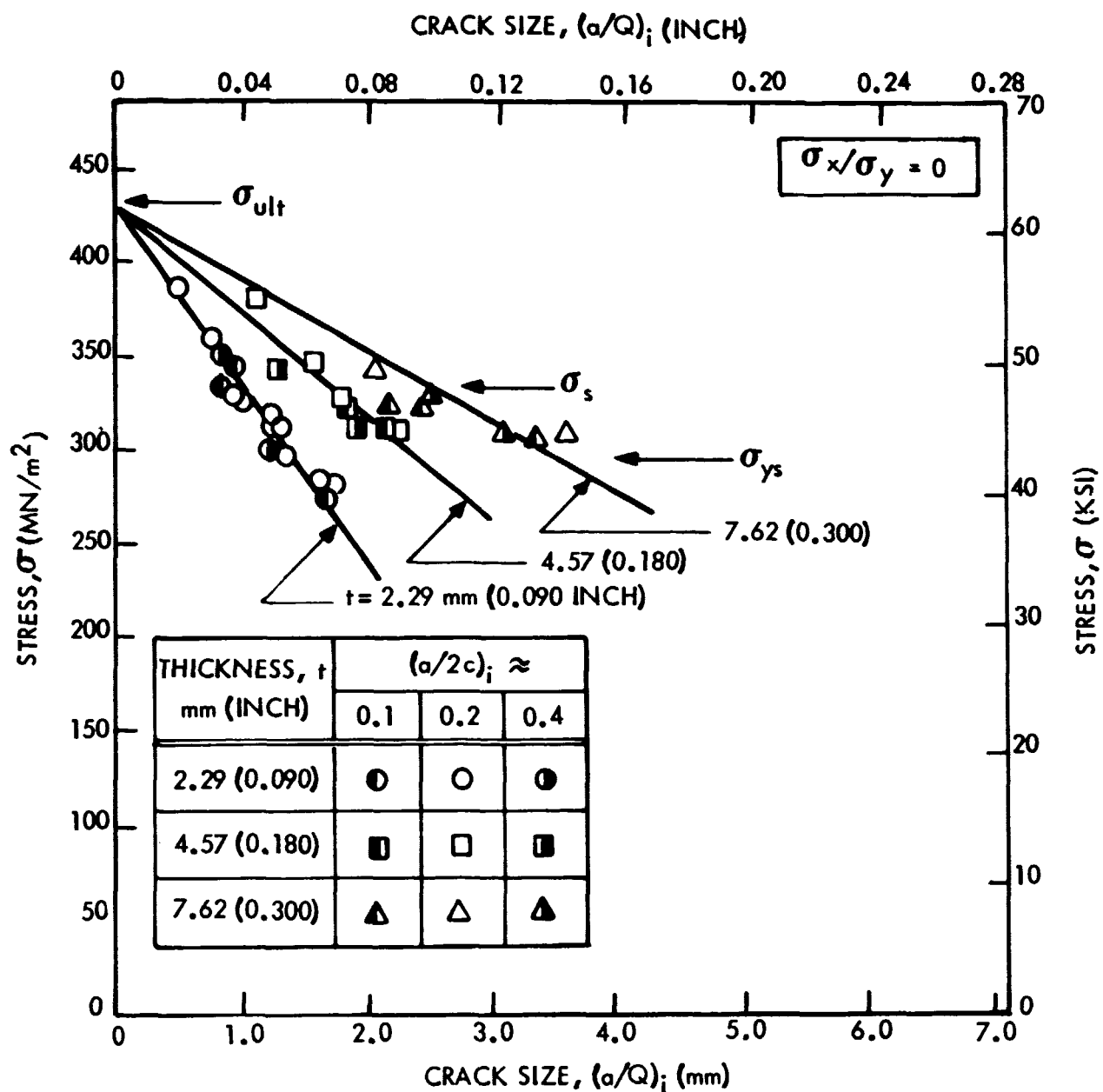


FIGURE 21: FAILURE LOCI FOR 2219-T62 ALUMINUM BASE METAL AS A FUNCTION OF a/Q .

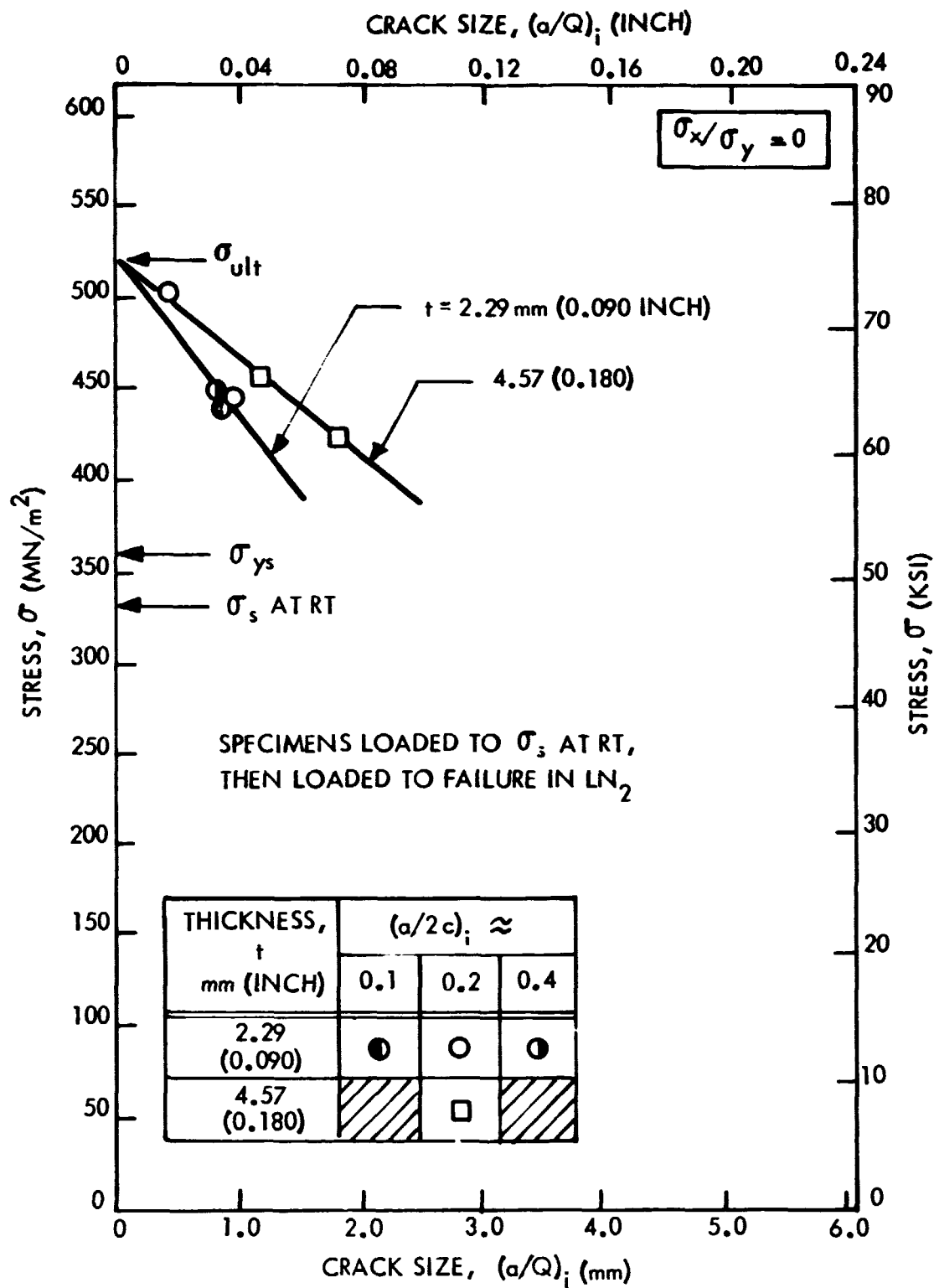


FIGURE 22: FAILURE LOCI FOR 2219-T62 ALUMINUM BASE METAL AT 78K (-320°F) AS A FUNCTION OF a/Q .

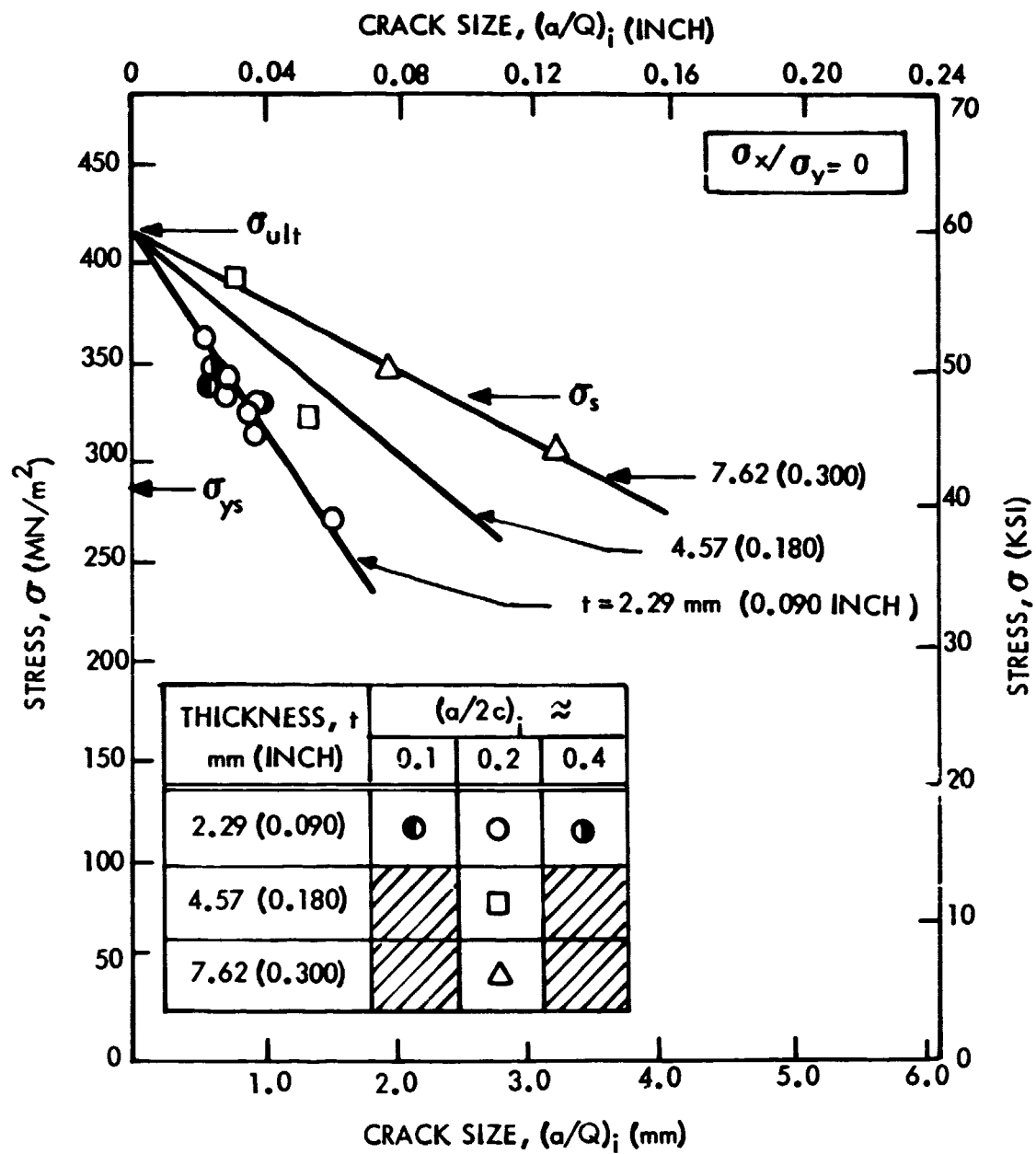


FIGURE 23: FAILURE LOCI FOR 2219-T62 ALUMINUM WELD METAL AS A FUNCTION OF a/Q .

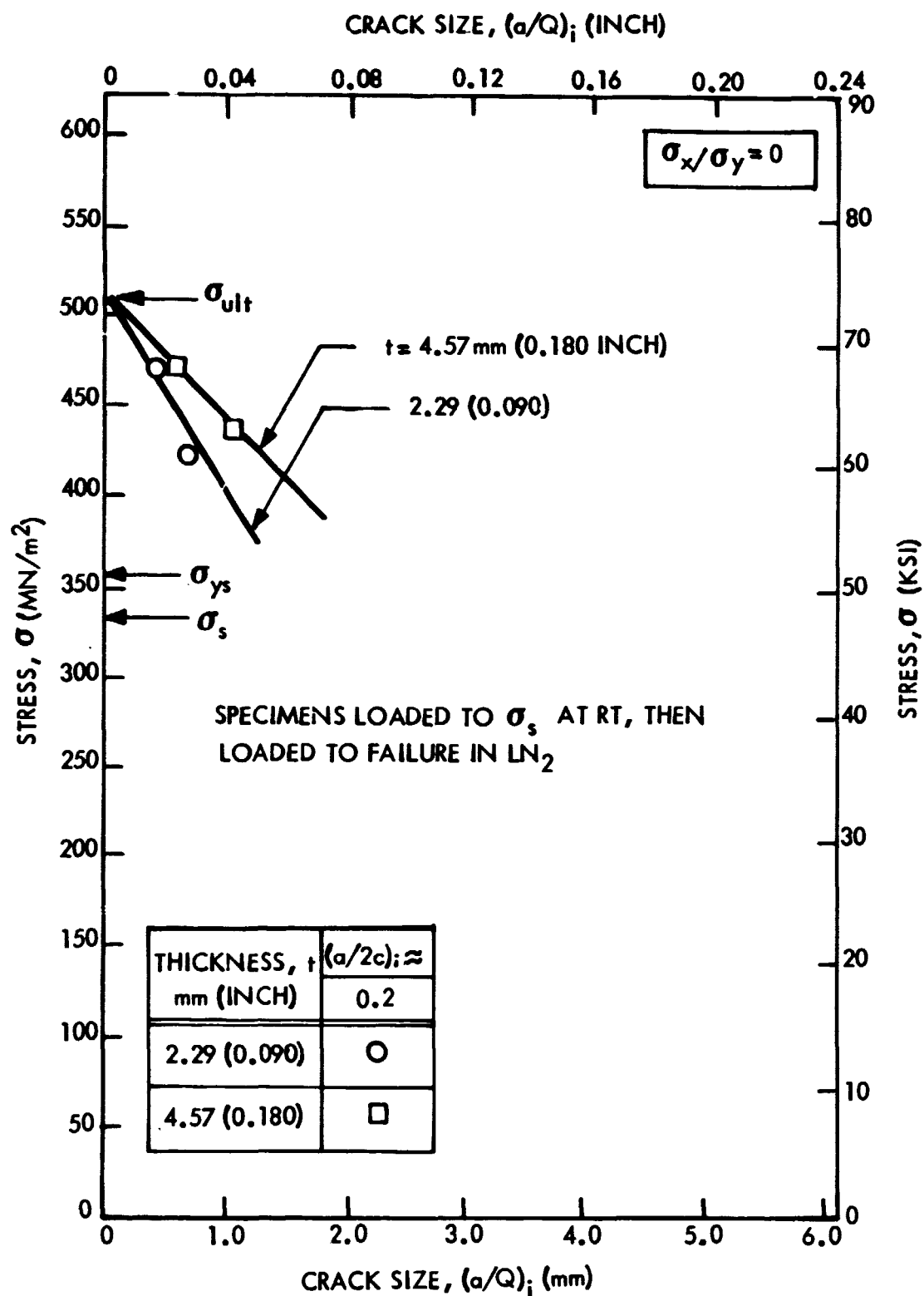


FIGURE 24: FAILURE LOCI FOR 2219-T62 ALUMINUM WELD METAL AT 78K (-320°F) AS A FUNCTION OF a/Q .

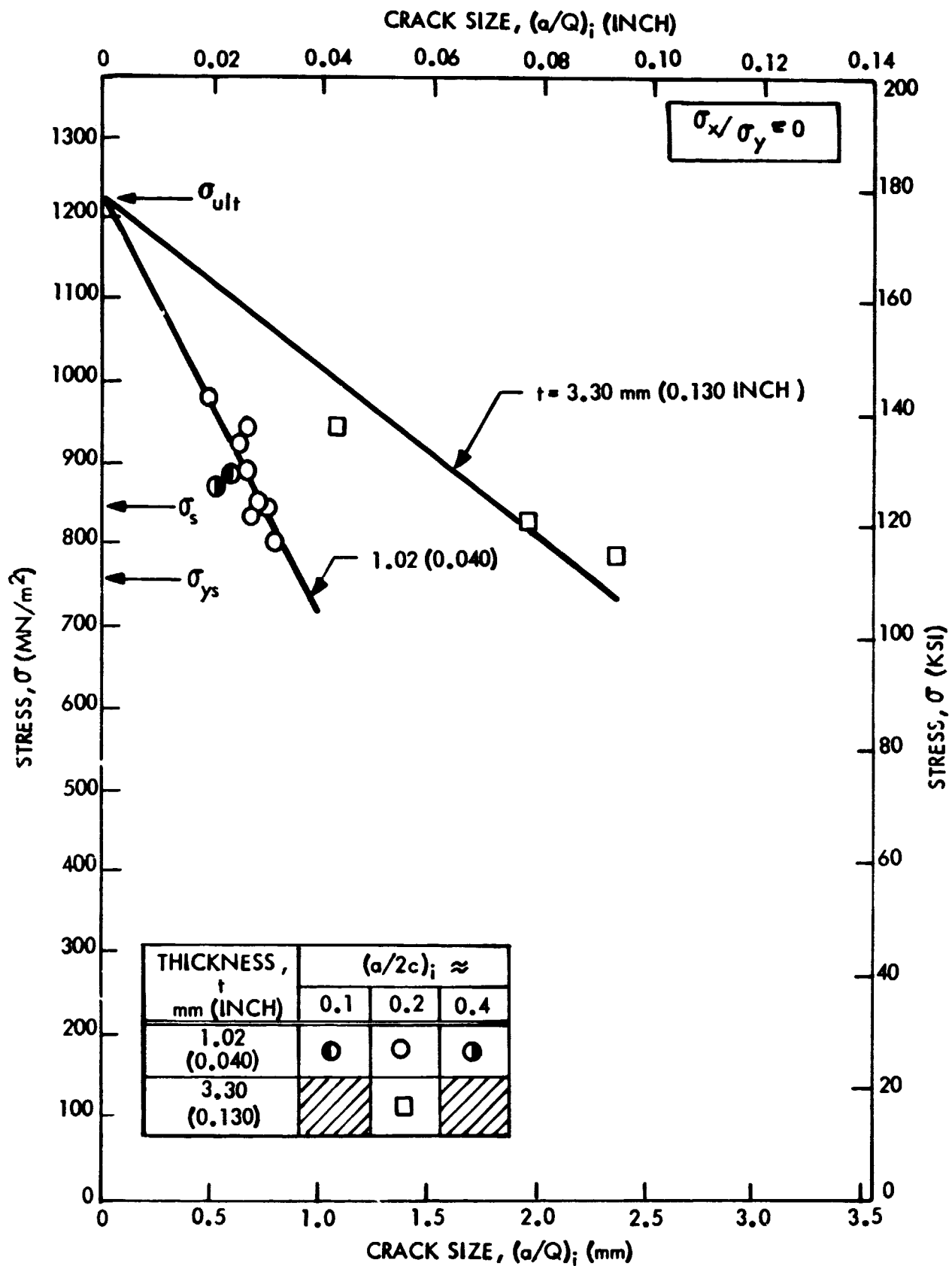


FIGURE 25: FAILURE LOCI FOR INCONEL X750 STA BASE METAL AS A FUNCTION OF a/Q .

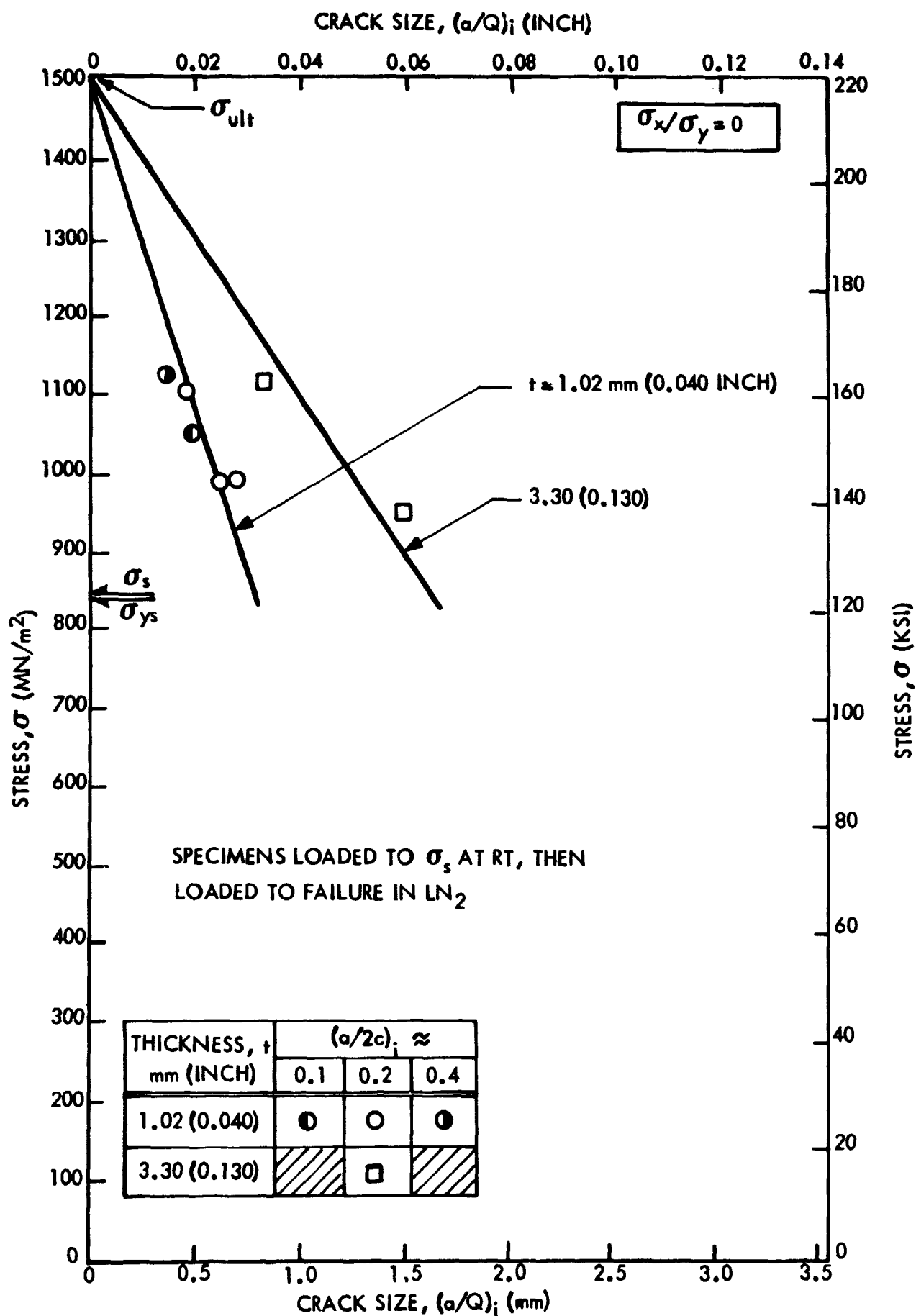


FIGURE 26: FAILURE LOCI FOR INCONEL X750 STA BASE METAL AT 78 K (-320°F) AS A FUNCTION OF a/Q .

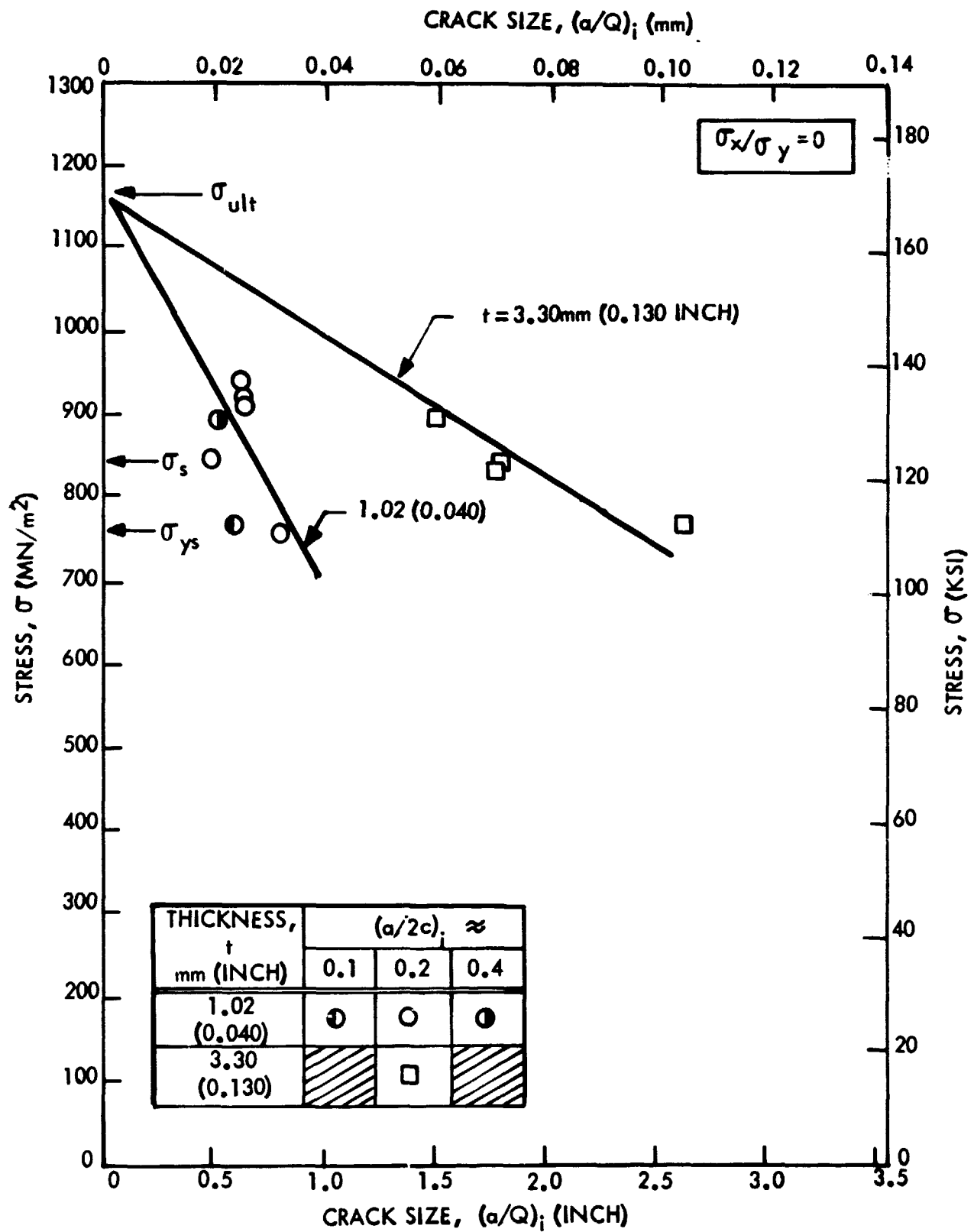


FIGURE 27: FAILURE LOCI FOR INCONEL X750 STA WELD METAL AS A FUNCTION OF a/Q

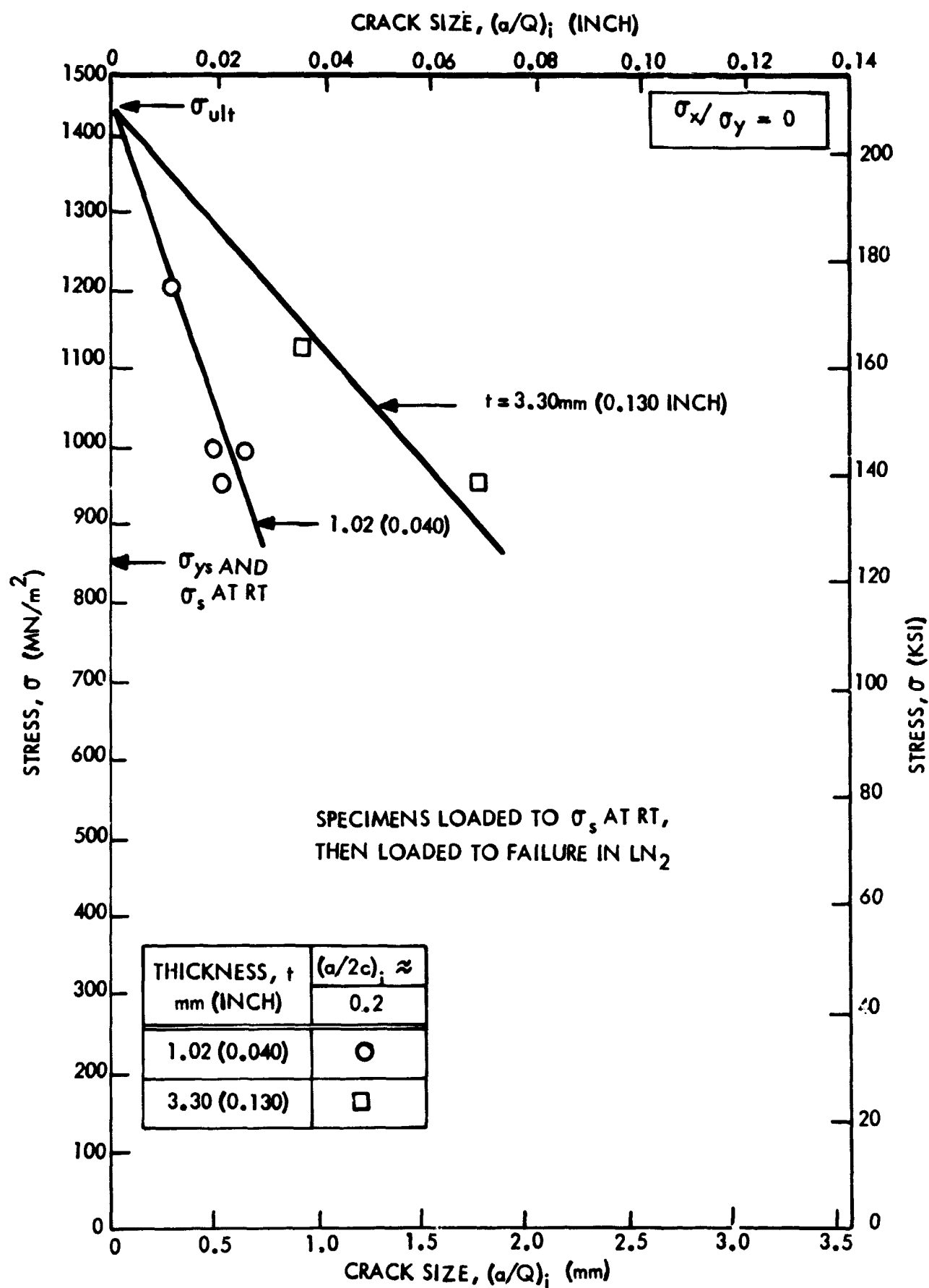


FIGURE 28: FAILURE LOCI FOR INCONEL X750 STA STA WELD METAL AT 78K (-320°F) AS A FUNCTION OF a/Q

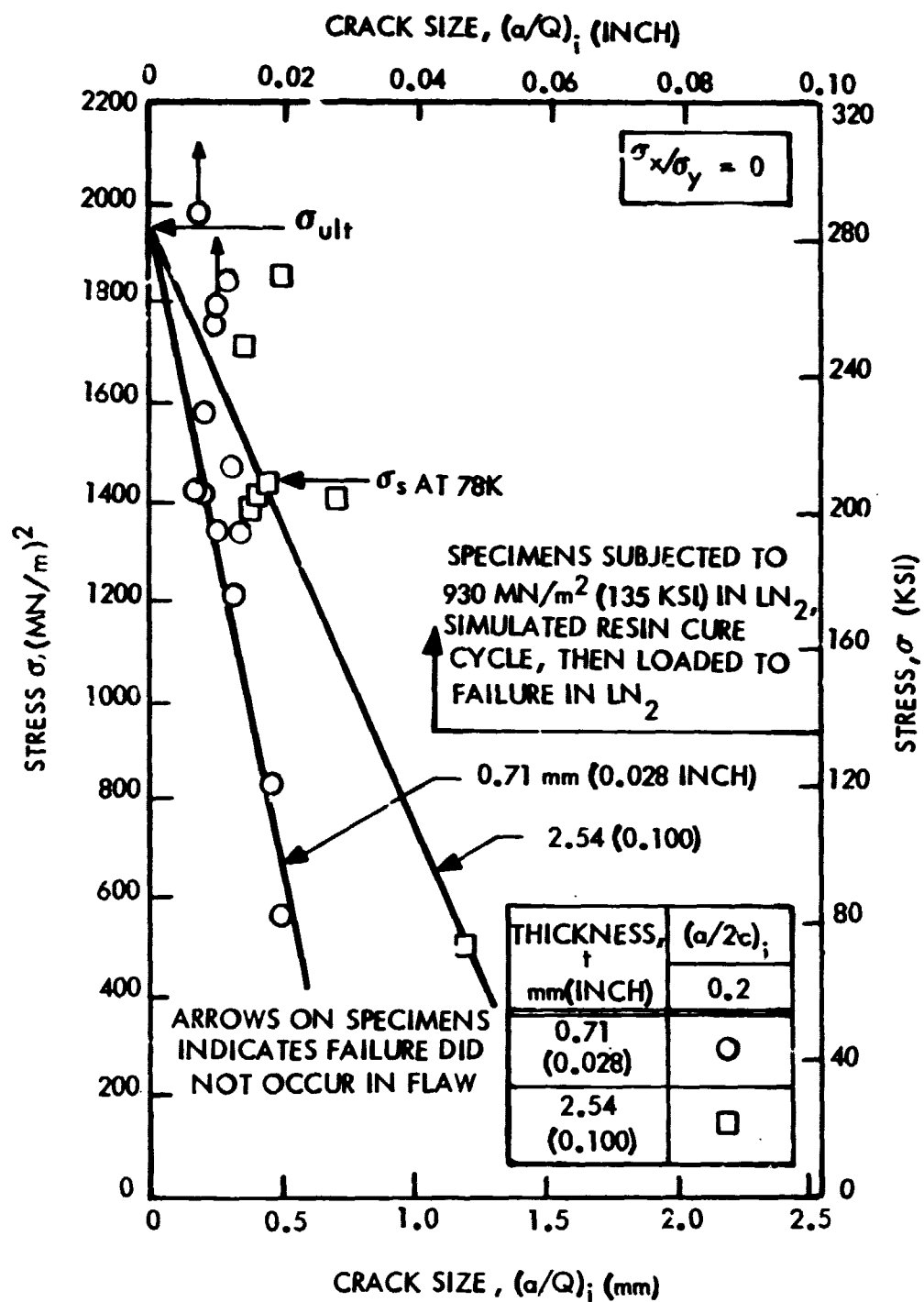


FIGURE 29: FAILURE LOCI FOR CRYOSTRETCHED 301 STAINLESS STEEL BASE METAL AT 78K (-320°F) AS A FUNCTION OF a/Q .

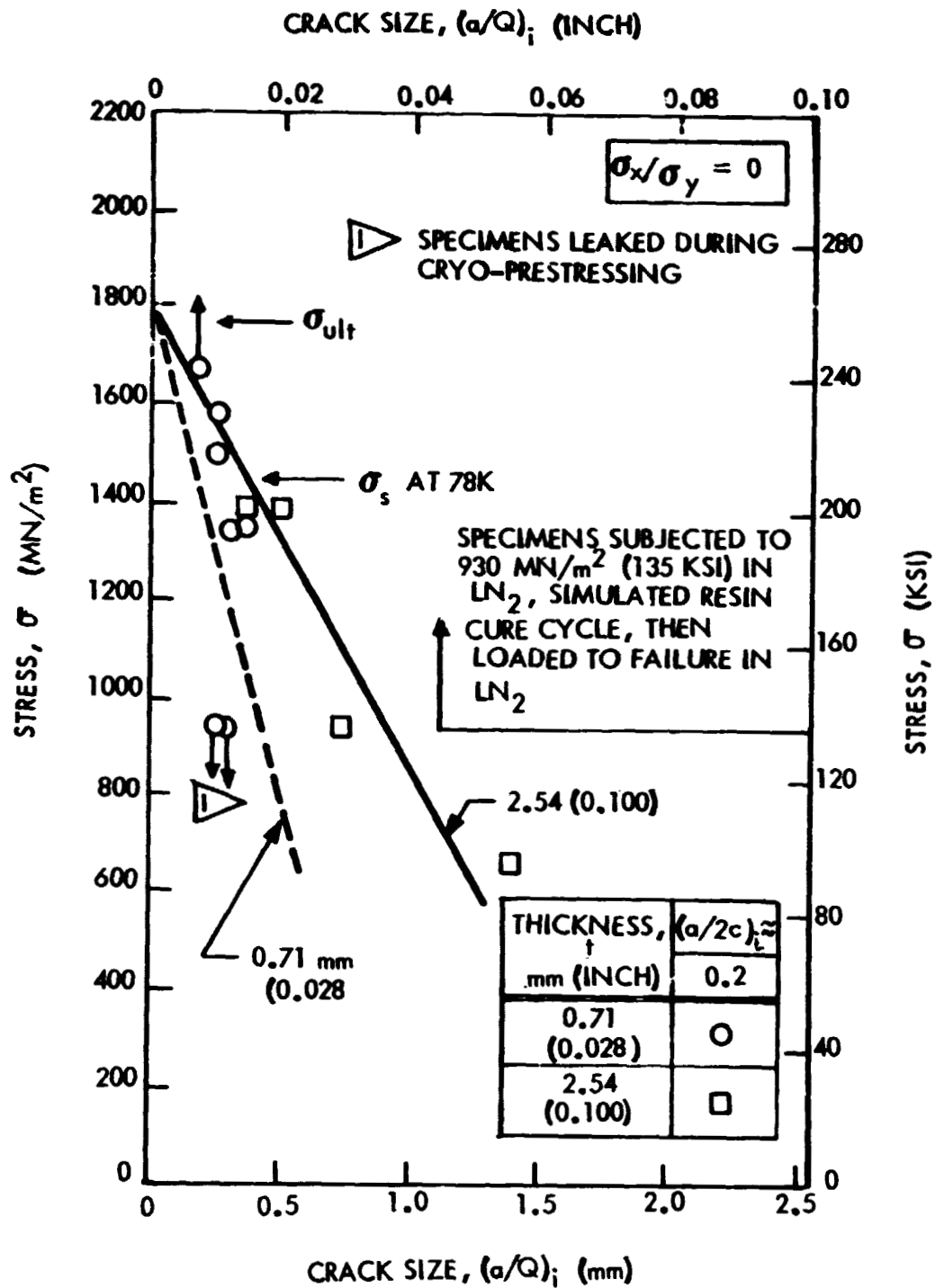


FIGURE 30: FAILURE LOCI FOR CRYOSTRETCHED 301 STAINLESS STEEL WELD METAL AT 78K (-320°F) AS FUNCTION OF a/Q .

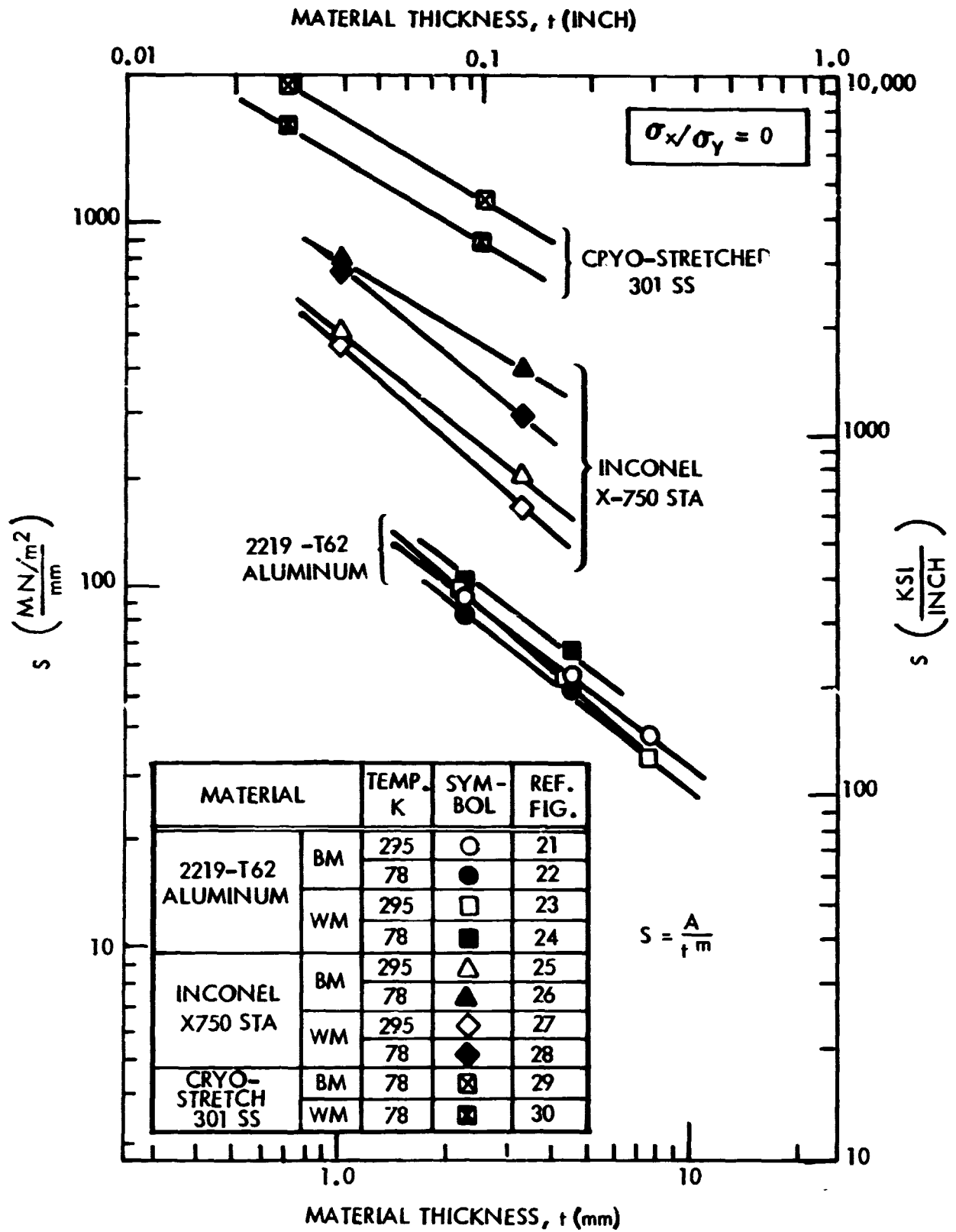


FIGURE 31: RELATIONSHIP BETWEEN S AND

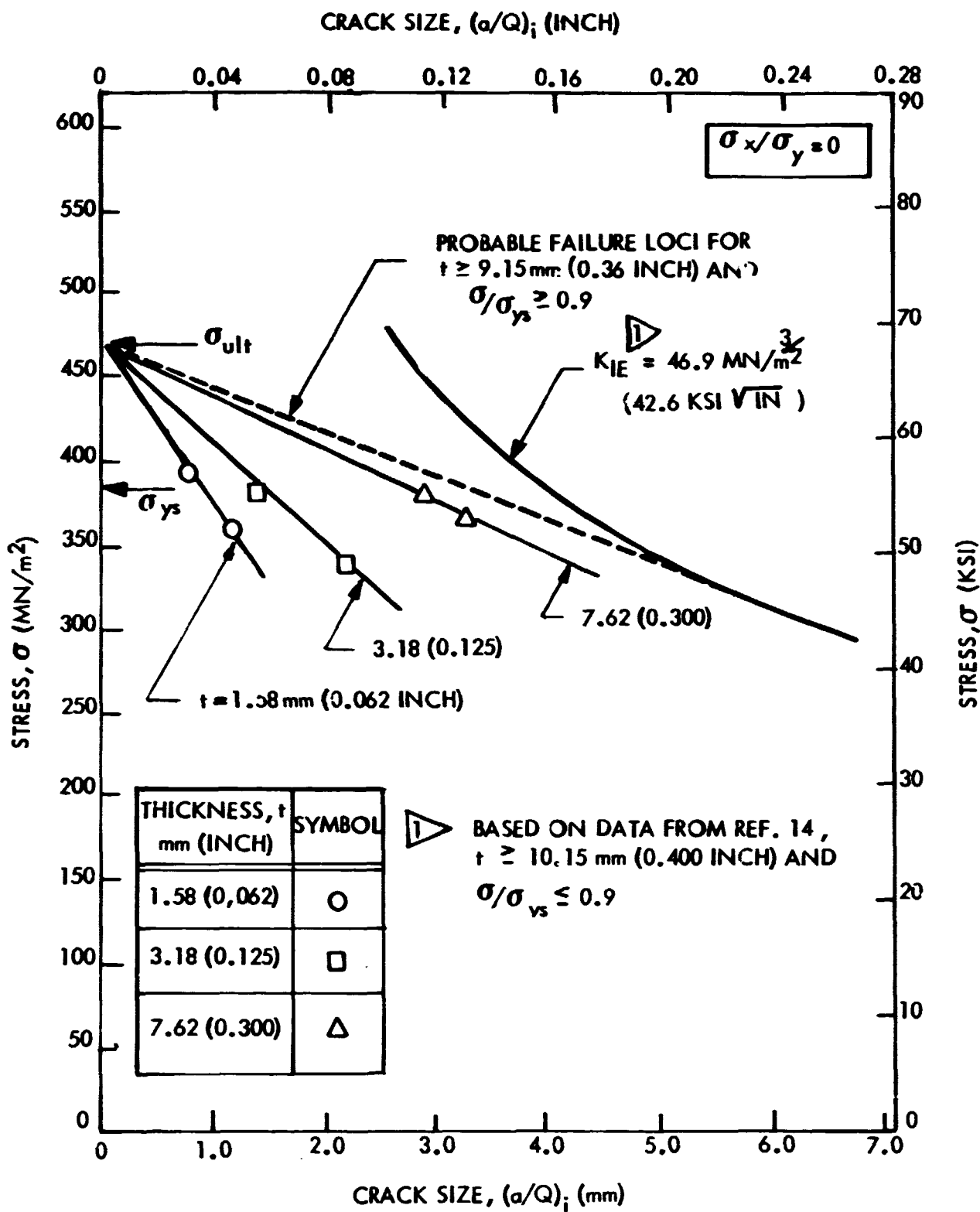


FIGURE 32: FAILURE LOCI FOR 2219-T87 ALUMINUM BASE METAL AS A FUNCTION OF a/Q (REFERENCE 12)

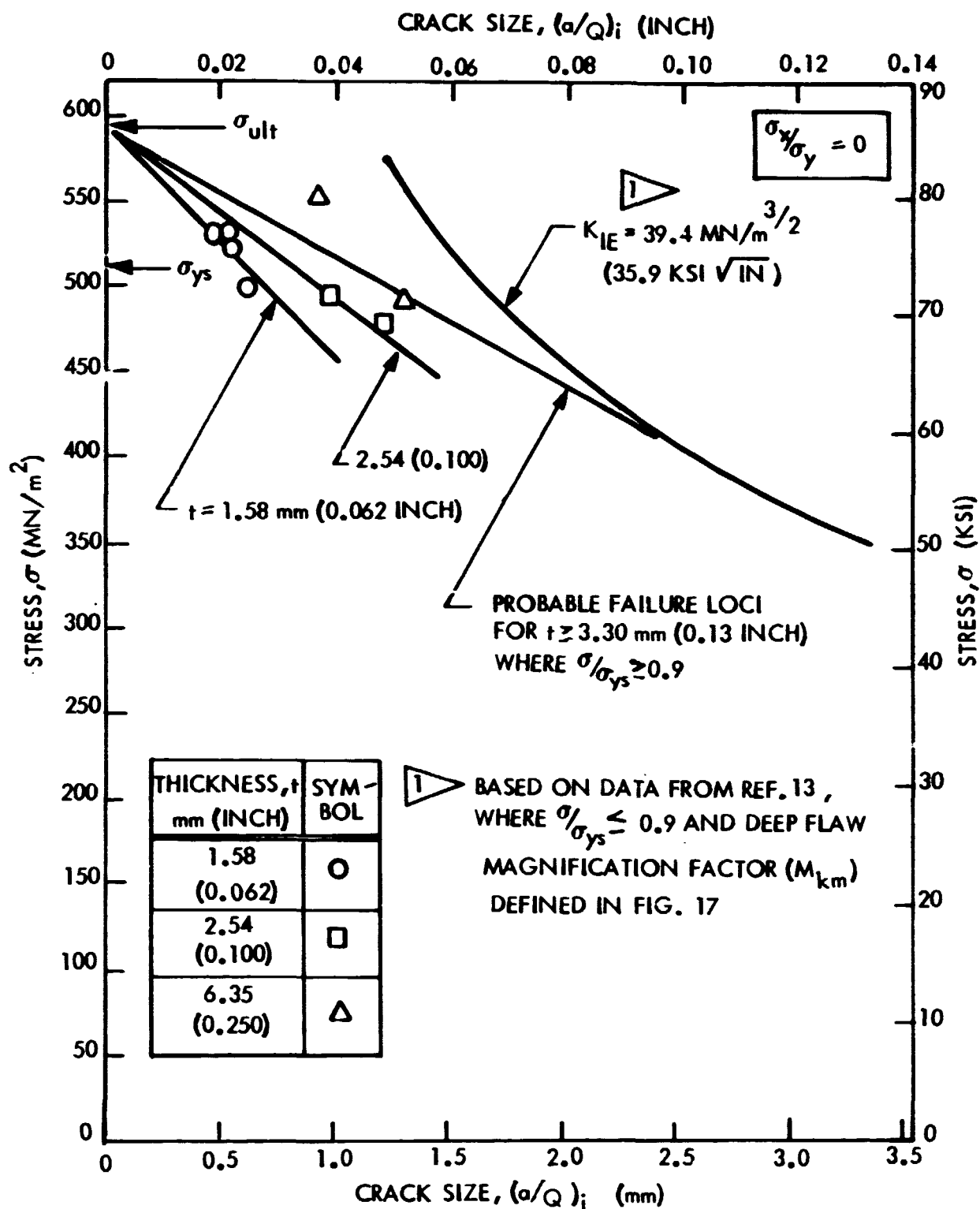


FIGURE 33: FAILURE LOCI FOR 7075-T651 ALUMINUM BASE METAL AS A FUNCTION OF a/Q (REFERENCE 13)

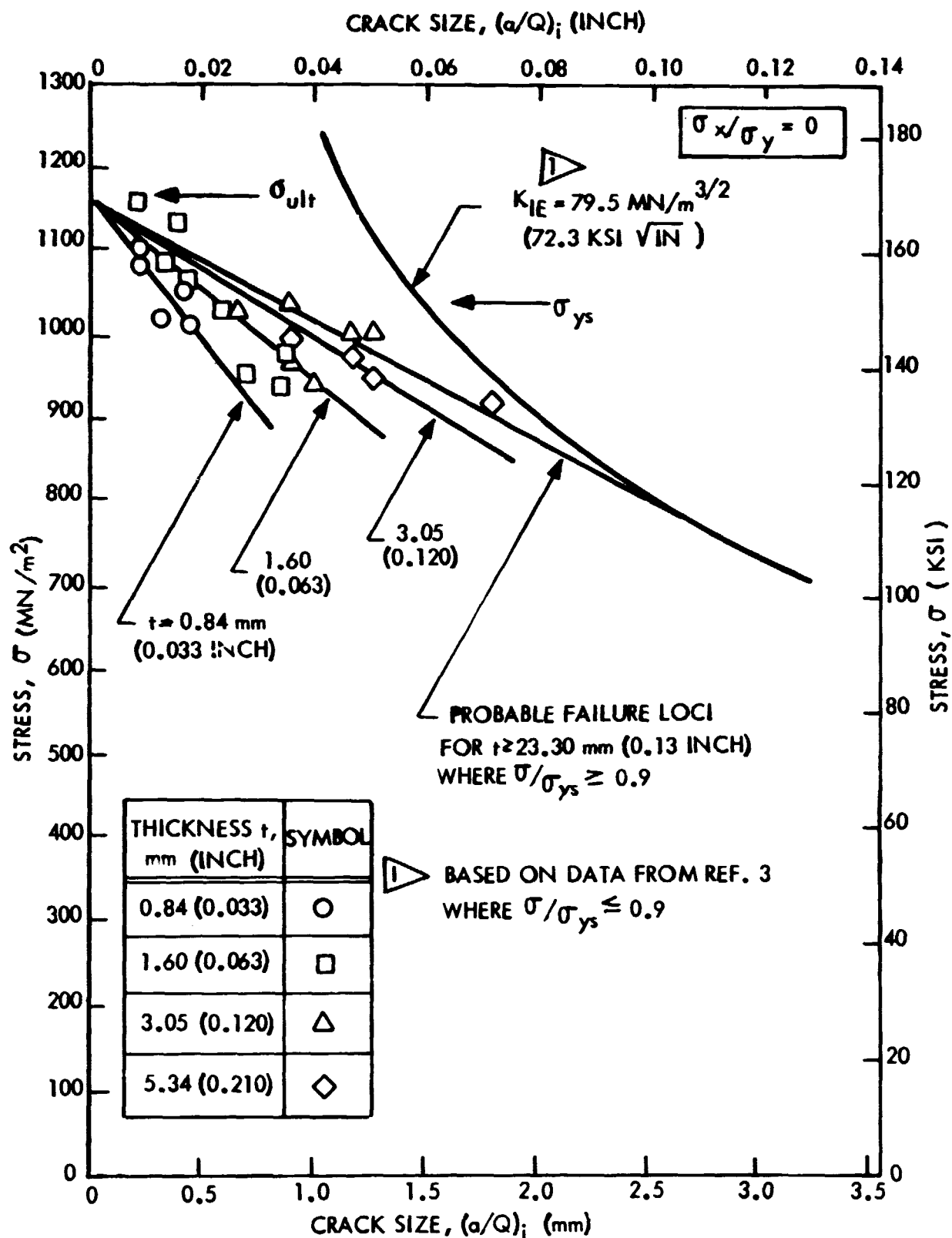


FIGURE 34: FAILURE LOCI FOR 6Al-4V STA TITANIUM BASE METAL AS A FUNCTION OF a/Q (REFERENCE 3)



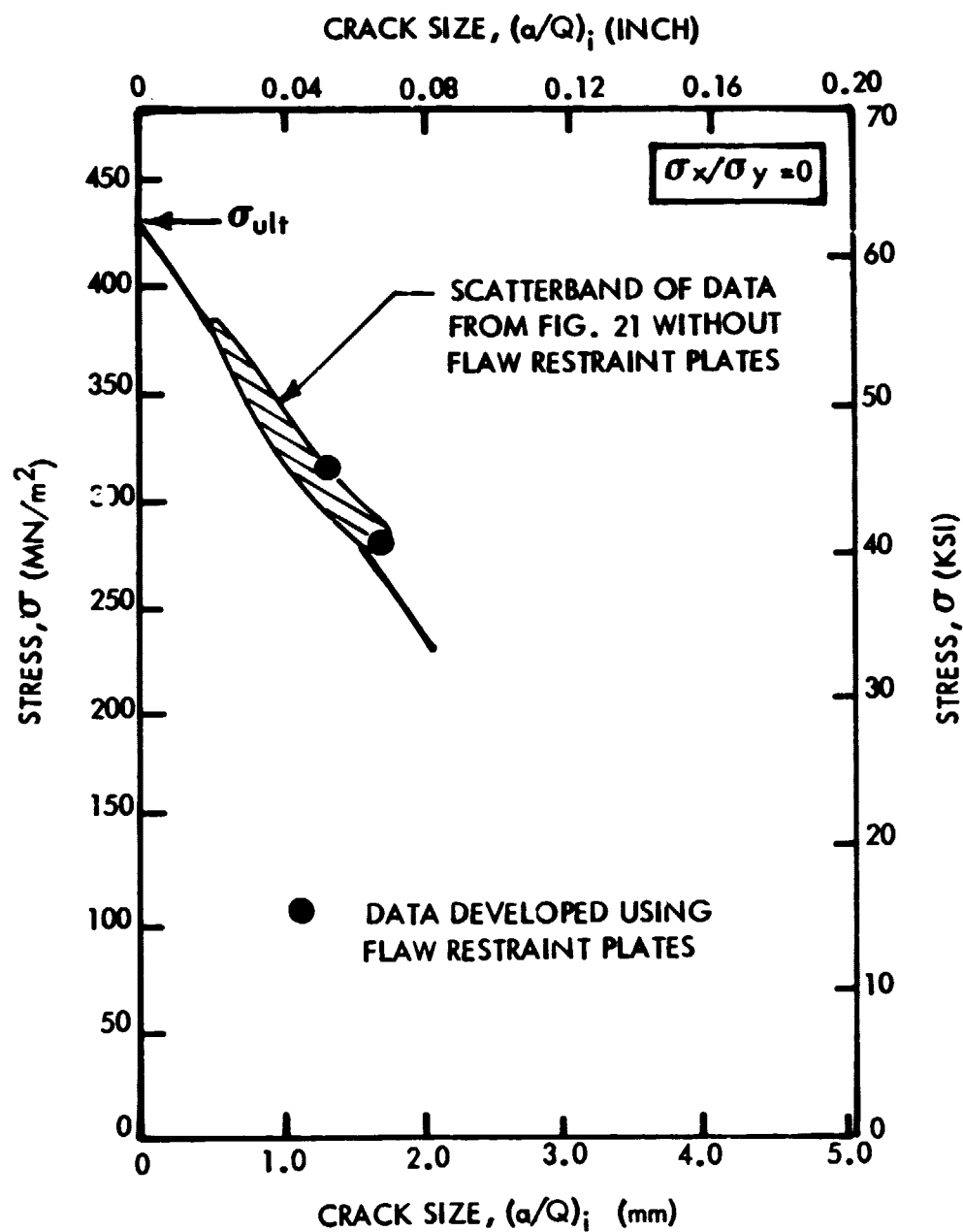


FIGURE 36: COMPARISON OF STATIC FRACTURE DATA DEVELOPED WITH AND WITHOUT FLAW RESTRAINT PLATES - 2.29 mm (0.090 INCH) THICK 2219-T62 ALUMINUM BM AT 295 K (72° F)

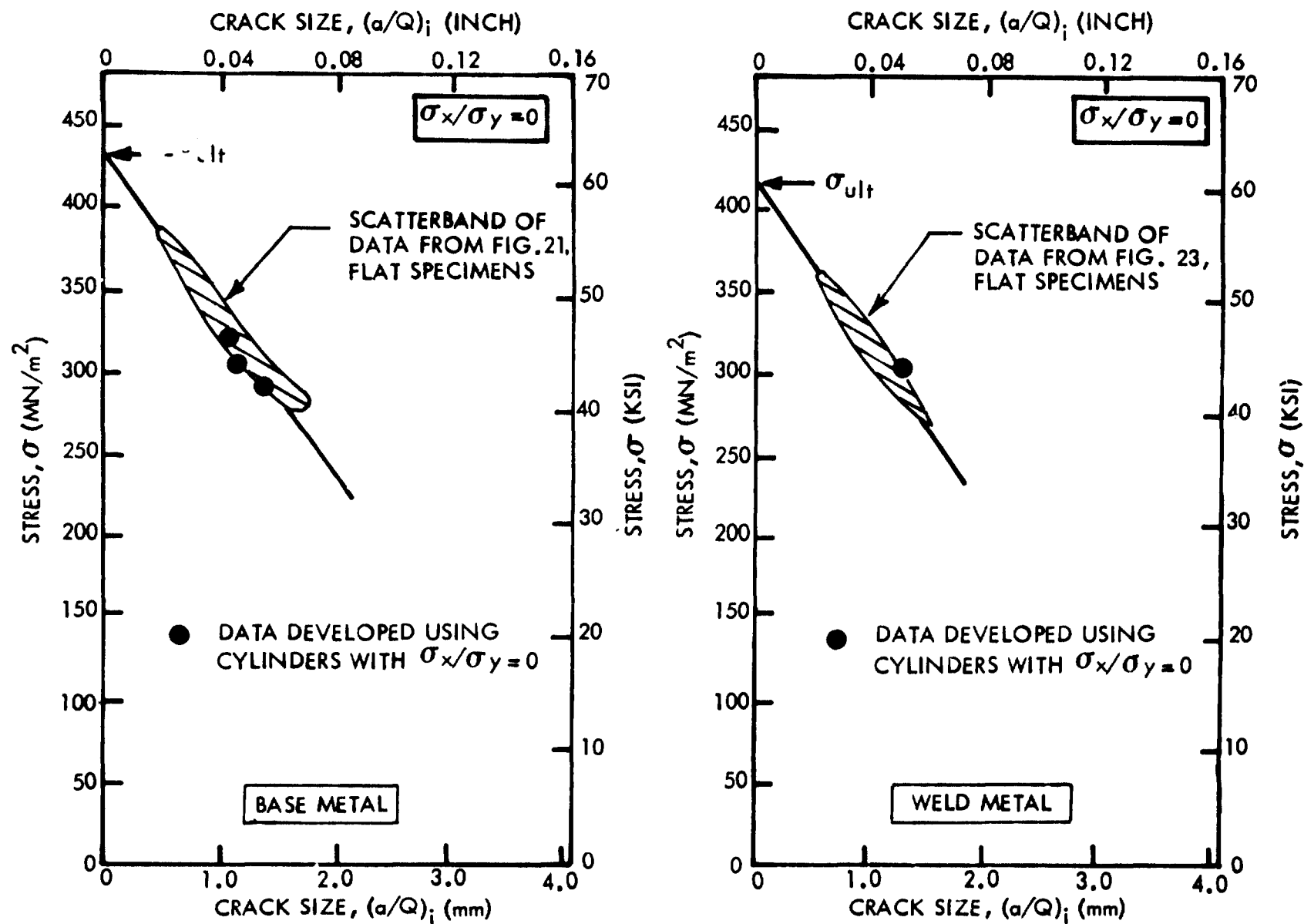


FIGURE 37: COMPARISON OF STATIC FRACTURE DATA DEVELOPED USING FLAT AND CURVED SPECIMENS MADE OF 2.29 mm (0.090 INCH) THICK 2219-T62 ALUMINUM AT 295 K (72°F)

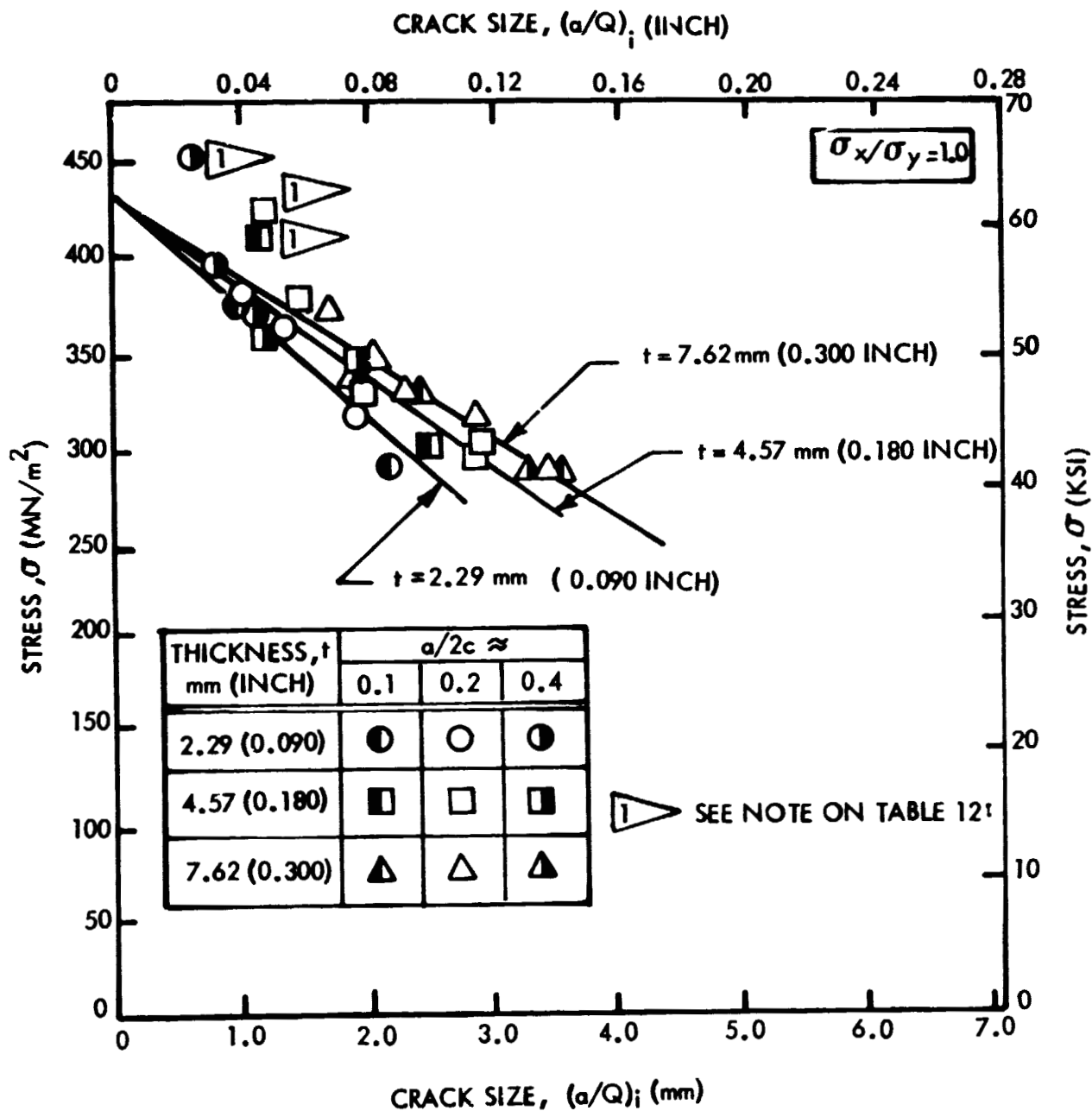


FIGURE 38: FAILURE LOCI FOR EQUAL BIAXIALY LOADED (SPHERICAL CAP SPECIMENS) 2219-T62 ALUMINUM BM AS A FUNCTION OF a/Q .

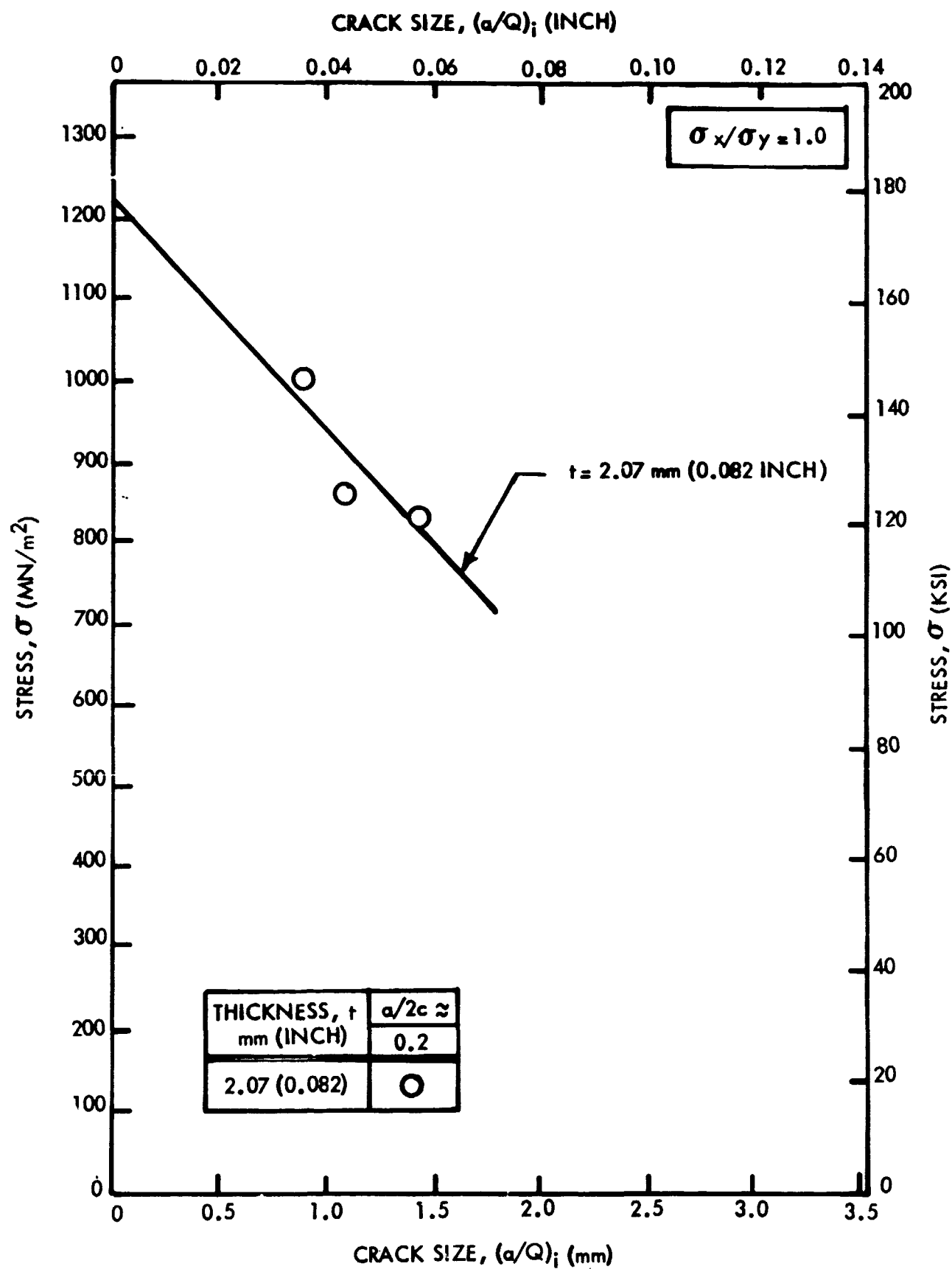


FIGURE 39: FAILURE LOCI FOR EQUAL BIAXIALLY LOADED (SPHERICAL CAP SPECIMENS) INCONEL X 750 STA BM AS A FUNCTION OF a/Q

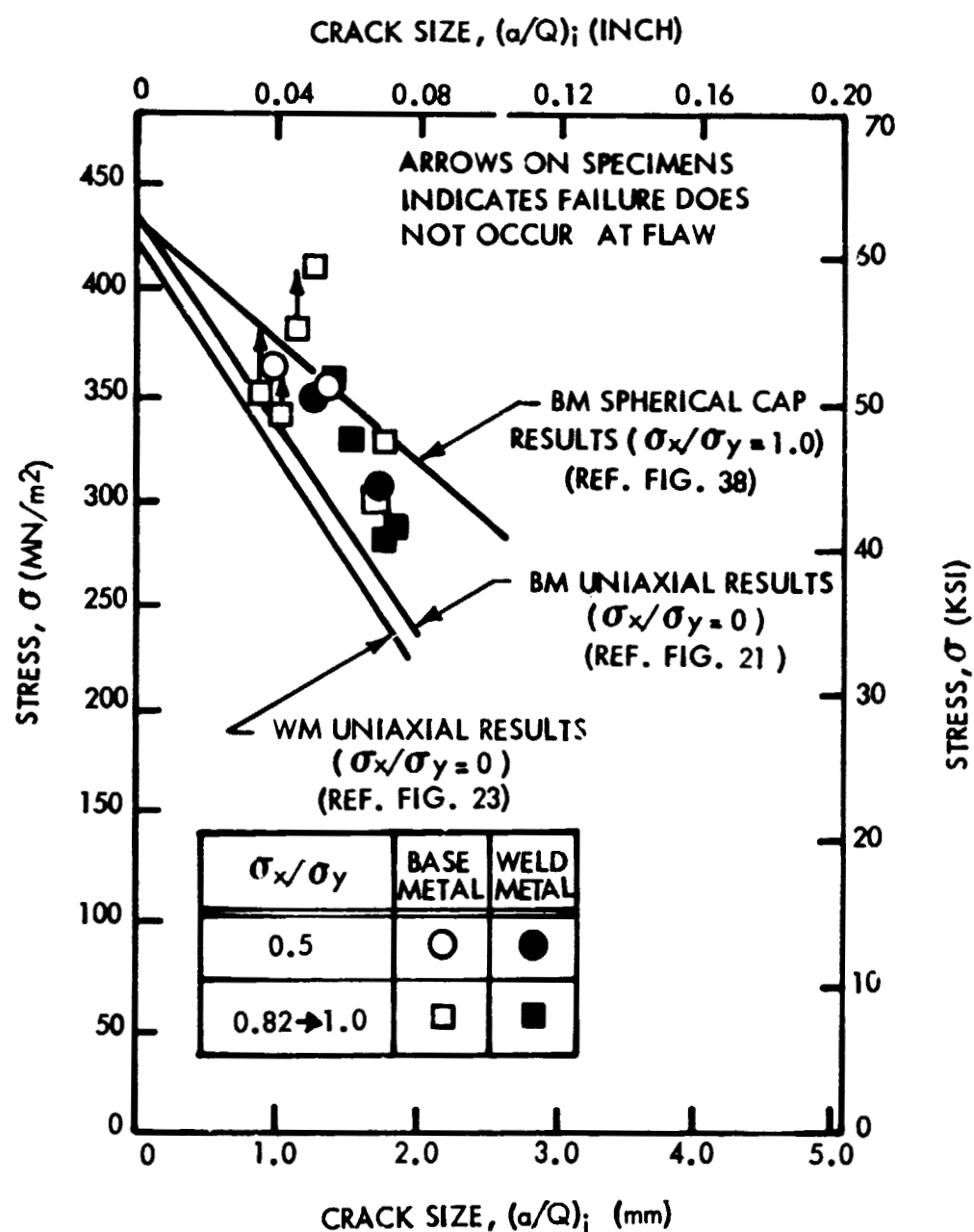


FIGURE 40: FAILURE LOCI OF 2.29 mm (0.090 INCH) 2219-T62 ALUMINUM CYLINDRICAL TANK SPECIMENS (NON-OVERWRAPPED AND OVERWRAPPED) AS A FUNCTION OF a/Q

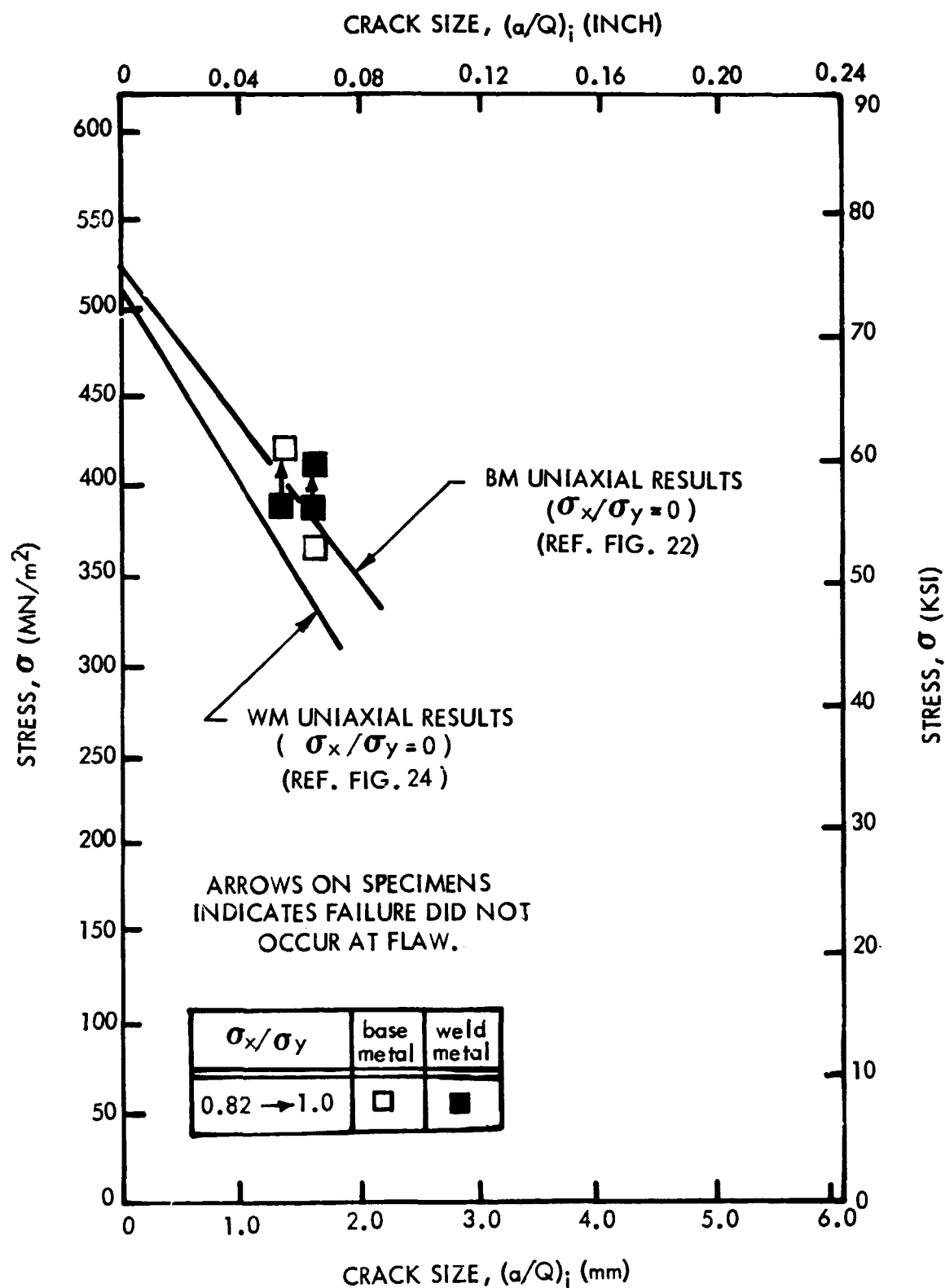


FIGURE 41: FAILURE LOCI OF 2.29 mm(0.090 INCH) 2219-T62 ALUMINUM CYLINDRICAL TANK SPECIMENS (OVERWRAPPED) AS A FUNCTION OF a/Q AT 78K (-320°F)

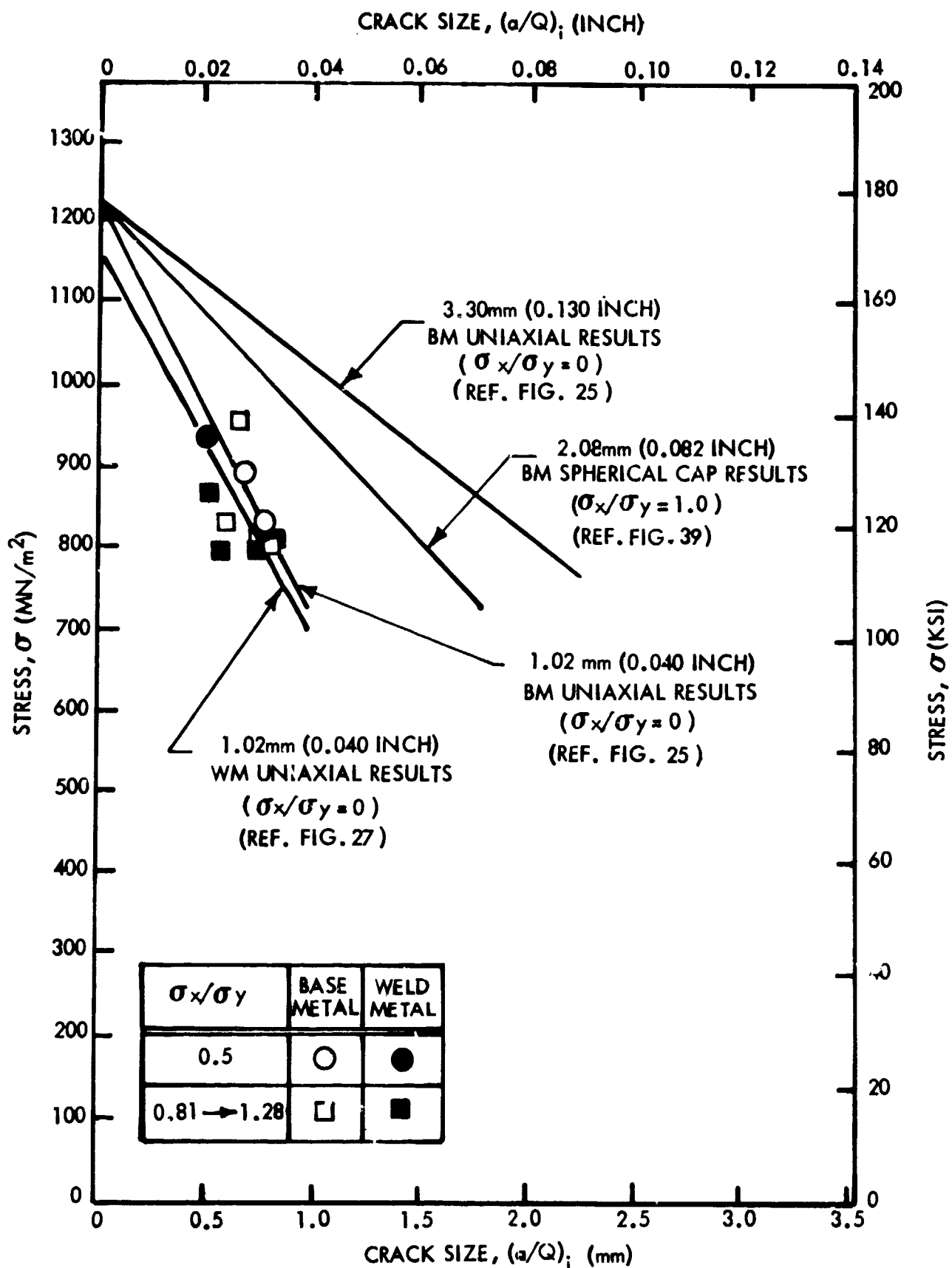


FIGURE 42: FAILURE LOCI OF 1.02mm (0.040 INCH) INCONEL X750 STA CYLINDRICAL TANK SPECIMENS (NON-OVERWRAPPED AND OVERWRAPPED) AS A FUNCTION OF a/Q .

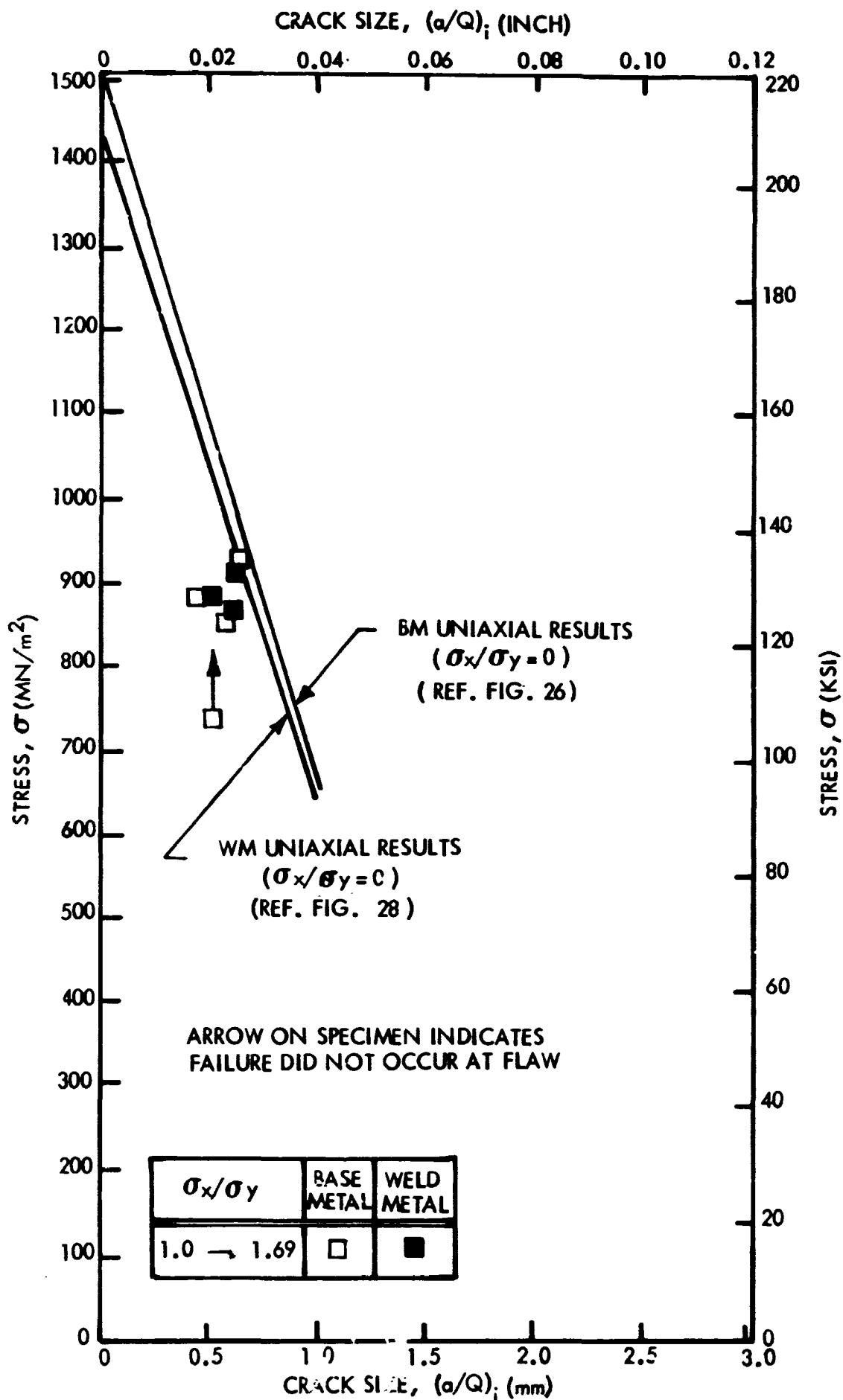


FIGURE 43: FAILURE LOCI OF 1.02mm (0.040 INCH) INCONEL X750 STA CYLINDRICAL TANK SPECIMENS (OVERWRAPPED) AS A FUNCTION OF a/Q AT 78 K (-320°F)

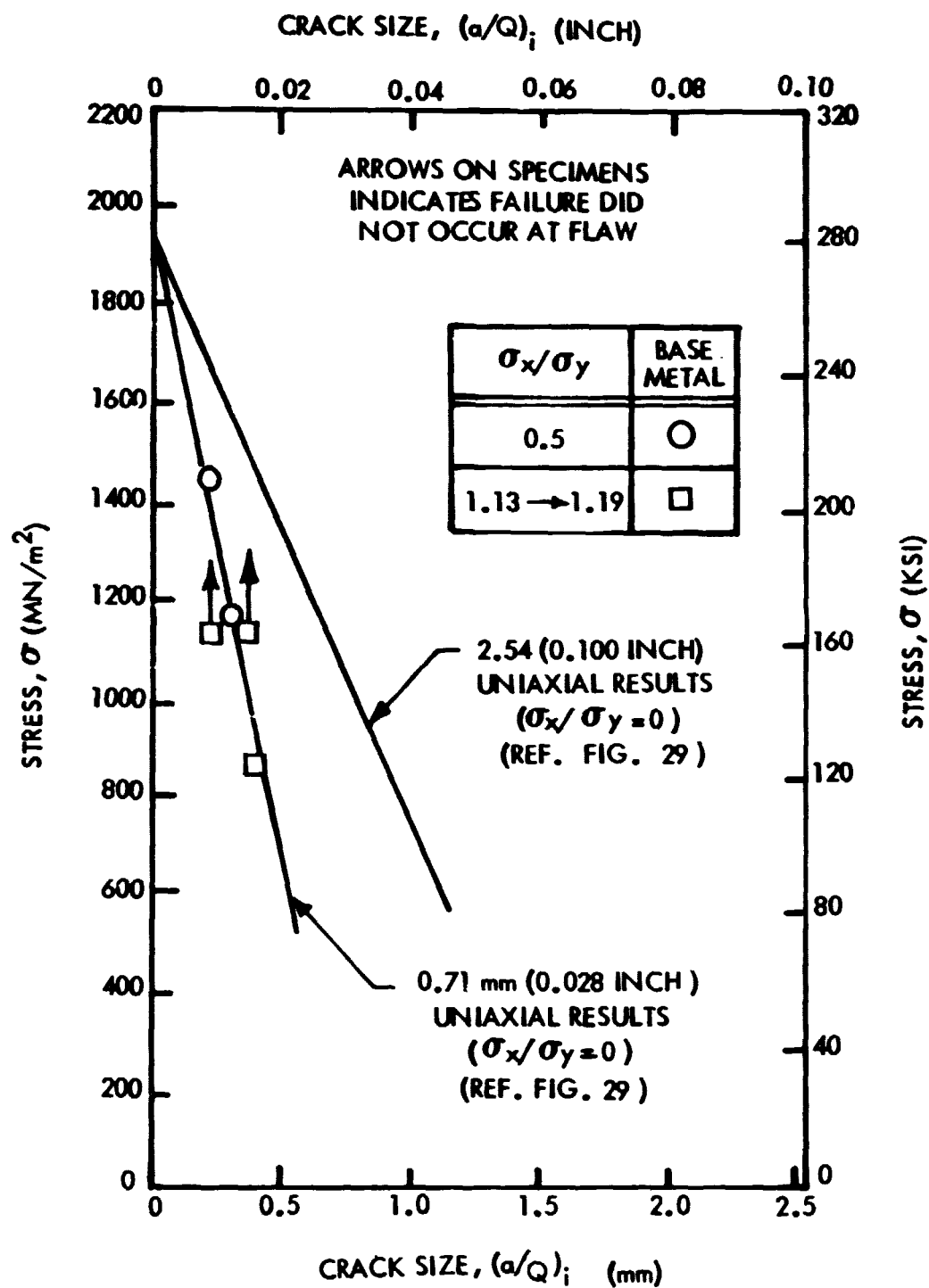


FIGURE 44: FAILURE LOCI OF 0.89 mm (0.035 INCH) CRYOFORMED 301 STAINLESS STEEL TANK SPECIMENS (NON-OVERWRAPPED AND OVERWRAPPED) AS A FUNCTION OF a/Q AT 78 K (-320°F)

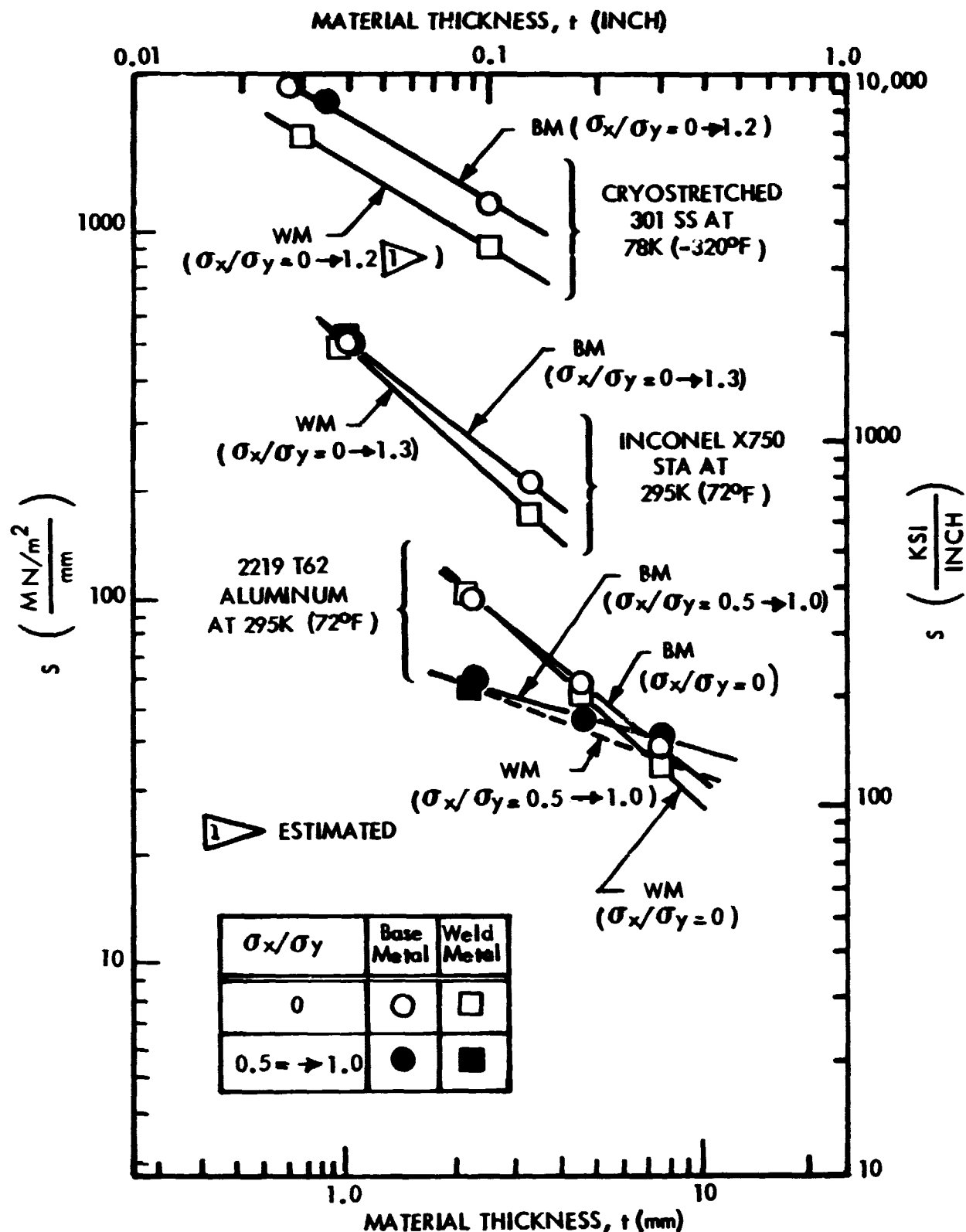


FIGURE 45: RELATIONSHIP BETWEEN S AND t FOR UNIAXIAL AND BIAXIAL STATIC FRACTURE RESULTS

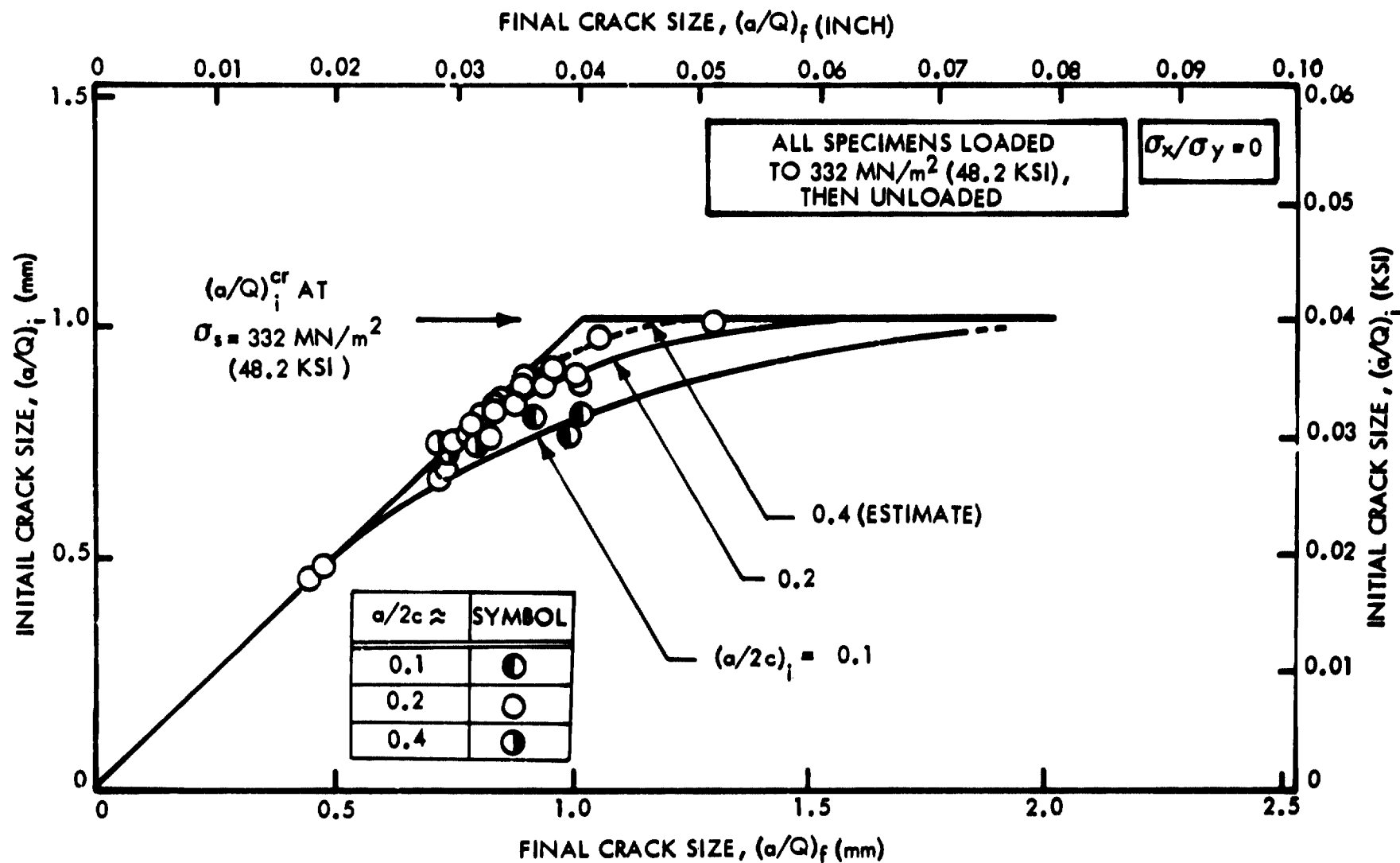


FIGURE 46: CRACK GROWTH-ON- LOADING FOR 2.29mm (0.090 INCH) THICK 2219-T62 ALUMINUM BASE METAL

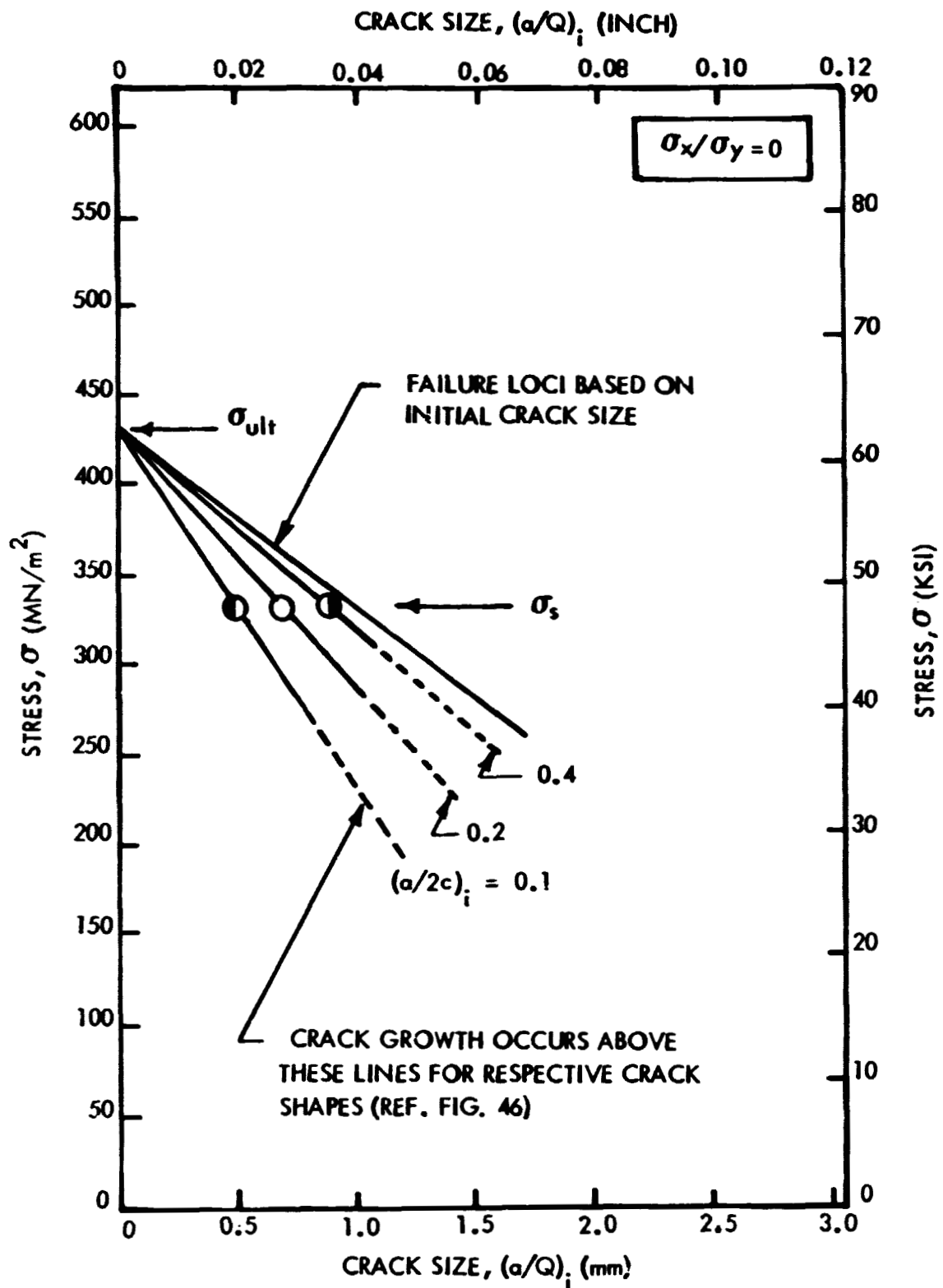


FIGURE 47 : NO GROWTH LOCI FOR 2.29 mm (0.090 INCH) THICK 2219-T62 ALUMINUM BASE METAL

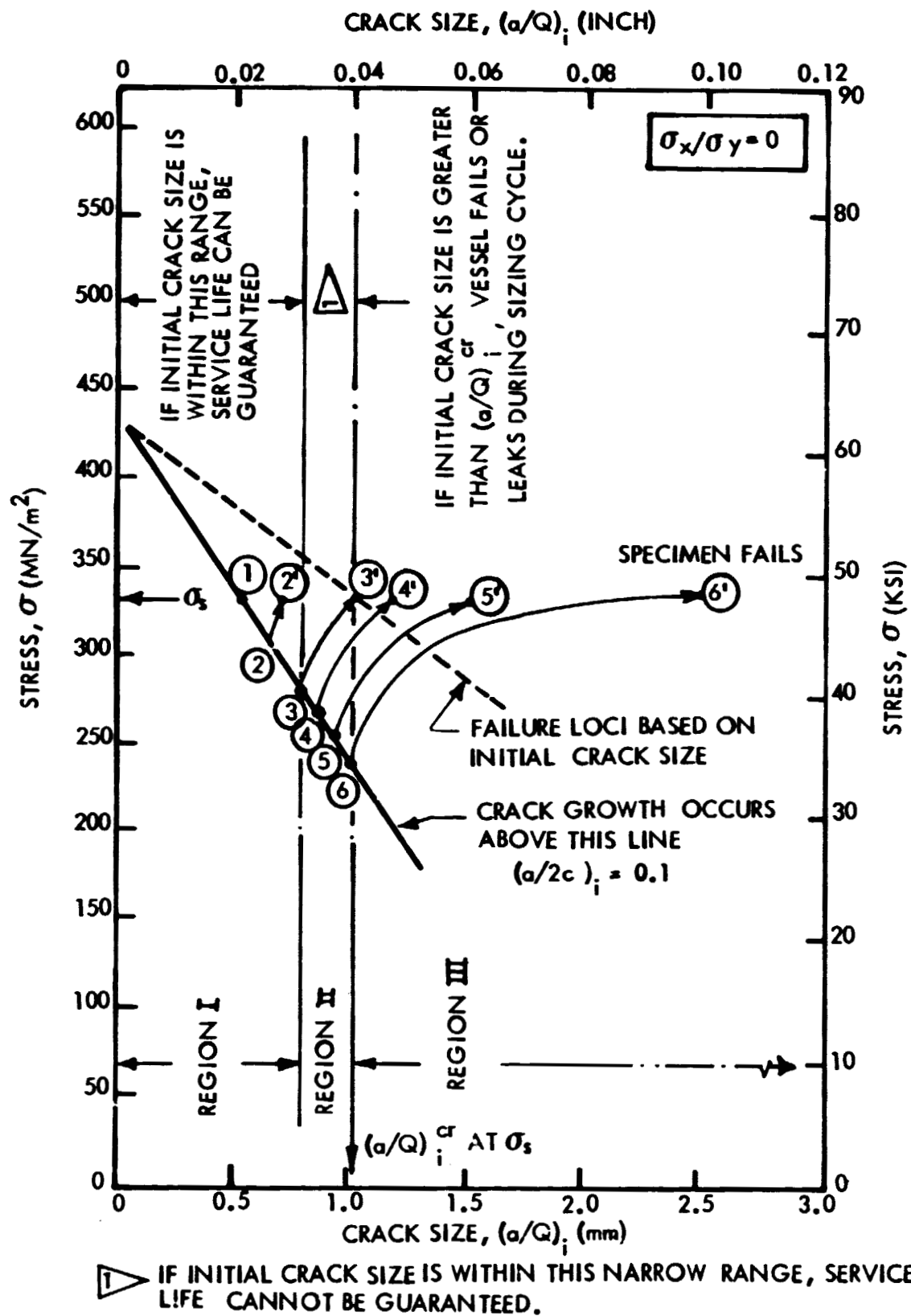


FIGURE 48: CRACK GROWTH OCCURING DURING SIZING FOR 2.29 mm (0.090 INCH) THICK 2219-T62 ALUMINUM BASE METAL, $(a/2c)_i = 0.1$

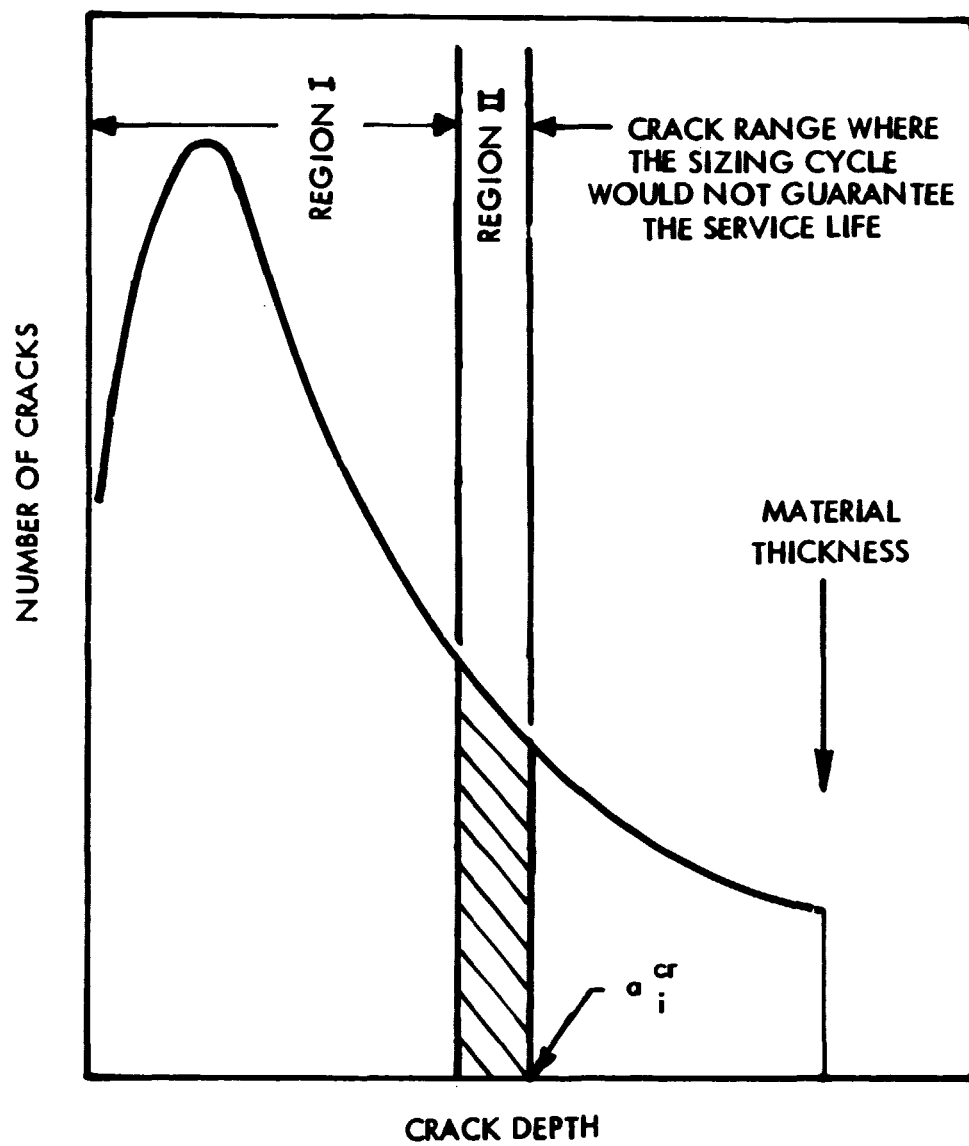


FIGURE 49: DISTRIBUTION OF CRACKS IN A TYPICAL STRUCTURE

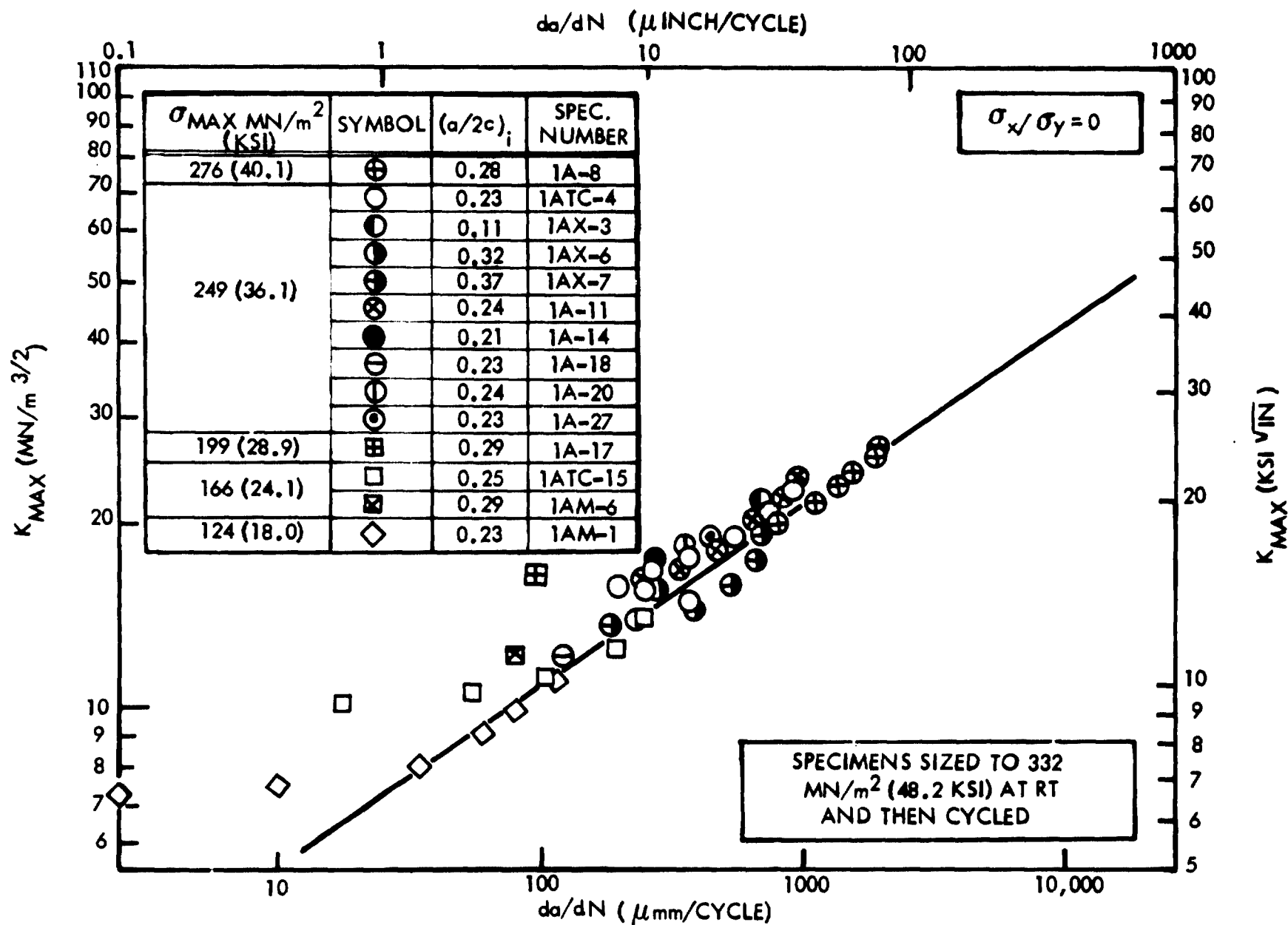


FIGURE 50: BASELINE CYCLIC CRACK GROWTH RATES FOR 2.29 mm (0.090 INCH) THICK 2219-T62 ALUMINUM BM AT 295K (72°F) AND $R = 0$

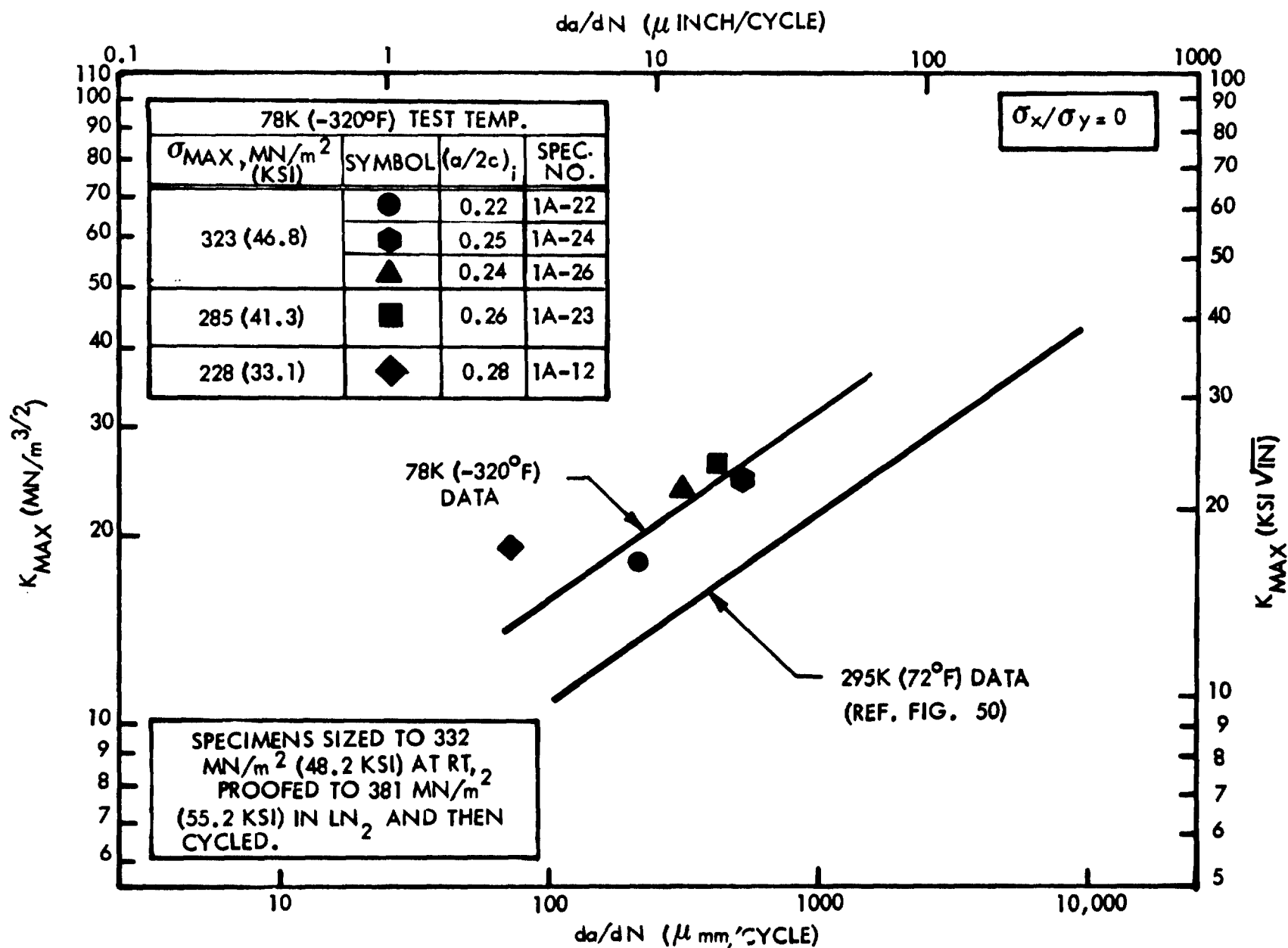


FIGURE 51: BASELINE CYCLIC CRACK GROWTH RATES FOR 2.29mm (0.090 INCH) THICK 2219-T62 ALUMINUM BM AT 78K (-320°F) AND $R = 0$

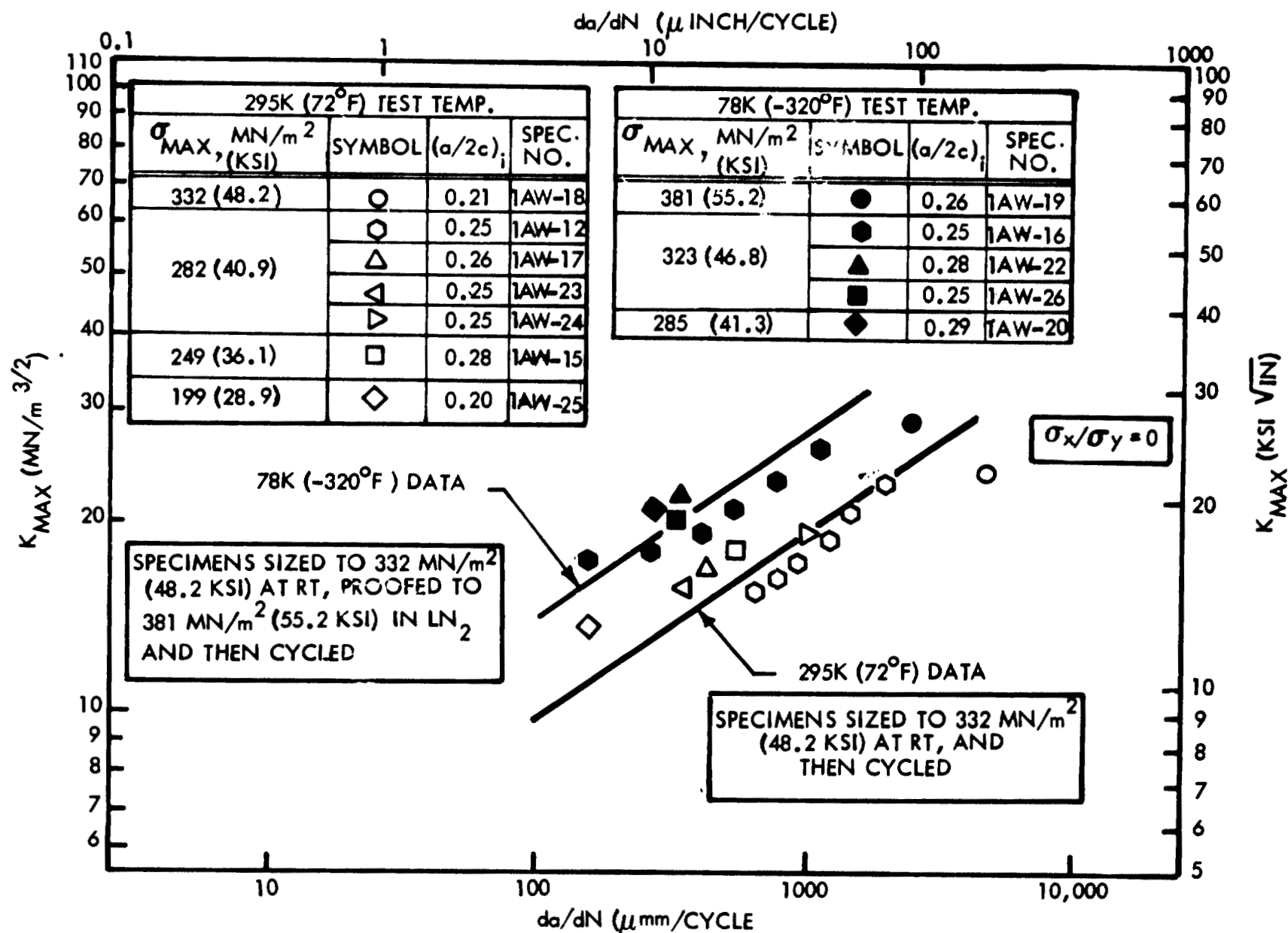


FIGURE 52: BASELINE CYCLIC CRACK GROWTH RATES FOR 2.29mm (0.090 INCH) THICK 2219-T62 ALUMINUM WM AT 295K (72°F) AND 78K (-320°F) AND R = 0

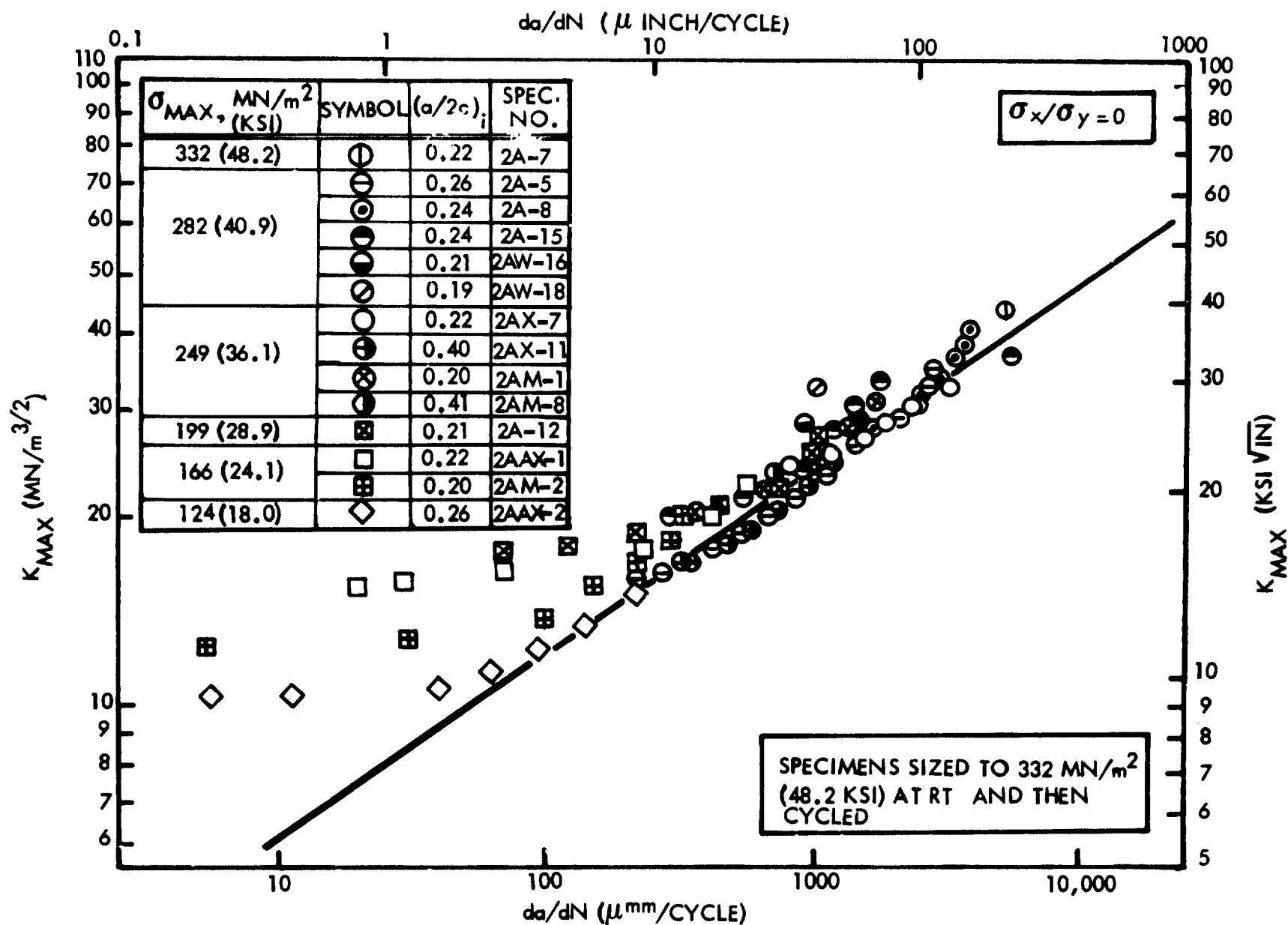


FIGURE 53: BASELINE CYCLIC CRACK GROWTH RATES FOR 4.57mm (0.180 INCH) THICK 2219-T62 ALUMINUM BM AT 295K (72°F) AND $R = 0$

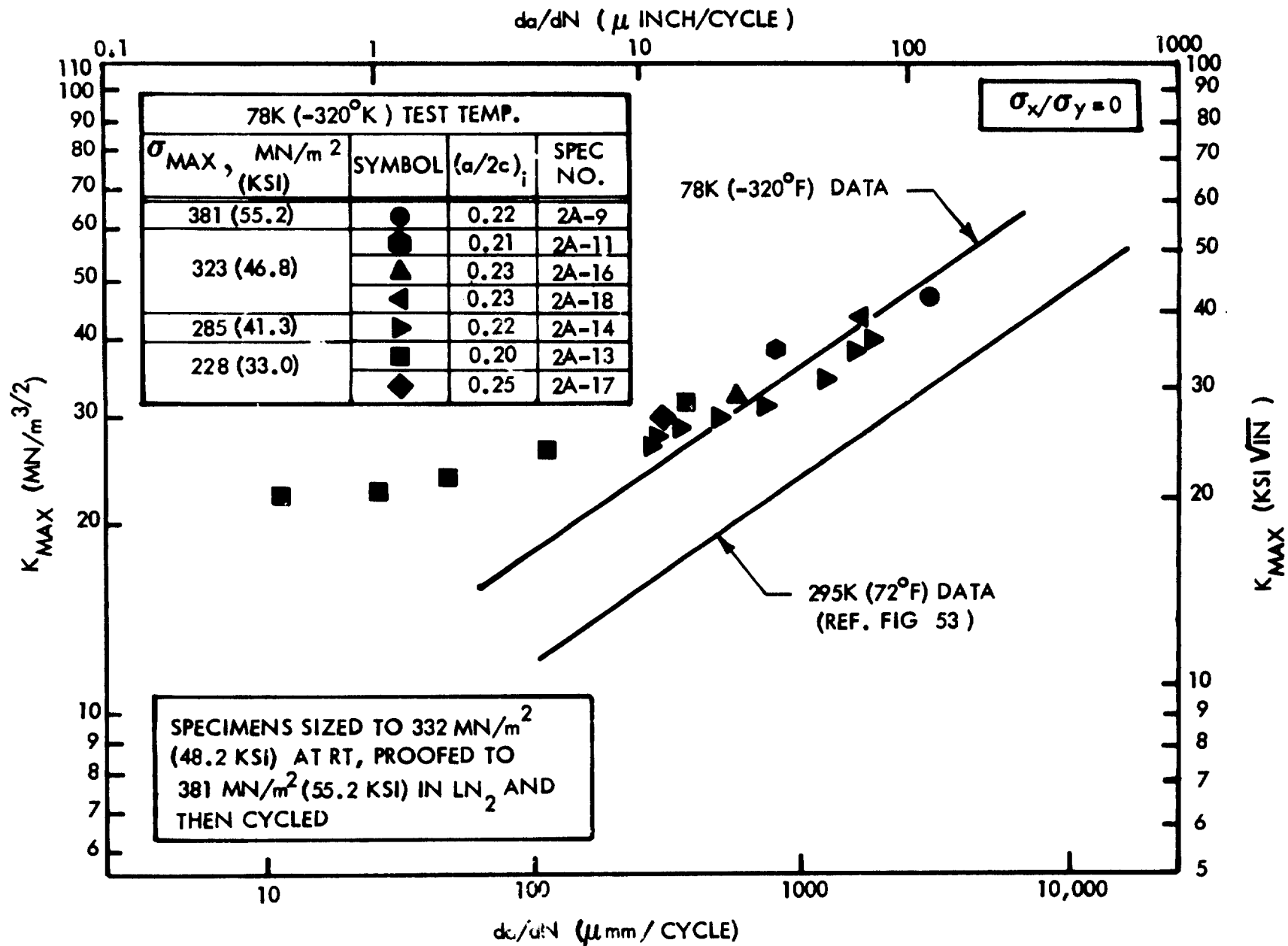


FIGURE 54: BASELINE CYCLIC CRACK GROWTH RATES FOR 4.57mm (0.180 INCH) THICK 2219-T62 ALUMINUM BM AT 78K (-320°F) AND $R = 0$

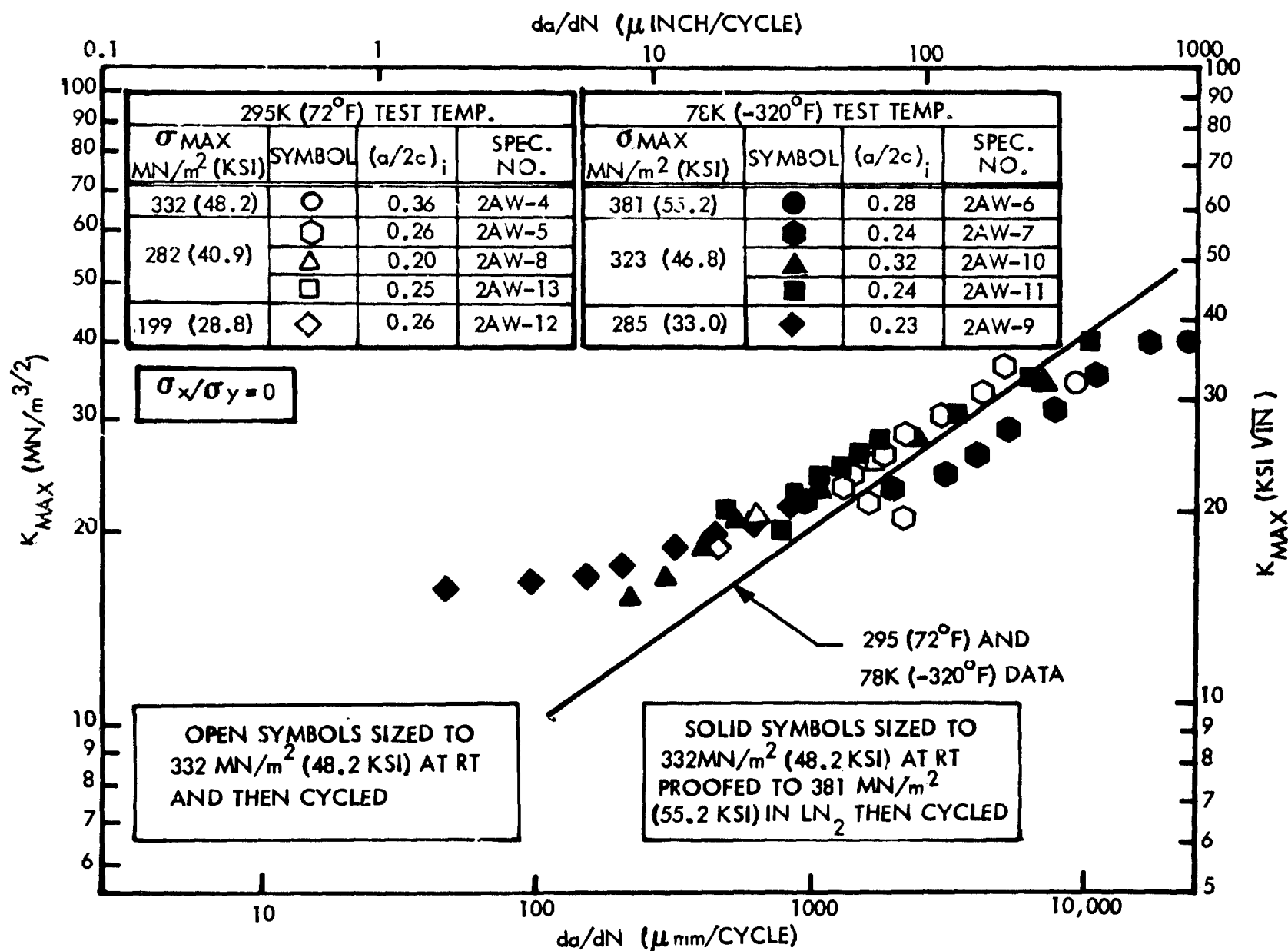


FIGURE 55: BASELINE CYCLIC CRACK GROWTH RATES FOR 4.57mm (0.180 INCH) THICK 2219-T62 ALUMINUM WM AT 295K (72°F) AND 78K (-320°F) AND $R = 0$

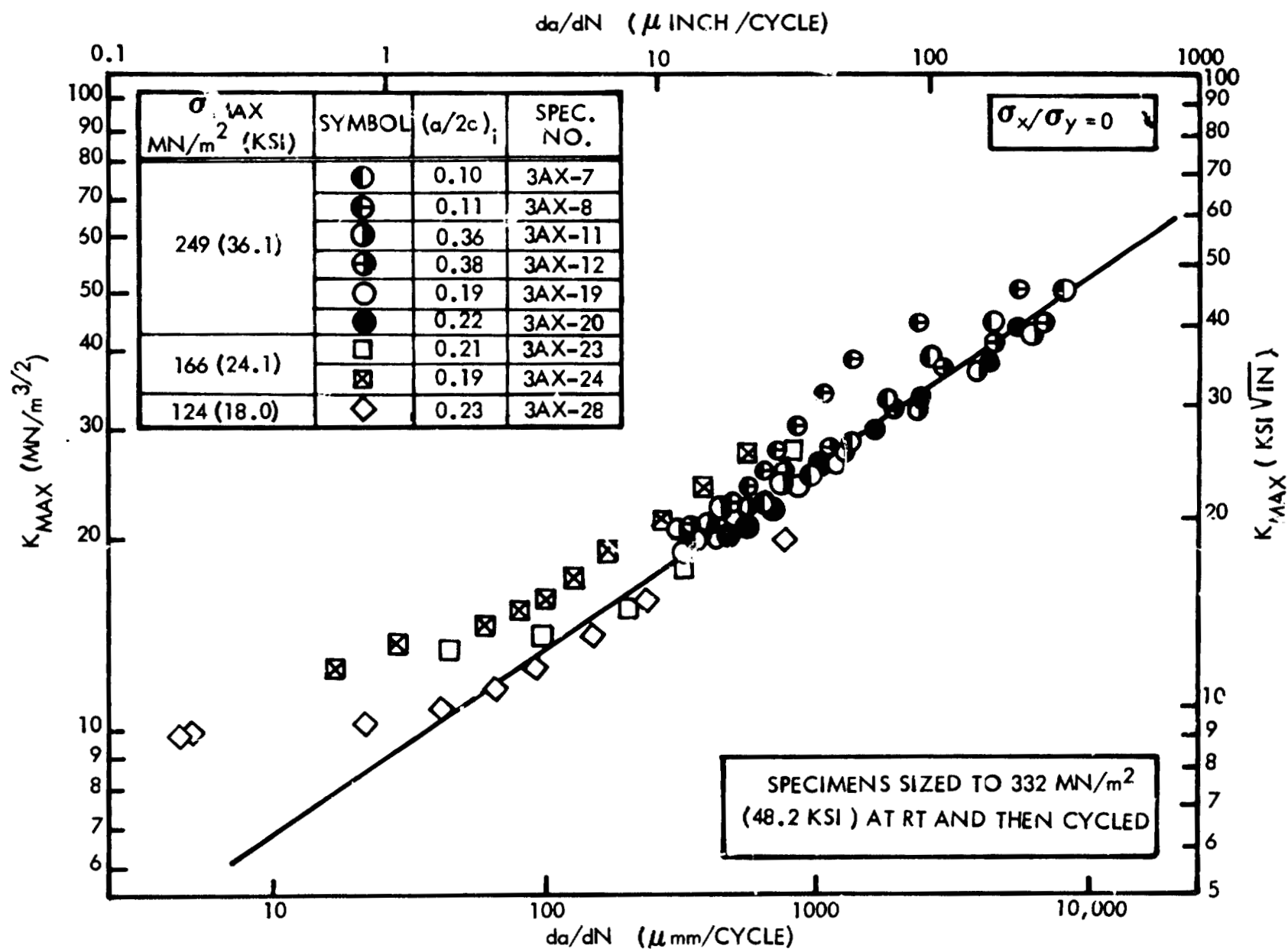


FIGURE 56: BASELINE CYCLIC CRACK GROWTH RATES FOR 7.62mm (0.300 INCH) THICK 2219-T62 ALUMINUM BM AT 295K (72°F) AND $R = 0$

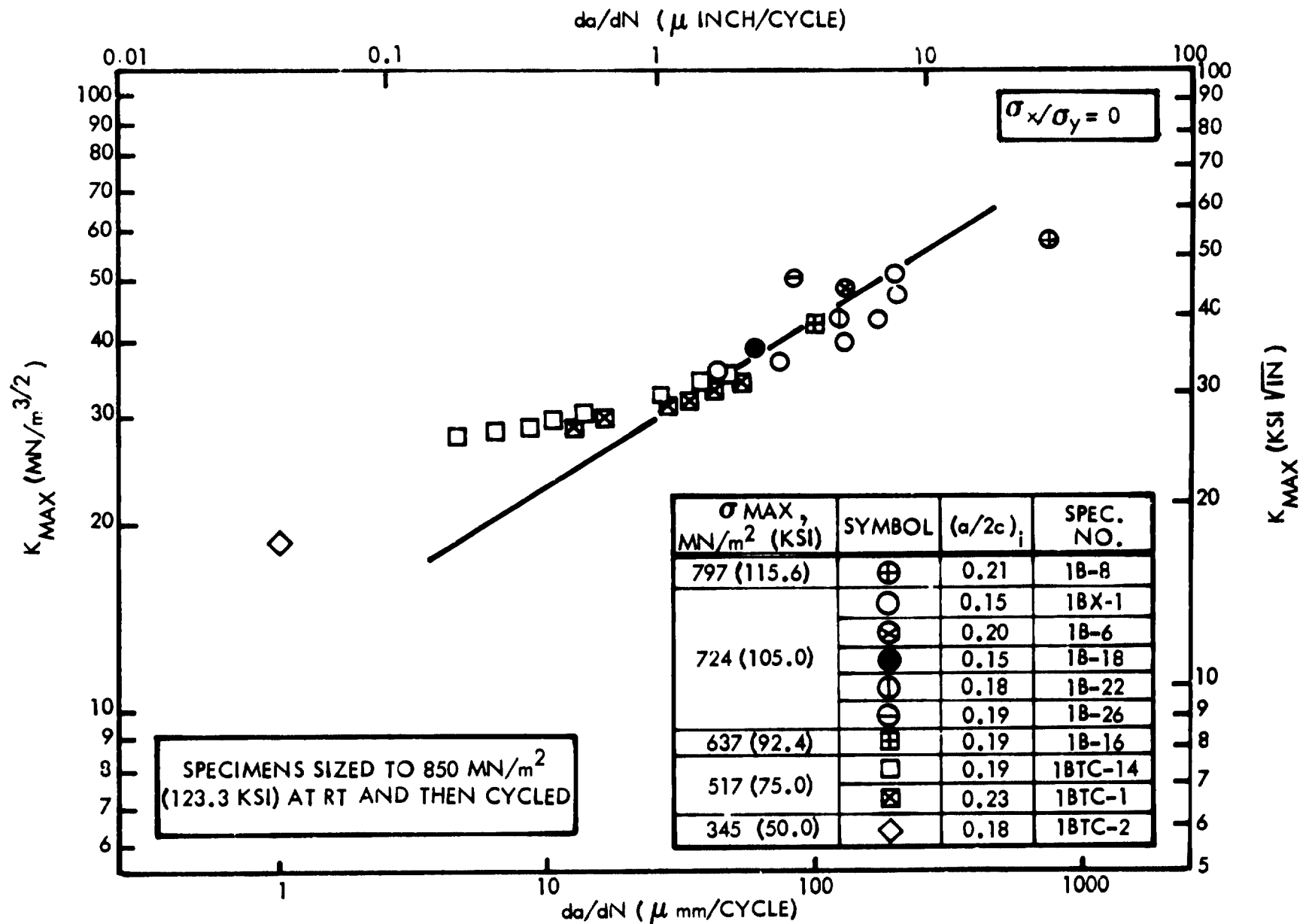


FIGURE 57: BASELINE CYCLIC CRACK GROWTH RATES FOR 1.02mm (0.040 INCH) THICK INCONEL X750 STA BM AT 295 K (72°F) AND $R = 0$

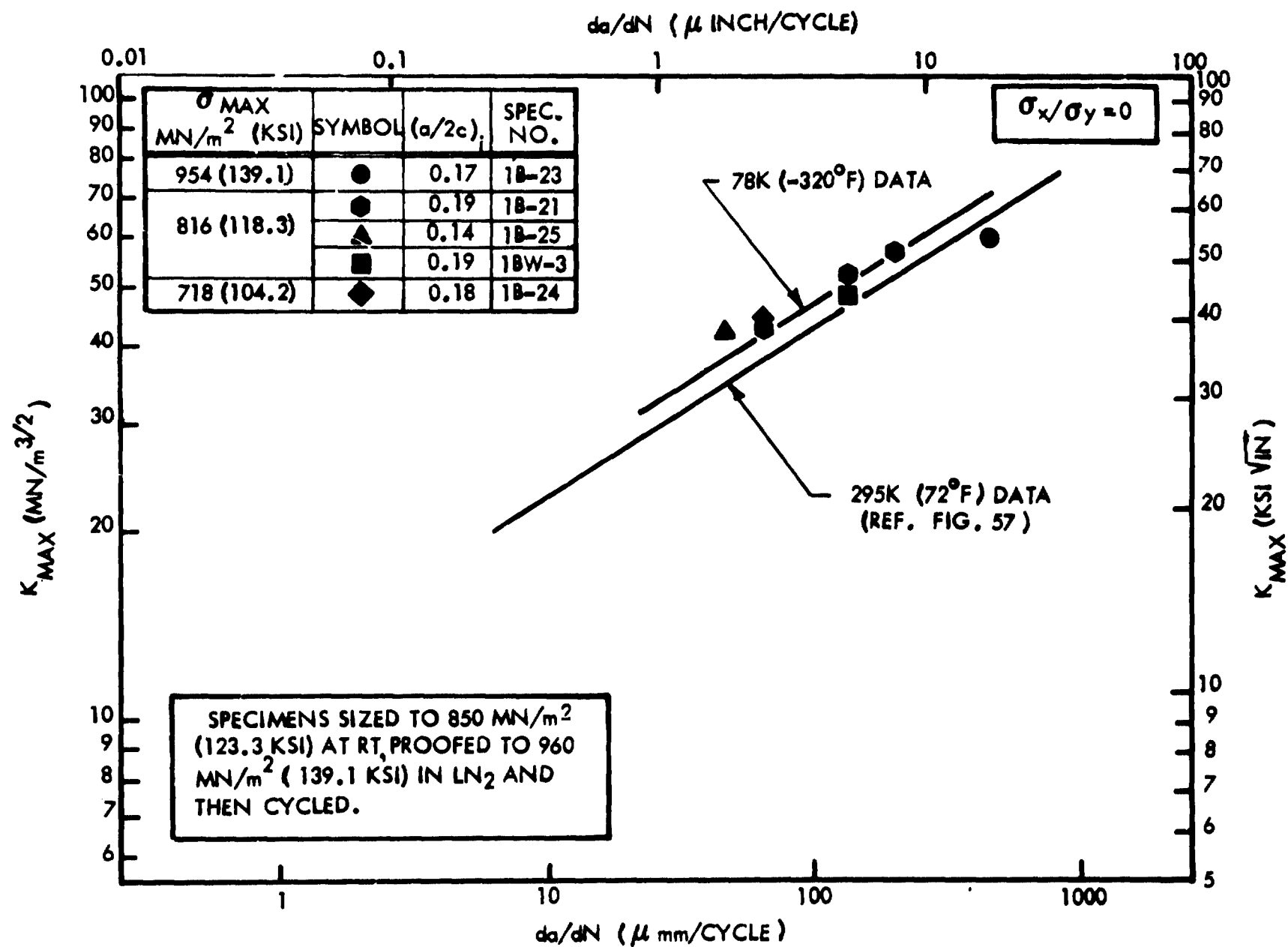


FIGURE 58: BASELINE CYCLIC CRACK GROWTH RATES FOR 1.02mm (0.040 INCH) THICK INCONEL X750 STA BM AT 78K (-320°F) AND $R = 0$.

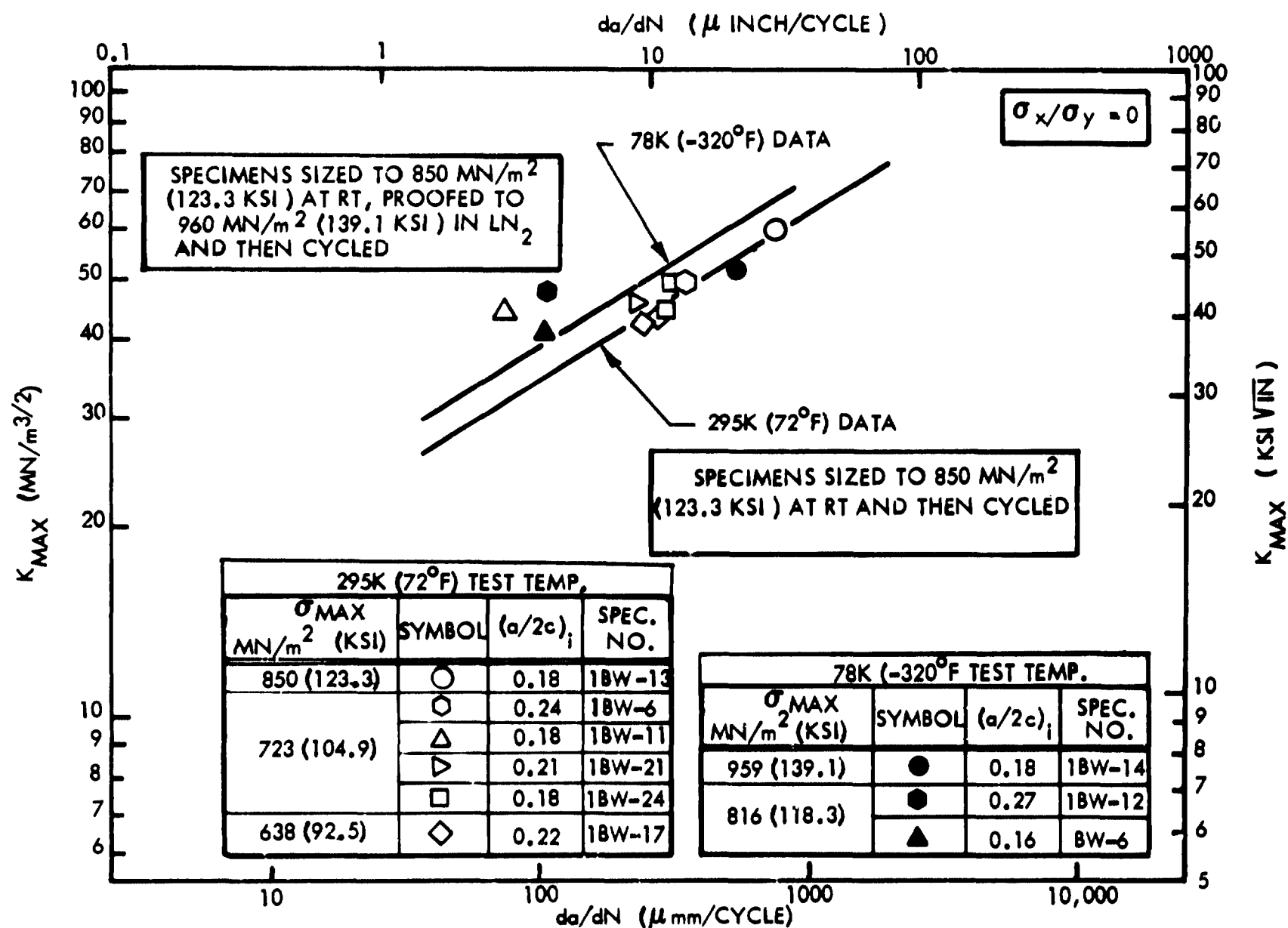


FIGURE 59: BASELINE CYCLIC CRACK GROWTH RATES FOR 1.02 mm (0.040 INCH) THICK INCONEL X750 STA WM AT 295K (72°F) AND 78K (-320°F) AND $R = 0$

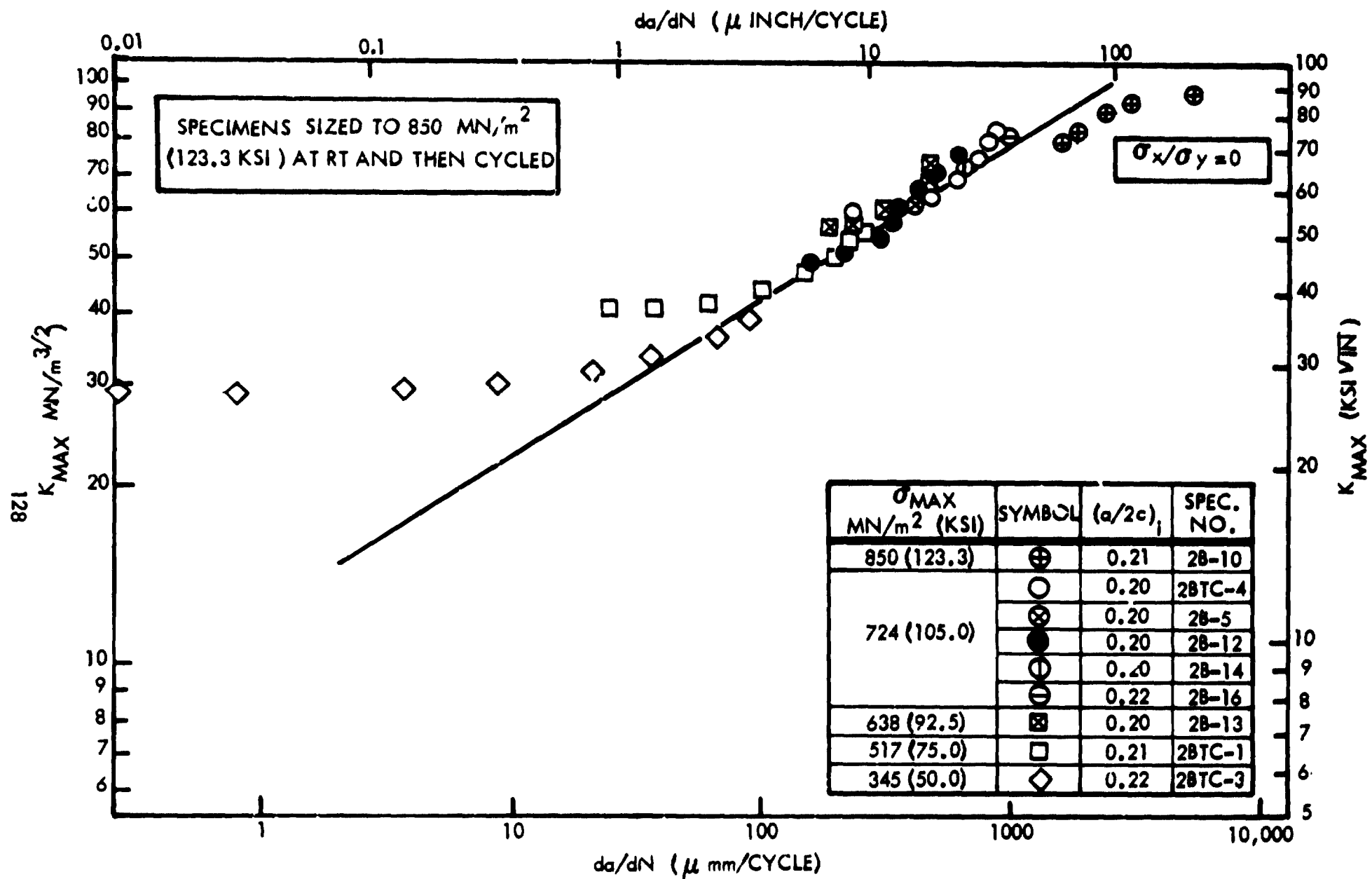


FIGURE 60: BASELINE CYCLIC CRACK GROWTH RATES FOR 3.30mm (0.130 INCH) THICK INCONEL X750 STA 8M AT 295K (72°F) AND $R = 0$.

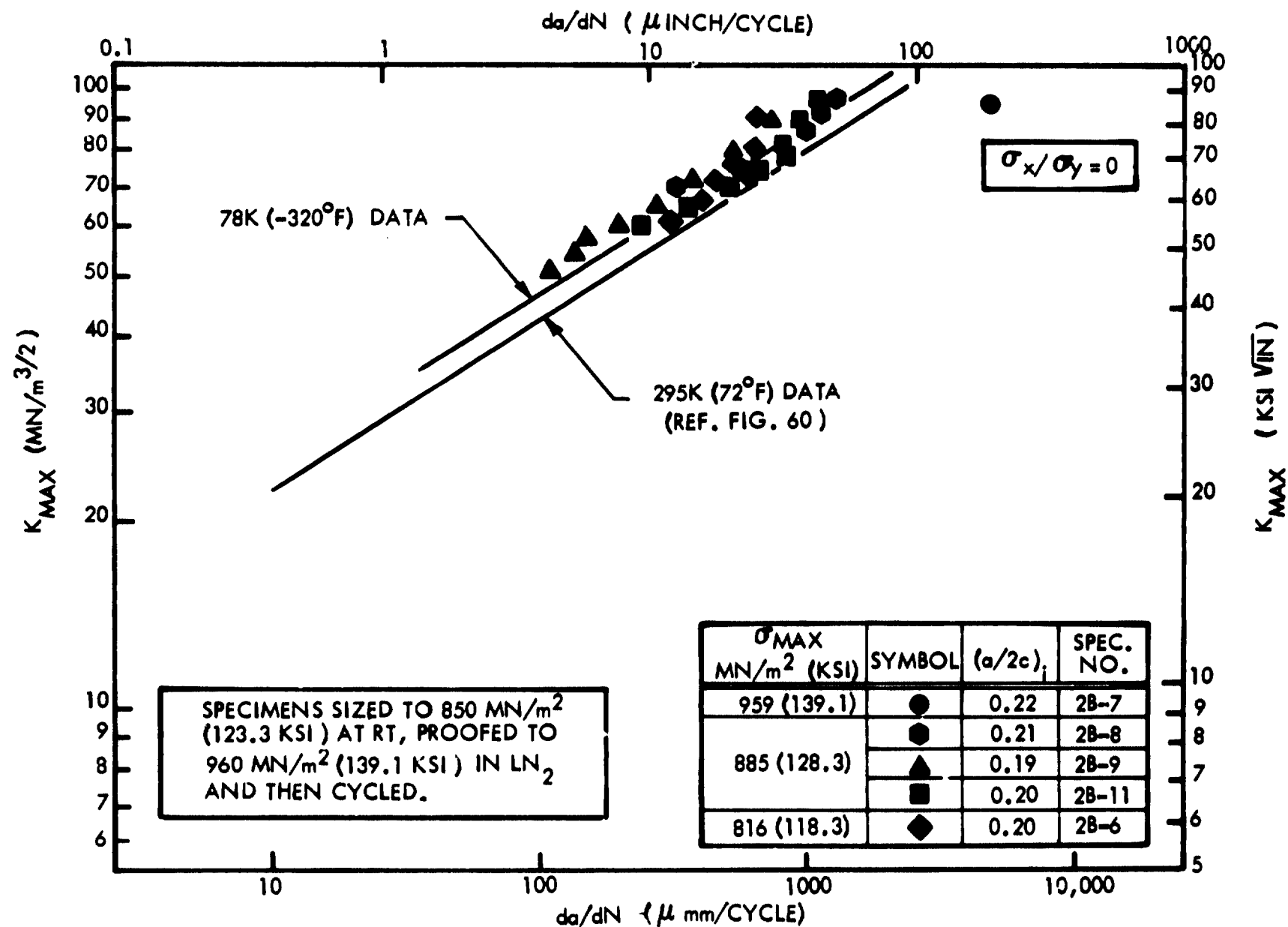


FIGURE 61: BASELINE CYCLIC CRACK GROWTH RATES FOR 3.30mm (0.130 INCH) THICK INCONEL X750 STA BM AT 78K (-320°F) AND $R = 0$.

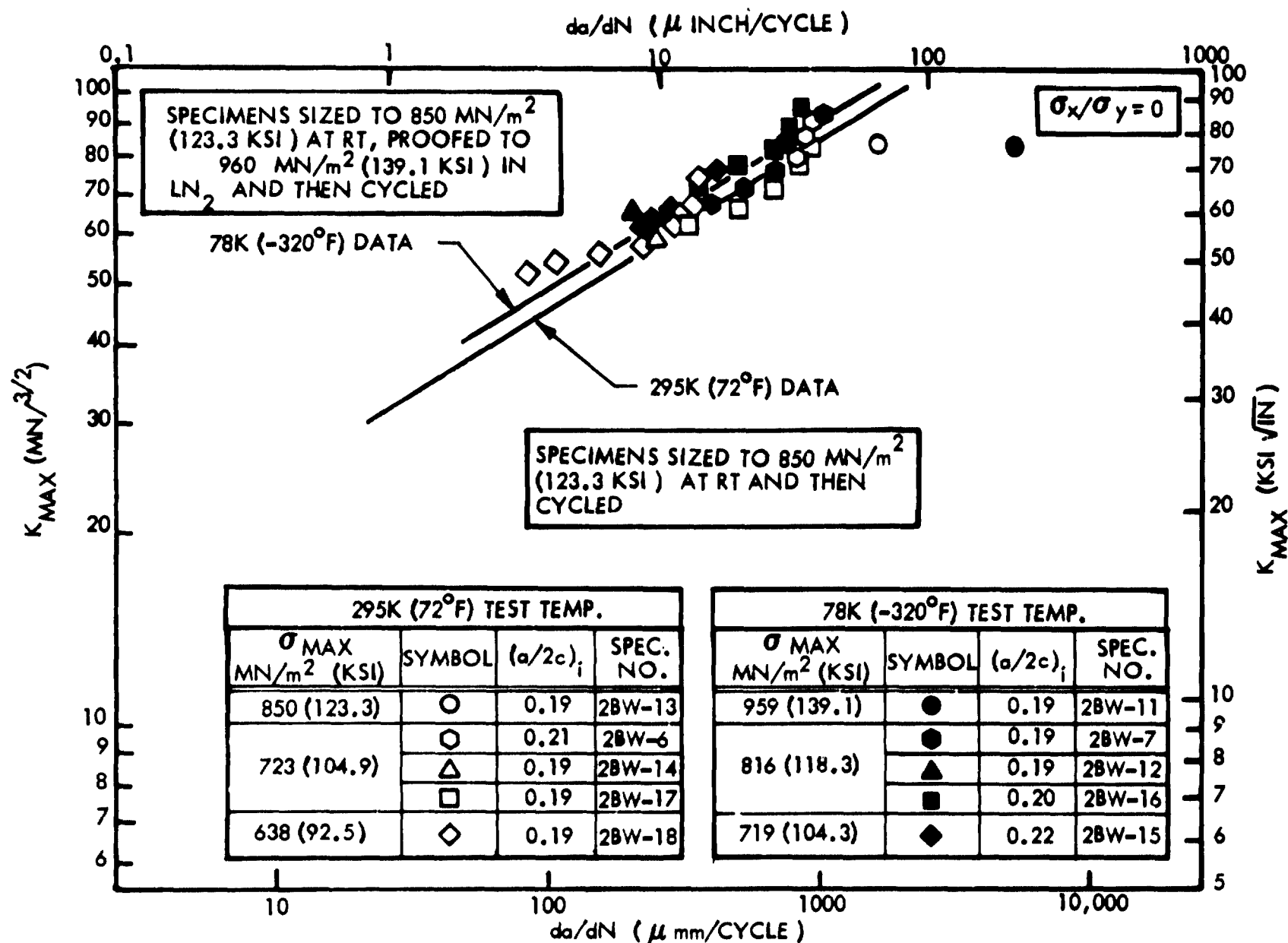


FIGURE 62: BASELINE CYCLIC CRACK GROWTH RATES FOR 3.30mm (0.130 INCH) THICK INCONEL X 750 STA WM AT 295K ($72^\circ F$), AND 78K ($-320^\circ F$) AND $R = 0$.

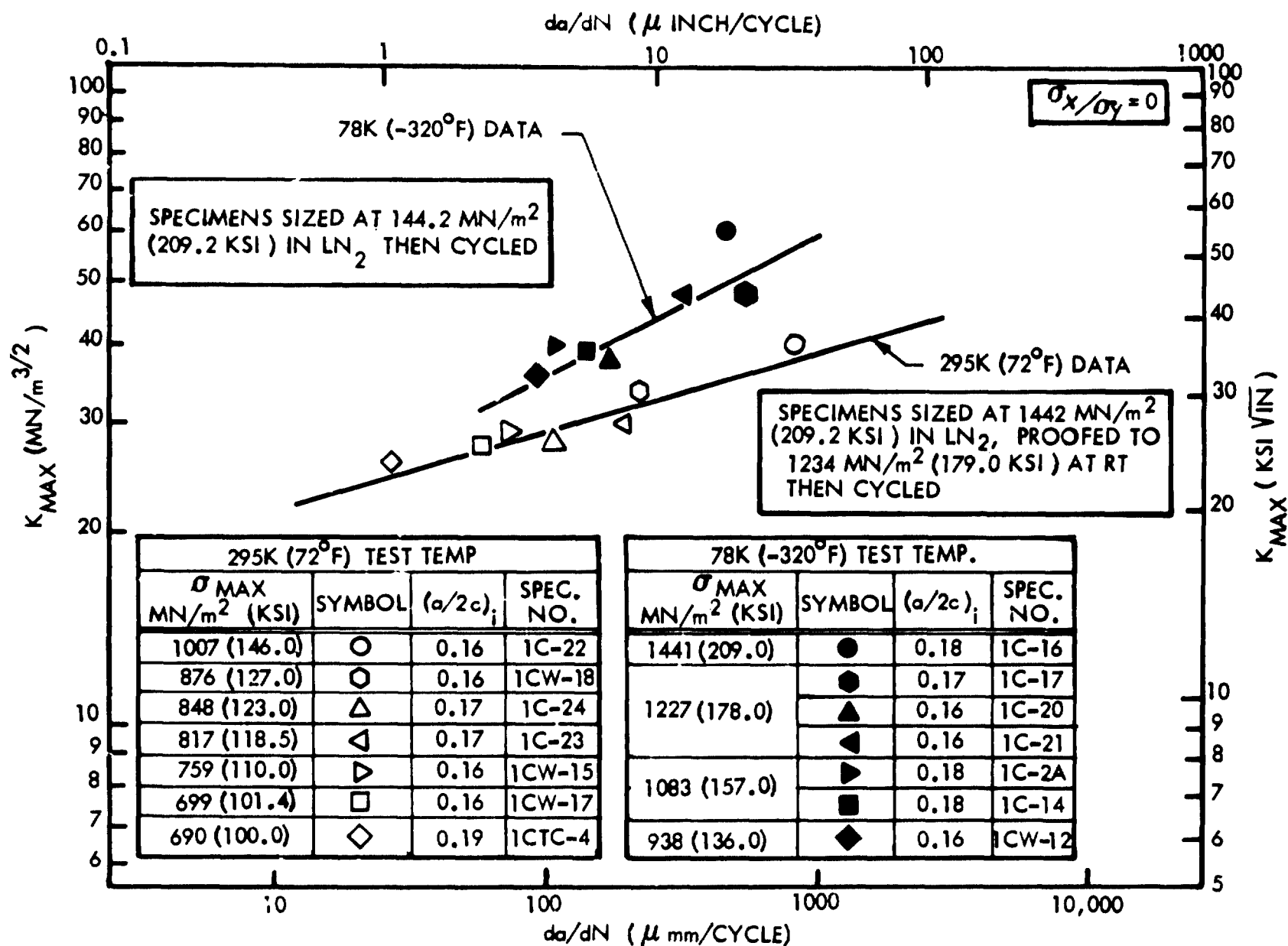


FIGURE 63: BASELINE CYCLIC CRACK GROWTH RATES FOR 0.71mm (0.028 INCH) THICK CRYOSTRETCHED 301 SS BM AT 295K (72°F) AND 78K (-320°F) AND $R = 0$.

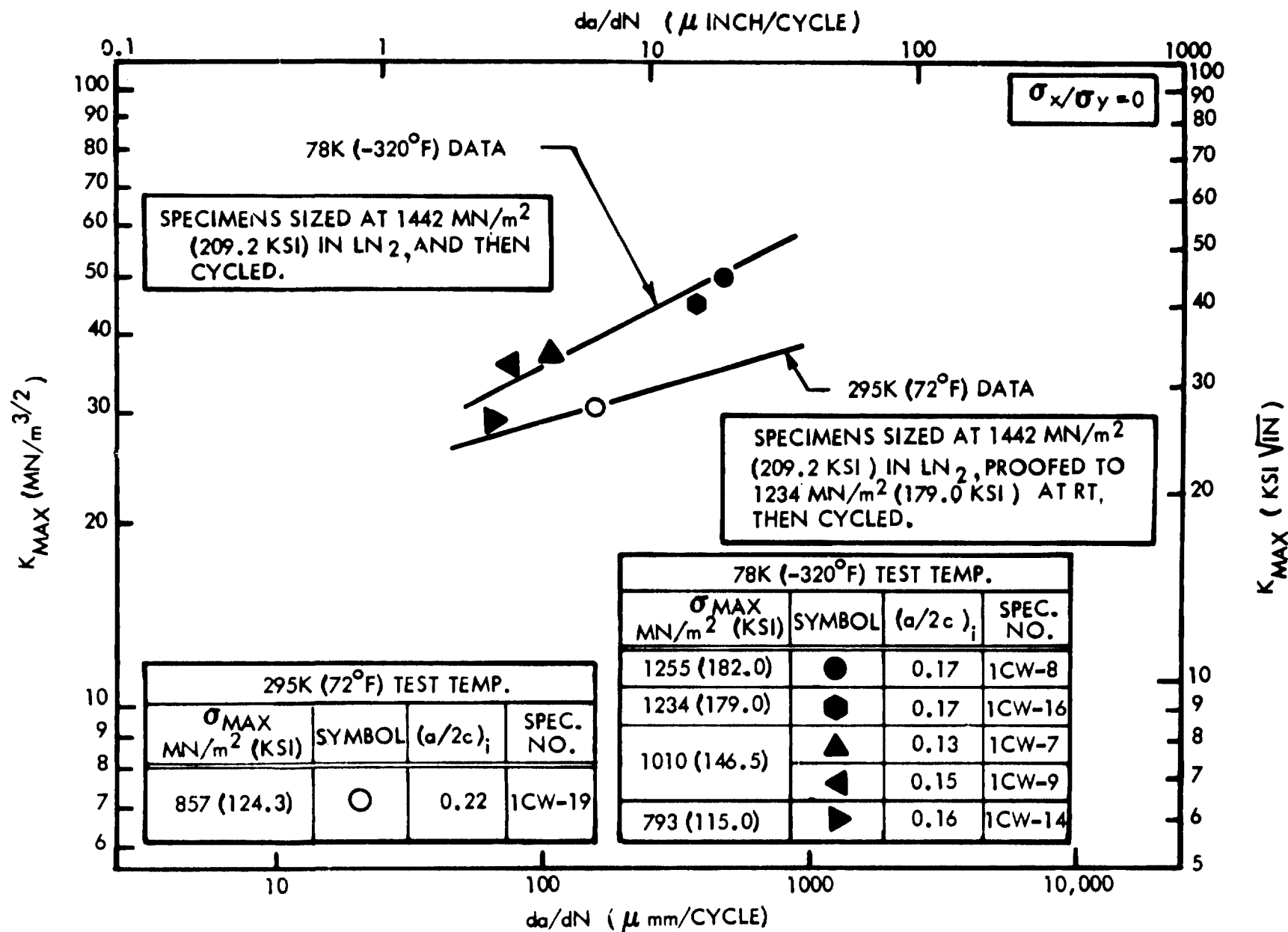


FIGURE 64: BASELINE CYCLIC CRACK GROWTH RATES FOR 0.71 mm (0.028 INCH) THICK CRYOSTRETCHED 301 SS WM AT 295K (72°F) AND 78K (-320°F) AND $R = 0$.

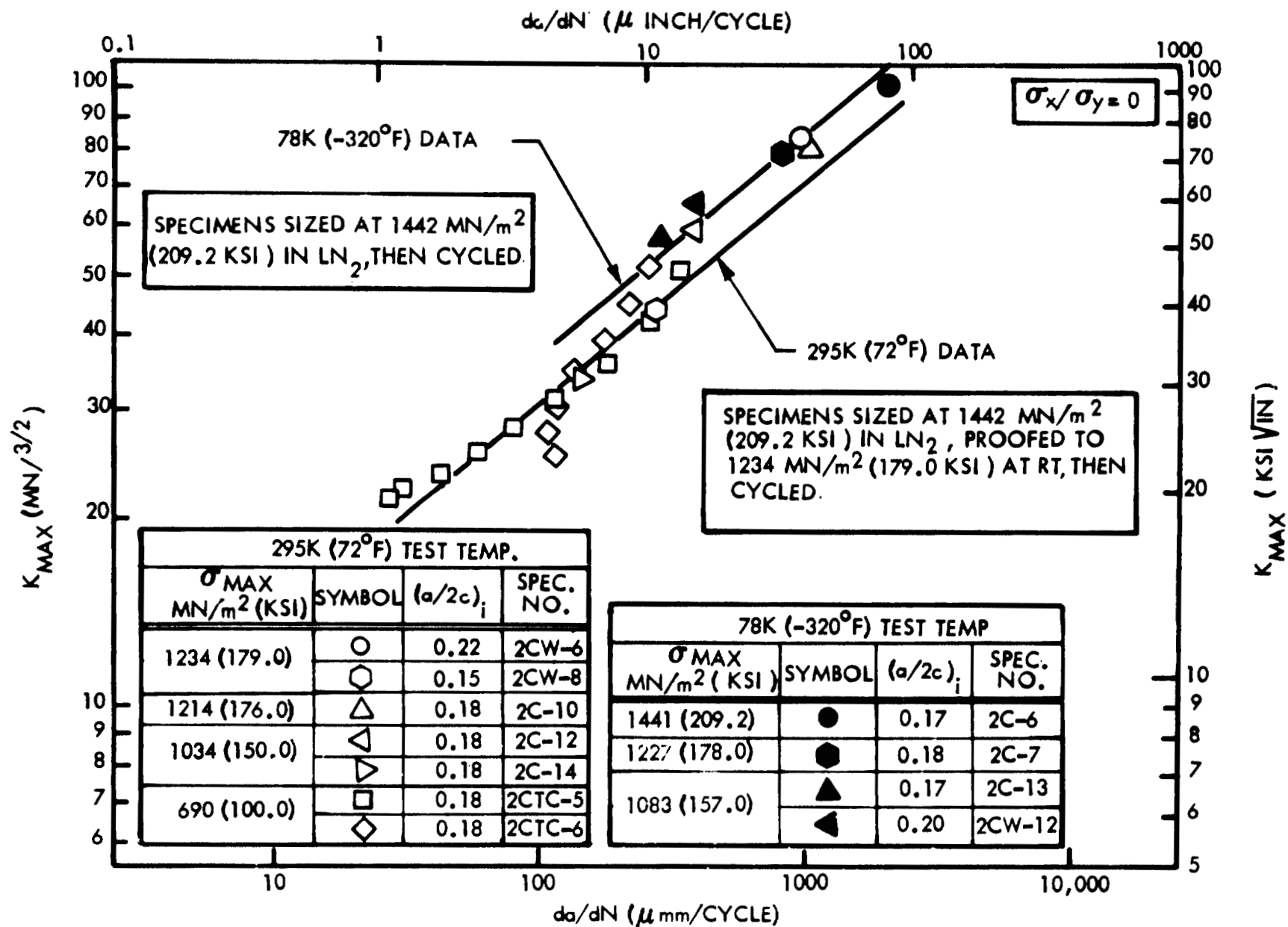


FIGURE 65 : BASELINE CYCLIC CRACK GROWTH RATES FOR 2.54 mm (0.100 INCH) THICK CRYOSTRETCHED 301 SS BM AT 295K (72°F) AND 78K (-320°F) AND $R = 0$.

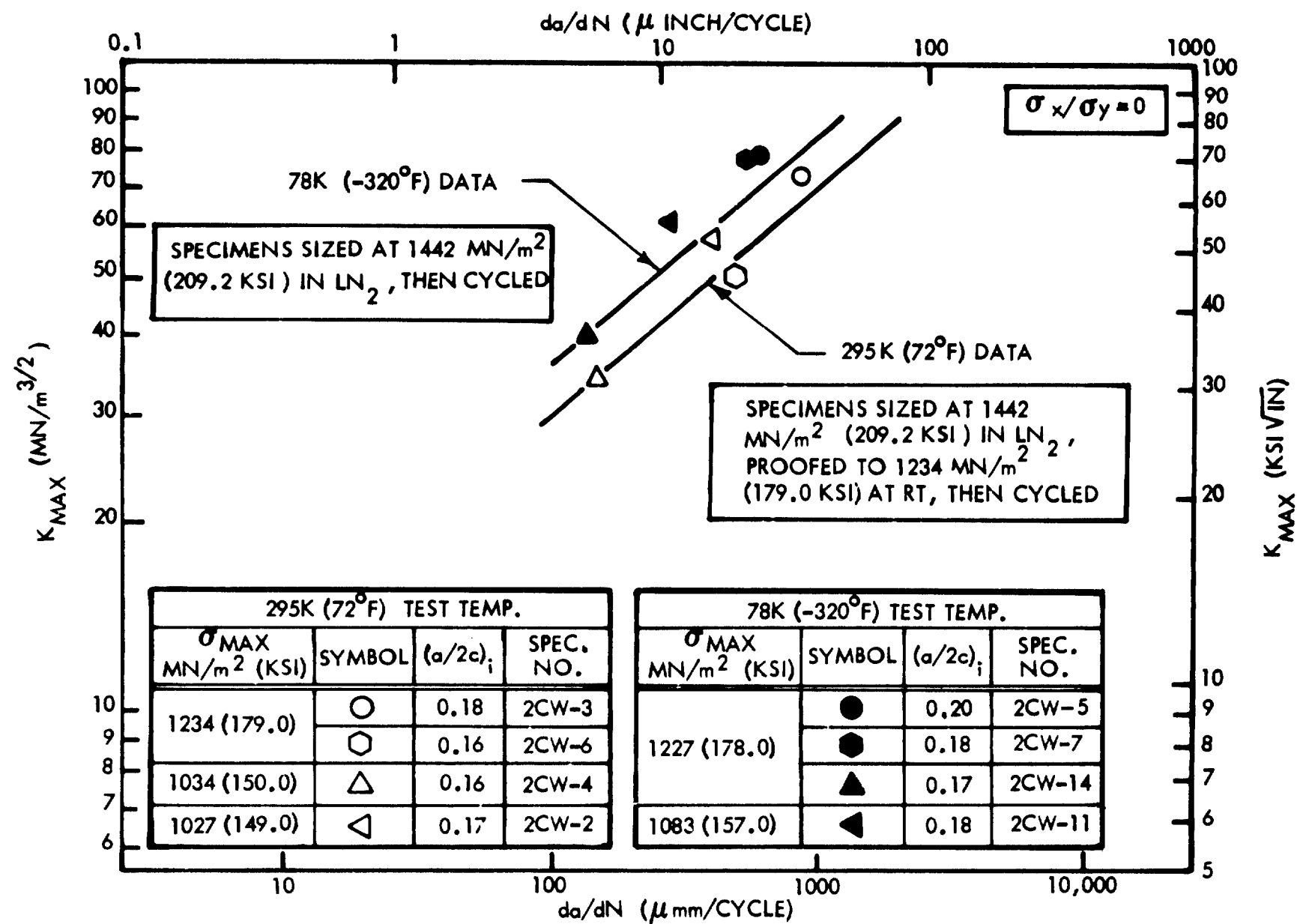


FIGURE 66: BASELINE CYCLIC CRACK GROWTH RATES FOR 2.54mm (0.100 INCH) THICK CRYOSTRETCHED 301 SS WM AT 295K (72°F) AND 78K (-320°F) AND $R = 0$

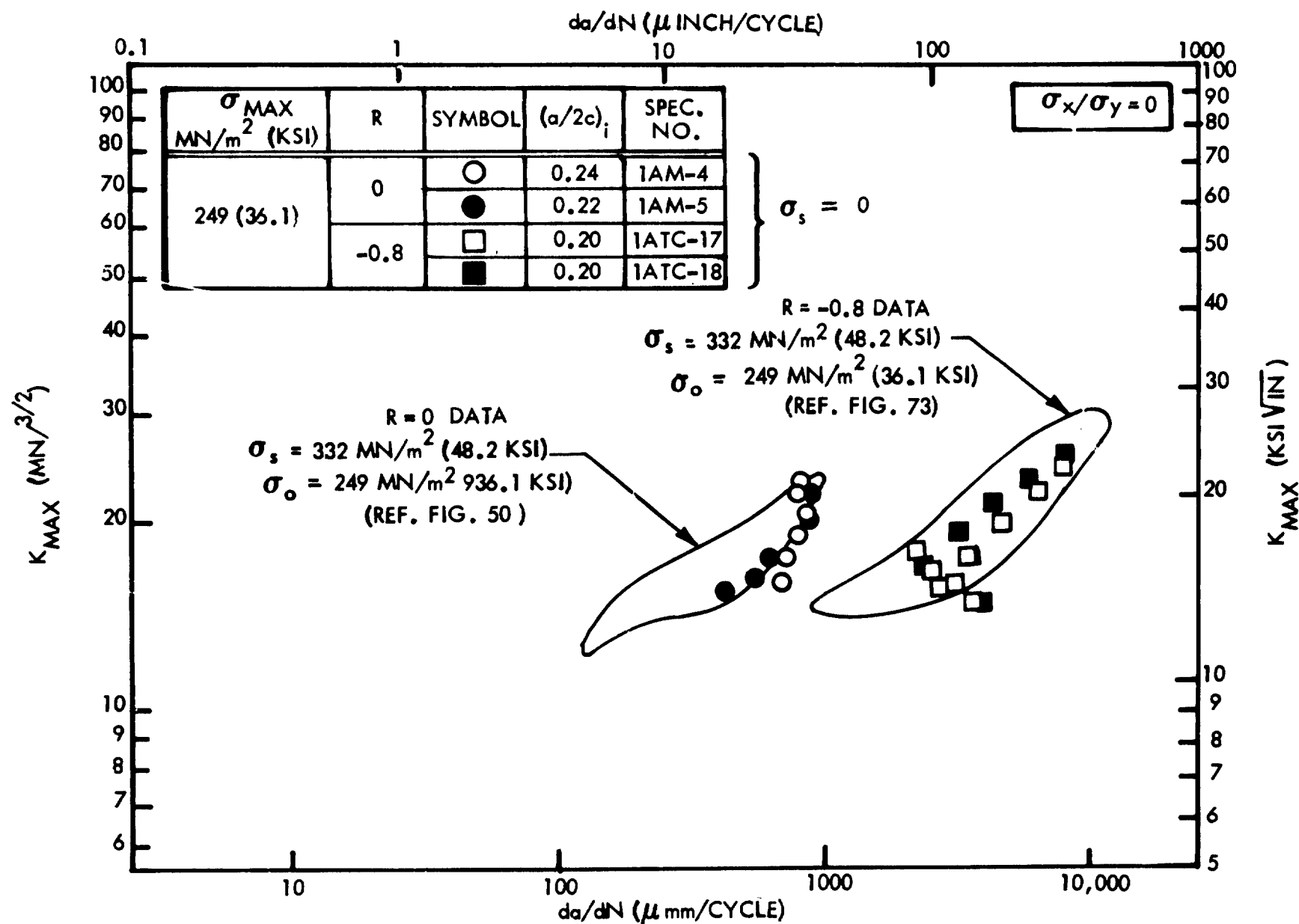


FIGURE 67 : COMPARISON OF CYCLIC CRACK GROWTH RATES WITH AND WITHOUT SIZING CYCLE FOR 2.29 mm (0.090 INCH) THICK 2219-T62 ALUMINUM BM AT 295K (72°F)

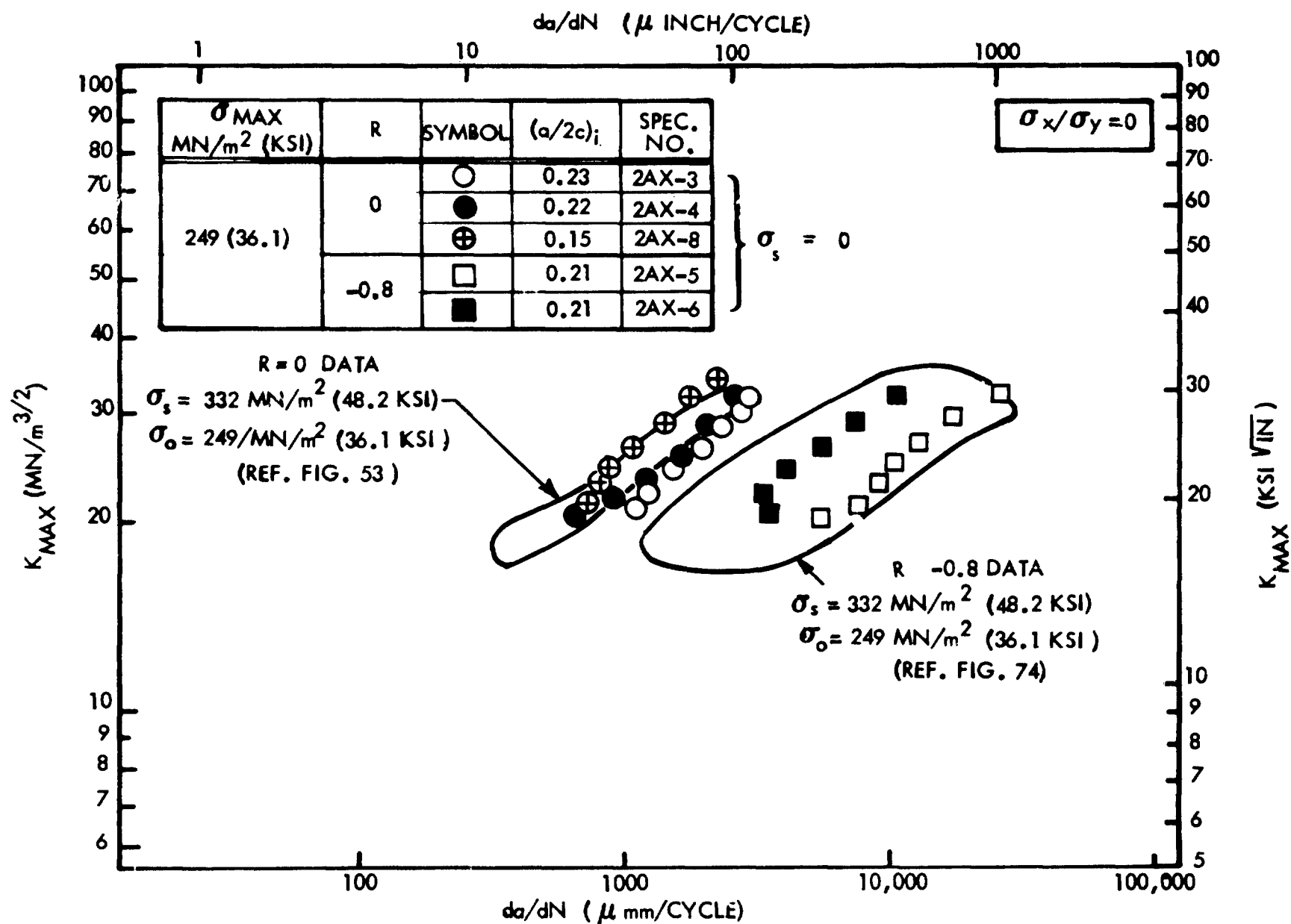


FIGURE 68: COMPARISON OF CYCLIC CRACK GROWTH RATES WITH AND WITHOUT SIZING CYCLE FOR 4.57 mm (0.180 INCH) THICK 2219-T62 ALUMINUM BM AT 295K (72°F).

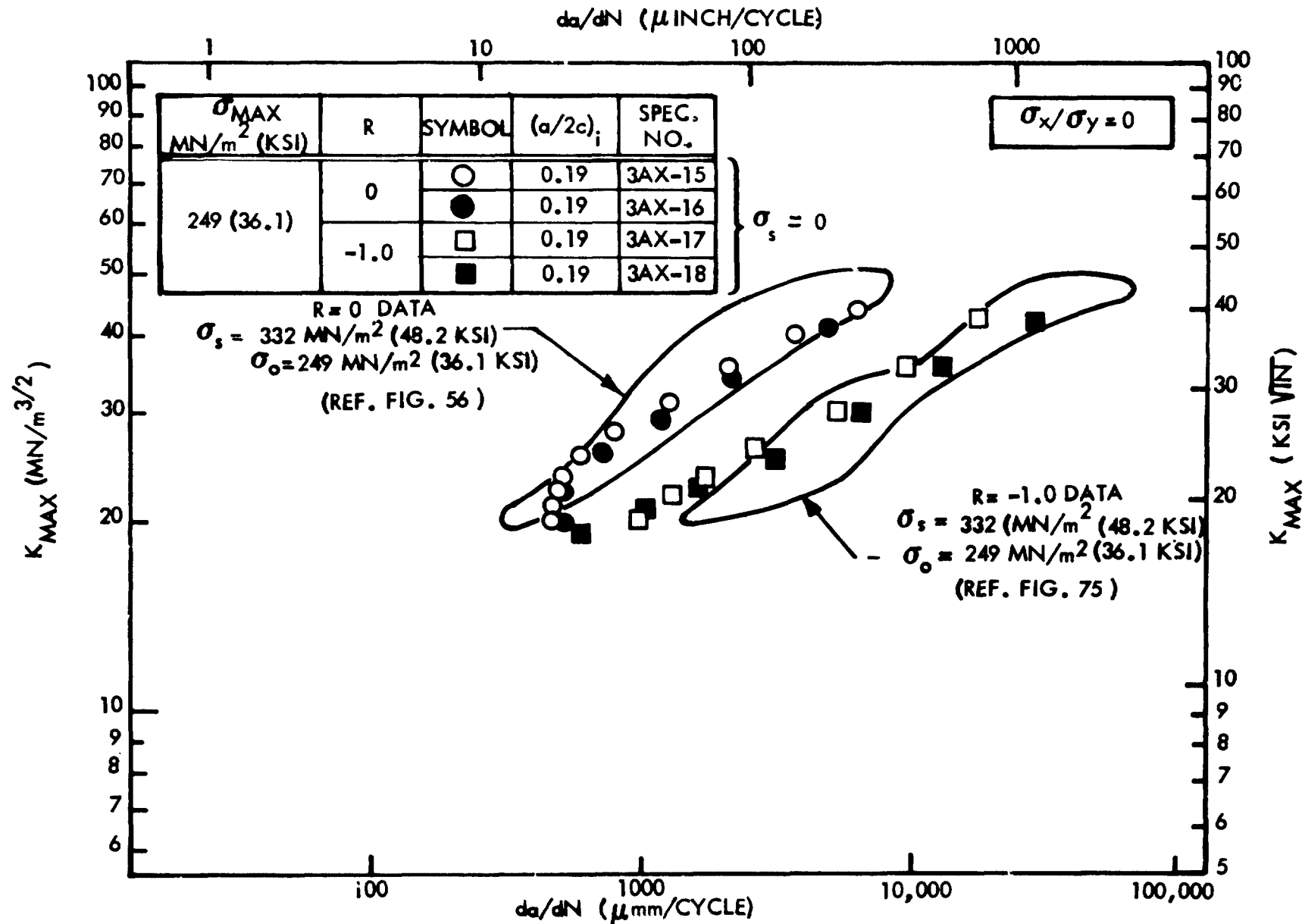


FIGURE 69: COMPARISON OF CYCLIC CRACK GROWTH RATES WITH AND WITHOUT SIZING CYCLE FOR 7.62mm (0.300 INCH) THICK 2219-T62 ALUMINUM BM AT 295K (72°F)

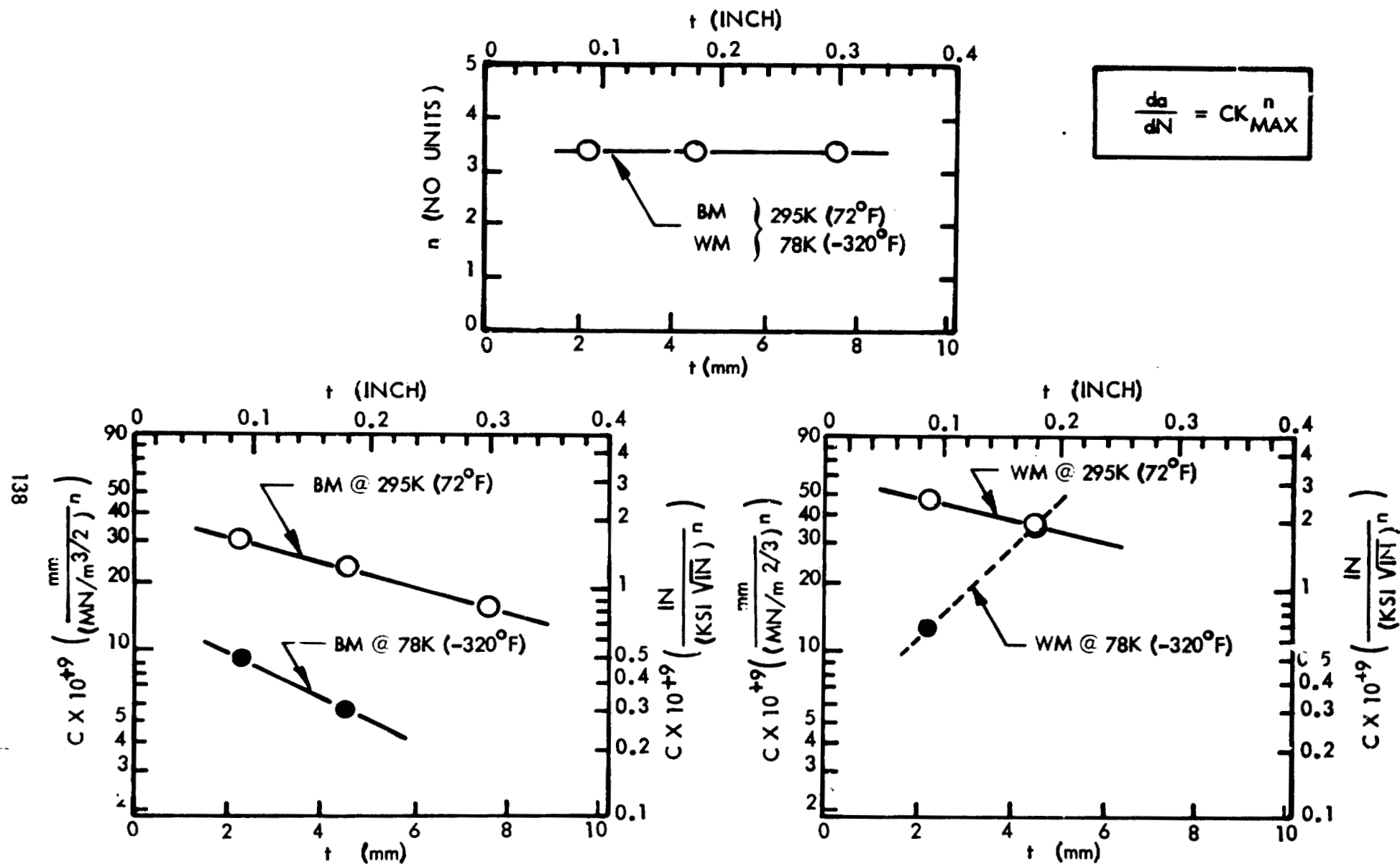


FIGURE 70: CYCLIC CRACK GROWTH RATE CONSTANTS FOR 2219-T62 ALUMINUM (R= 0)

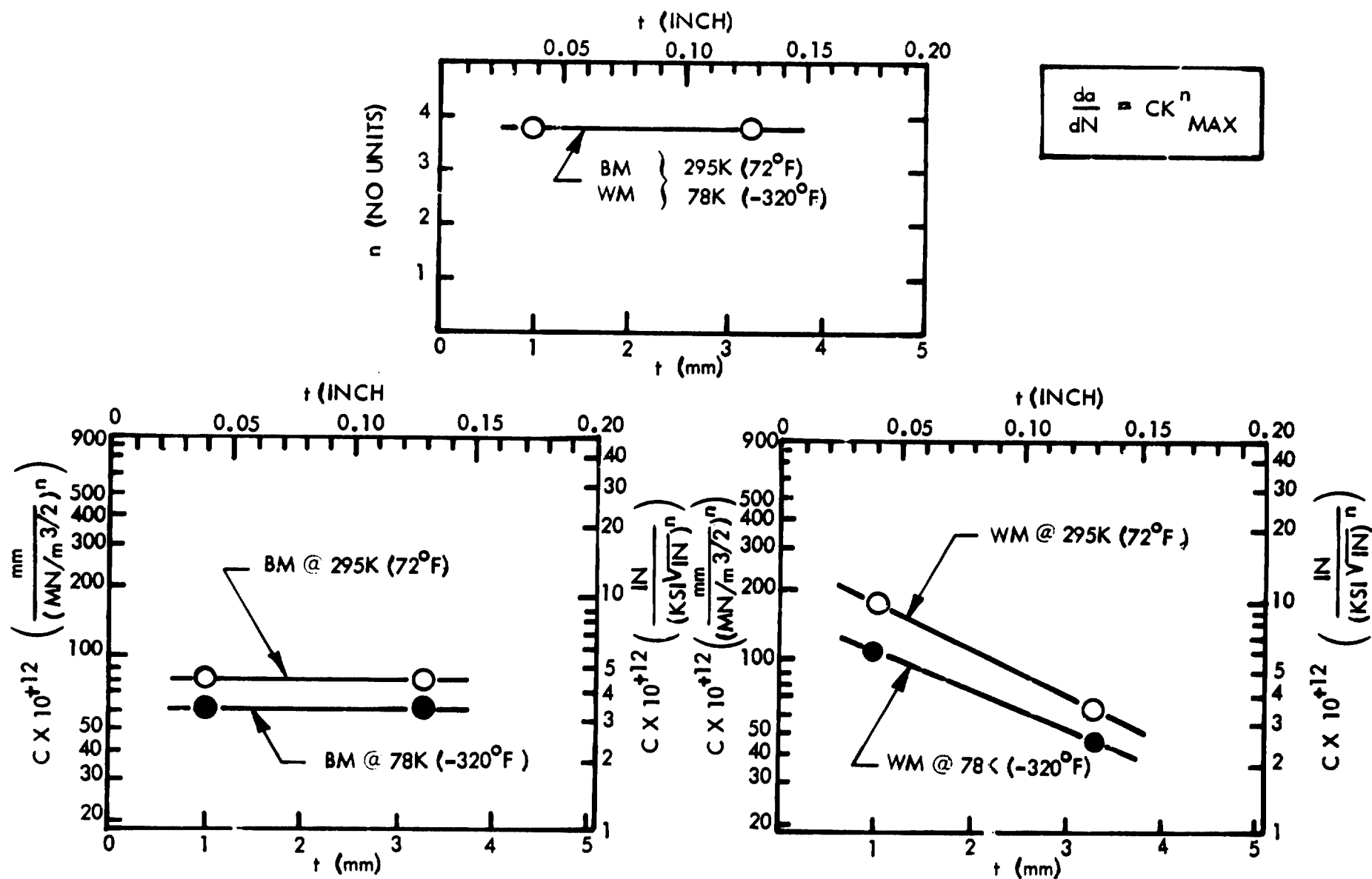


FIGURE 71: CYCLIC CRACK GROWTH RATE CONSTANTS FOR INCCINEL X750 STA (R = 0)

$$\frac{da}{dN} = CK_{MAX}^n$$

n VALUES

THICKNESS, t mm (INCH) TEMP. T K (°F)	0.71 (0.028)	2.54 (0.100)
295 (72)	7.90	2.78
78 (-320)	4.51	2.78

C VALUES

$$\frac{\text{mm}}{(\text{MN/m}^{3/2})^n} \quad \left(\frac{\text{IN}}{(\text{KSI} \sqrt{\text{IN}})^n} \right)$$

THICKNESS, t mm (INCH) Temp. T, K (°F)	0.71 (0.028)	2.54 (0.100)
295 (72)	2.91×10^{-16} (2.43×10^{-17})	7.19×10^{-9} (3.69×10^{-10})
78 (-320)	1.02×10^{-11} (6.20×10^{-13})	4.42×10^{-9} (2.27×10^{-10})

FIGURE 72: CYCLIC CRACK GROWTH RATE CONSTANTS FOR CRYOSTRETCHED 301 SS
BM AND WM (R = 0).

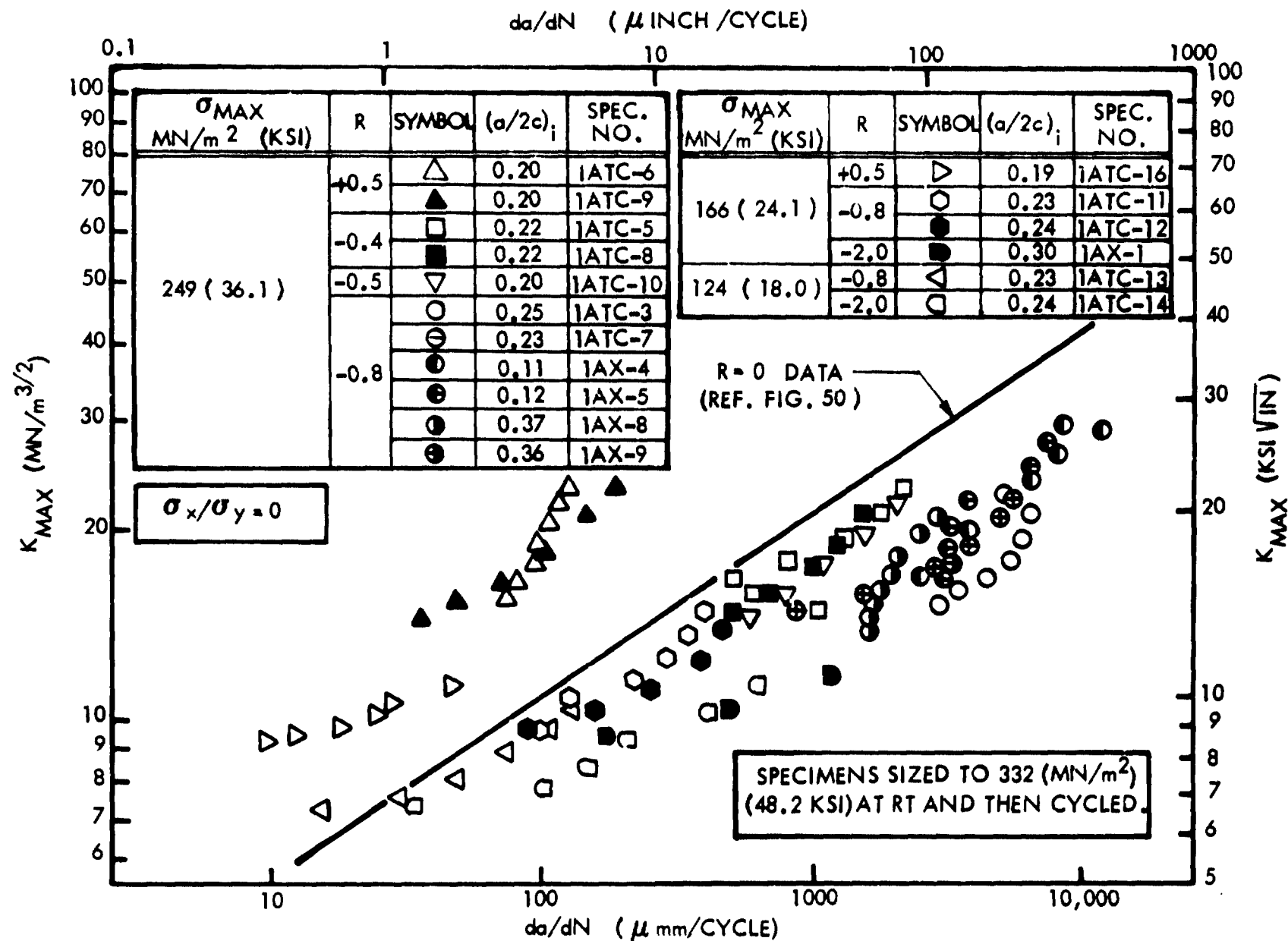


FIGURE 73: CYCLIC CRACK GROWTH RATES FOR 2.29 mm (0.090 INCH) THICK 2219-T62 ALUMINUM BM AT 295K (72°F) AND VARIOUS R RATIOS.

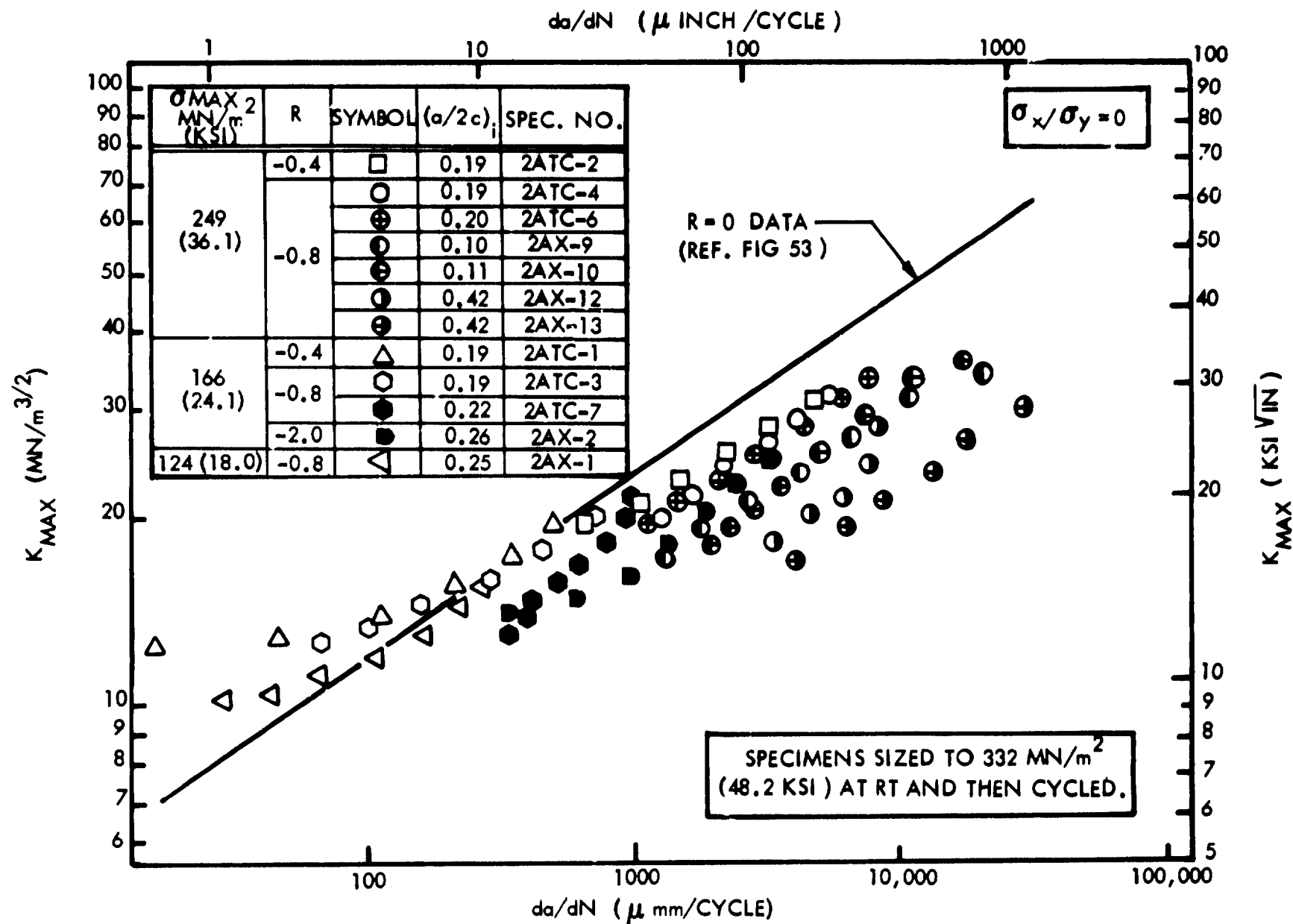


FIGURE 74: CYCLIC CRACK GROWTH RATES FOR 4.57mm (0.180 INCH) THICK 2219-T62 ALUMINUM BM AT 295K (72°F) AND VARIOUS R RATIOS.

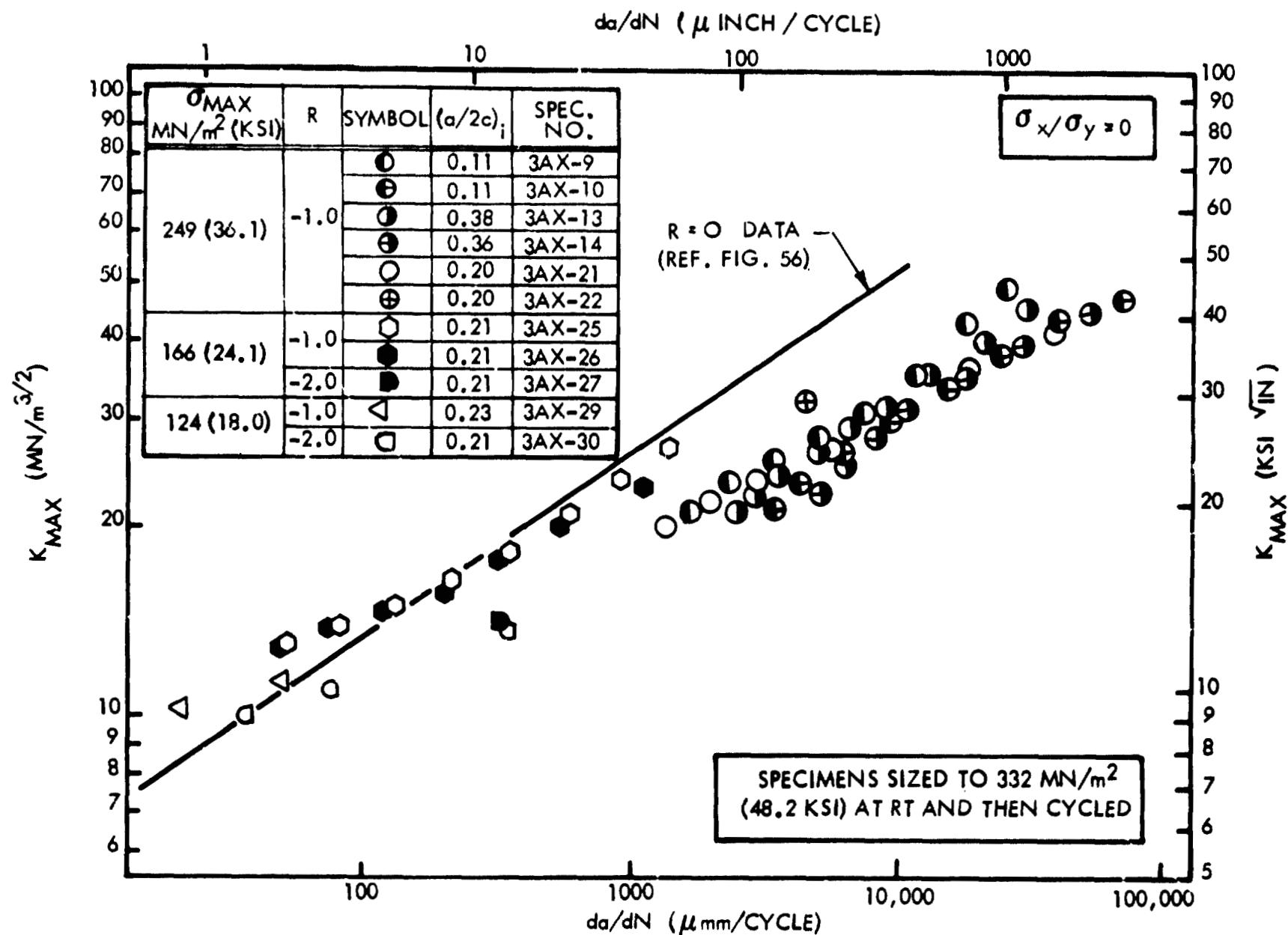


FIGURE 75: CYCLIC CRACK GROWTH RATES FOR 7.62mm (0.300 INCH) THICK 2219-T62 ALUMINUM BM AT 295K (72°F) AND VARIOUS R RATIOS.

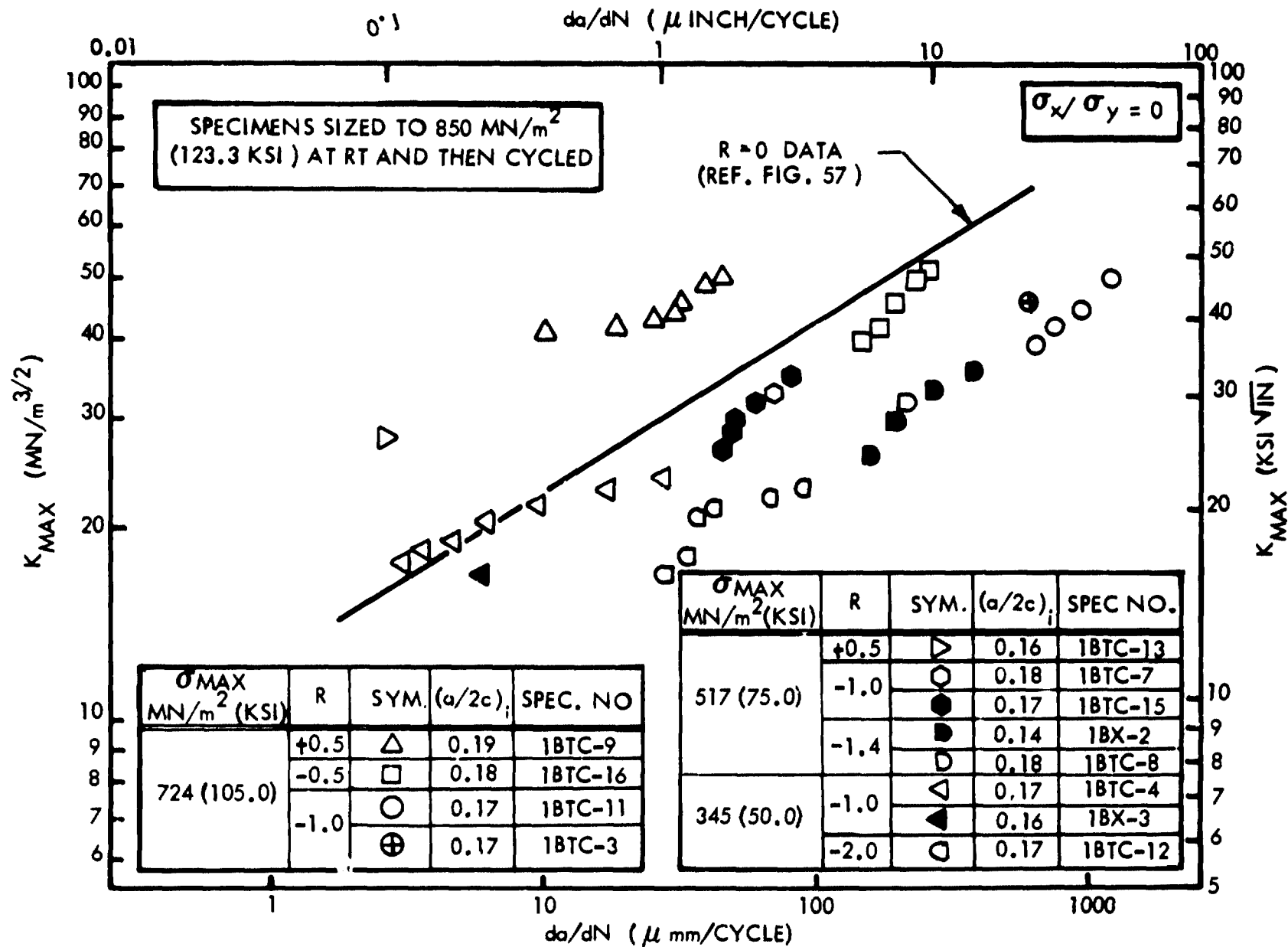


FIGURE 76: CYCLIC CRACK GROWTH RATES FOR 1.02mm (0.040 INCH) THICK INCONEL X750 STA BM AT 295K (72°F) AND VARIOUS R RATIOS

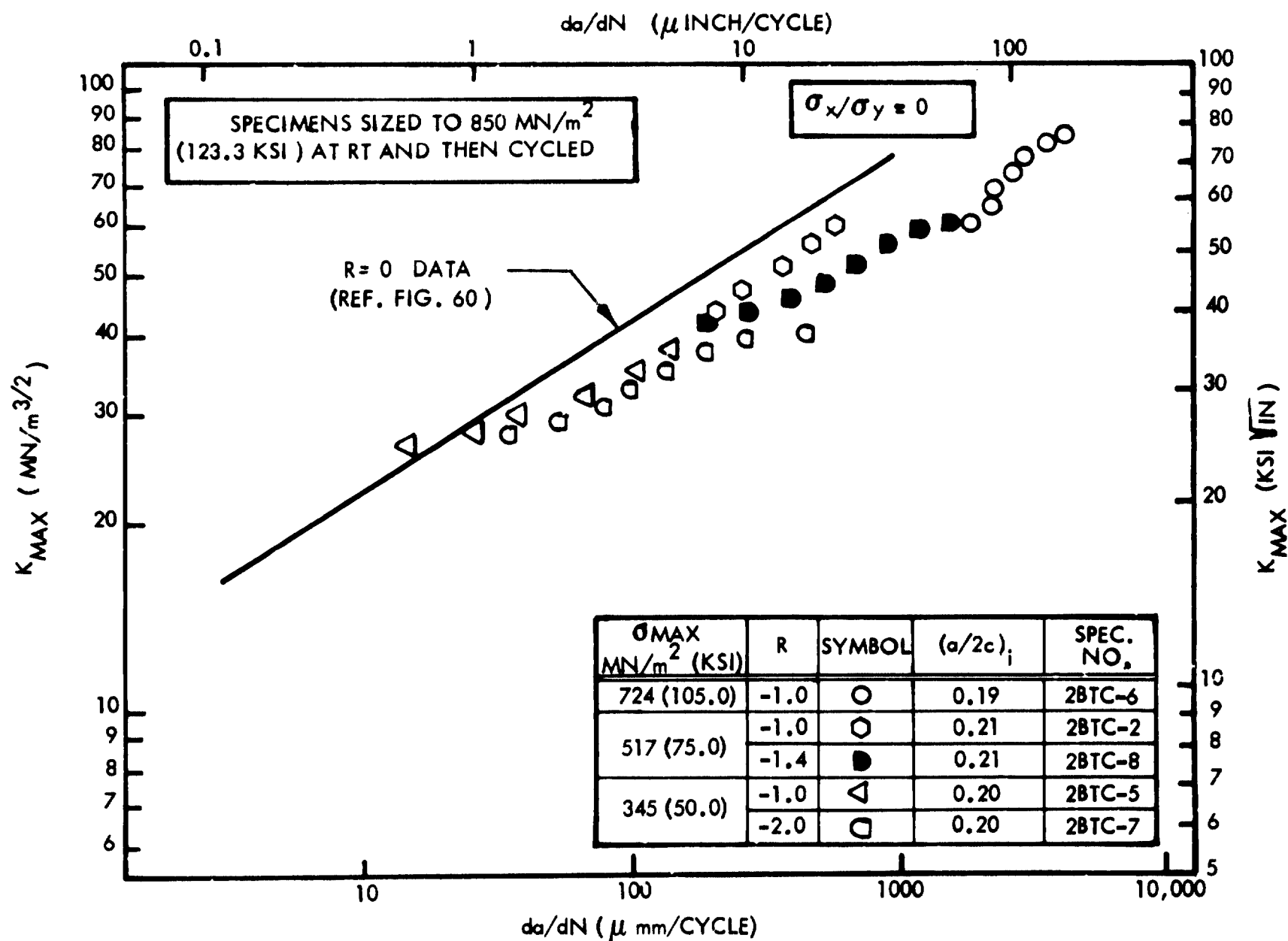


FIGURE 77: CYCLIC CRACK GROWTH RATES FOR 3.30 mm (0.130 INCH) THICK INCONEL X750 STA BM AT 295K(72°F) AND VARIOUS R RATIOS.

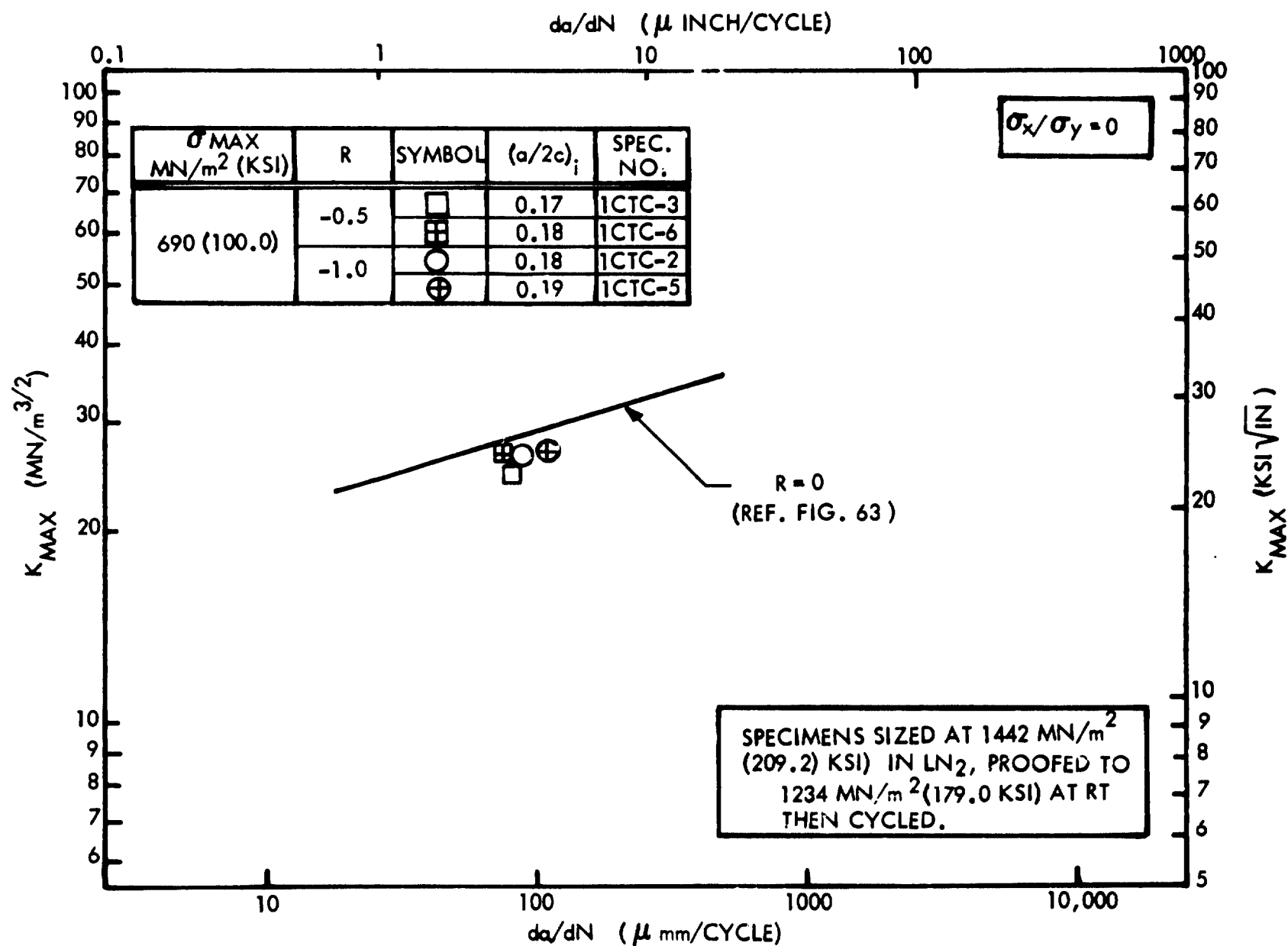


FIGURE 78: CYCLIC CRACK GROWTH RATES FOR 0.71mm (0.028 INCH) THICK CRYOSTRETCHED 301 SS BM AT 295K (72°F) AND VARIOUS R RATIOS

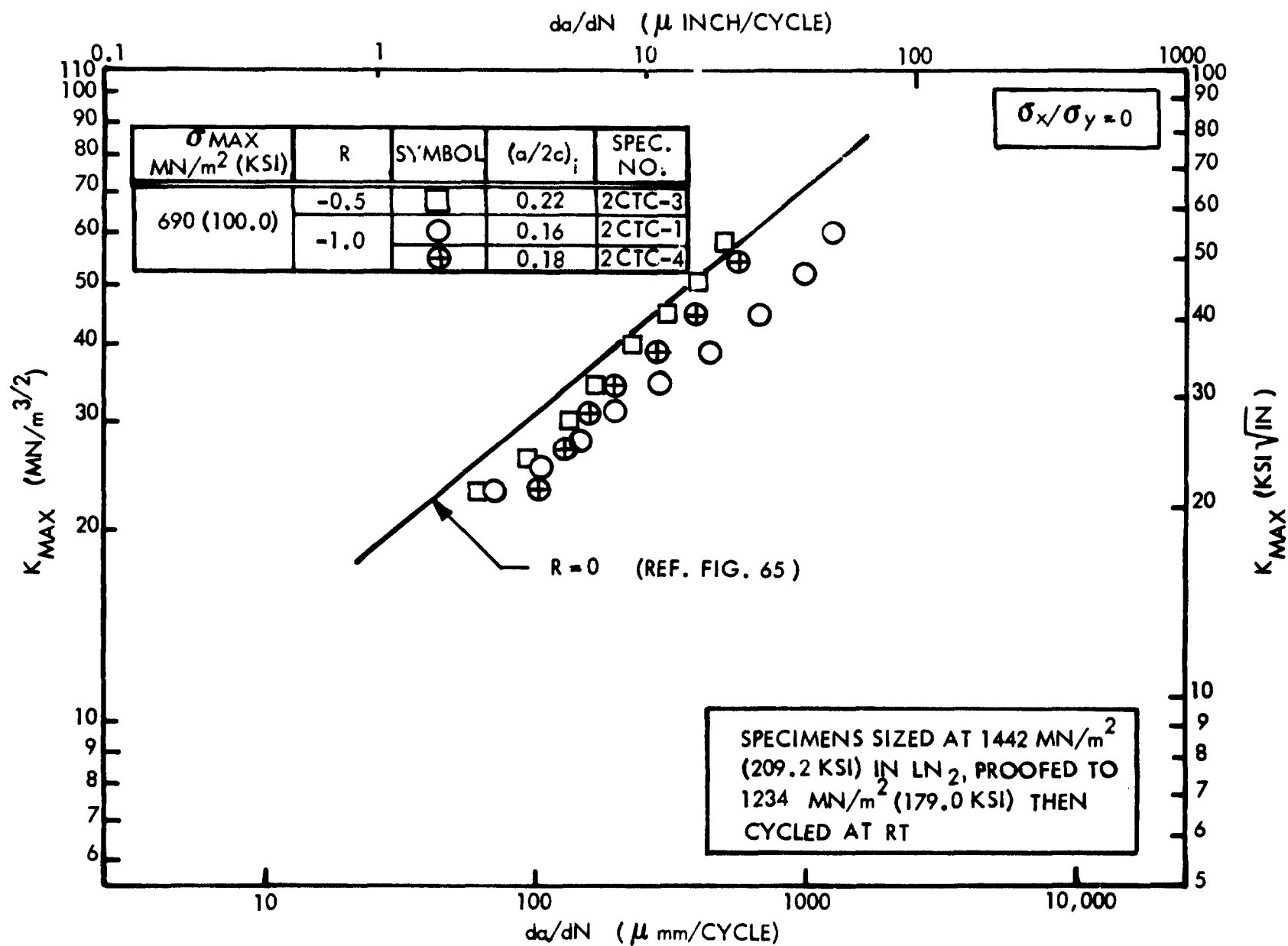


FIGURE 79: CYCLIC CRACK GROWTH RATES FOR 2.54 mm (0.100) THICK CRYOSTRETCHED 301 SS BM AT 295K (72°F) AND VARIOUS R RATIOS.

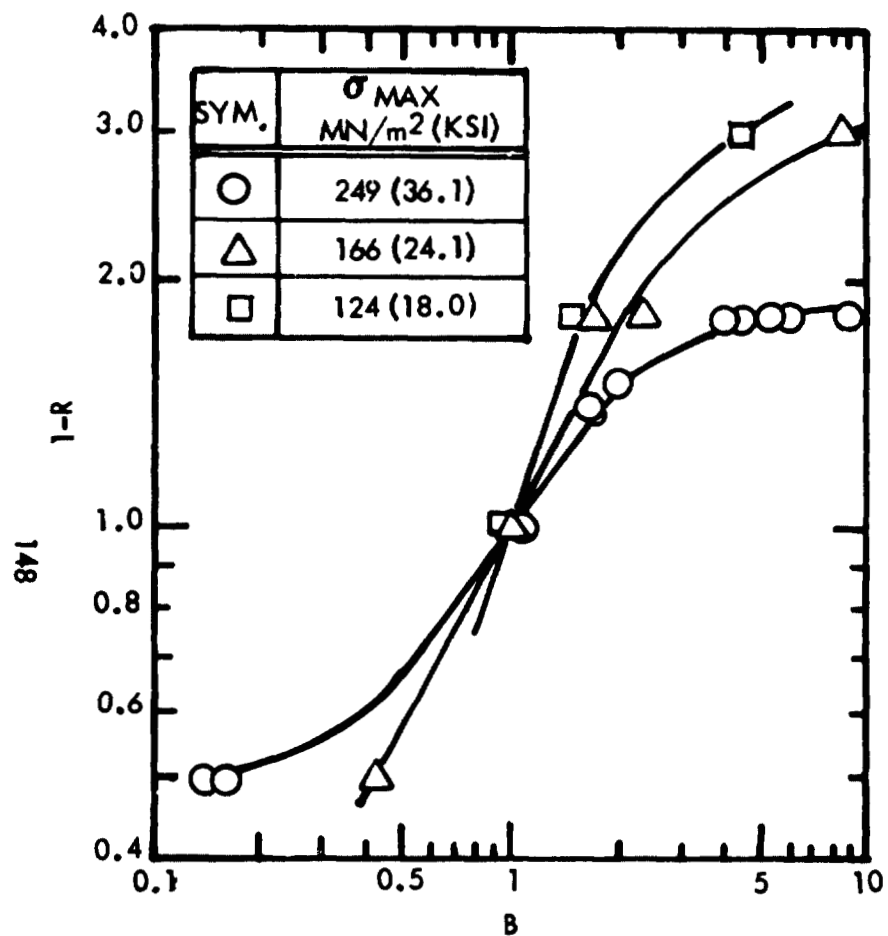


FIGURE 80: INFLUENCE OF R RATIO ON CYCLIC CRACK GROWTH RATES FOR 2.29mm (0.090 INCH) THICK 2219-T62 ALUMINUM BM AT 295K (72°F)

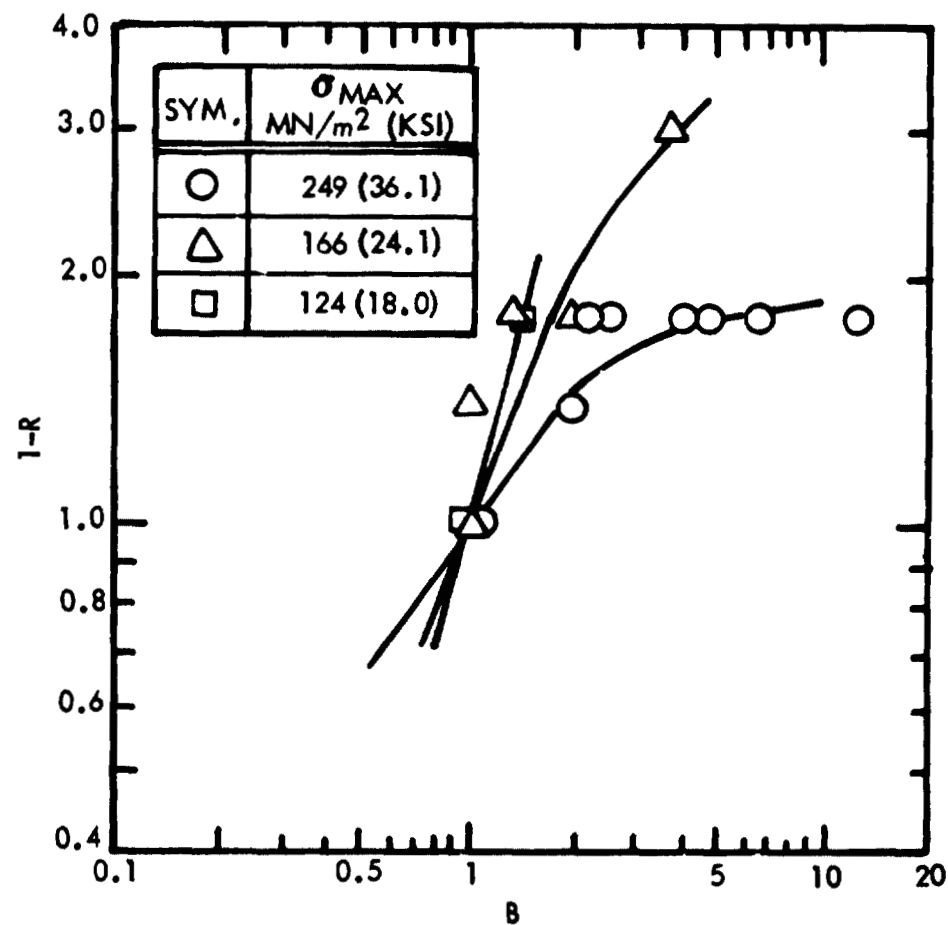


FIGURE 81: INFLUENCE OF R RATIO ON CYCLIC CRACK GROWTH RATES FOR 4.57 mm (0.180 INCH) THICK 2219-T62 ALUMINUM BM AT 295K (72°F)

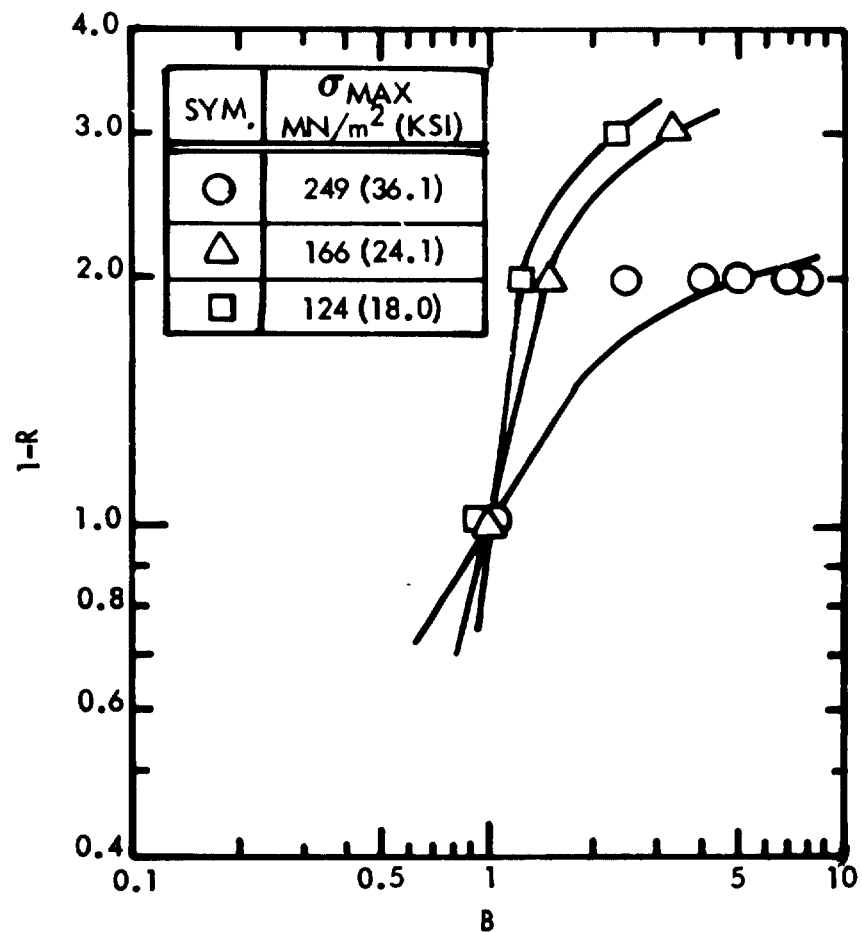


FIGURE 82: INFLUENCE OF R RATIO ON CYCLIC CRACK GROWTH RATES FOR 7.62mm (0.300 INCH) THICK 2219-T62 ALUMINUM BM AT 295K (72°F)

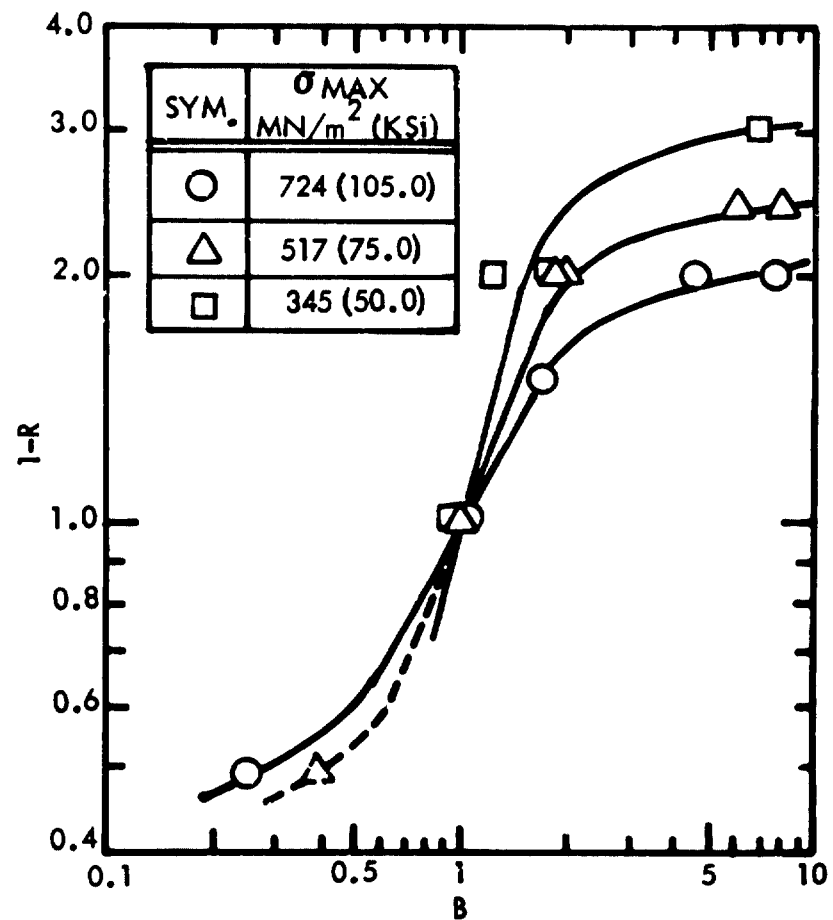


FIGURE 83: INFLUENCE OF R RATIO ON CYCLIC CRACK GROWTH RATES FOR 1.02mm (0.040 INCH) THICK INCONEL X750 STA BM AT 295K (72°F)

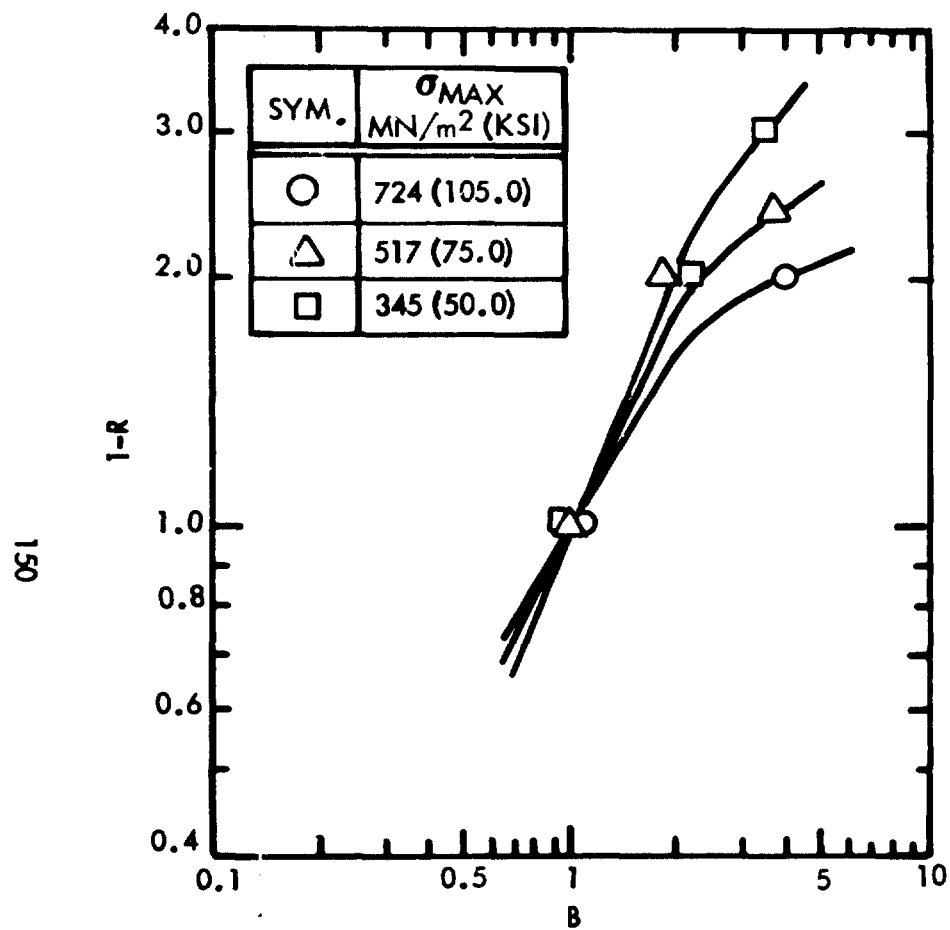


FIGURE 84: INFLUENCE OF R RATIO ON CYCLIC CRACK GROWTH RATES FOR 3.30mm (0.130 INCH) THICK INCONEL X750 STA BM AT 295K (72°F)

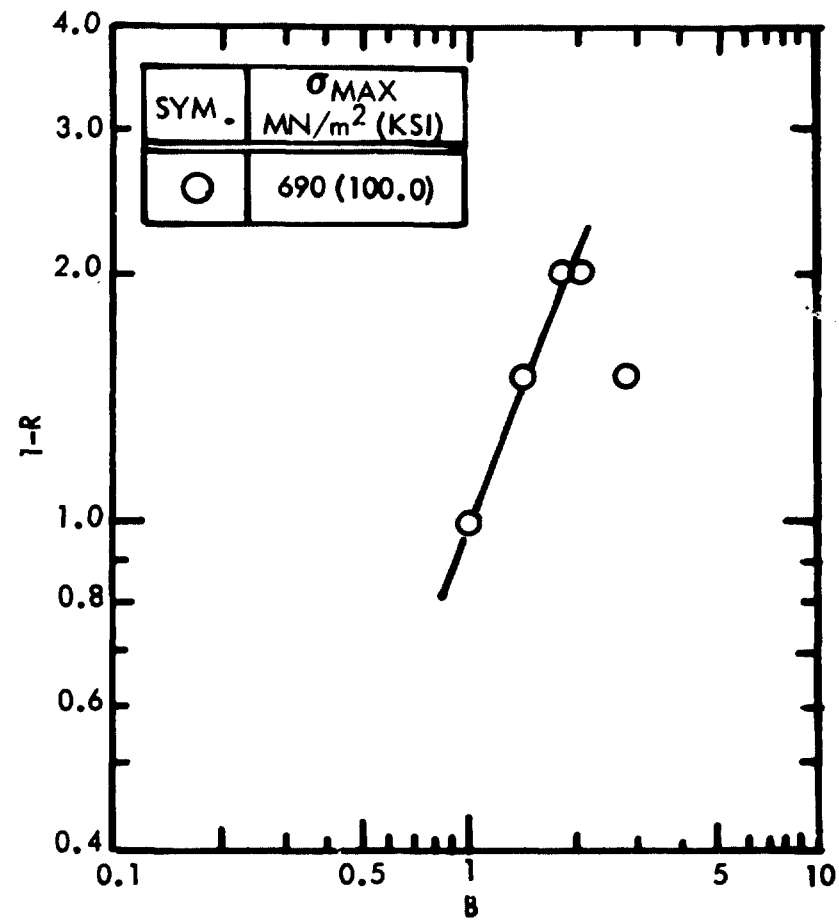


FIGURE 85: INFLUENCE OF R RATIO ON CYCLIC CRACK GROWTH RATES FOR 0.71mm (0.028 INCH) THICK CRYOSTRETCHED STEEL BM AT 295K (72°F)

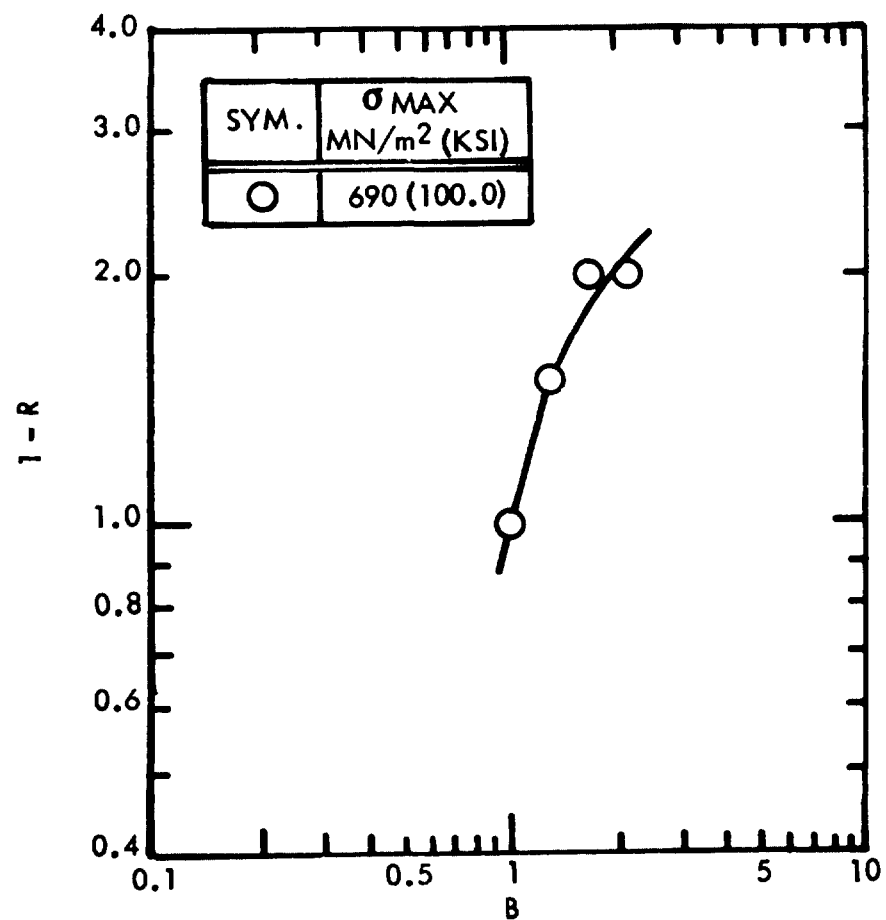


FIGURE 86: INFLUENCE OF R RATIO ON CYCLIC CRACK GROWTH RATES FOR 2.54mm (0.100 INCH) THICK CRYOSTRETCHED 301 STAINLESS STEEL BM AT 295K (72°F)

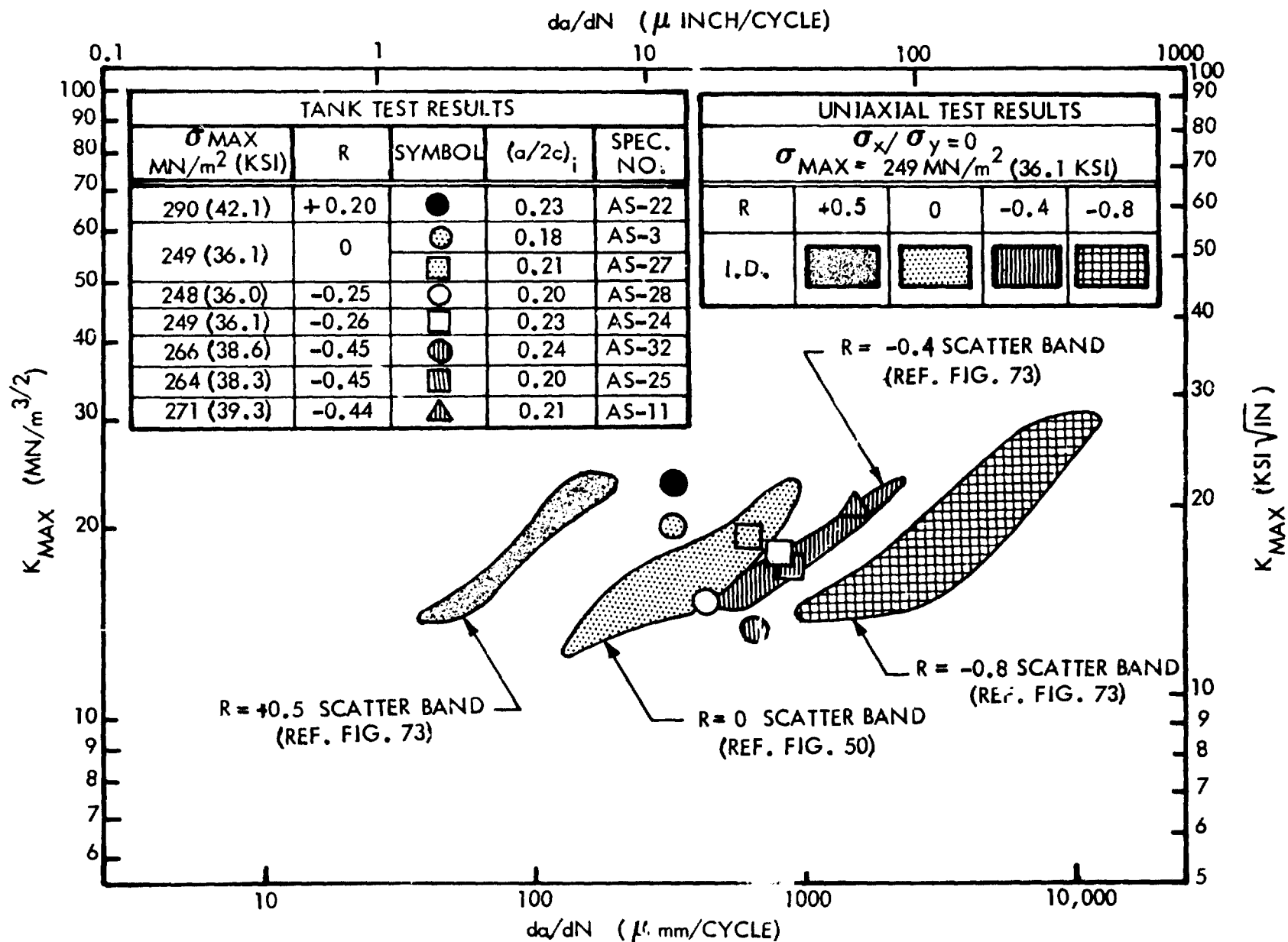


FIGURE 87: COMPARISON OF UNIAXIAL AND TANK TEST CYCLIC CRACK GROWTH RATES FOR 2.29mm (0.090 INCH) THICK 2219-T62 ALUMINUM BM AT 295K (72°F)

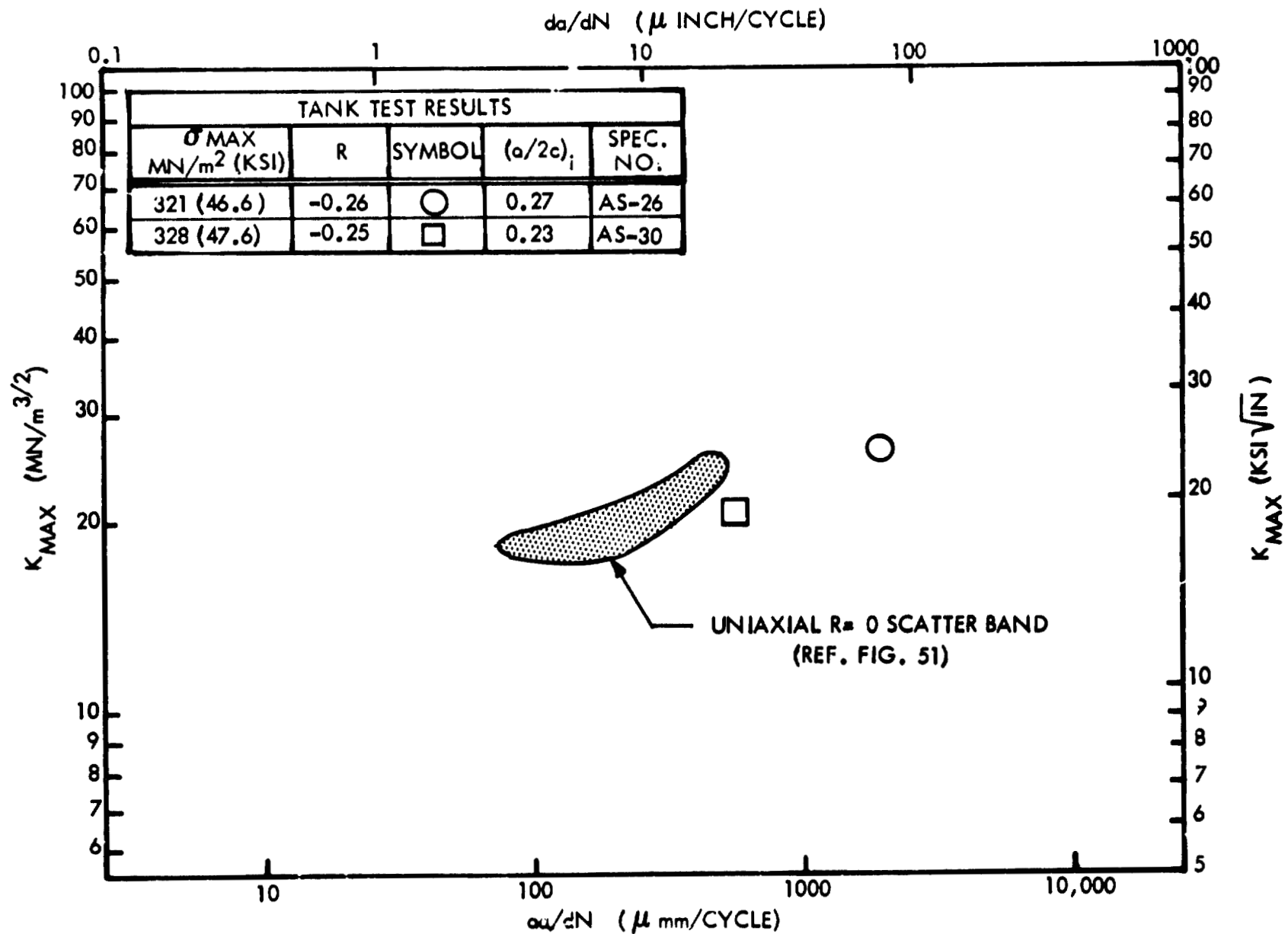


FIGURE 88: COMPARISON OF UNIAXIAL AND TANK TEST CYCLIC CRACK GROWTH RATES FOR 2.29mm (0.090 INCH) THICK 2219-T62 ALUMINUM BM AT 78K (-320°F)

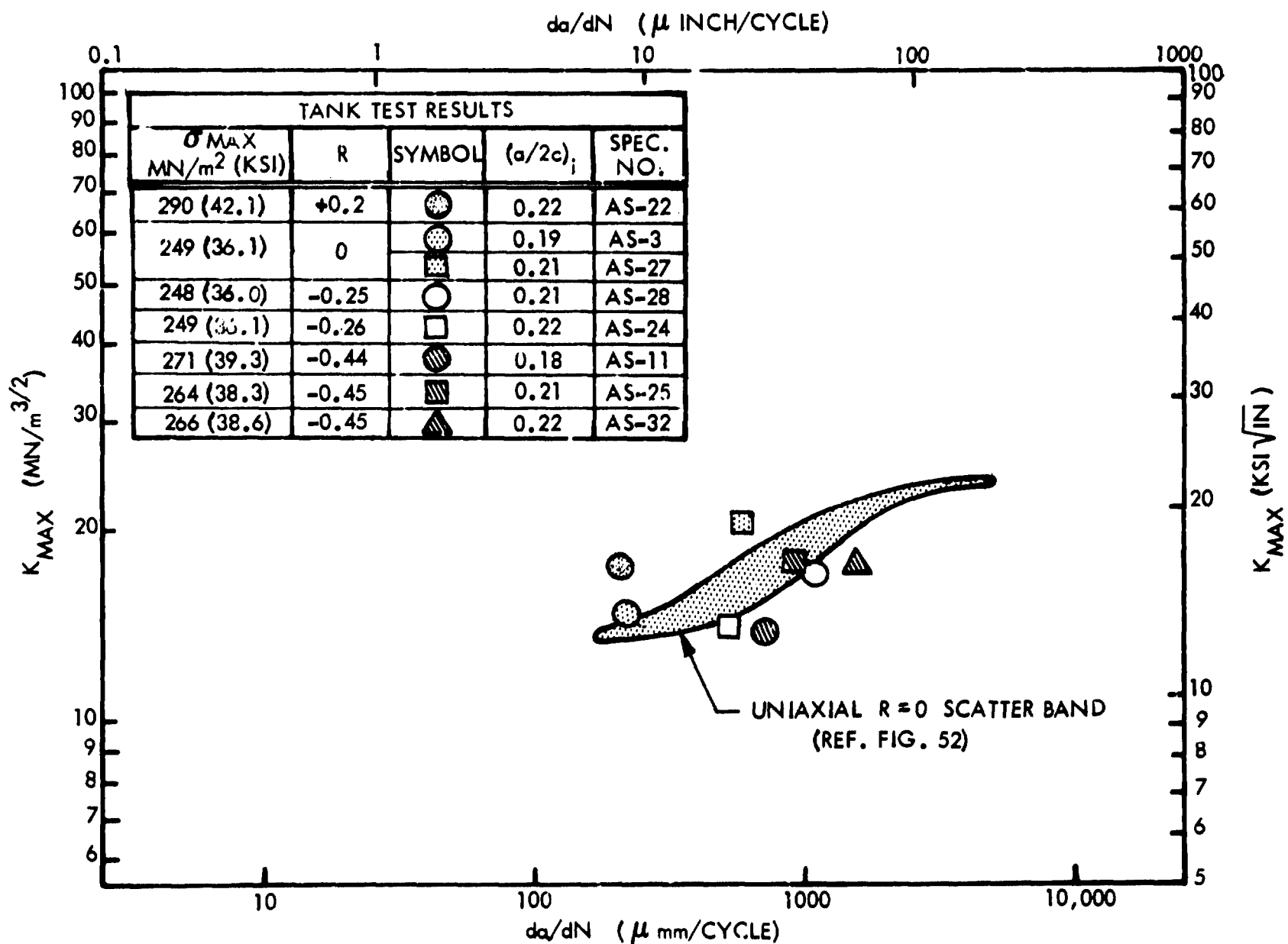


FIGURE 89: COMPARISON OF UNIAXIAL AND TANK TEST CYCLIC CRACK GROWTH RATES FOR 2.29mm (0.090 INCH) THICK 2219-T62 ALUMINUM WM AT 295K (72°F)

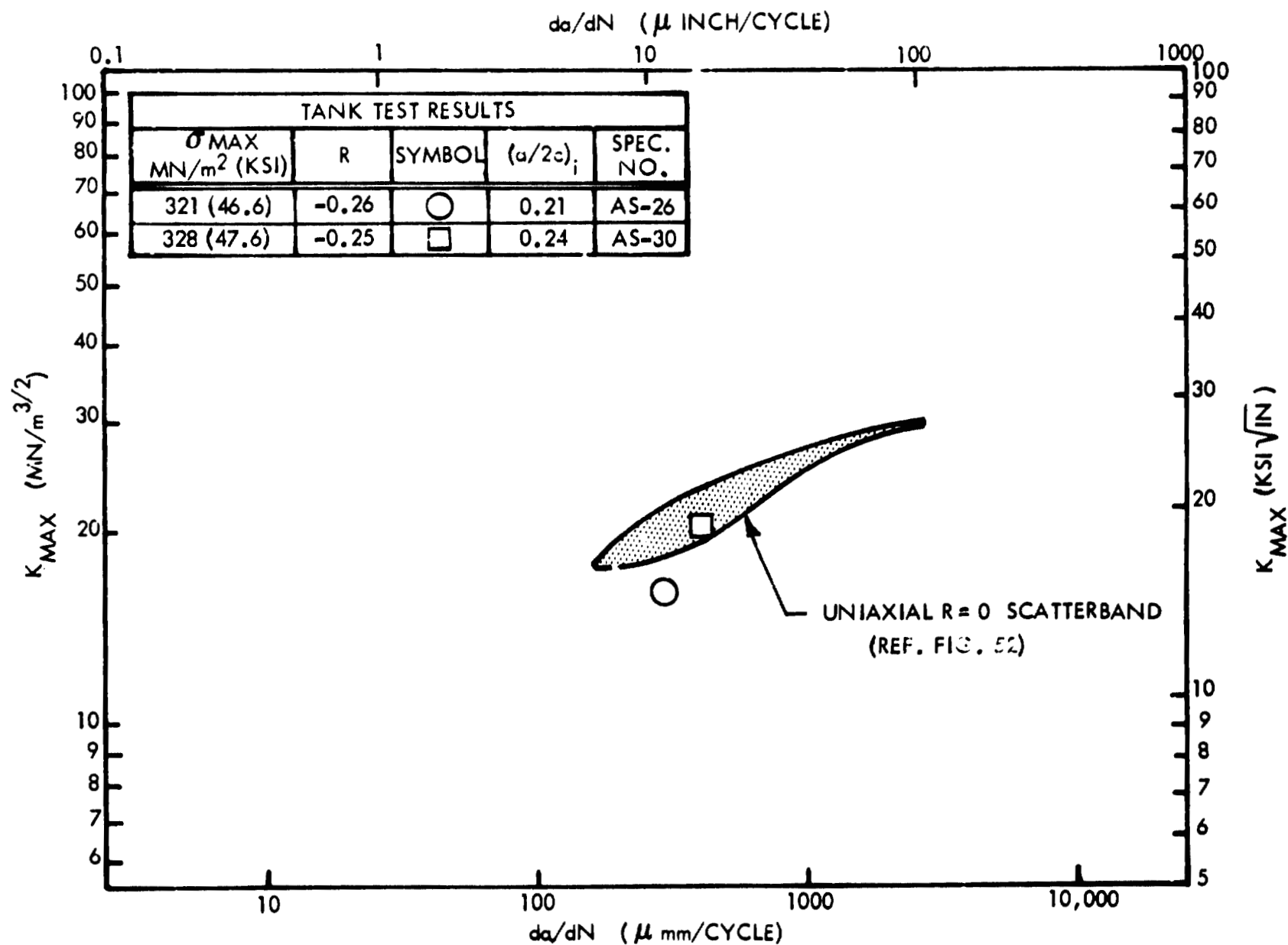


FIGURE 90: COMPARISON OF UNIAXIAL AND TANK TEST CYCLIC CRACK GROWTH RATES FOR 2.29mm (0.090 INCH) THICK 2219-T62 ALUMINUM WM AT 78K (-320°F)

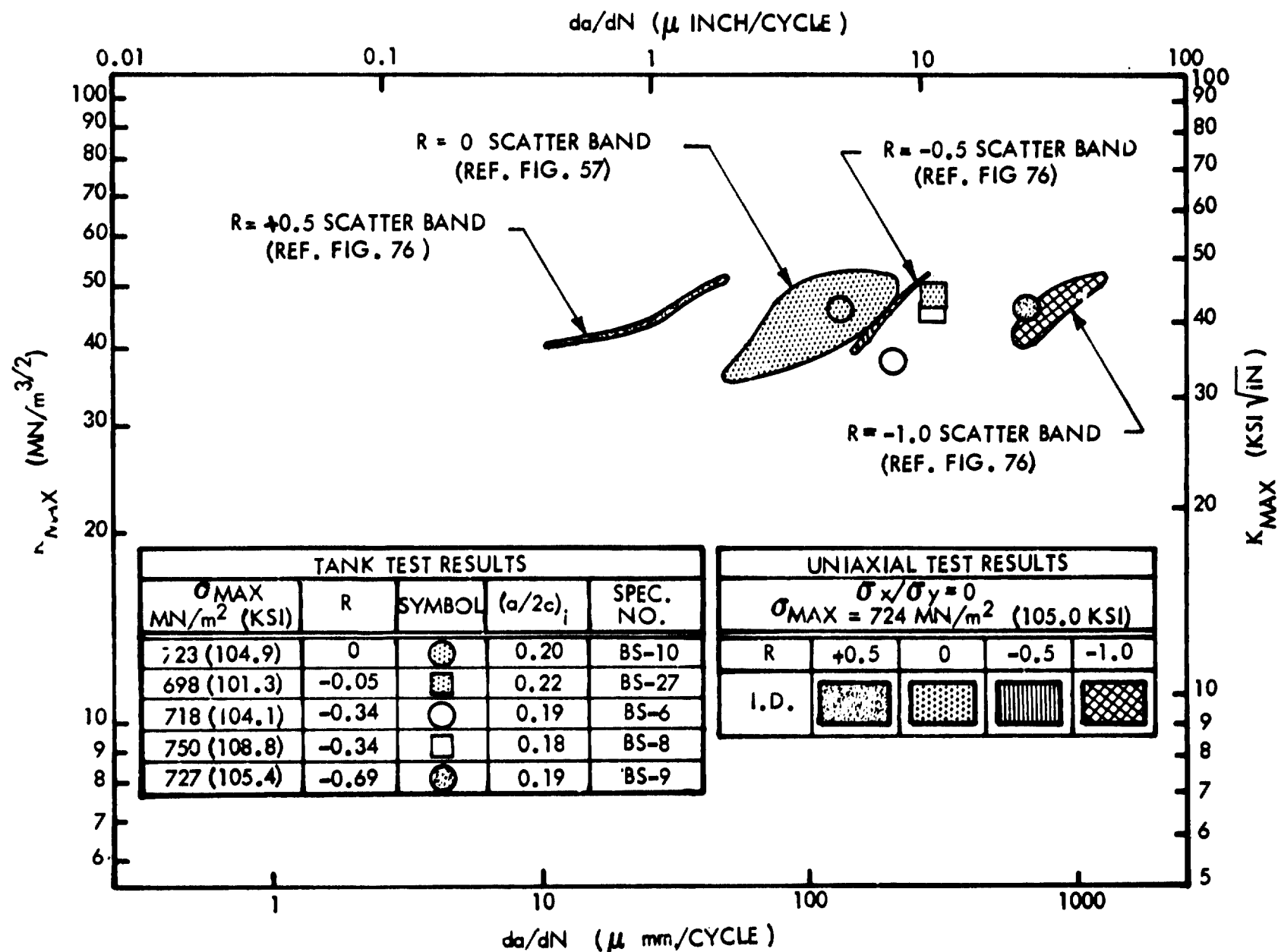


FIGURE 91: COMPARISON OF UNIAXIAL AND TANK TEST CYCLIC CRACK GROWTH RATES FOR 1.02mm (0.040 INCH) THICK INCONEL X 750 STA BM AT 295K (72°F)

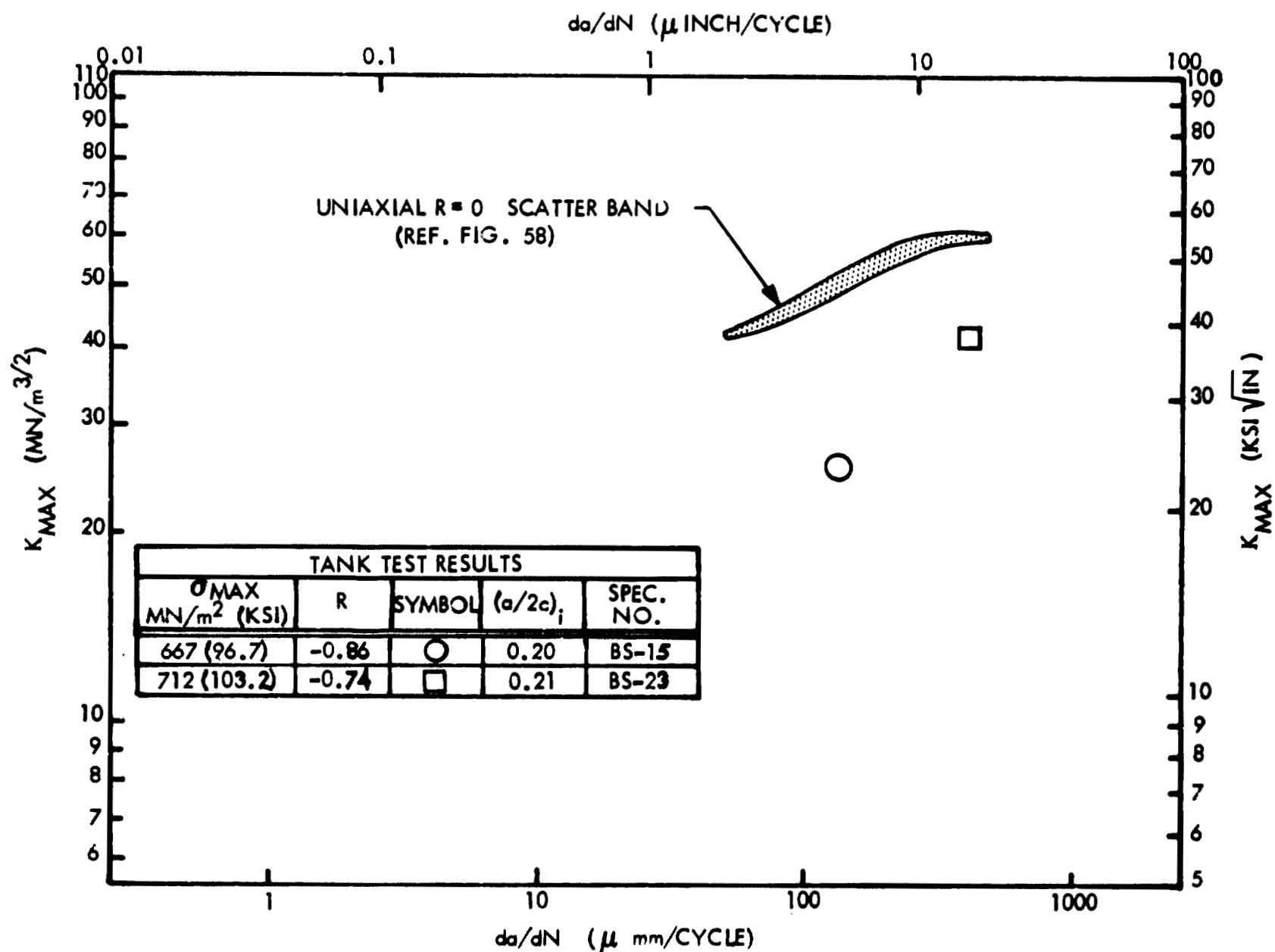


FIGURE 92: COMPARISON OF UNIAXIAL AND TANK TEST CYCLIC CRACK GROWTH RATES FOR 1.02mm (0.040 INCH) THICK INCONEL X 750 STA 6M AT 70K (-320°F)

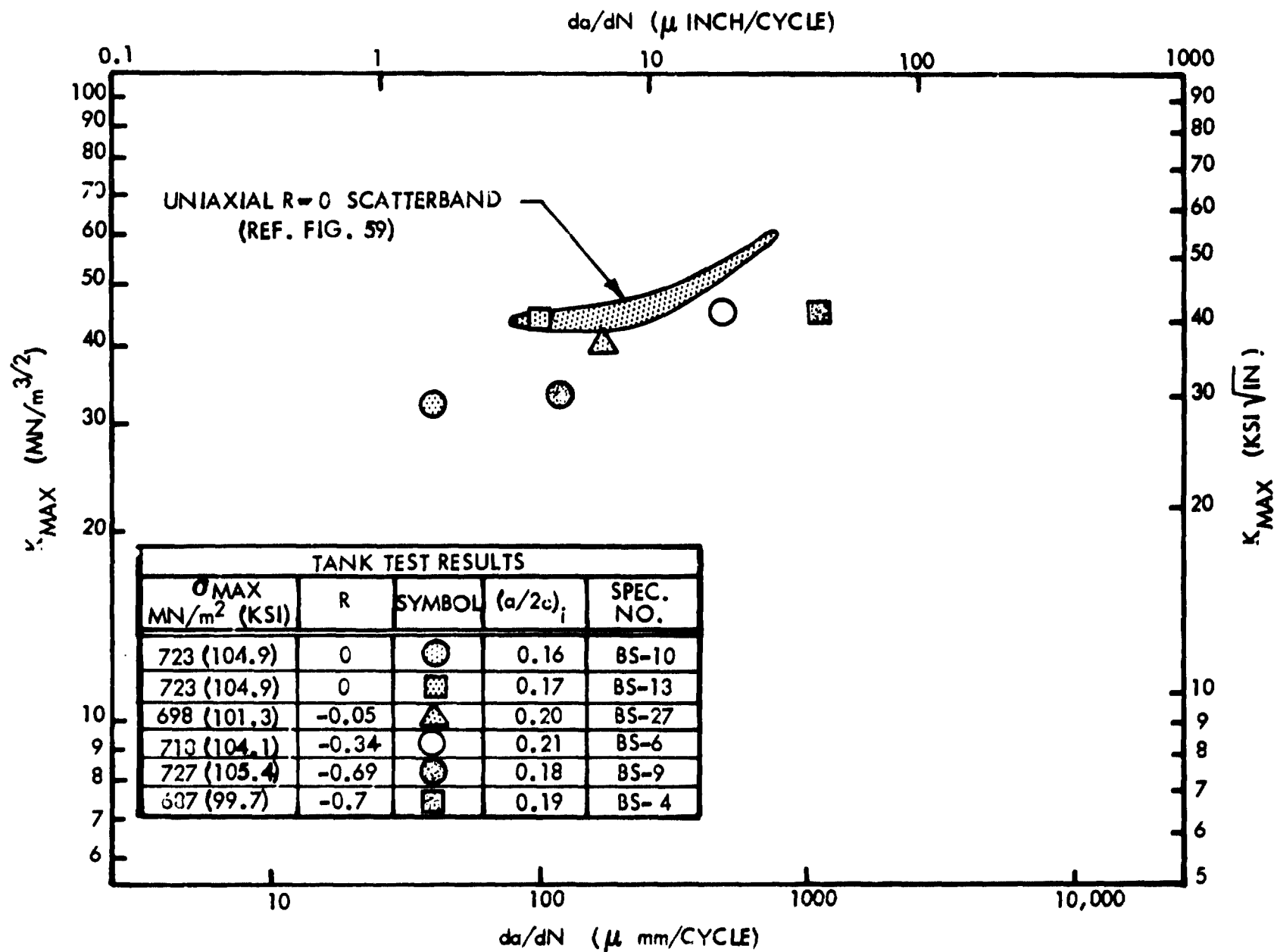


FIGURE 93: COMPARISON OF UNIAxIAL AND TANK TEST CYCLIC CRACK GROWTH RATES FOR 1.02mm (0.040 INCH) THICK INCONEL X 750 STA WM AT 295K (72°F)

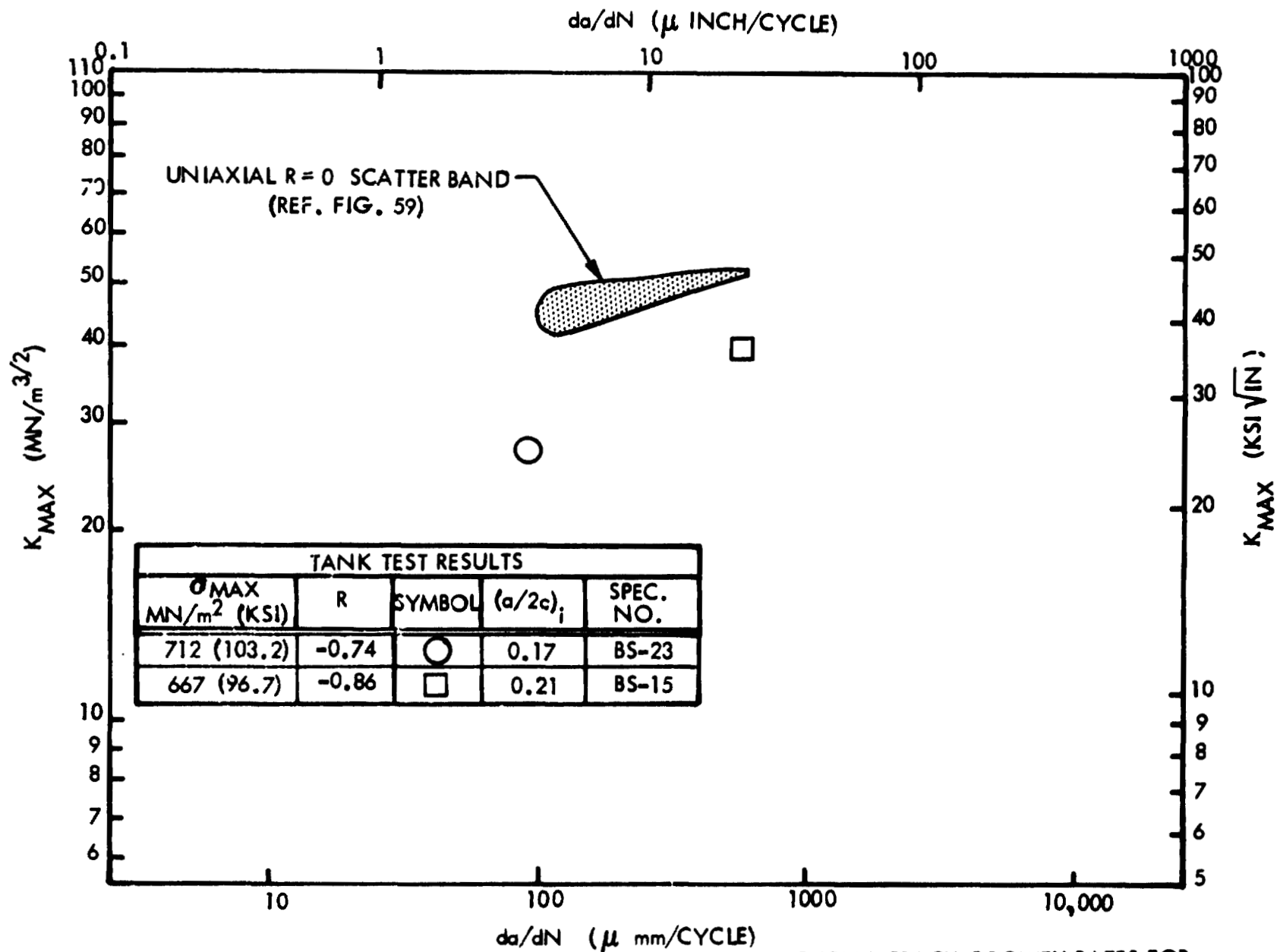


FIGURE 94: COMPARISON OF UNIAXIAL AND TANK TEST CYCLIC CRACK GROWTH RATES FOR 1.02mm (0.040 INCH) THICK INCONEL X 750 STA WM AT 73K ($-320^{\circ}F$)

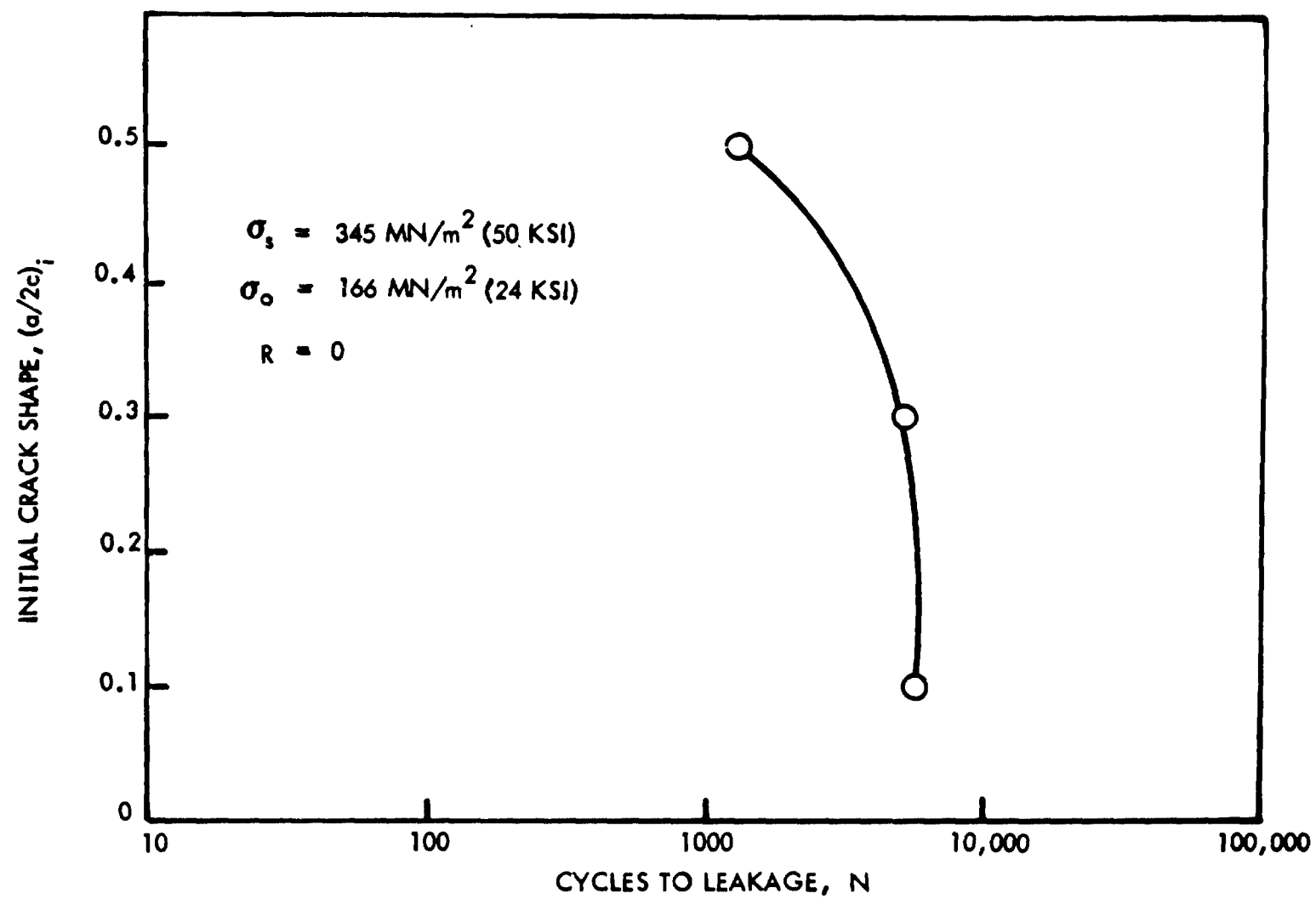


FIGURE 95: INFLUENCE OF ASSUMED INITIAL CRACK SHAPE ON CYCLIC LIFE FOR 4.57mm (0.18 INCH) 2219-T62 ALUMINUM BM

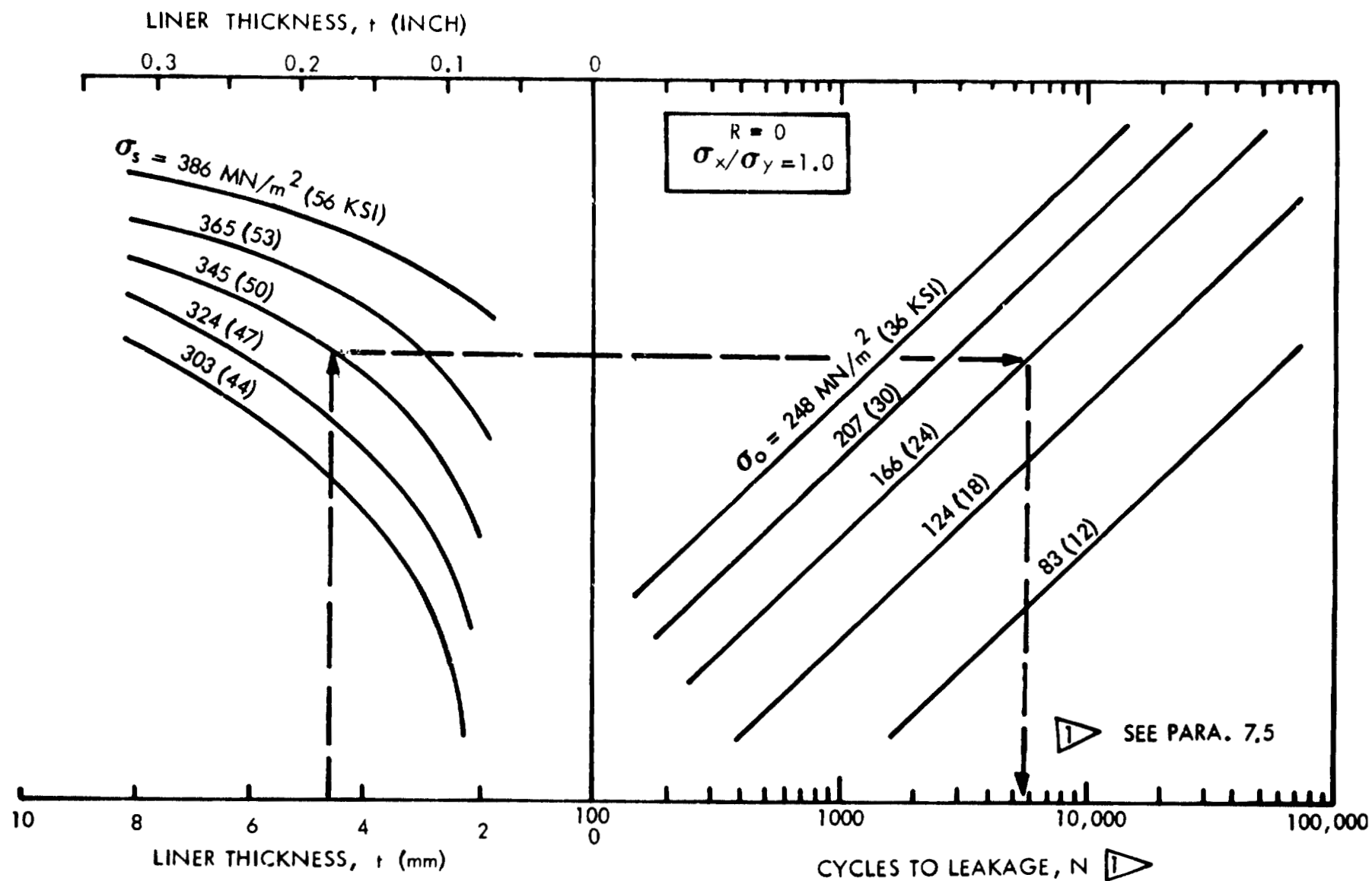


FIGURE 96: SERVICE LIFE FOR 2219-T62 ALUMINUM LINERS (BM) AT RT - INITIAL FLAW SHAPE OF 0.10

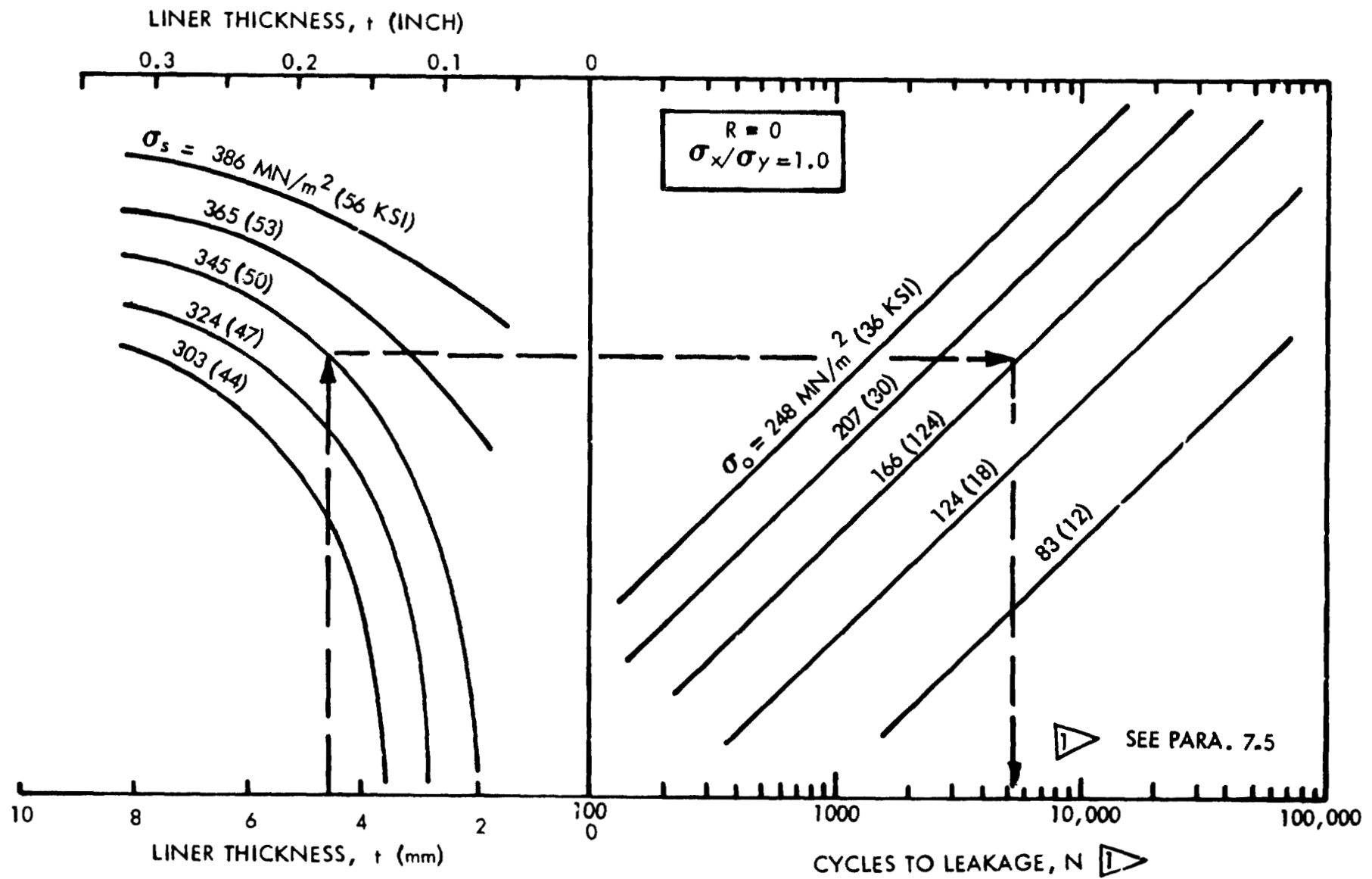


FIGURE 97: SERVICE LIFE FOR 2219-T62 ALUMINUM LINERS (BM) AT RT- INITIAL FLAW SHAPE OF 0.030

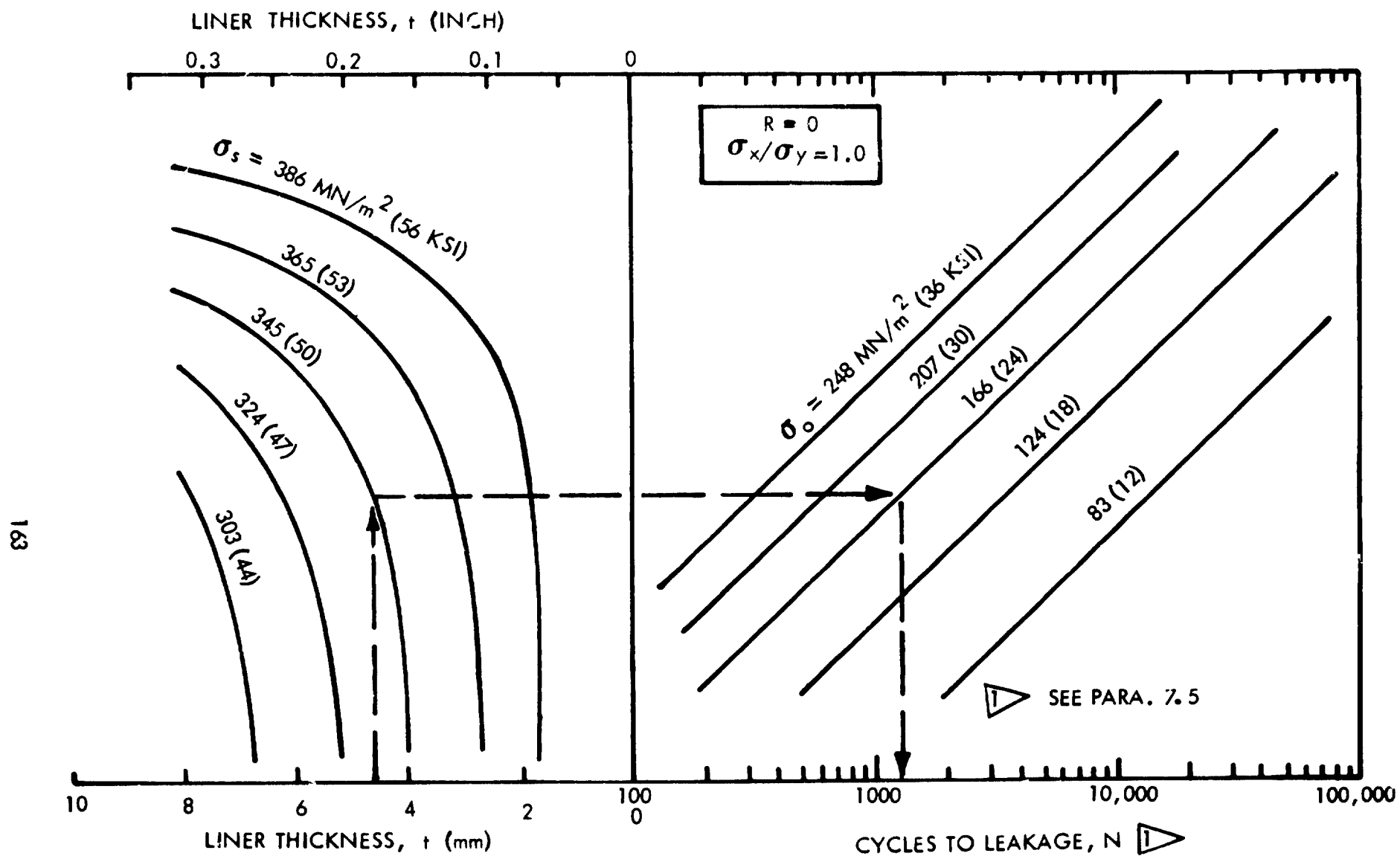


FIGURE 98: SERVICE LIFE FOR 2219-T62 ALUMINUM LINERS (BM) AT RT - INITIAL FLAW SHAPE OF 0.50

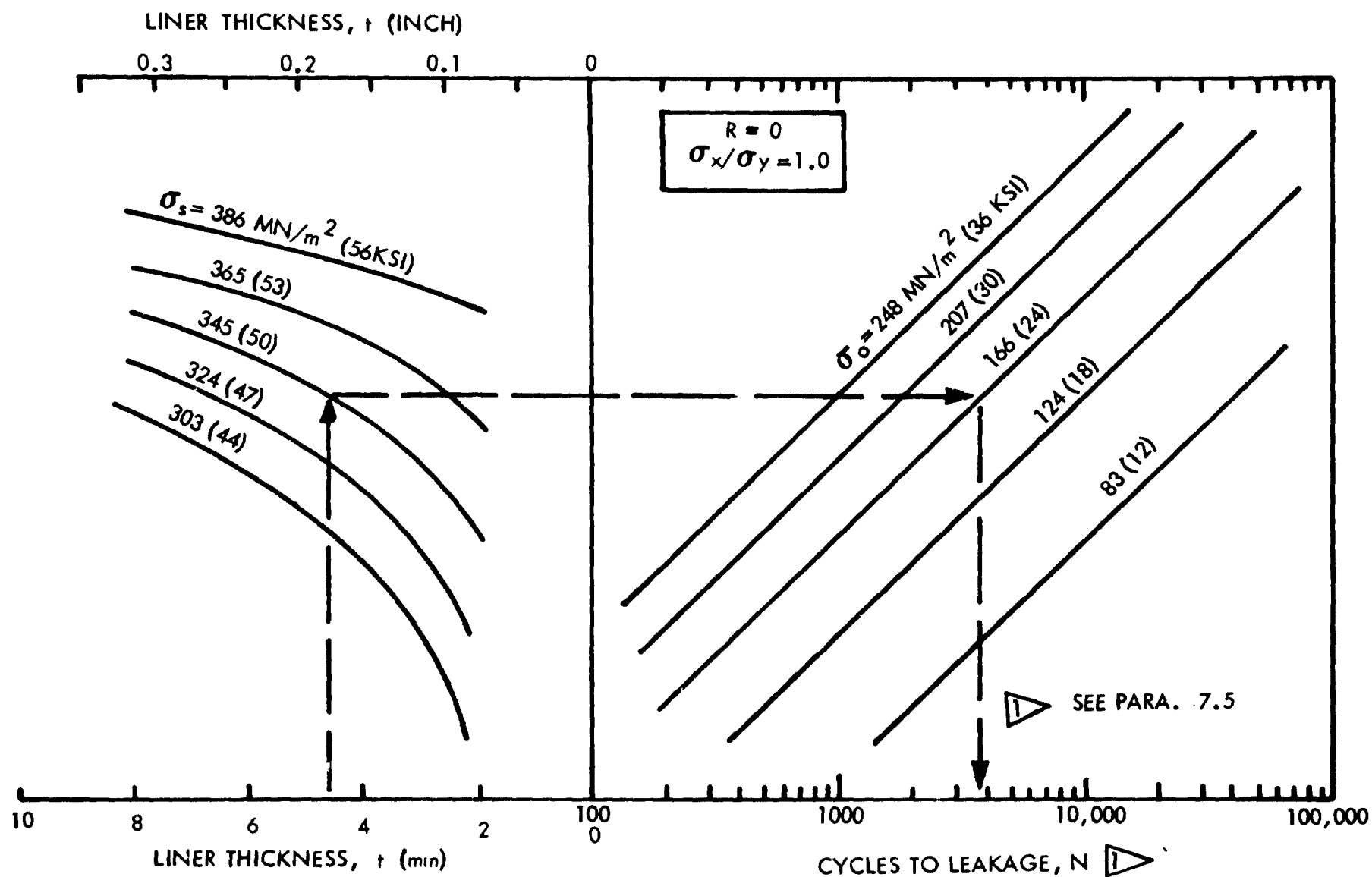


FIGURE 99: SERVICE LIFE FOR 2219-T62 ALUMINUM LINERS (WM) AT RT - INITIAL FLAW SHAPE OF 0.10

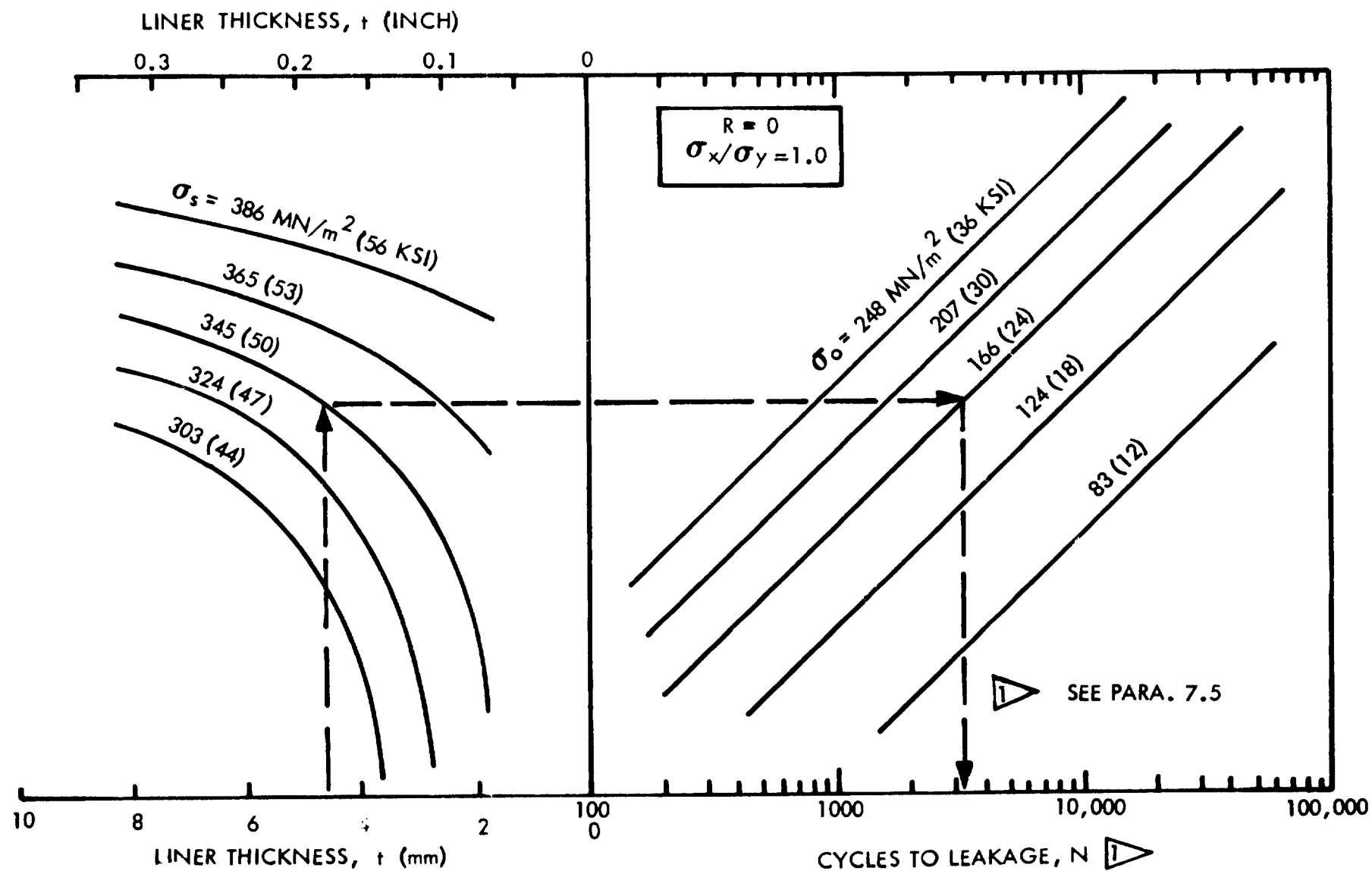


FIGURE 100: SERVICE LIFE FOR 2219-T62 ALUMINUM LINERS (WM) AT RT - INITIAL FLAW SHAPE OF 0.3

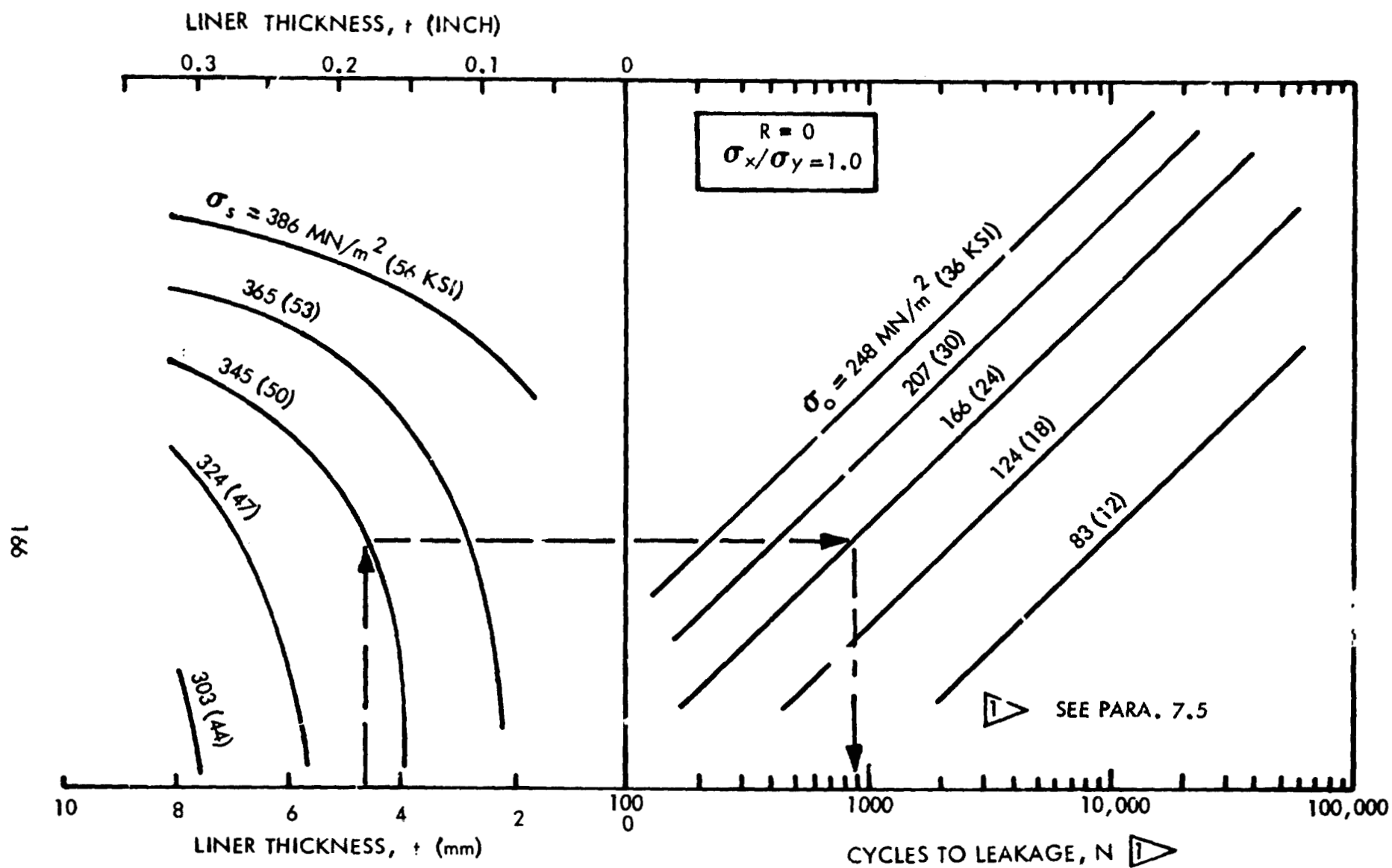


FIGURE 101: SERVICE LIFE FOR 2219-T62 ALUMINUM LINERS (WM) AT RT - INITIAL FLAW SHAPE OF 0.5

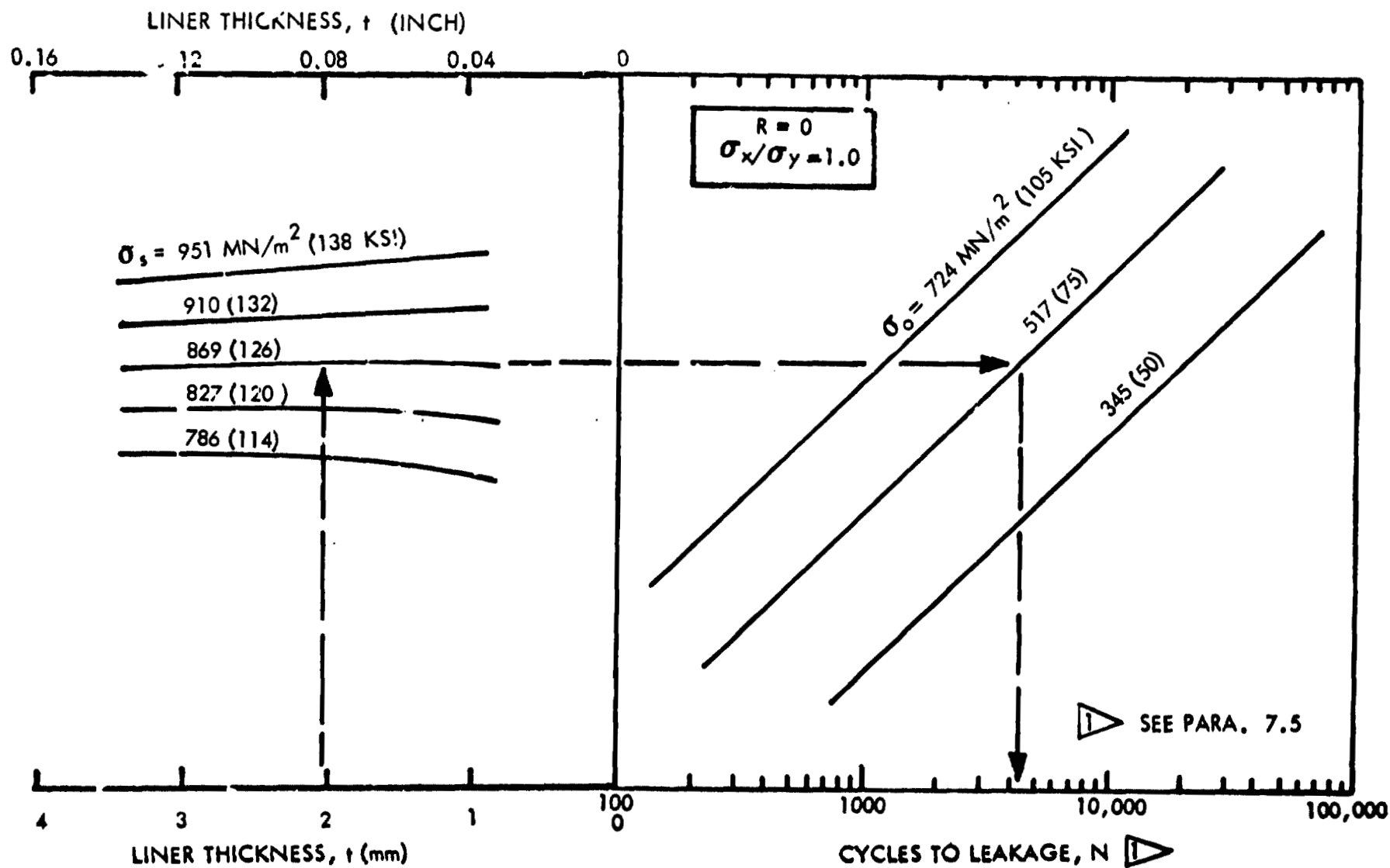


FIGURE 102: SERVICE LIFE FOR INCONEL X750 STA LINERS (BM) AT RT - INITIAL FLAW SHAPE OF 0.10

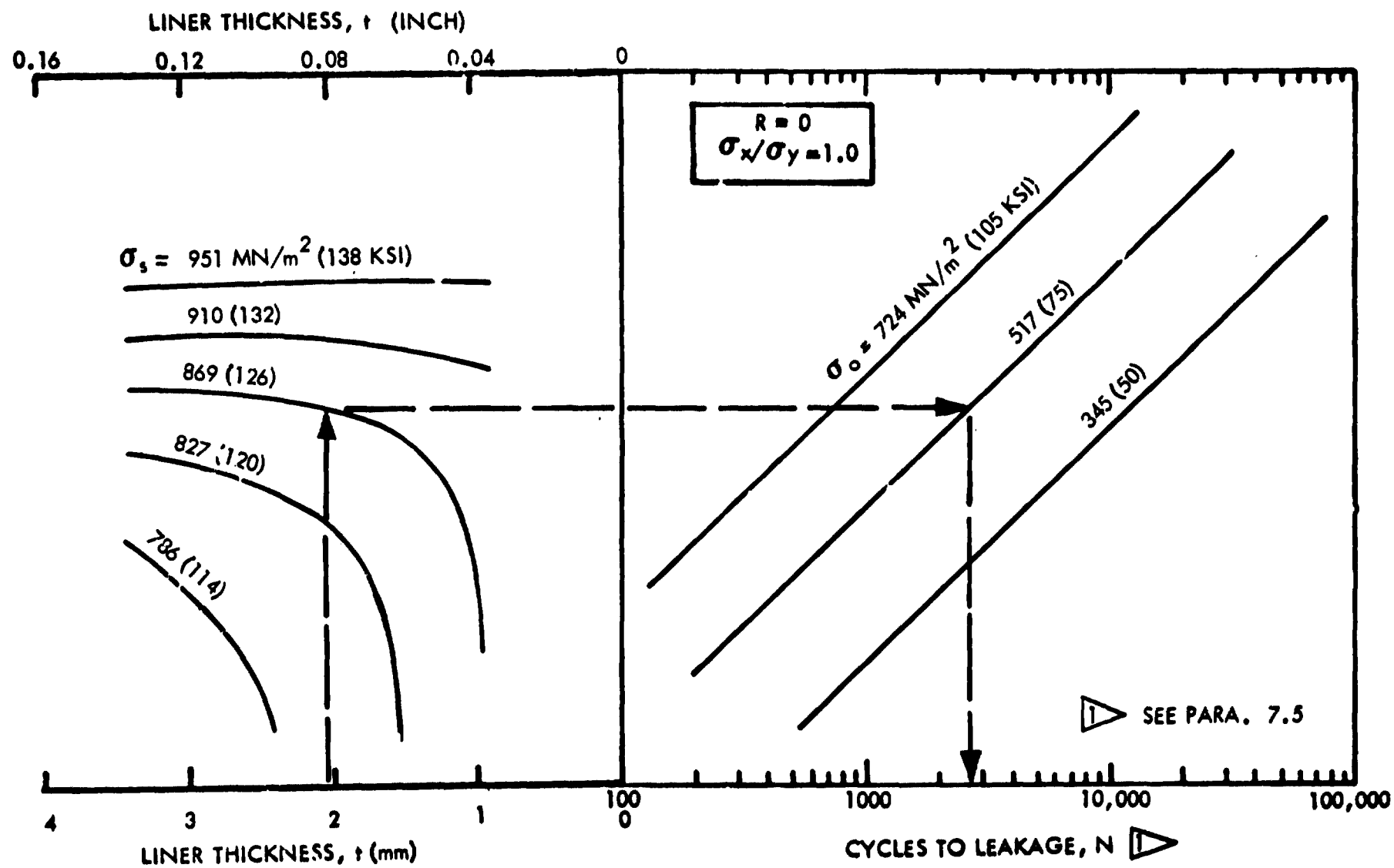


FIGURE 103: SERVICE LIFE FOR INCONEL X750 STA LINERS (BM) AT RT - INITIAL FLAW SHAPE OF 0.30

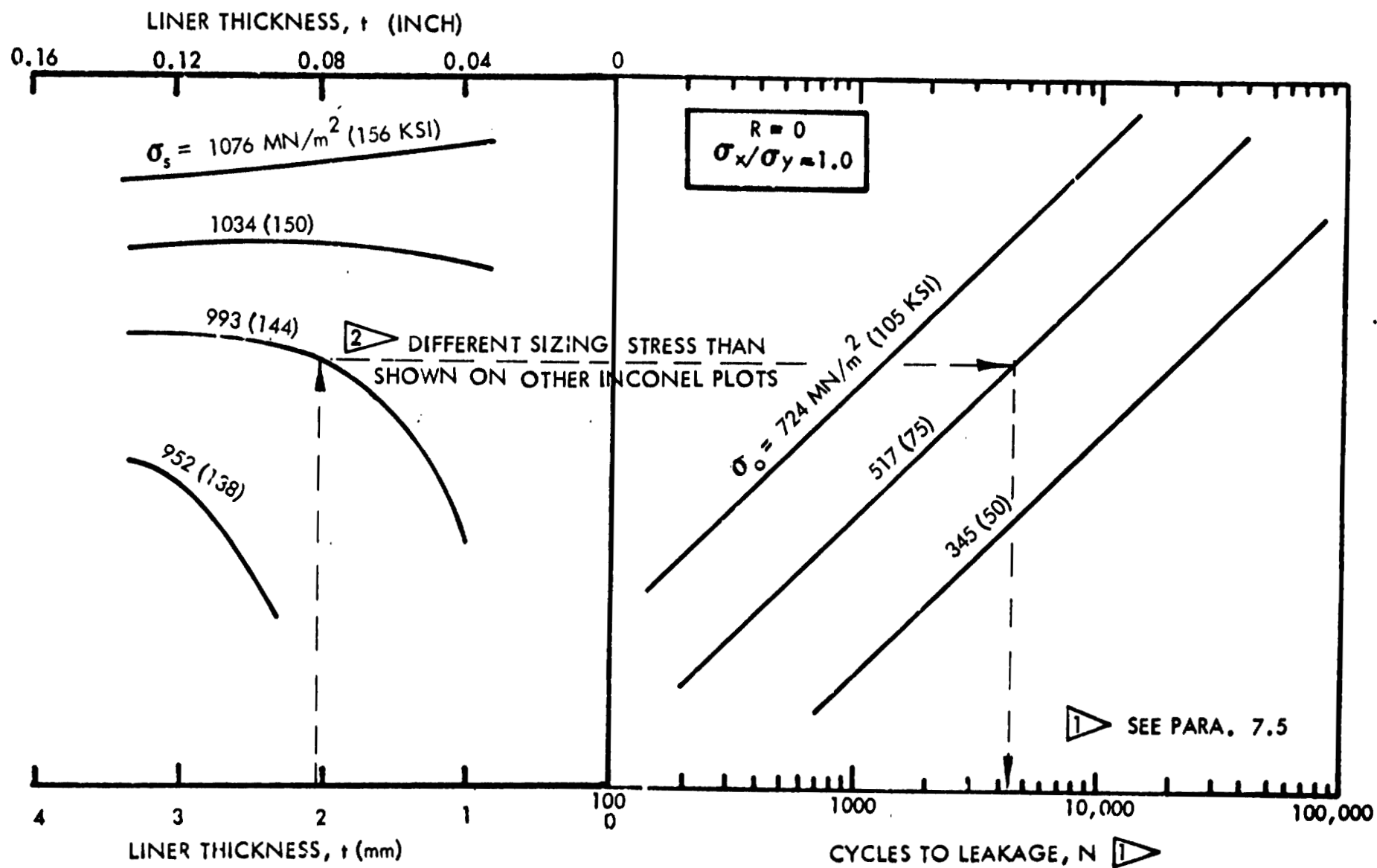


FIGURE 104: SERVICE LIFE FOR INCONEL X750 STA LINERS (BM) AT RT - INITIAL FLAW SHAPE OF 0.50

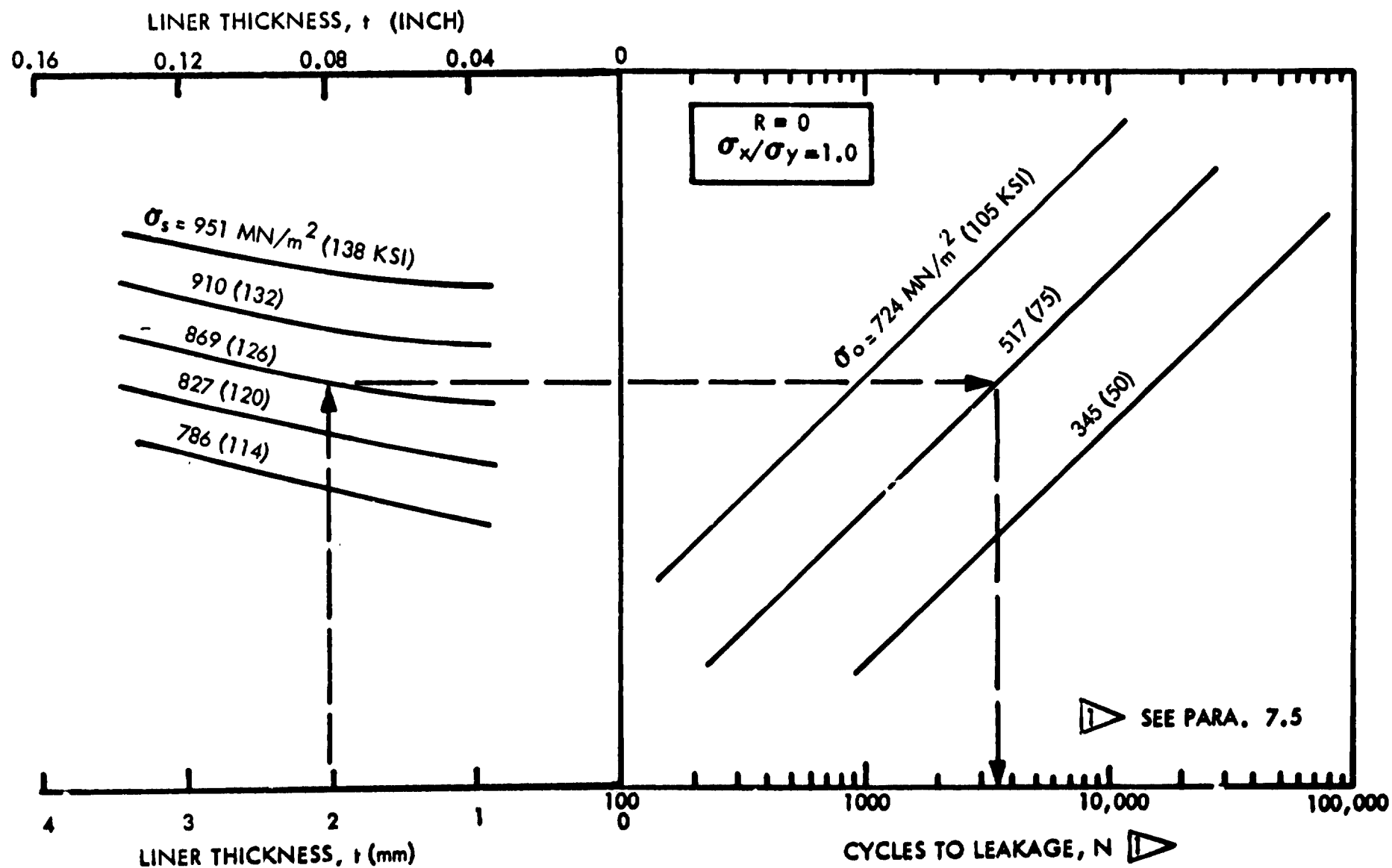


FIGURE 105: SERVICE LIFE FOR INCONEL X750 STA LINERS (WM) AT-RT - INITIAL FLAW SHAPE OF 0.10

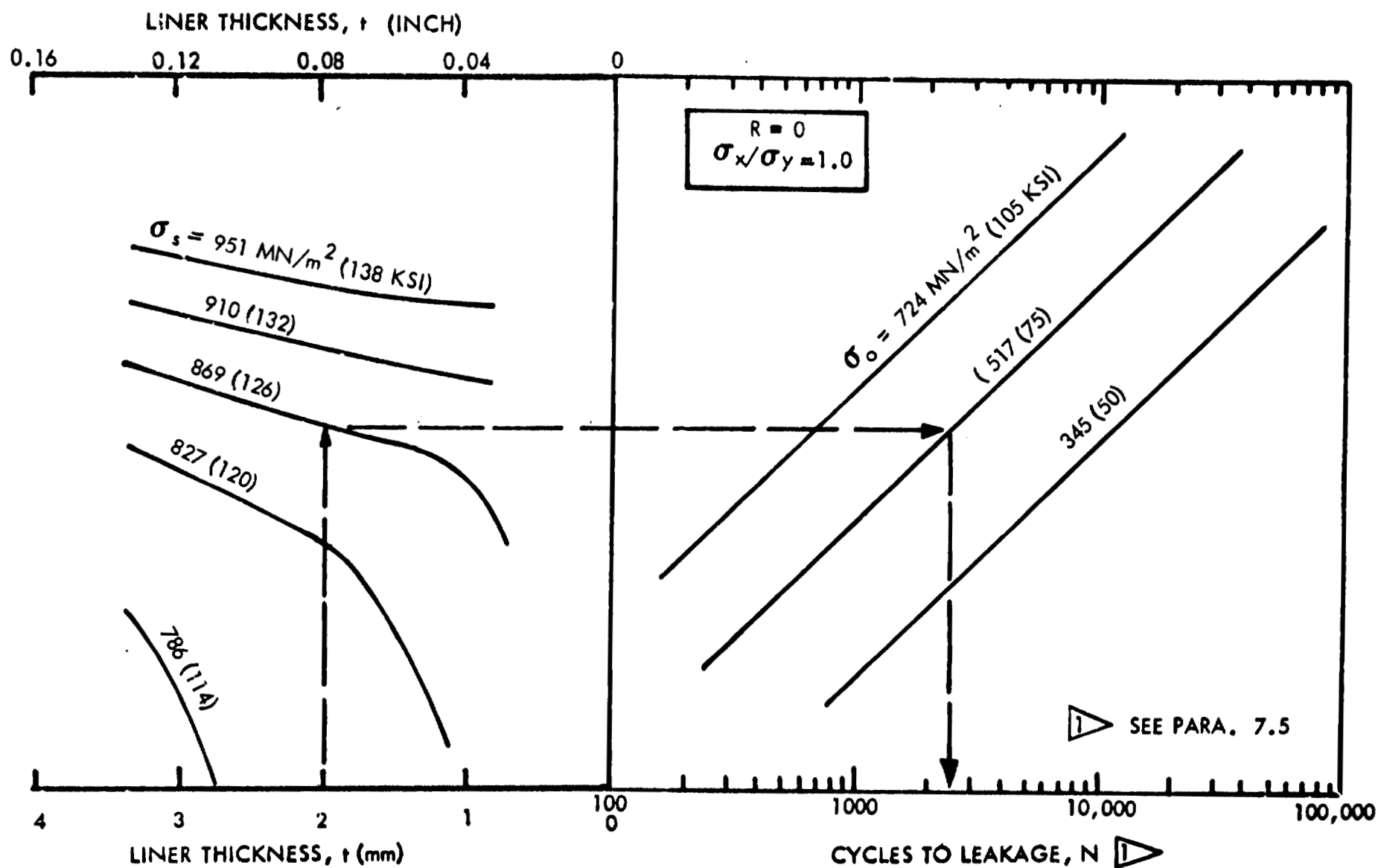


FIGURE 106: SERVICE LIFE FOR INCONEL X750 STA LINERS (WM) AT RT - INITIAL FLAW SHAPE OF 0.3

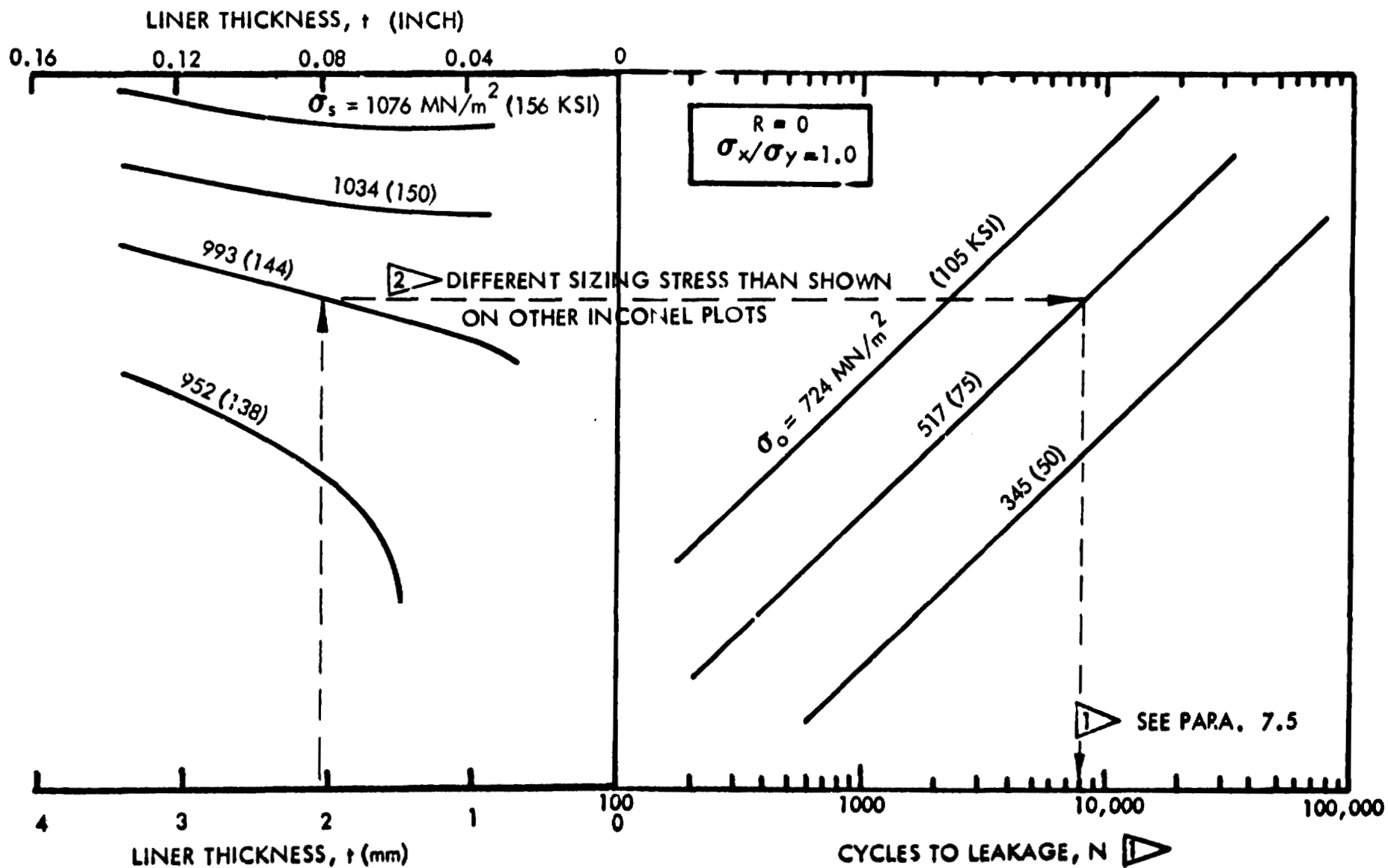


FIGURE 107: SERVICE LIFE FOR INCONEL X750 STA LINERS (WM) AT RT - INITIAL FLAW SHAPE OF 0.50

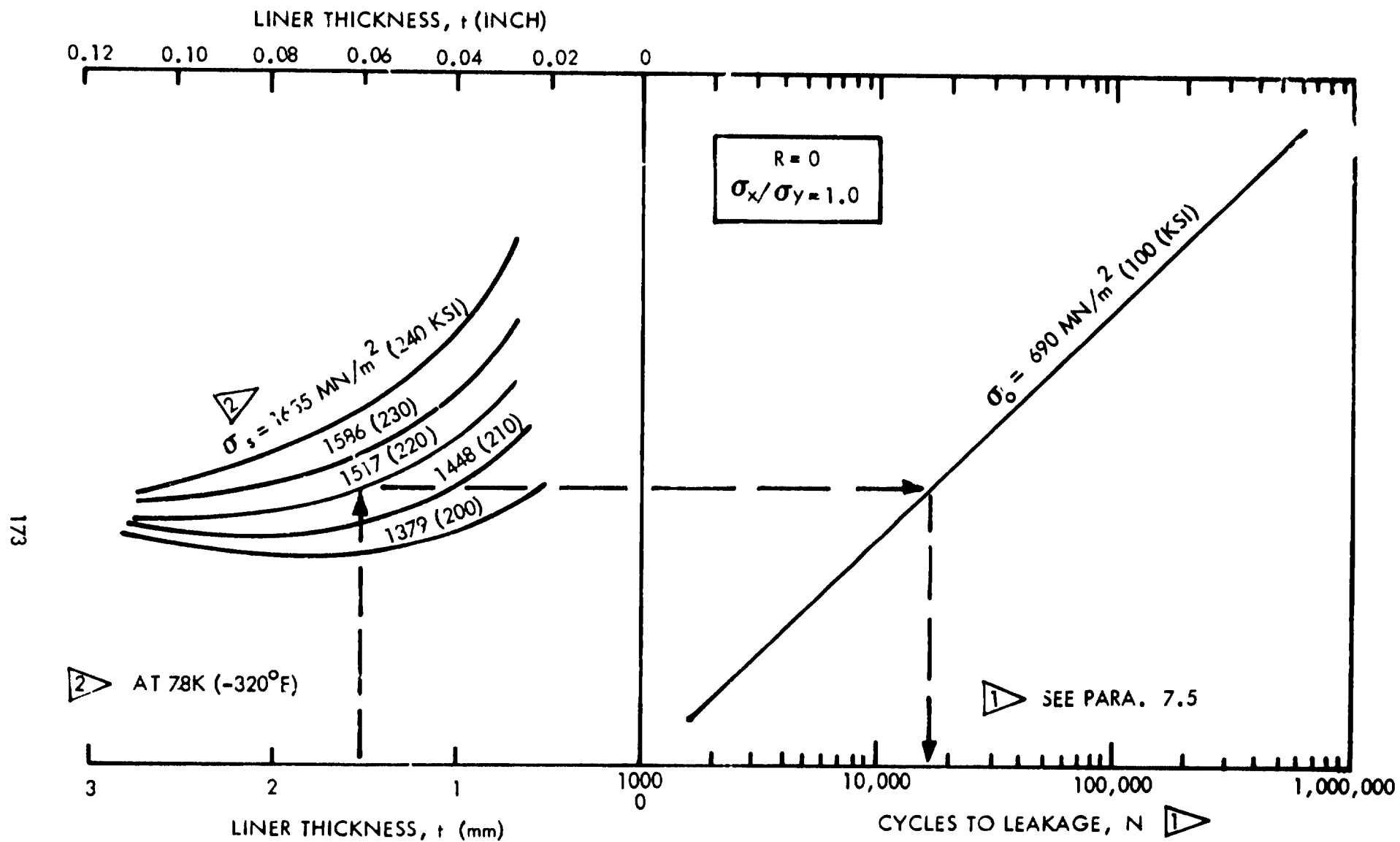


FIGURE 108: SERVICE LIFE FOR CRYOFORMED 301 STAINLESS STEEL LINERS (BM) AT RT - INITIAL FLAW SHAPE OF 0.1

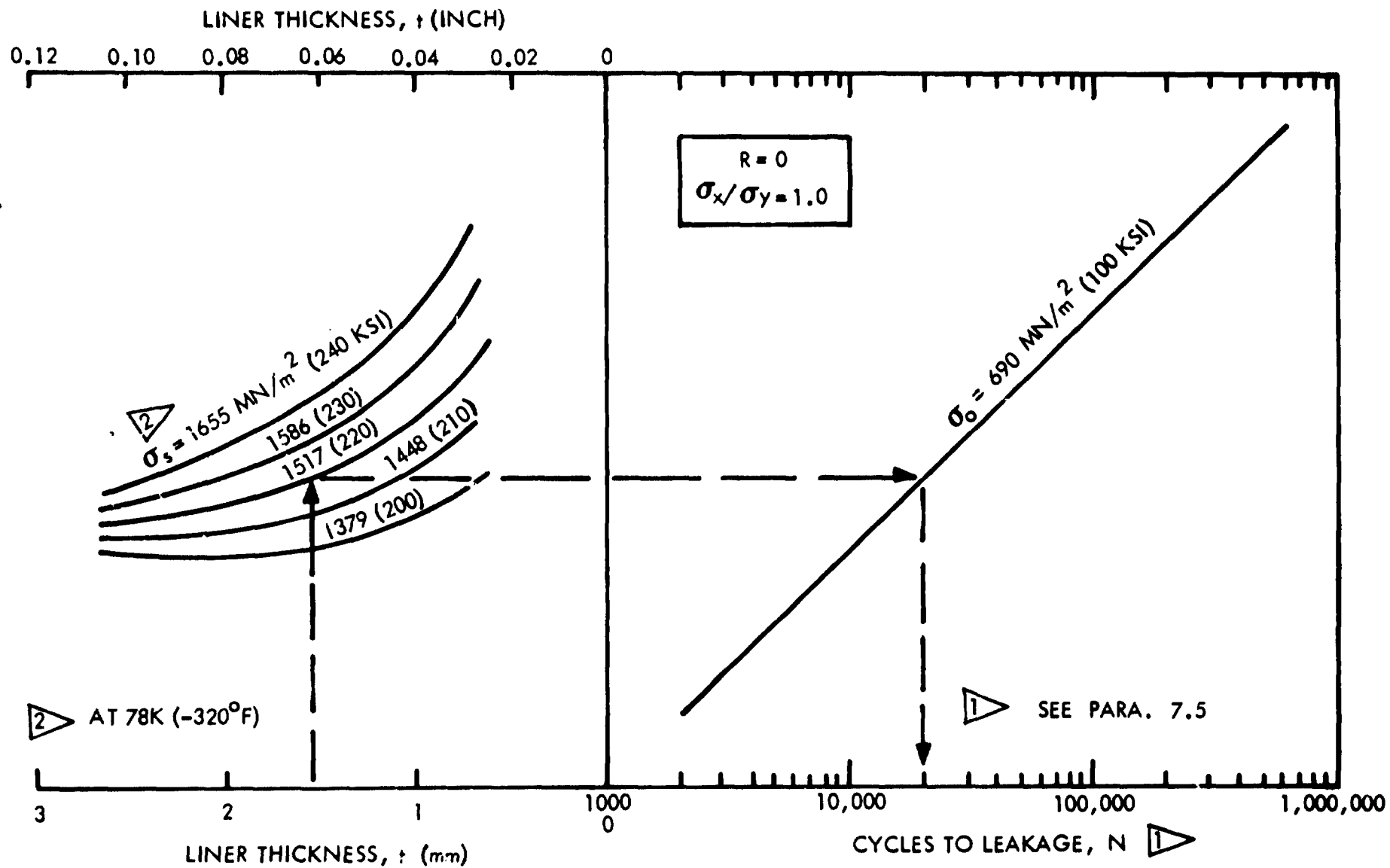


FIGURE 109: SERVICE LIFE FOR CRYOFORMED 301 STAINLESS STEEL LINERS (BM) AT RT - INITIAL FLAW SHAPE OF 0.3

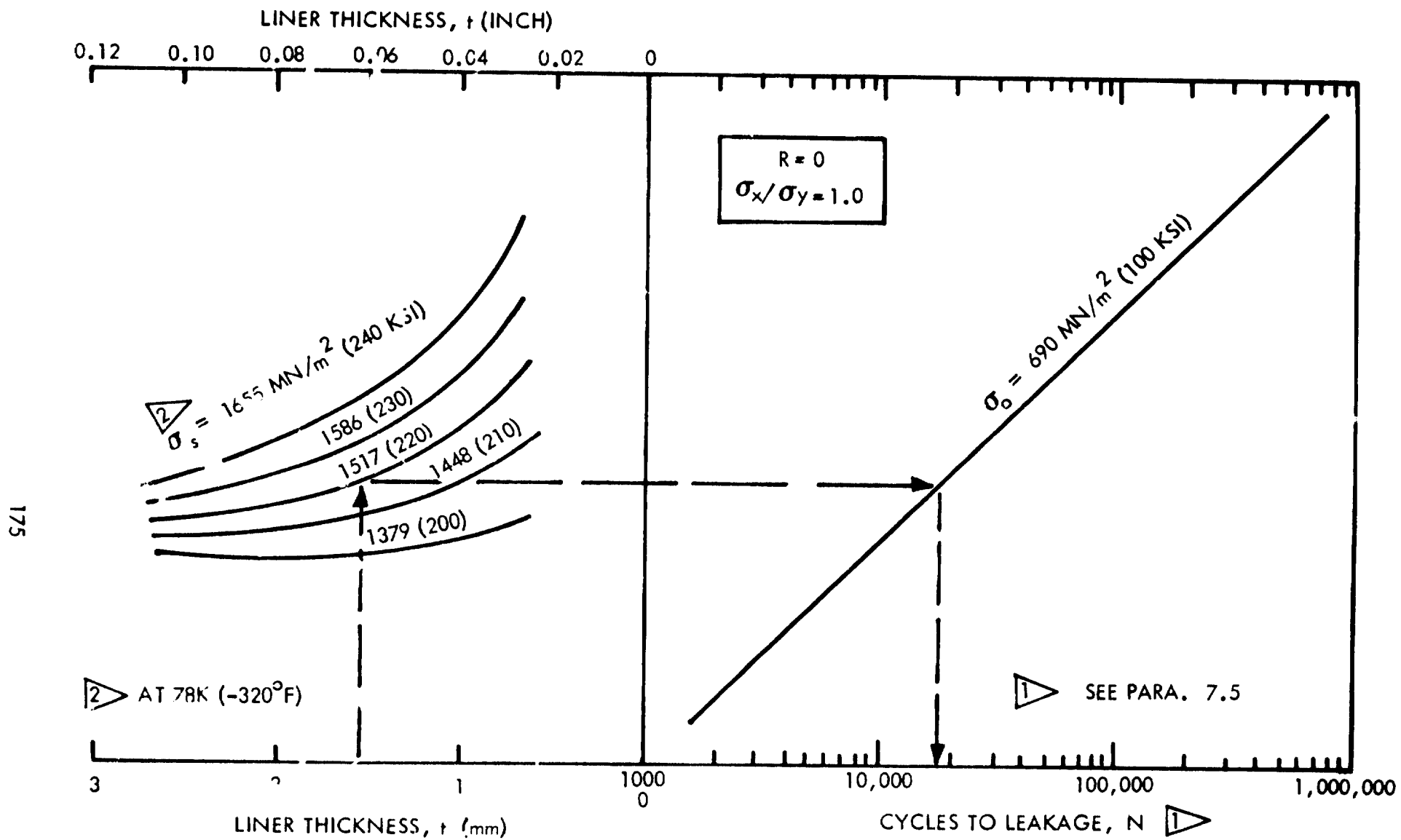


FIGURE 110: SERVICE LIFE FOR CRYOFORMED 301 STAINLESS STEEL LINERS (BM) AT RT - INITIAL FLAW SHAPE OF 0.5

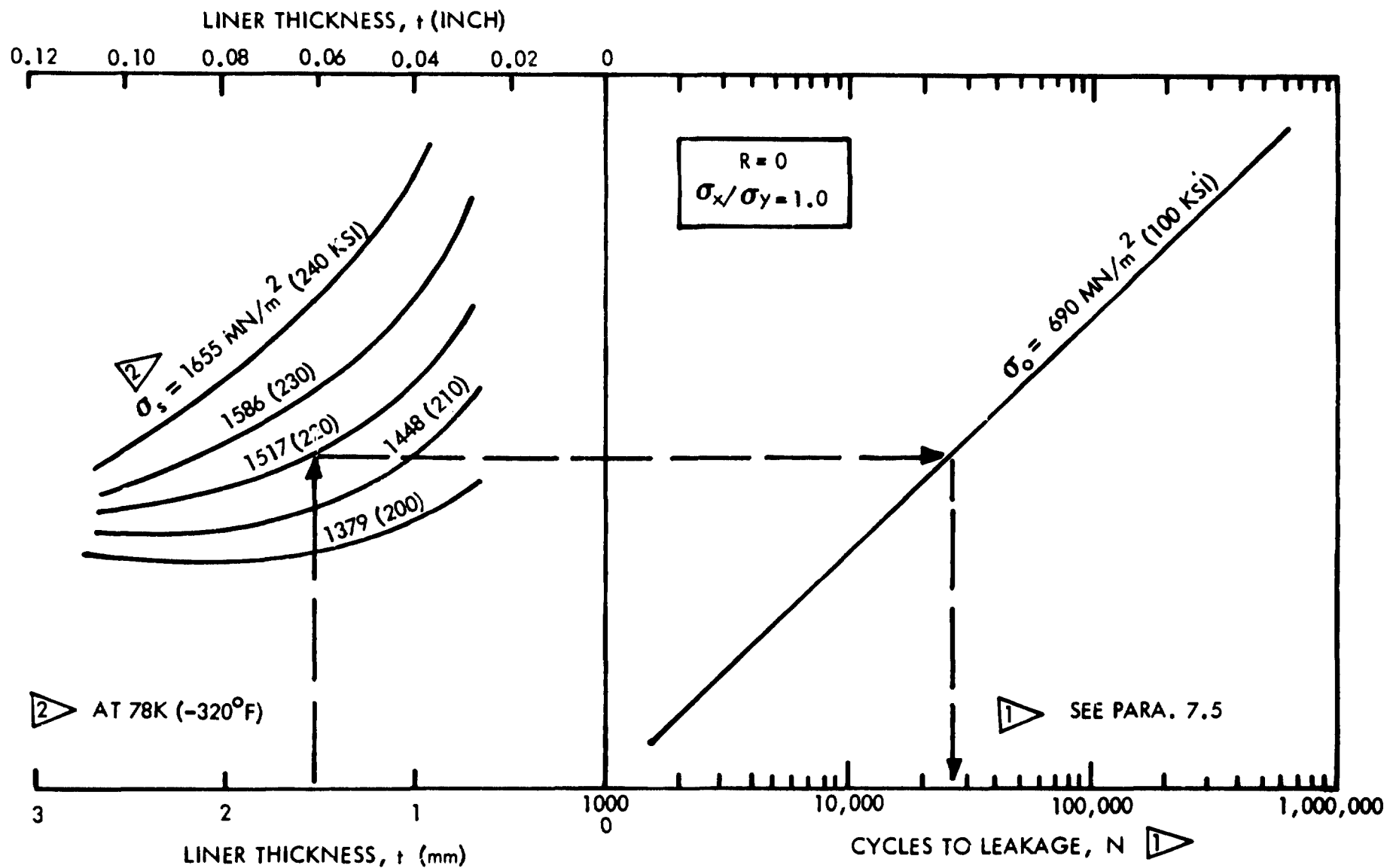


FIGURE 111: SERVICE LIFE FOR CRYOFORMED 301 STAINLESS STEEL LINERS (WM) AT RT - INITIAL FLAW SHAPE OF 0.1

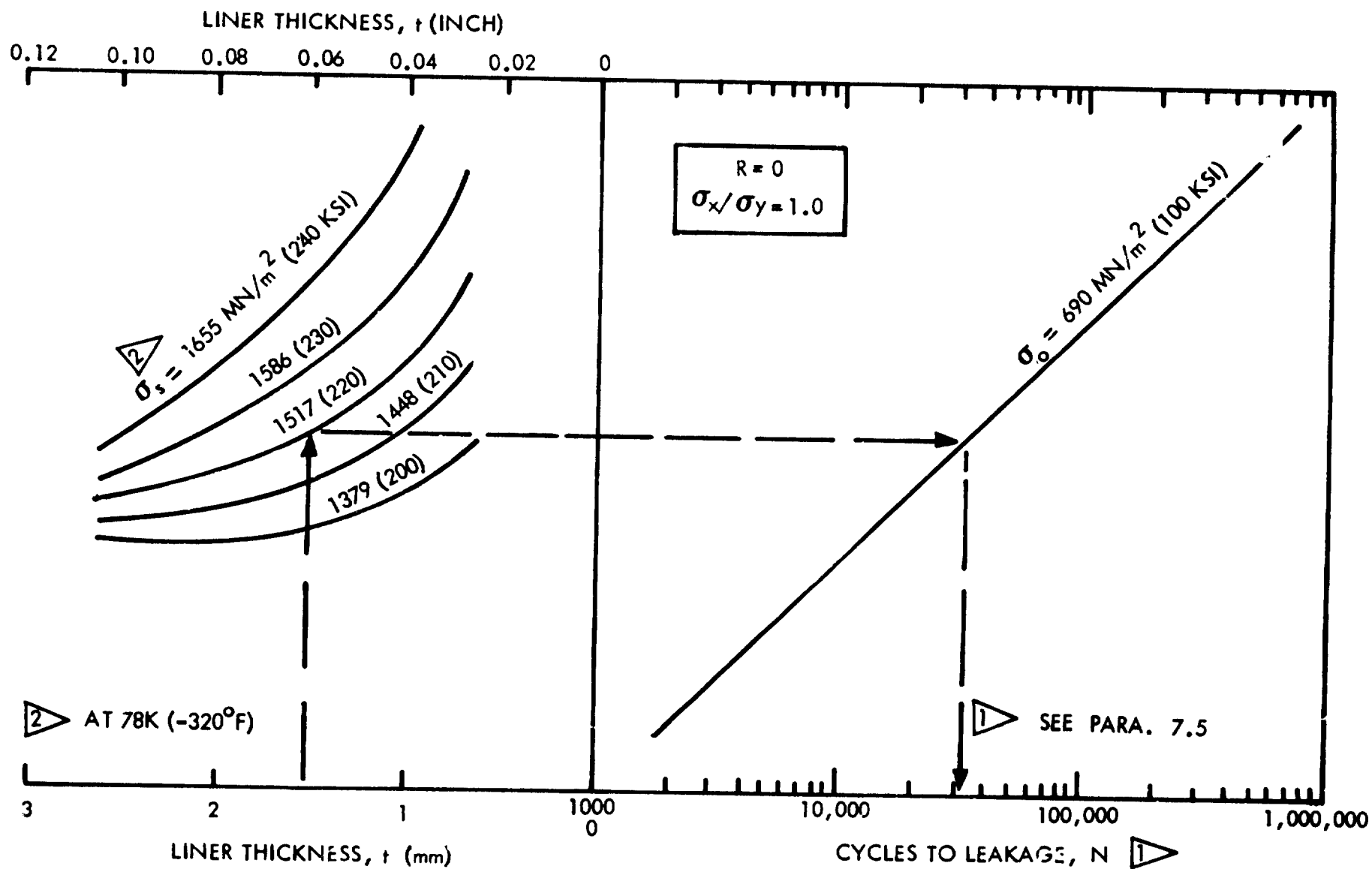


FIGURE 112: SERVICE LIFE FOR CRYOFORMED 301 STAINLESS STEEL LINERS (WM) AT RT - INITIAL FLAW SHAPE OF 0.3

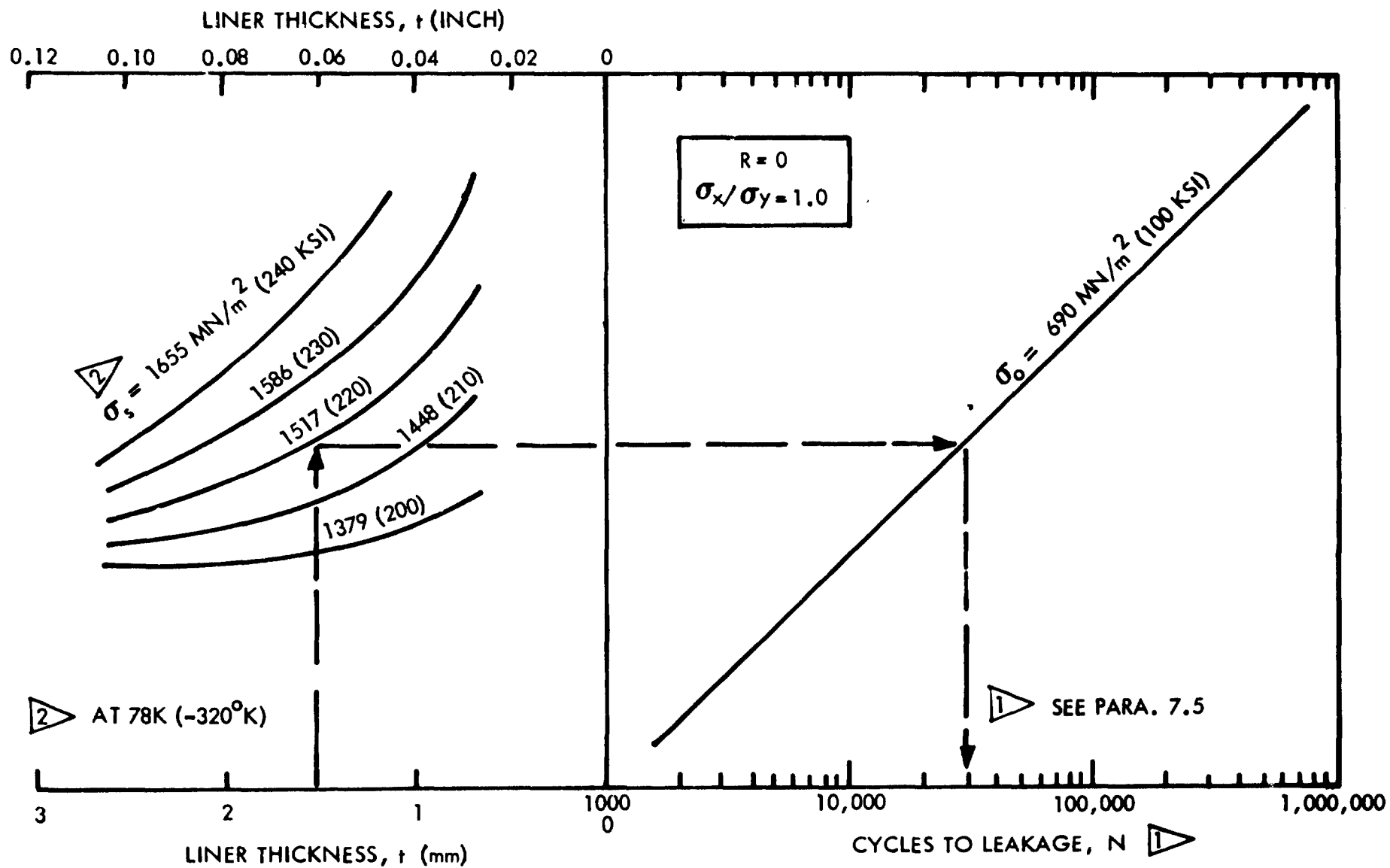


FIGURE 113: SERVICE LIFE FOR CRYOFORMED 301 STAINLESS STEEL LINERS (WM) AT RT - INITIAL FLAW SHAPE OF 0.5

TABLE 1: UNIAXIAL STATIC FRACTURE TEST MATRIX

MATERIAL		THICK- NESS, t mm (INCH)	TEMPERATURE, T					
			295K (72°F)			78K (-320°F)		
			FLAW SHAPE, a/2c			FLAW SHAPE, a/2c		
			0.1	0.2	0.4	0.1	0.2	0.4
2219-T62 ALUMINUM	BM	2.29 (0.090)	X	X	X	X	X	X
		4.57 (0.180)	X	X	X		X	
		7.62 (0.300)	X	X	X			
	WM	2.29 (0.090)	X	X	X		X	
		4.57 (0.180)		X			X	
		7.62 (0.300)		X				
INCONEL X750 S.A	BM	1.02 (0.040)	X	X	X	X	X	X
		3.30 (0.130)		X			X	
	WM	1.02 (0.040)	X	X	X		X	
		3.30 (0.130)		X			X	
CRYOSTRETCHED 301 STAINLESS STEEL	BM	0.71 (0.028)		X			X	
		2.54 (0.100)		X			X	
	WM	0.71 (0.028)		X			X	
		2.54 (0.100)		X			X	

TABLE 2: EQUAL BIAXIAL STATIC FRACTURE TEST MATRIX

MATERIAL		THICKNESS, t mm (INCH)	TEMPERATURE, T 295K (72°F)		
			FLAW SHAPE, $a/2c$		
			0.1	0.2	0.4
2219-T62 ALUMINUM	BM	2.29 (0.090)	X	X	X
		4.57 (0.180)	X	X	X
		7.62 (0.300)	X	X	X
INCONEL X750 STA	BM	2.03 (0.080)		X	

TABLE 3: TANK BURST TEST MATRIX

TANK MATERIAL	THICKNESS t mm (INCH)	TANK CONFIG.	MATERIAL CONDITION	TEMPERATURE, T	
				295K (72°F)	78K (-320°F)
				FLAW SHAPE, a/2c	FLAW SHAPE, a/2c
				0.2	0.2
2219-T62 ALUMINUM	2.29 (0.090)	ALL METAL	BM	X	
			WM	X	
		OW	BM	X	X
			WM	X	X
INCONEL X750 STA	1.02 (0.040)	ALL-METAL	BM	X	
			WM	X	
		OW	BM	X	X
			WM	X	X
CRYOFORMED 301 STAINLESS STEEL	0.71 (0.028)	ALL-METAL	BM		X
		OW	BM		X








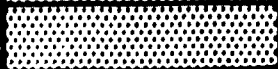
TABLE 4: UNIAXIAL CYCLIC LIFE TEST MATRIX

MATERIAL		THICKNESS, t mm (INCH)	TEMPERATURE, T								
			295K (72°F)								78K (-320°F)
			$\sigma_{\text{MIN}} / \sigma_{\text{MAX}}$ (R) RATIO								R RATIO
			+ 0.5	0	- 0.4	-0.5	-0.8	-1.0	-1.4	-2.0	0
2219-T62 ALUMINUM	BM	2.29 (0.090)	X	X	X	X	X			X	X
		4.57 (0.180)		X	X		X			X	X
		7.62 (0.300)		X				X		X	
	WM	2.29 (0.090)		X							X
		4.57 (0.180)		X							X
		7.62 (0.300)									
INCONEL X750 STA	BM	1.02 (0.040)	X	X		X		X	X	X	X
		3.30 (0.130)		X				X	X	X	X
	WM	1.02 (0.040)		X							X
		3.30 (0.130)		X							X
CRYOSTRETCHED 301 STAINLESS STEEL	BM	0.71 (0.028)		X		X		X			X
		2.54 (0.100)		X		X		X			X
	WM	0.71 (0.028)		X							X
		2.54 (0.100)		X							X

TABLE 5: TANK CYCLIC LIFE TEST MATRIX

TANK MATERIAL	THICK- NESS, t mm (INCH)	TANK CONFIG.	MATERIAL COND.	TEMPERATURE, T									
				295K (72°F)							78K (-320°F)		
				$\sigma_{\text{MIN}} / \sigma_{\text{MAX}}$ (R) RATIO							R RATIO		
				+ 0.2	0	-0.3	-0.4	-0.5	-0.7	-0.8	-0.3	-0.7	-0.9
2219-T62 ALUMINUM	2.29 (0.090)	ALL- METAL	BM		X								
			WM		X								
		OW	BM	X		X	X	X			X		
			WM	X		X	X	X			X		
INCONEL X750 STA	1.02 (0.040)	ALL- METAL	BM		X								
			WM		X								
		OW	BM		X	X			X			X	X
			WM		X	X			X	X		X	X


TABLE 6: SUMMARY OF MECHANICAL PROPERTIES OF THE LINER MATERIALS

MATERIAL		TEMPERATURE, T K (°F)	0.2% OFFSET YIELD STRENGTH, σ_{ys}  MN/m ² (KSI)	ULTIMATE STRENGTH, σ_{ult} MN/m ² (KSI)	% ELONGATION 	ELASTIC MODULUS $\times 10^{-6}$ kN/m ² (PSI)
2219-T62 ALUMINUM	BM	295 (72)	297 (43.1)	431 (62.5)	8.3	70.3 (10.2)
		78 (-320)	361 (52.3)	525 (76.1)	14.3	77.2 (11.2)
	WM	295 (72)	294 (42.4)	422 (61.2)	7.3	76.5 (11.1)
		78 (-320)	355 (51.5)	508 (73.7)	8.0	84.8 (12.3)
INCONEL X750 STA	BM	295 (72)	763 (110.6)	1229 (178.2)	26.6	205.5 (29.8)
		78 (-320)	846 (122.7)	1520 (220.5)	32.9	224.1 (32.5)
	WM	295 (72)	768 (111.4)	1172 (170.0)	14.0	211.0 (30.6)
		78 (-320)	851 (123.4)	1438 (208.5)	19.4	213.8 (31.0)
CRYOFORMED 301 STAINLESS STEEL	BM	295 (72)	1198 (173.7)	1448 (210.0)	13.6	144.1 (20.9)
		78 (-320)	1349 (195.7)	1955 (283.5)	21.2	168.2 (24.4)
	WM	295 (72)		1245 (180.5)		
		78 (-320)		1772 (257.0)		



MEASURED IN 51mm (2.0 INCH) FOR ALUMINUM AND INCONEL AND
12.7mm (0.5 INCH) FOR STAINLESS STEEL.

TABLE 7: MATERIAL / SPECIMEN UTILIZATION

MATERIAL USED TO FABRICATE	MATERIAL	TEST SECTION THICKNESS mm(INCH)	MACHINED FROM THICKNESS mm (INCH)	MATERIAL SPECIFICATION	HEAT NUMBER
UNIAXIAL SPECIMENS	2219-T62 ALUMINUM	2.29 (0.090)	3.18 (0.125)	BMS 7-105C	
		4.57 (0.180)	6.35 (0.250)	MIL-A8920	NOT AVAILABLE
		7.62 (0.300)	12.70 (0.500)	USED ON NAS 3-16770	
	INCONEL X750 STA	1.02 (0.040)	1.02 (0.040)	AMS 5542 REVISION G	HT 76C 7X5
		3.30 (0.130)	3.30 (0.130)		HT 10F 8 X K
	CRYO-STRETCHED 301 SS	0.71 (0.028)	0.71 (0.028)	ARDE SPEC AES 252	76235
		2.54 (0.100)	3.30 (0.130)		
SPHERICAL CAP SPECIMENS	2219-T62 ALUMINUM	2.29 (0.090)	6.35 (0.250)	MIL-A-8920	NOT AVAILABLE
		4.57 (0.180)	12.70 (0.500)	USED ON NAS 3-16770	
		7.62 (0.300)	29.36 (1.156)		
	INCONEL X750 STA	2.03 (0.080)	4.78 (0.188)	AMS 5542 REVISION G	NOT AVAILABLE
TANKS	CRYO-301 SS	1.02 (0.040)	1.02 (0.040)	ARDE SPEC AES 252	76235






SAME MATERIAL USED TO FABRICATE 2.29mm (0.090 INCH) THICK SPECIMENS REPORTED IN INTERIM REPORT.

TABLE 8: HEAT TREATMENT OF LINER MATERIALS

MATERIAL	PROCEDURE
2219-T62 ALUMINUM	HEATED IN AIR AT 808K (995°F) FOR 4 HOURS AND THEN IMMEDIATELY QUENCHED IN WATER. AGED IN AIR AT RT FOR 96 HOURS AND THEN AGED IN AIR AT 463K (375°F) FOR 36 HOURS.
INCONEL X750 STA	ANNEALED IN A VACUUM AT 1325K (1925°F) FOR 30 MINUTES FOLLOWED BY A RAPID QUENCH BY FLOODING THE FURNACE WITH NITROGEN GAS. HEATED IN AIR AT 978K (1300°F) FOR 20 HOURS AND AIR COOLED
CRYOFORMED 301 STAINLESS STEEL	HEATED IN AIR AT 1340K (1950°F) FOR 15 MINUTES AND THEN IMMEDIATELY QUENCHED IN WATER.

TABLE 9: MECHANICAL PROPERTIES OF 7.62mm (0.300 INCH) 2219-T62 ALUMINUM AT 295K (72°F)

MATERIAL	SPECIMEN NUMBER	THICKNESS, t mm (INCH)	WIDTH, w mm (INCH)	YIELD STRENGTH, σ_{ys}   MN/m ² (KSI)	ULTIMATE STRENGTH, σ_{ult} MN/m ² (KSI)	% ELONGATION 	ELASTIC MODULUS, E $\times 10^6$ kN/m ² (PSI)
BASE METAL	3A-1	3.23 (0.127)	12.73 (0.501)	301 (43.6)	430 (62.3)	7.6	69.6 (10.1)
	3A-2	3.23 (0.127)	12.75 (0.502)	300 (43.5)	432 (62.6)	8.5	64.8 (9.4)
WELD METAL	3AW-1	3.20 (0.126)	12.80 (0.504)	301 (43.7)	430 (62.4)	6.3	74.5 (10.8)
	3AW-2	3.23 (0.127)	12.75 (0.502)	298 (43.2)	428 (62.0)	8.0	71.7 (10.4)








0.2% OFFSET




MEASURED IN 51mm (2.0 INCH)

Table 10: UNIAXIAL STATIC FRACTURE TESTS OF 2219-T62 ALUMINUM

SPECIMEN NUMBER	THICKNESS, t mm (Inch)	WIDTH, W mm (Inch)	TEST PARAMETERS AT:	CRACK DEPTH, a mm (Inch)	CRACK LENGTH, $2c$ mm (Inch)	CRACK SHAPE $a/2c$	STRESS, σ MN/m^2 (KSI)	TEMPERATURE, T K ($^{\circ}\text{F}$)	ENVIRONMENT	REMARKS:
1AX -2	2.39 (0.094)	50.8 (2.00)	FAILURE	0.787 (0.031)	6.73 (0.265)	0.117	332 (48.2)	295 (72)	AIR	FAIL MODE
1AM -2	2.29 (0.090)	63.5 (2.50)	FAILURE	1.676 (0.066)	11.94 (0.470)	0.140	274 (39.8)			FAIL MODE
1AM -3	2.31 (0.091)	63.5 (2.50)	LEAKAGE	2.286 (0.090)	5.69 (0.224)	0.402	225 (32.6)			LEAK MODE 
1AW -27	2.34 (0.092)	63.5 (2.50)	LEAKAGE	1.905 (0.075)	9.83 (0.387)	0.194	281 (40.8)			LEAK MODE 
1AW -28	2.34 (0.092)	63.5 (2.50)	FAILURE	1.448 (0.057)	7.47 (0.294)	0.194	315 (45.7)			FAIL MODE 
2ATC -8	4.62 (0.182)	63.5 (2.50)	FAILURE	1.803 (0.071)	8.38 (0.330)	0.215	346 (50.2)			FAIL MODE
2AAX -3	4.55 (0.179)	88.9 (3.50)	FAILURE	3.302 (0.130)	8.66 (0.341)	0.382	310 (44.9)			FAIL MODE
2AAX -4	4.60 (0.181)	88.9 (3.50)	FAILURE	2.210 (0.087)	5.84 (0.230)	0.378	341 (49.5)			FAIL MODE
2AM -5	4.57 (0.180)	127.0 (5.00)	FAILURE	1.956 (0.077)	20.57 (0.810)	0.095	307 (44.5)			FAIL MODE
2AM -7	4.60 (0.181)	127.0 (5.00)	FAILURE	1.626 (0.064)	15.80 (0.622)	0.103	323 (46.8)			FAIL MODE
3AX -1	7.77 (0.306)	127.3 (5.01)	FAILURE	2.311 (0.091)	11.68 (0.460)	0.198	341 (49.4)			FAIL MODE
3AX -2	7.75 (0.305)	127.0 (5.00)	FAILURE	2.997 (0.118)	30.73 (1.210)	0.098	306 (44.4)			FAIL MODE
3AX -3	7.82 (0.308)	127.3 (5.01)	FAILURE	4.369 (0.172)	11.43 (0.450)	0.382	325 (47.2)			FAIL MODE
3AX -4	7.75 (0.305)	127.3 (5.01)	FAILURE	4.013 (0.153)	19.86 (0.782)	0.202	309 (44.8)			FAIL MODE
3AX -5	7.70 (0.303)	127.3 (5.01)	FAILURE	5.410 (0.213)	14.07 (0.554)	0.385	308 (44.6)			FAIL MODE
3AX -6	7.82 (0.308)	127.3 (5.01)	FAILURE	2.184 (0.086)	22.35 (0.880)	0.098	321 (46.6)			FAIL MODE
3AWX -1	7.62 (0.300)	127.3 (5.01)	FAILURE	3.632 (0.143)	17.53 (0.690)	0.207	306 (44.4)			FAIL MODE 
3AWX -2	7.75 (0.305)	127.0 (5.00)	FAILURE	2.083 (0.082)	11.25 (0.443)	0.185	346 (50.2)			FAIL MODE 

 FAILURE OCCURRED AT 298 MN/m^2 (43.2 KSI)


 FAILURE OCCURRED AT 278 MN/m^2 (41.6 KSI)

 SPECIMEN FITTED WITH FLAW RESTRAINT PLATES (PARA. 4.1); FLAW IN BASE METAL

 FLAWS LOCATED IN WELD ζ

ORIGINAL PAGE IS
OF POOR QUALITY

Table 11: UNIAXIAL CYLINDER BURST TESTS OF 2219-T62 ALUMINUM

TANK	SPECIMEN NUMBER	LINER THICKNESS, t_L mm (INCH)	FILAMENT THICKNESS, t_{ow} mm (INCH)	LINER DIAMETER, D_L mm (INCH)	TEST PARAMETERS AT	CRACK DEPTH, a mm (INCH)	CRACK LENGTH, $2c$ mm (INCH)	CRACK SHAPE, $a/2c$	TANK PRESSURE, P MN/m ² (PSIG)	FILAMENT STRESS, σ_{ow} MN/m ² (KSI)	LINER HOOP STRESS, σ_L MN/m ² (KSI)	LINER LONG. STRESS $\sigma_L \phi$ MN/m ² (KSI)	TEMPERATURE, T K (°F)	ENVIRONMENT	REMARKS
NON OVERWRAP $\sigma_x/\sigma_y = 0$	AS23 -1	2.54 (0.100)	—	155.1 (6.50)	FAILURE	1.346 (0.053)	6.35 (0.250)	0.212	9.34 (1355)	—	304 (44.1)	0	295 (72)	AIR	FAIL MODE
	AS23 -2	2.54 (0.100)	—	165.1 (6.50)	FAILURE	1.626 (0.064)	7.52 (0.296)	0.216	8.92 (1293)	—	290 (42.0)	0			FAIL MODE
	CYL -1	2.49 (0.098)	—	165.1 (6.50)	FAILURE	1.422 (0.056)	7.57 (0.298)	0.188	9.17 (1330)	—	304 (44.1)	0			FAIL MODE 
	CYL -2	2.49 (0.098)	—	165.1 (6.50)	FAILURE	1.219 (0.048)	6.35 (0.250)	0.192	9.62 (1395)	—	319 (46.3)	0			FAIL MODE

 CRACK LOCATED IN WELD ϕ

Table 12: EQUAL BIAxIAL STATIC FRACTURE TESTS OF 2219-T62 ALUMINUM SPHERICAL CAP SPECIMENS

SPECIMEN NUMBER	THICKNESS, t mm (INCH)	RADIUS, R mm (INCH)	TEST PARAMETERS AT	CRACK DEPTH, a mm (INCH)	CRACK LENGTH, $2c$ mm (INCH)	CRACK SHAPE $a/2c$	PRESSURE, P MN/m ² (PSI)	STRESS, σ MN/m ² (KSI)	TEMPERATURE, T K (°F)	ENVIRONMENT	REMARKS
1AB-2	2.39 (0.094)	179.1 (7.05)	FAILURE	1.473 (0.058)	7.95 (0.313)	0.185	9.65 (1400)	362 (52.5)	295 (72)	AIR	FAIL MODE
1AB-3	2.34 (0.092)	179.1 (7.05)	FAILURE	1.118 (0.044)	6.10 (0.240)	0.183	9.92 (1440)	381 (55.2)			FAIL MODE
1AB-4	2.44 (0.096)	179.1 (7.05)	FAILURE	0.889 (0.035)	10.16 (0.400)	0.088	10.17 (1475)	375 (54.4)			FAIL MODE
1AB-5	2.41 (0.095)	179.1 (7.05)	LEAKAGE	2.311 (0.091)	10.16 (0.400)	0.228	8.48 (1230)	314 (45.6)			LEAK MODE
1AB-6	2.26 (0.089)	179.1 (7.05)	FAILURE	2.083 (0.082)	17.91 (0.705)	0.116	7.24 (1050)	288 (41.8)			FAIL MODE
1AB-7	2.21 (0.087)	179.1 (7.05)	FAILURE	1.118 (0.044)	2.97 (0.117)	0.376	11.17 (1620)	453 (65.7)			FAIL MODE
1AB-8	2.26 (0.089)	179.1 (7.05)	FAILURE	1.930 (0.076)	5.13 (0.202)	0.376	931 (1350)	368 (53.4)			FAIL MODE
1AB-9	2.24 (0.088)	179.1 (7.05)	FAILURE	1.422 (0.056)	3.76 (0.148)	0.378	9.89 (1435)	395 (57.3)			FAIL MODE
2AB-1	4.83 (0.190)	180.3 (7.10)	FAILURE	2.286 (0.090)	22.00 (0.866)	0.104	15.99 (2320)	299 (43.3)			FAIL MODE
2AB-2	4.90 (0.193)	180.3 (7.10)	FAILURE	2.184 (0.086)	11.46 (0.451)	0.191	17.75 (2575)	326 (47.3)			FAIL MODE
2AB-3	4.62 (0.182)	180.1 (7.09)	FAILURE	1.245 (0.049)	7.62 (0.300)	0.163	21.65 (3140)	424 (61.5)			FAIL MODE
2AB-4	4.62 (0.182)	180.1 (7.09)	LEAKAGE	3.200 (0.126)	16.38 (0.645)	0.195	14.99 (2175)	2.92 (42.3)			LEAK MODE
2AB-5	4.70 (0.185)	180.1 (7.09)	LEAKAGE	3.124 (0.123)	17.40 (0.685)	0.180	15.65 (2270)	300 (43.5)			LEAK MODE
2AB-6	4.88 (0.192)	180.3 (7.10)	LEAKAGE	2.159 (0.085)	5.41 (0.213)	0.399	19.31 (2800)	356 (51.7)			LEAK MODE
2AB-7	4.95 (0.195)	180.3 (7.10)	LEAKAGE	3.480 (0.137)	8.89 (0.350)	0.391	18.96 (2750)	345 (50.0)			LEAK MODE
2AB-8	4.70 (0.185)	180.1 (7.09)	FAILURE	1.041 (0.041)	11.28 (0.444)	0.092	21.37 (3100)	410 (59.4)			FAIL MODE
2AB-9	4.75 (0.187)	180.1 (7.09)	LEAKAGE	1.727 (0.068)	8.31 (0.327)	0.208	19.82 (2875)	376 (54.5)			LEAK MODE
3AB-1	7.77 (0.306)	257.8 (10.15)	FAILURE	3.251 (0.128)	32.13 (1.265)	0.101	17.10 (2480)	285 (41.3)			FAIL MODE
3AB-2	7.85 (0.307)	257.8 (10.15)	FAILURE	3.937 (0.155)	19.74 (0.785)	0.197	17.38 (2520)	285 (41.4)			FAIL MODE

1 ACTUAL FAILURE STRESSES ARE BELIEVED LOWER THAN CALCULATED VALUES WHICH WERE BASED ON $\sigma = pr/2t$ WHERE r IS THE UNSTRAINED RADIUS. WHEN EXCESSIVE PLASTIC DEFORMATION TAKES PLACE IN THE CAP THE LOCAL APEX RADIUS OF CURVATURE DECREASES SIGNIFICANTLY THEREBY RESULTING IN A LOWER STRESS THAN CALCULATED

2 FLAW LOCATED ON INSIDE OF SPECIMEN

Table 12: Continued

SPECIMEN NUMBER	THICKNESS, t mm (INCH)	RADIUS, R mm (INCH)	TEST PARAMETERS AT	CRACK DEPTH, a mm (INCH)	CRACK LENGTH, $2c$ mm (INCH)	CRACK SHAPE $a/2c$	PRESSURE, P MN/m ² (PSI)	STRESS, σ MN/m ² (KSI)	TEMPERATURE, T K (°F)	ENVIRONMENT	REMARKS
3AB -3	7.72 (0.304)	257.8 (10.15)	FAILURE	2.692 (0.106)	12.70 (0.500)	0.212	19.65 (2850)	328 (47.6)	295 (72)	AIR	FAIL MODE
3AB -4	7.72 (0.304)	257.8 (10.15)	FAILURE	5.918 (0.233)	15.32 (0.603)	0.386	17.03 (2470)	284 (41.2)			FAIL MODE
3AB -5	7.82 (0.308)	257.8 (10.15)	FAILURE	3.251 (0.128)	16.13 (0.635)	0.202	19.03 (2760)	314 (45.5)			FAIL MODE
3AB -6	7.75 (0.305)	257.8 (10.15)	FAILURE	1.981 (0.078)	9.40 (0.370)	0.211	22.20 (3220)	370 (53.6)			FAIL MODE
3AB -7	7.72 (0.304)	257.8 (10.15)	FAILURE	2.261 (0.089)	19.30 (0.760)	0.117	19.58 (2840)	327 (47.4)			FAIL MODE
3AB -8	7.77 (0.306)	257.8 (10.15)	FAILURE	3.404 (0.134)	8.64 (0.340)	0.394	20.20 (2930)	335 (48.6)			FAIL MODE
3AB -9	7.82 (0.308)	257.8 (10.15)	FAILURE	2.261 (0.089)	11.68 (0.460)	0.193	20.82 (3020)	343 (49.8)			FAIL MODE

Table 13: EQUAL BIAXIAL STATIC FRACTURE TESTS OF INCONEL X750 STA
SPHERICAL CAP SPECIMENS

SPECIMEN NUMBER	THICKNESS, t mm (INCH)	RADIUS, R mm (INCH)	TEST PARAMETERS AT:	CRACK DEPTH, a mm (INCH)	CRACK LENGTH, $2c$ mm (INCH)	CRACK SHAPE $a/2c$	PRESSURE, P MN/m ² (PSI)	STRESS, σ MN/m ² (KSI)	TEMPERATURE, T K (°F)	ENVIRONMENT	REMARKS
288 -1	2.18 (0.086)	178.8 (7.04)	LEAKAGE	1.600 (0.063)	8.00 (0.315)	0.200	20.34 (2950)	838 (121.5)	295 (72)	AIR	LEAK MODE
288 -2	2.08 (0.082)	178.8 (7.04)	LEAKAGE	1.245 (0.049)	5.84 (0.230)	0.209	20.13 (2920)	864 (125.3)			LEAK MODE
288 -3	1.96 (0.077)	178.8 (7.04)	LEAKAGE	1.118 (0.044)	4.70 (0.185)	0.238	22.06 (3200)	1009 (146.3)			LEAK MODE

Table 14: BURST TESTS OF TANKS WITH CRYO FORMED 301 STAINLESS STEEL LINERS AT 78K (-320°F)

TANK	SPECIMEN NUMBER	LINER THICKNESS, t_L mm (INCH)	FILAMENT THICKNESS, t_{ow} mm (INCH)	LINER DIAMETER, D_L mm (INCH)	TEST PARAMETERS AT	CRACK DEPTH, a mm (INCH)	CRACK LENGTH, $2c$ mm (INCH)	CRACK SHAPE, $a/2c$	TANK PRESSURE, p MN/m^2 (PSIG)	FILAMENT STRESS, σ_{ow} MN/m^2 (KSI)	LINER HOOP STRESS, σ_L MN/m^2 (KSI)	LINER LONG. STRESS $\sigma_L \phi$ MN/m^2 (KSI)	TEMPERATURE, T K (°F)	ENVIRONMENT	REMARKS
NON OW	3	0.889 (0.035)	-	153.4 (6.04)	LEAKAGE	0.305 (0.012)	1.83 (0.072)	0.167	13.45 (1950)	-	1160 (168.3)	580 (84.1)	78 (-320)	LN ₂	LEAK MODE
	23	0.864 (0.034)	-	155.4 (6.12)	FAILURE	0.203 (0.008)	1.65 (0.065)	0.123	16.06 (2330)	-	1446 (209.7)	723 (104.9)			FAIL MODE
OW	16	0.914 (0.036)	0.813 (0.032)	149.6 (5.89)	FAILURE	0.533 (0.021)	1.91 (0.075)	0.280	25.86 (3750)	1875 (272.0)	855 (124.0)	1020 (148.0)			FAIL MODE
	10	0.889 (0.035)	0.813 (0.032)	150.4 (5.92)	FAILURE	0.356 (0.014)	2.49 (0.098)	0.143	31.72 (4600)	2296 (333.0)	1131 (164.0)	1303 (189.0)			TANK DID NOT FAIL AT FLAW
	26	0.864 (0.034)	0.813 (0.032)	150.4 (5.92)	FAILURE	0.229 (0.009)	1.35 (0.053)	0.170	30.20 (4380)	2324 (337.0)	1124 (163.0)	127.6 (185.0)			TANK DID NOT FAIL AT FLAW

Table 15: UNIAXIAL CYCLIC TESTS OF 2.29 mm (0.090 INCH) 2219-T62 ALUMINUM

SPECIMEN NUMBER	THICKNESS, t mm (Inch)	WIDTH, W mm (Inch)	TEST PARAMETERS DURING		CRACK DEPTH, a mm (Inch)	CRACK LENGTH, $2c$ mm (Inch)	CRACK SHAPE $a/2c$	Max STRESS, σ_{Max} MIN/m ² (Ksi)	STRESS RATIO, $\sigma_{Min} / \sigma_{Max}$	TEMPERATURE, T K (°F)	ENVIRONMENT	REMARKS
IATC -3	2.29 (0.090)	45.7 (1.80)	SIZING	START	1.041 (0.041)	4.32 (0.170)	0.241	332		295 (72)	AIR	246 Cycles to Breakthrough
				STOP	1.092 (0.043)	4.32 (0.170)	0.253	(48.2)				
			CYCLING	START	1.092 (0.043)	4.32 (0.170)	0.253	249	-0.8			
				STOP	2.286 (0.090)	6.17 (0.243)	0.370	(36.1)				
IATC -4	2.31 (0.091)	45.7 (1.80)	SIZING	START	0.838 (0.033)	4.27 (0.168)	0.196	332		295 (72)	AIR	2,943 Cycles to Breakthrough
				STOP	0.991 (0.039)	4.27 (0.168)	0.232	(48.2)				
			CYCLING	START	0.991 (0.039)	4.27 (0.168)	0.232	249	0			
				STOP	2.311 (0.091)	6.76 (0.266)	0.365	(36.1)				
IATC -5	2.31 (0.091)	45.7 (1.80)	SIZING	START	0.940 (0.037)	4.34 (0.171)	0.216	332		295 (72)	AIR	1,213 Cycles to Breakthrough
				STOP	0.965 (0.038)	4.34 (0.171)	0.222	(48.2)				
			CYCLING	START	0.965 (0.038)	4.34 (0.171)	0.222	249	-0.4			
				STOP	2.311 (0.091)	7.24 (0.285)	0.319	(36.1)				
IATC -6	2.29 (0.090)	45.7 (1.80)	SIZING	START	0.940 (0.037)	4.98 (0.196)	0.189	332		295 (72)	AIR	13,416 Cycles to Breakthrough
				STOP	0.991 (0.039)	4.98 (0.196)	0.199	(48.2)				
			CYCLING	START	0.991 (0.039)	4.98 (0.196)	0.199	249	+0.5			
				STOP	2.286 (0.090)	6.96 (0.274)	0.328	(36.1)				
IATC -7	2.29 (0.090)	45.7 (1.80)	SIZING	START	0.965 (0.038)	4.42 (0.174)	0.218	332		295 (72)	AIR	461 Cycles to Breakthrough
				STOP	1.016 (0.040)	4.42 (0.174)	0.230	(48.2)				
			CYCLING	START	1.016 (0.040)	4.42 (0.174)	0.230	249	-0.8			
				STOP	2.286 (0.090)	6.86 (0.270)	0.333	(36.1)				

Table 15: Continued

SPECIMEN NUMBER	THICKNESS, t mm (inch)	WIDTH, W mm (inch)	TEST PARAMETERS DURING		CRACK DEPTH, a mm (inch)	CRACK LENGTH, 2c mm (inch)	CRACK SHAPE a/2c	Max STRESS, σ_{Max} MN/m ² (Ksi)	STRESS RATIO, $\sigma_{Min}/\sigma_{Max}$	TEMPERATURE, T K (°F)	ENVIRONMENT	REMARKS
IATC -8	2.29 (0.090)	45.7 (1.80)	SIZING	START	0.914 (0.036)	4.42 (0.174)	0.207	332		295 (72)	AIR	1,347 Cycles to Breakthrough
				STOP	0.965 (0.038)	4.42 (0.174)	0.218	(48.2)				
			CYCLING	START	0.965 (0.038)	4.42 (0.174)	0.218	249	-0.4			
				STOP	2.286 (0.090)	6.35 (0.250)	0.360	(36.1)				
IATC -9	2.31 (0.091)	45.7 (1.80)	SIZING	START	0.889 (0.035)	4.50 (0.177)	0.198	332				15,577 Cycles to Breakthrough
				STOP	0.889 (0.035)	4.50 (0.177)	0.198	(48.2)				
			CYCLING	START	0.889 (0.035)	4.50 (0.177)	0.198	249	+0.5			
				STOP	2.311 (0.091)	7.06 (0.278)	0.327	(36.1)				
IATC -10	2.31 (0.091)	45.7 (1.80)	SIZING	START	0.838 (0.033)	4.37 (0.172)	0.192	332				1,234 Cycles to Breakthrough
				STOP	0.889 (0.035)	4.37 (0.172)	0.203	(48.2)				
			CYCLING	START	0.889 (0.035)	4.37 (0.172)	0.203	249	-0.5			
				STOP	2.311 (0.091)	7.01 (0.276)	0.330	(36.1)				
IATC -11	2.29 (0.090)	45.7 (1.80)	SIZING	START	0.940 (0.037)	4.39 (0.173)	0.214	332				5,965 Cycles to Breakthrough
				STOP	0.991 (0.039)	4.39 (0.173)	0.225	(48.2)				
			CYCLING	START	0.991 (0.039)	4.39 (0.173)	0.225	166	-0.8			
				STOP	2.286 (0.090)	7.01 (0.276)	0.326	(24.1)				
IATC -12	2.31 (0.091)	45.7 (1.80)	SIZING	START	0.965 (0.038)	4.37 (0.172)	0.221	332				4,898 Cycles to Breakthrough
				STOP	1.041 (0.041)	4.37 (0.172)	0.238	(48.2)				
			CYCLING	START	1.041 (0.041)	4.37 (0.172)	0.238	166	-0.8			
				STOP	2.311 (0.091)	6.30 (0.248)	0.367	(24.1)				

Table 15: Continued

SPECIMEN NUMBER	THICKNESS, t mm (Inch)	WIDTH, w mm (Inch)	TEST PARAMETERS DURING:		CRACK DEPTH, a mm (Inch)	CRACK LENGTH, $2c$ mm (Inch)	CRACK SHAPE $a/2c$	Max STRESS, σ_{Max} MN/m ² (Ksi)	STRESS RATIO, $\sigma_{Min}/\sigma_{Max}$	TEMPERATURE, T K (°F)	ENVIRONMENT	REMARKS
IATC -13	2.39 (0.094)	45.7 (1.80)	SIZING	START	0.965 (0.038)	4.39 (0.173)	0.220	332		295 (72)	AIR	22,360 Cycles to Breakthrough
				STOP	1.016 (0.040)	4.39 (0.173)	0.231	(48.2)				
			CYCLING	START	1.016 (0.040)	4.39 (0.173)	0.231	124	-0.8			
				STOP	2.388 (0.094)	6.68 (0.263)	0.357	(18.0)				
IATC -14	2.34 (0.092)	45.7 (1.80)	SIZING	START	0.940 (0.037)	4.39 (0.173)	0.214	332				6,450 Cycles to Breakthrough
				STOP	0.991 (0.039)	4.39 (0.173)	0.225	(48.2)				
			CYCLING	START	0.991 (0.039)	4.39 (0.173)	0.225	124	-2.0			
				STOP	2.337 (0.092)	7.29 (0.287)	0.321	(18.0)				
IATC -15	2.29 (0.090)	45.7 (1.80)	SIZING	START	1.118 (0.044)	4.52 (0.178)	0.247	332				9,451 Cycles to Breakthrough
				STOP	1.143 (0.045)	4.52 (0.178)	0.253	(48.2)				
			CYCLING	START	1.143 (0.045)	4.52 (0.178)	0.253	166	0			
				STOP	2.286 (0.090)	6.35 (0.250)	0.360	(24.1)				
IATC -16	2.31 (0.091)	45.7 (1.80)	SIZING	START	0.838 (0.033)	4.45 (0.175)	0.189	332		295 (72)	AIR	Test Machine Malfunction at 29,982 Cycles
				STOP	0.864 (0.034)	4.45 (0.175)	0.194	(48.2)				
			CYCLING	START	0.864 (0.034)	4.45 (0.175)	0.194	166	+0.5			
				STOP	1.575 (0.062)	5.03 (0.198)	0.313	(24.1)				
IAX -1	2.44 (0.096)	50.8 (2.00)	SIZING	START	1.092 (0.043)	3.71 (0.146)	0.295	332				1,924 Cycles to Breakthrough
				STOP	1.092 (0.043)	3.71 (0.146)	0.295	(48.2)				
			CYCLING	START	1.092 (0.043)	3.71 (0.146)	0.295	166	-2.0			
				STOP	2.438 (0.096)	6.73 (0.265)	0.362	(24.1)				

Table 15: Continued

SPECIMEN NUMBER	THICKNESS, t mm (Inch)	WIDTH, w mm (Inch)	TEST PARAMETERS DURING		CRACK DEPTH, a mm (Inch)	CRACK LENGTH, $2c$ mm (Inch)	CRACK SHAPE $a/2c$	Max STRESS, σ_{Max} MN/m ² (Ksi)	STRESS RATIO, $\sigma_{Min}/\sigma_{Max}$	TEMPERATURE, T K (°F)	ENVIRONMENT	REMARKS
IAX -3	2.36 (0.093)	50.8 (2.00)	SIZING	START	0.711 (0.028)	7.77 (0.306)	0.092	332 (48.2)		295 (72)	AIR	Test Machine Malfunction; Overloaded to 47.2 ksi Re- peatedly. 2,192 Cycles to Breakthrough.
				STOP	0.838 (0.033)	7.77 (0.306)	0.108					
			CYCLING	START	0.838 (0.033)	7.77 (0.306)	0.108	249 (36.1)	0			
				STOP	2.362 (0.093)	8.94 (0.352)	0.264					
IAX -4	2.39 (0.094)	50.8 (2.00)	SIZING	START	0.660 (0.026)	8.00 (0.315)	0.083	332 (48.2)				295 Cycles to Breakthrough
				STOP	0.914 (0.036)	8.00 (0.315)	0.114					
			CYCLING	START	0.914 (0.036)	8.00 (0.315)	0.114	249 (36.1)	-0.8			
				STOP	2.388 (0.094)	10.03 (0.395)	0.238					
IAX -5	2.34 (0.092)	50.8 (2.00)	SIZING	START	0.711 (0.028)	8.03 (0.316)	0.089	332 (48.2)				301 Cycles to Breakthrough
				STOP	0.940 (0.037)	8.03 (0.316)	0.117					
			CYCLING	START	0.940 (0.037)	8.03 (0.316)	0.117	249 (36.1)	-0.8			
				STOP	2.337 (0.092)	10.03 (0.395)	0.233					
IAX -6	2.29 (0.090)	50.8 (2.00)	SIZING	START	1.168 (0.046)	3.38 (0.133)	0.346	332 (48.2)				Test Machine Malfunction at 1,520 Cycles
				STOP	1.194 (0.047)	3.71 (0.146)	0.322					
			CYCLING	START	1.194 (0.047)	3.71 (0.146)	0.322	249 (36.1)	0			
				STOP	1.600 (0.063)	4.62 (0.182)	0.346					
IAX -7	2.39 (0.094)	50.8 (2.00)	SIZING	START	1.219 (0.048)	3.28 (0.129)	0.372	332 (48.2)				2,448 Cycles to Breakthrough
				STOP	1.245 (0.049)	3.35 (0.132)	0.371					
			CYCLING	START	1.245 (0.049)	3.35 (0.132)	0.371	249 (36.1)	0			
				STOP	2.388 (0.094)	5.92 (0.233)	0.403					

Table 15: Continued

SPECIMEN NUMBER	THICKNESS, t mm (inch)	WIDTH, W mm (inch)	TEST PARAMETERS DURING:		CRACK DEPTH, a mm (inch)	CRACK LENGTH, $2c$ mm (inch)	CRACK SHAPE $a/2c$	Max STRESS, σ_{Max} MN/m ² (Ksi)	STRESS RATIO, $\sigma_{Min}/\sigma_{Max}$	TEMPERATURE, T K (°F)	ENVIRONMENT	REMARKS
1AX -8	2.26 (0.089)	50.8 (2.00)	SIZING	START	1.245 (0.049)	3.35 (0.132)	0.371	332 (48.2)		295 (72)	AIR	436 Cycles to Breakthrough
				STOP	1.245 (0.049)	3.35 (0.132)	0.371					
			CYCLING	START	1.245 (0.049)	3.35 (0.132)	0.371	249 (36.1)	-0.8			
				STOP	2.261 (0.089)	6.35 (0.250)	0.356					
1AX -9	2.36 (0.093)	50.8 (2.00)	SIZING	START	1.219 (0.048)	3.38 (0.133)	0.361	332 (48.2)				352 Cycles to Breakthrough
				STOP	1.219 (0.048)	3.38 (0.133)	0.361					
			CYCLING	START	1.219 (0.048)	3.38 (0.133)	0.361	249 (36.1)	-0.8			
				STOP	2.162 (0.093)	6.35 (0.250)	0.372					
1AM -1	2.31 (0.091)	63.5 (2.50)	SIZING	START	0.965 (0.038)	4.37 (0.172)	0.221	332 (48.2)				45,210 Cycles to Breakthrough
				STOP	0.991 (0.039)	4.37 (0.172)	0.227					
			CYCLING	START	0.991 (0.039)	4.37 (0.172)	0.227	124 (18.0)	0			
				STOP	2.311 (0.091)	7.04 (0.277)	0.329					
1AM -6	2.26 (0.089)	63.5 (2.50)	SIZING	START	1.143 (0.045)	3.94 (0.155)	0.290	332 (48.2)				13,782 Cycles to Breakthrough
				STOP	1.143 (0.045)	3.94 (0.155)	0.290					
			CYCLING	START	1.143 (0.045)	3.94 (0.155)	0.290	166 (24.1)	0			
				STOP	2.261 (0.089)	6.27 (0.247)	0.360					

ORIGINAL PAGE 13
OF POOR QUALITY

Table 16: UNIAXIAL CYCLIC TESTS OF 4.57 mm (0.180 INCH) 2219-T62 ALUMINUM

SPECIMEN NUMBER	THICKNESS, t mm (Inch)	WIDTH, w mm (Inch)	TEST PARAMETERS DURING:		CRACK DEPTH, a mm (Inch)	CRACK LENGTH, $2c$ mm (Inch)	CRACK SHAPE $a/2c$	Max STRESS, σ_{Max} MN/m ² (Ksi)	STRESS RATIO, $\sigma_{Min}/\sigma_{Max}$	TEMPERATURE, T K (°F)	ENVIRONMENT	REMARKS
2ATC -1	4.60 (0.181)	63.8 (2.51)	SIZING	START	1.549 (0.061)	8.38 (0.330)	0.185	332 (48.2)		295 (72)	AIR	22,706 Cycles to Breakthrough
				STOP	1.549 (0.061)	8.38 (0.330)	0.185					
			CYCLING	START	1.549 (0.061)	8.38 (0.330)	0.185	166 (24.1)	-0.4			
				STOP	4.597 (0.181)	12.24 (0.482)	0.376					
2ATC -2	4.62 (0.182)	63.5 (2.50)	SIZING	START	1.549 (0.061)	8.33 (0.328)	0.186	332 (48.2)		295 (72)	AIR	1,770 Cycles to Breakthrough
				STOP	1.549 (0.061)	8.33 (0.328)	0.186					
			CYCLING	START	1.549 (0.061)	8.33 (0.328)	0.186	249 (36.1)	-0.4			
				STOP	4.623 (0.182)	12.50 (0.492)	0.370					
2ATC -3	4.62 (0.182)	63.5 (2.50)	SIZING	START	1.549 (0.061)	8.20 (0.323)	0.189	332 (48.2)		295 (72)	AIR	13,115 Cycles to Breakthrough
				STOP	1.549 (0.061)	8.20 (0.323)	0.189					
			CYCLING	START	1.549 (0.061)	8.20 (0.323)	0.189	166 (24.1)	-0.8			
				STOP	4.623 (0.182)	12.88 (0.507)	0.359					
2ATC -4	4.62 (0.182)	63.5 (2.50)	SIZING	START	1.549 (0.061)	8.18 (0.322)	0.189	332 (48.2)		295 (72)	AIR	1,251 Cycles to Breakthrough
				STOP	1.549 (0.061)	8.18 (0.322)	0.189					
			CYCLING	START	1.549 (0.061)	8.18 (0.322)	0.189	249 (36.1)	-0.8			
				STOP	4.623 (0.182)	13.13 (0.517)	0.352					
2ATC -5	4.65 (0.183)	63.8 (2.51)	SIZING	START	1.372 (0.054)	7.93 (0.312)	0.173	332 (48.2)		295 (72)	AIR	Min. Stress of -28.9 ksi. Cycled for 44,300 Cycles
				STOP	1.372 (0.054)	7.93 (0.312)	0.173					
			CYCLING	START	1.372 (0.054)	7.93 (0.312)	0.173					
				STOP	1.372 (0.054)	7.93 (0.312)	0.173		-∞			

Table 16: Continued

SPECIMEN NUMBER	THICKNESS, t mm (inch)	WIDTH, W mm (inch)	TEST PARAMETERS DURING	CRACK DEPTH, a mm (inch)	CRACK LENGTH, $2c$ mm (inch)	CRACK SHAPE $a/2c$	Max STRESS, σ_{Max} MN/m ² (Ksi)	STRESS RATIO, $\sigma_{Min}/\sigma_{Max}$	TEMPERATURE, T K (°F)	ENVIRONMENT	REMARKS
2ATC -6	4.62 (0.182)	63.5 (2.50)	SIZING	START	1.651 (0.065)	8.18 (0.322)	0.202	332	295 (72)	AIR	1,048 Cycles to Breakthrough
				STOP	1.651 (0.065)	8.18 (0.322)	0.202	(48.2)			
			CYCLING	START	1.651 (0.065)	8.18 (0.322)	0.202	249			
				STOP	4.623 (0.182)	14.61 (0.575)	0.317	(36.1)			
2ATC -7	4.60 (0.181)	63.5 (2.50)	SIZING	START	1.676 (0.066)	8.15 (0.321)	0.206	332			4,558 Cycles to Breakthrough
				STOP	1.803 (0.071)	8.15 (0.322)	0.220	(48.2)			
			CYCLING	START	1.803 (0.071)	8.15 (0.322)	0.220	166			
				STOP	4.597 (0.181)	13.77 (0.542)	0.334	(24.1)			
2AX -1	4.57 (0.180)	69.9 (2.75)	SIZING	START	1.803 (0.071)	8.08 (0.318)	0.223	332			24,158 Cycles to Breakthrough
				STOP	2.032 (0.080)	8.31 (0.327)	0.245	(48.2)			
			CYCLING	START	2.032 (0.080)	8.31 (0.327)	0.245	124			
				STOP	4.572 (0.180)	13.46 (0.530)	0.340	(18.0)			
2AX -2	4.55 (0.179)	69.9 (2.75)	SIZING	START	1.778 (0.070)	8.13 (0.320)	0.219	332			1,905 Cycles to Breakthrough
				STOP	2.210 (0.087)	8.43 (0.332)	0.262	(48.2)			
			CYCLING	START	2.210 (0.087)	8.43 (0.332)	0.262	166			
				STOP	4.547 (0.179)	17.53 (0.690)	0.259	(24.1)			
2AX -7	4.62 (0.182)	69.9 (2.75)	SIZING	START	1.321 (0.052)	10.67 (0.420)	0.124	332			1,189 Cycles to Breakthrough
				STOP	2.362 (0.093)	10.67 (0.420)	0.221	(48.2)			
			CYCLING	START	2.362 (0.093)	10.67 (0.420)	0.221	249			
				STOP	4.623 (0.182)	13.77 (0.542)	0.336	(36.1)	0		

Table 16: Continued

SPECIMEN NUMBER	THICKNESS, t mm (inch)	WIDTH, W mm (inch)	TEST PARAMETERS DURING		CRACK DEPTH, a mm (inch)	CRACK LENGTH, 2c mm (inch)	CRACK SHAPE a/2c	Max STRESS, σ_{Max} MN/m ² (Ksi)	STRESS RATIO, $\sigma_{Min}/\sigma_{Max}$	TEMPERATURE, T K (°F)	ENVIRONMENT	REMARKS
2AX -9	4.67 (0.184)	69.9 (2.75)	SIZING	START	0.940 (0.037)	10.87 (0.428)	0.086	332		295 (72)	AIR	790 Cycles to Breakthrough
				STOP	1.041 (0.041)	10.87 (0.428)	0.096	(48.2)				
			CYCLING	START	1.041 (0.041)	10.87 (0.428)	0.096	249	-0.8			
				STOP	4.674 (0.184)	14.91 (0.587)	0.313	(36.1)				
2AX -10	4.55 (0.179)	69.9 (2.75)	SIZING	START	1.143 (0.045)	10.92 (0.430)	0.105	332				656 Cycles to Breakthrough
				STOP	1.143 (0.045)	10.92 (0.430)	0.105	(48.2)				
			CYCLING	START	1.143 (0.045)	10.92 (0.430)	0.105	249	-0.8			
				STOP	4.547 (0.179)	15.75 (0.620)	0.289	(36.1)				
2AX -11	4.57 (0.180)	69.9 (2.75)	SIZING	START	2.007 (0.079)	5.00 (0.197)	0.401	332				3,195 Cycles to Breakthrough
				STOP	2.083 (0.082)	5.21 (0.205)	0.400	(48.2)				
			CYCLING	START	2.083 (0.082)	5.21 (0.205)	0.400	249	0			
				STOP	4.572 (0.180)	11.43 (0.450)	0.400	(36.1)				
2AX -12	4.62 (0.182)	69.9 (2.75)	SIZING	START	2.057 (0.081)	5.08 (0.200)	0.405	332				431 Cycles to Breakthrough
				STOP	2.210 (0.087)	5.28 (0.208)	0.418	(48.2)				
			CYCLING	START	2.210 (0.087)	5.28 (0.208)	0.418	249	-0.8			
				STOP	4.623 (0.182)	11.05 (0.435)	0.418	(36.1)				
2AX -13	4.60 (0.181)	70.1 (2.76)	SIZING	START	1.956 (0.077)	4.88 (0.192)	0.401	332				274 Cycles to Breakthrough
				STOP	2.083 (0.082)	4.98 (0.196)	0.418	(48.2)				
			CYCLING	START	2.083 (0.082)	4.98 (0.196)	0.418	249	-0.8			
				STOP	4.597 (0.181)	12.45 (0.490)	0.369	(36.1)				

Table 16: Continued

SPECIMEN NUMBER	THICKNESS, t mm (Inch)	WIDTH, W mm (Inch)	TEST PARAMETERS DURING		CRACK DEPTH, a mm (Inch)	CRACK LENGTH, 2c mm (Inch)	CRACK SHAPE a/2c	Max STRESS, σ_{Max} MN/m ² (Ksi)	STRESS RATIO, $\sigma_{Min}/\sigma_{Max}$	TEMPERATURE, T K (°F)	ENVIRONMENT	REMARKS
2AAX -1	4.60 (0.181)	88.9 (3.50)	SIZING	START	1.956 (0.077)	8.23 (0.324)	0.238	332		295 (72)	AIR	15,040 Cycles to Breakthrough
				STOP	2.311 (0.091)	10.54 (0.415)	0.219	(48.2)				
			CYCLING	START	2.311 (0.091)	10.54 (0.415)	0.219	166	0			
				STOP	4.597 (0.181)	15.82 (0.623)	0.291	(24.1)				
2AAX -2	4.60 (0.181)	88.9 (3.50)	SIZING	START	1.854 (0.073)	8.33 (0.328)	0.223	332				37,000 Cycles to Breakthrough
				STOP	2.159 (0.085)	8.38 (0.330)	0.258	(48.2)				
			CYCLING	START	2.159 (0.085)	8.38 (0.330)	0.258	124	0			
				STOP	4.597 (0.181)	13.16 (0.518)	0.349	(18.0)				
2AM -1	4.60 (0.180)	127.0 (5.00)	SIZING	START	1.651 (0.065)	8.18 (0.322)	0.202	332				3,844 Cycles to Breakthrough
				STOP	1.651 (0.065)	8.18 (0.322)	0.202	(48.2)				
			CYCLING	START	1.651 (0.065)	8.18 (0.322)	0.202	249	0			
				STOP	4.572 (0.180)	12.70 (0.500)	0.360	(36.1)				
2AM -2	4.55 (0.179)	127.0 (5.00)	SIZING	START	1.600 (0.063)	8.13 (0.320)	0.197	332				28,278 Cycles to Breakthrough
				STOP	1.600 (0.063)	8.13 (0.320)	0.197	(48.2)				
			CYCLING	START	1.600 (0.063)	8.13 (0.320)	0.197	166	0			
				STOP	4.547 (0.179)	12.65 (0.498)	0.359	(24.1)				
2AM -4	4.55 (0.179)	127. (5.00)	SIZING	START	1.499 (0.059)	8.23 (0.324)	0.182	332				16,409 Cycles to Breakthrough
				STOP	1.499 (0.059)	8.23 (0.324)	0.182	(48.2)				
			CYCLING	START	1.499 (0.059)	8.23 (0.324)	0.182	249	+0.5			
				STOP	4.547 (0.179)	12.70 (0.500)	0.358	(36.1)				

Table 16: Continued


SPECIMEN NUMBER	THICKNESS, t mm (inch)	WIDTH, W mm (inch)	TEST PARAMETERS DURING:		CRACK DEPTH, a mm (inch)	CRACK LENGTH, $2c$ mm (inch)	CRACK SHAPE $a/2c$	Max STRESS, σ_{Max} MN/m ² (Ksi)	STRESS RATIO, $\sigma_{Min}/\sigma_{Max}$	TEMPERATURE, T K (°F)	ENVIRONMENT	REMARKS
2AM -8	4.57 (0.180)	127.0 (5.00)	SIZING	START	1.778 (0.070)	4.67 (0.184)	0.380	332		295 (72)	AIR	3,639 Cycles to Breakthrough
				STOP	1.905 (0.075)	4.95 (0.195)	0.385	(48.2)				
			CYCLING	START	1.905 (0.075)	4.95 (0.195)	0.385	249	0			
				STOP	4.572 (0.180)	11.94 (0.470)	0.383	(36.1)				

Table 17: UNIAXIAL CYCLIC TESTS OF 7.62 mm (0.300 INCH) 2219-T62 ALUMINUM

SPECIMEN NUMBER	THICKNESS, t mm (Inch)	WIDTH, W mm (Inch)	TEST PARAMETERS DURING:		CRACK DEPTH, a mm (Inch)	CRACK LENGTH, 2c mm (Inch)	CRACK SHAPE a/2c	Max STRESS, σ_{Max} MN/m ² (Ksi)	STRESS RATIO, $\sigma_{Min}/\sigma_{Max}$	TEMPERATURE, T K (°F)	ENVIRONMENT	REMARKS
3AX -7	7.44 (0.293)	127.3 (5.01)	SIZING	START	1.270 (0.050)	14.73 (0.580)	0.086	332 (48.2)		295 (72)	AIR	3,960 Cycles to Breakthrough
				STOP	1.524 (0.060)	14.73 (0.580)	0.104					
			CYCLING	START	1.524 (0.060)	14.73 (0.580)	0.104	249 (36.1)	0			
				STOP	7.442 (0.293)	28.96 (1.140)	0.257					
3AX -8	7.42 (0.292)	127.3 (5.01)	SIZING	START	1.270 (0.050)	14.73 (0.580)	0.086	332 (48.2)				5,546 Cycles to Breakthrough
				STOP	1.600 (0.063)	14.73 (0.580)	0.109					
			CYCLING	START	1.600 (0.063)	14.73 (0.580)	0.109	249 (36.1)	0			
				STOP	7.417 (0.292)	30.99 (1.220)	0.239					
3AX -9	7.49 (0.295)	127.3 (5.01)	SIZING	START	1.295 (0.051)	14.88 (0.586)	0.087	332 (48.2)				GOL Estimated ----- 953 Cycles to Breakthrough
				STOP	1.600 (0.063)	14.88 (0.586)	0.107					
			CYCLING	START	1.600 (0.063)	14.88 (0.586)	0.107	249 (36.1)	-1.0			
				STOP	7.493 (0.295)	29.13 (1.147)	0.257					
3AX -10	7.44 (0.293)	127.3 (5.01)	SIZING	START	1.321 (0.052)	14.73 (0.580)	0.090	332 (48.2)				GOL Estimated ----- 525 Cycles to Breakthrough
				STOP	1.651 (0.065)	14.73 (0.580)	0.112					
			CYCLING	START	1.651 (0.065)	14.73 (0.580)	0.112	249 (36.1)	-1.0			
				STOP	7.442 (0.293)	26.92 (1.060)	0.276					
3AX -11	7.65 (0.301)	127.3 (5.01)	SIZING	START	2.845 (0.112)	7.595 (0.299)	0.375	332 (48.2)				3,633 Cycles to Breakthrough
				STOP	2.972 (0.117)	8.179 (0.322)	0.364					
			CYCLING	START	2.972 (0.117)	8.179 (0.322)	0.364	249 (36.1)	0			
				STOP	7.645 (0.301)	23.88 (0.940)	0.320					

Table 17: Continued

SPECIMEN NUMBER	THICKNESS, t mm (inch)	WIDTH, W mm (inch)	TEST PARAMETERS DURING:		CRACK DEPTH, a mm (inch)	CRACK LENGTH, $2c$ mm (inch)	CRACK SHAPE $a/2c$	Max STRESS, σ_{Max} MN/m ² (Ksi)	STRESS RATIO, $\sigma_{Min}/\sigma_{Max}$	TEMPERATURE, T K (°F)	ENVIRONMENT	REMARKS
3AX -12	7.82 (0.308)	127.3 (5.01)	SIZING	START	2.769 (0.109)	7.54 (0.297)	0.368	332		295 (72)	AIR	3,775 Cycles to Breakthrough
				STOP	3.124 (0.123)	8.18 (0.322)	0.382	(48.2)				
			CYCLING	START	3.124 (0.123)	8.18 (0.322)	0.382	249	0			
				STOP	7.823 (0.308)	25.40 (1.000)	0.308	(36.1)				
3AX -13	7.72 (0.304)	127.3 (5.01)	SIZING	START	2.769 (0.109)	7.65 (0.301)	0.362	332				GOL Estimated
				STOP	3.124 (0.123)	8.18 (0.322)	0.382	(48.2)				
			CYCLING	START	3.124 (0.123)	8.18 (0.322)	0.382	249	-1.0			630 Cycles to Breakthrough
				STOP	7.722 (0.304)	26.42 (1.040)	0.292	(36.1)				
3AX -14	7.70 (0.303)	127.0 (5.00)	SIZING	START	2.921 (0.115)	8.20 (0.323)	0.356	332				GOL Estimated
				STOP	3.251 (0.128)	9.14 (0.360)	0.356	(48.2)				
			CYCLING	START	3.251 (0.128)	9.14 (0.360)	0.356	249	-1.0			369 Cycles to Breakthrough
				STOP	7.696 (0.303)	25.78 (1.015)	0.298	(36.1)				
3AX -19	7.72 (0.304)	127.3 (5.01)	SIZING	START	1.524 (0.060)	8.89 (0.350)	0.172	332				Grip Failure at 4,076 Cycles
				STOP	1.727 (0.068)	8.89 (0.350)	0.194	(48.2)				
			CYCLING	START	1.727 (0.068)	8.89 (0.350)	0.194	249	0			
				STOP	1.727 (0.168)	13.79 (0.543)	0.310	(36.1)				
3AX -20	7.77 (0.306)	127.3 (5.01)	SIZING	START	1.651 (0.065)	8.97 (0.353)	0.184	332				3,929 Cycles to Breakthrough
				STOP	2.007 (0.079)	8.97 (0.353)	0.224	(48.2)				
			CYCLING	START	2.007 (0.079)	8.97 (0.353)	0.224	249	0			
				STOP	7.772 (0.306)	24.33 (0.958)	0.319	(36.1)				

Table 17: Continued

SPECIMEN NUMBER	THICKNESS, t mm (Inch)	WIDTH, W mm (Inch)	TEST PARAMETERS DURING:		CRACK DEPTH, a mm (Inch)	CRACK LENGTH, $2c$ mm (Inch)	CRACK SHAPE $a/2c$	Max STRESS, σ_{Max} MN/m ² (Ksi)	STRESS RATIO, $\sigma_{Min}/\sigma_{Max}$	TEMPERATURE, T K (°F)	ENVIRONMENT	REMARKS
3AX -21	7.77 (0.306)	127.3 (5.01)	SIZING	START	1.575 (0.062)	8.76 (0.345)	0.180	332 (48.2)		295 (72)	AIR	GOL Estimated
				STOP	1.778 (0.070)	8.76 (0.345)	0.203					
			CYCLING	START	1.778 (0.070)	8.76 (0.345)	0.203	249 (36.1)	-1.0			1,113 Cycles to Breakthrough
				STOP	7.772 (0.306)	24.13 (0.950)	0.322					
3AX -22	7.65 (0.301)	127.3 (5.01)	SIZING	START	1.600 (0.063)	8.84 (0.348)	0.181	332 (48.2)		295 (72)	AIR	GOL Estimated
				STOP	1.803 (0.071)	8.84 (0.348)	0.204					
			CYCLING	START	1.803 (0.071)	8.84 (0.348)	0.204	249 (36.1)	-1.0			1,310 Cycles to Breakthrough
				STOP	7.645 (0.301)	24.89 (0.980)	0.307					
3AX -23	7.70 (0.303)	127.3 (5.01)	SIZING	START	1.651 (0.065)	9.30 (0.366)	0.178	332 (48.2)		295 (72)	AIR	21,533 Cycles to Breakthrough
				STOP	1.930 (0.076)	9.30 (0.366)	0.208					
			CYCLING	START	1.930 (0.076)	9.30 (0.366)	0.208	166 (24.1)	0			
				STOP	7.696 (0.303)	24.23 (0.954)	0.318					
3AX -24	7.70 (0.303)	127.3 (5.01)	SIZING	START	1.600 (0.063)	8.89 (0.350)	0.180	332 (48.2)		295 (72)	AIR	66,668 Cycles to Breakthrough
				STOP	1.651 (0.065)	8.89 (0.350)	0.186					
			CYCLING	START	1.651 (0.065)	8.89 (0.350)	0.186	166 (24.1)	0			
				STOP	7.696 (0.303)	23.37 (0.920)	0.329					
3AX -25	7.75 (0.305)	127.3 (5.01)	SIZING	START	1.651 (0.065)	8.94 (0.352)	0.185	332 (48.2)		295 (72)	AIR	GOL Estimated
				STOP	1.880 (0.074)	8.94 (0.352)	0.210					
			CYCLING	START	1.880 (0.074)	8.94 (0.352)	0.210	166 (24.1)	-1.0			22,659 Cycles to Breakthrough
				STOP	7.747 (0.305)	22.99 (0.905)	0.337					

Table 17: Continued

SPECIMEN NUMBER	THICKNESS, t mm (inch)	WIDTH, W mm (inch)	TEST PARAMETERS DURING:		CRACK DEPTH, a mm (inch)	CRACK LENGTH, $2c$ mm (inch)	CRACK SHAPE $a/2c$	Max STRESS, σ_{Max} MN/m ² (Ksi)	STRESS RATIO, $\sigma_{Min}/\sigma_{Max}$	TEMPERATURE, T K (°F)	ENVIRONMENT	REMARKS
3AX -26	7.67 (0.302)	127.3 (5.01)	SIZING	START	1.651 (0.065)	8.84 (0.348)	0.187	332		295 (72)	AIR	GOL Estimated
				STOP	1.880 (0.074)	8.84 (0.348)	0.212	(48.2)				
			CYCLING	START	1.880 (0.074)	8.84 (0.348)	0.212	166	-1.0			Test Section Fatigue Failure at 21,369 Cycles
				STOP	6.426 (0.253)	19.76 (0.778)	0.326	(24.1)				
3AX -27	7.72 (0.304)	127.3 (5.01)	SIZING	START	1.651 (0.065)	8.99 (0.354)	0.184	332		295 (72)	AIR	GOL Estimated
				STOP	1.880 (0.074)	8.99 (0.354)	0.209	(48.2)				
			CYCLING	START	1.880 (0.074)	8.99 (0.354)	0.209	166	-2.0			Test Section Fatigue Failure at 2880 Cycles
				STOP	2.794 (0.110)	12.07 (0.475)	0.232	(24.1)				
3AX -28	7.72 (0.304)	127.3 (5.01)	SIZING	START	1.727 (0.068)	8.94 (0.352)	0.193	332		295 (72)	AIR	125,187 Cycles to Breakthrough
				STOP	2.032 (0.080)	8.94 (0.352)	0.227	(48.2)				
			CYCLING	START	2.032 (0.080)	8.94 (0.352)	0.227	124	0			
				STC	7.722 (0.304)	24.77 (0.975)	0.154	(18.0)				
3AX -29	7.67 (0.302)	127.3 (5.01)	SIZING	START	1.753 (0.069)	8.94 (0.352)	0.196	332		295 (72)	AIR	GOL Estimated
				STOP	2.083 (0.082)	8.94 (0.352)	0.233	(48.2)				
			CYCLING	START	2.083 (0.082)	8.94 (0.352)	0.233	124	-1.0			Grip Fatigue Failure at 40,089 Cycles
				STOP	3.404 (0.134)	12.01 (0.473)	0.284	(18.0)				
3AX -30	7.75 (0.305)	127.3 (5.01)	SIZING	START	1.651 (0.065)	8.89 (0.350)	0.186	332		295 (72)	AIR	GOL Estimated
				STOP	1.880 (0.074)	8.89 (0.350)	0.212	(48.2)				
			CYCLING	START	1.880 (0.074)	8.89 (0.350)	0.212	124	-2.0			Test Section Fatigue Failure at 25,840 Cycles
				STOP	5.08 (0.200)	17.02 (0.670)	0.298	(18.0)				

Table 18: UNIAXIAL CYCLIC TESTS OF 1.02 mm (0.040 INCH) INCONEL X750 STA

SPECIMEN NUMBER	THICKNESS, t mm (inch)	WIDTH, W mm (inch)	TEST PARAMETERS DURING:		CRACK DEPTH, a mm (inch)	CRACK LENGTH, $2c$ mm (inch)	CRACK SHAPE $a/2c$	Max STRESS, σ_{Max} MN/m ² (Ksi)	STRESS RATIO, $\sigma_{Min}/\sigma_{Max}$	TEMPERATURE, T K (°F)	ENVIRONMENT	REMARKS
IBTC -1	1.02 (0.040)	25.4 (1.00)	SIZING	START	0.610 (0.024)	3.05 (0.120)	0.200	850 (123.3)		295 (72)	AIR	10,933 Cycles to Breakthrough
				STOP	0.686 (0.027)	3.05 (0.120)	0.225					
			CYCLING	START	0.686 (0.027)	3.05 (0.120)	0.225	517 (75.0)	0			
				STOP	1.016 (0.040)	3.38 (0.133)	0.301					
IBTC -2	1.02 (0.040)	25.4 (1.00)	SIZING	START	0.559 (0.022)	3.12 (0.123)	0.179	850 (123.3)		295 (72)	AIR	Test Terminated After 261,320 Cycles
				STOP	0.559 (0.022)	3.12 (0.123)	0.179					
			CYCLING	START	0.559 (0.022)	3.12 (0.123)	0.179	345 (50.0)	0			
				STOP	0.762 (0.030)	3.12 (0.123)	0.244					
IBTC -3	1.02 (0.040)	25.4 (1.00)	SIZING	START	0.559 (0.022)	3.33 (0.131)	0.168	850 (123.3)		295 (72)	AIR	778 Cycles to Breakthrough
				STOP	0.559 (0.022)	3.33 (0.131)	0.168					
			CYCLING	START	0.559 (0.022)	3.33 (0.131)	0.168	724 (105.0)	-1.0			
				STOP	1.016 (0.040)	3.86 (0.152)	0.263					
IBTC -4	1.02 (0.040)	25.4 (1.00)	SIZING	START	0.559 (0.022)	3.33 (0.133)	0.168	850 (123.3)		295 (72)	AIR	62,048 Cycles to Breakthrough
				STOP	0.559 (0.022)	3.33 (0.131)	0.168					
			CYCLING	START	0.559 (0.022)	3.33 (0.131)	0.168	345 (50.0)	-1.0			
				STOP	1.016 (0.040)	3.86 (0.152)	0.263					
IBTC -7	1.02 (0.040)	31.75 (1.25)	SIZING	START	0.584 (0.023)	3.30 (0.130)	0.177	850 (123.3)		295 (72)	AIR	6,294 Cycles to Breakthrough
				STOP	0.584 (0.023)	3.30 (0.130)	0.177					
			CYCLING	START	0.584 (0.023)	3.30 (0.130)	0.177	517 (75.0)	-1.0			
				STOP	1.016 (0.040)	3.99 (0.157)	0.250					

Table 18: Continued

SPECIMEN NUMBER	THICKNESS, t mm (Inch)	WIDTH, W mm (Inch)	TEST PARAMETERS DURING:		CRACK DEPTH, a mm (Inch)	CRACK LENGTH, $2c$ mm (Inch)	CRACK SHAPE $a/2c$	Max STRESS, σ_{Max} MN/m ² (Ksi)	STRESS RATIO, $\sigma_{Min}/\sigma_{Max}$	TEMPERATURE, T K (°F)	ENVIRONMENT	REMARKS
IBTC -8	1.04 (0.041)	25.4 (1.00)	SIZING	START	0.584 (0.023)	3.25 (0.128)	0.180	850 (123.3)		295 (72)	AIR	2,157 Cycles to Breakthrough
				STOP	0.584 (0.023)	3.25 (0.128)	0.180					
			CYCLING	START	0.534 (0.021)	3.25 (0.128)	0.180	517 (75.0)	-1.4			
				STOP	1.041 (0.041)	3.76 (0.148)	0.277					
IBTC -9	1.04 (0.041)	25.4 (1.00)	SIZING	START	0.610 (0.024)	3.30 (0.130)	0.185	850 (123.3)				13,388 Cycles to Breakthrough
				STOP	0.635 (0.025)	3.30 (0.130)	0.192					
			CYCLING	START	0.635 (0.025)	3.30 (0.130)	0.192	724 (105.0)	+0.5			
				STOP	1.041 (0.041)	3.56 (0.140)	0.293					
IBTC -11	1.02 (0.040)	25.4 (1.00)	SIZING	START	0.559 (0.022)	3.30 (0.130)	0.169	850 (123.3)				509 Cycles to Breakthrough
				STOP	0.559 (0.022)	3.30 (0.130)	0.169					
			CYCLING	START	0.559 (0.022)	3.30 (0.130)	0.169	724 (105.0)	-1.0			
				STOP	1.016 (0.040)	3.56 (0.140)	0.286					
IBTC -12	1.02 (0.040)	25.4 (1.00)	SIZING	START	0.533 (0.021)	3.20 (0.126)	0.167	850 (123.3)				11,192 Cycles to Breakthrough
				STOP	0.533 (0.021)	3.20 (0.126)	0.167					
			CYCLING	START	0.533 (0.021)	3.20 (0.126)	0.167	345 (50.0)	-2.0			
				STOP	1.016 (0.040)	3.68 (0.145)	0.276					
IBTC -13	1.02 (0.040)	25.4 (1.00)	SIZING	START	0.533 (0.021)	3.25 (0.128)	0.164	850 (123.3)				Test Machine Malfunction, Specimen Over- loaded at 49,156 Cycles
				STOP	0.533 (0.021)	3.25 (0.128)	0.154					
			CYCLING	START	0.533 (0.021)	3.25 (0.128)	0.164	517 (75.0)	+0.5			
				STOP	0.660 (0.026)	3.25 (0.128)	0.203					

Table 18: Continued

SPECIMEN NUMBER	THICKNESS, t mm (inch)	WIDTH, w mm (inch)	TEST PARAMETERS DURING:		CRACK DEPTH, a mm (inch)	CRACK LENGTH, $2c$ mm (inch)	CRACK SHAPE $a/2c$	Max STRESS, σ_{Max} MN/m ² (Ksi)	STRESS RATIO, $\sigma_{Min}/\sigma_{Max}$	TEMPERATURE, T K (°F)	ENVIRONMENT	REMARKS
IBTC -14	1.02 (0.040)	25.4 (1.00)	SIZING	START	0.559 (0.022)	3.25 (0.128)	0.172	850 (123.3)		295 (72)	AIR	22,037 Cycles to Breakthrough
				STOP	0.610 (0.024)	3.25 (0.128)	0.188					
			CYCLING	START	0.610 (0.024)	3.25 (0.128)	0.188	517 (75.0)	0			
				STOP	1.016 (0.040)	3.53 (0.139)	0.288					
IBTC -15	1.02 (0.040)	25.4 (1.00)	SIZING	START	0.559 (0.022)	3.28 (0.129)	0.171	850 (123.3)		295 (72)	AIR	7,318 Cycles to Breakthrough
				STOP	0.559 (0.022)	3.28 (0.129)	0.171					
			CYCLING	START	0.559 (0.022)	3.28 (0.129)	0.171	517 (75.0)	-1.0			
				STOP	1.016 (0.040)	3.81 (0.150)	0.267					
IBTC -16	1.02 (0.040)	25.4 (1.00)	SIZING	START	0.584 (0.023)	3.33 (0.131)	0.176	850 (123.3)		295 (72)	AIR	2,174 Cycles to Breakthrough
				STOP	0.584 (0.023)	3.33 (0.131)	0.176					
			CYCLING	START	0.584 (0.023)	3.33 (0.131)	0.176	724 (105.0)	-0.5			
				STOP	1.016 (0.040)	3.68 (0.145)	0.276					
IBX -1	1.02 (0.040)	31.8 (1.25)	SIZING	START	0.483 (0.019)	3.30 (0.130)	0.146	850 (123.3)		295 (72)	AIR	3,660 Cycles to Breakthrough
				STOP	0.483 (0.019)	3.30 (0.130)	0.146					
			CYCLING	START	0.483 (0.019)	3.30 (0.130)	0.146	724 (105.0)	0			
				STOP	1.016 (0.040)	3.56 (0.140)	0.286					
IBX -2	1.04 (0.041)	31.8 (1.25)	SIZING	START	0.508 (0.020)	3.53 (0.139)	0.144	850 (123.3)		295 (72)	AIR	6,118 Cycles to Breakthrough
				STOP	0.508 (0.020)	3.53 (0.139)	0.144					
			CYCLING	START	0.508 (0.020)	3.53 (0.139)	0.144	517 (75.0)	-1.4			
				STOP	1.041 (0.041)	3.81 (0.150)	0.273					

Table 18: Continued

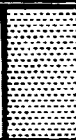
SPECIMEN NUMBER	THICKNESS, t mm (inch)	WIDTH, W mm (inch)	TEST PARAMETERS DURING:		CRACK DEPTH, a mm (inch)	CRACK LENGTH, $2c$ mm (inch)	CRACK SHAPE $a/2c$	Max STRESS, σ_{Max} MN/m ² (Ksi)	STRESS RATIO, $\sigma_{Min}/\sigma_{Max}$	TEMPERATURE, T K (°F)	ENVIRONMENT	REMARKS
IBX -3-	1.04 (0.041)	31.8 (1.25)	SIZING	START	0.508 (0.020)	3.25 (0.128)	0.156	850 (123.3)		295 (72)	AIR	Test Machine Malfunction, Specimen Over- loaded at 21,377 Cycles
				STOP	0.508 (0.020)	3.25 (0.128)	0.156					
			CYCLING	START	0.508 (0.020)	3.25 (0.128)	0.156	345 (50.0)	-1.0			
				STOP	0.635 (0.025)	3.43 (0.135)	0.185					

Table 19: UNIAXIAL CYCLIC TESTS OF 3.30 mm (0.130 INCH) INCONEL X750 STA

SPECIMEN NUMBER	THICKNESS, t mm (inch)	WIDTH, W mm (inch)	TEST PARAMETERS DURING	CRACK DEPTH, a mm (inch)	CRACK LENGTH, 2c mm (inch)	CRACK SHAPE a/2c	Max STRESS, σ_{Max} MN/m ² (Ksi)	STRESS RATIO, $\sigma_{Min}/\sigma_{Max}$	TEMPERATURE, T K (°F)	ENVIRONMENT	REMARKS
2BTC-1	338 (0.133)	57.2 (2.25)	SIZING	START	1.574 (0.062)	7.82 (0.308)	0.201	850 (123.3)	295 (72)	AIR	14,272 Cycles To Breakthrough
				STOP	1.626 (0.064)	7.82 (0.308)	0.208				
			CYCLING	START	1.626 (0.064)	7.82 (0.308)	0.208	517 (75.0)			
				STOP	3.378 (0.133)	9.50 (0.374)	0.356	0			
2BTC-2	3.33 (0.131)	57.2 (2.25)	SIZING	START	1.702 (0.067)	8.28 (0.326)	0.206	850 (123.3)			4,641 Cycles To Breakthrough
				STOP	1.702 (0.067)	8.28 (0.326)	0.206				
			CYCLING	START	1.702 (0.067)	8.28 (0.326)	0.206	517 (75.0)			
				STOP	3.327 (0.131)	10.59 (0.417)	0.314	-1.0			
2BTC-3	3.38 (0.133)	57.2 (2.25)	SIZING	START	1.702 (0.067)	8.43 (0.332)	0.202	850 (123.3)			146,919 Cycles To Breakthrough
				STOP	1.829 (0.072)	8.43 (0.332)	0.217				
			CYCLING	START	1.829 (0.072)	8.43 (0.332)	0.217	345 (50.0)			
				STOP	3.378 (0.133)	10.64 (0.419)	0.317	0			
2BTC-4	3.33 (0.131)	57.2 (2.25)	SIZING	START	1.626 (0.064)	8.36 (0.329)	0.195	850 (123.3)			2,704 Cycles To Breakthrough
				STOP	1.626 (0.065)	8.36 (0.329)	0.198				
			CYCLING	START	1.651 (0.065)	8.36 (0.329)	0.198	724 (105.0)			
				STOP	3.327 (0.131)	10.03 (0.395)	0.332	0			
2BTC-5	3.38 (0.133)	57.2 (2.25)	SIZING	START	1.626 (0.064)	8.18 (0.322)	0.199	850 (123.3)			29,233 Cycles To Breakthrough
				STOP	1.626 (0.064)	8.18 (0.322)	0.199				
			CYCLING	START	1.626 (0.064)	8.18 (0.322)	0.199	345 (50.0)			
				STOP	3.378 (0.133)	10.24 (0.403)	0.330	-1.0			

Table 19: Continued

SPECIMEN NUMBER	THICKNESS, t mm (inch)	WIDTH, W mm (inch)	TEST PARAMETERS DURING		CRACK DEPTH, a mm (inch)	CRACK LENGTH, 2c mm (inch)	CRACK SHAPE a/2c	Max STRESS, σ_{Max} MN/m ² (Ksi)	STRESS RATIO, $\sigma_{Min}/\sigma_{Max}$	TEMPERATURE, T K (°F)	ENVIRONMENT	REMARKS
2BTC -6	3.35 (0.132)	57.4 (2.26)	SIZING	START	1.574 (0.062)	8.33 (0.328)	0.189	850 (123.3)		295 (72)	AIR	650 Cycles To Breakthrough
				STOP	1.600 (0.063)	8.33 (0.328)	0.192					
			CYCLING	START	1.600 (0.063)	8.33 (0.328)	0.192	724 (105.0)	-1.0			
				STOP	3.353 (0.132)	10.36 (0.408)	0.324					
2BTC -7	3.35 (0.132)	57.4 (2.26)	SIZING	START	1.651 (0.065)	8.20 (0.323)	0.201	850 (123.3)				
				STOP	1.676 (0.066)	8.20 (0.323)	0.204					
			CYCLING	START	1.676 (0.066)	8.20 (0.323)	0.204	345 (50.0)	-2.0			
				STOP	3.353 (0.132)	11.10 (0.437)	0.302					
2BTC -8	3.38 (0.133)	57.4 (2.26)	SIZING	START	1.702 (0.067)	8.28 (0.326)	0.206	850 (123.3)		295 (72)	AIR	2,768 Cycles To Breakthrough
				STOP	1.702 (0.067)	8.28 (0.326)	0.206					
			CYCLING	START	1.702 (0.067)	8.28 (0.326)	0.206	517 (75.0)	-1.4			
				STOP	3.378 (0.133)	11.05 (0.435)	0.306					

Table 20: UNIAXIAL CYCLIC TESTS OF 0.71 mm (0.028 INCH) CRYOSTRETCHED STAINLESS STEEL BM

SPECIMEN NUMBER	THICKNESS, t mm (Inch)	WIDTH, w mm (Inch)	TEST PARAMETERS DURING		CRACK DEPTH, a mm (Inch)	CRACK LENGTH, 2c mm (Inch)	CRACK SHAPE a/2c	Max STRESS, σ_{Max} MN/m ² (Ksi)	STRESS RATIO, $\sigma_{Min}/\sigma_{Max}$	TEMPERATURE, T K (°F)	ENVIRONMENT	REMARKS
ICTC -2	0.71 (0.028)	12.2 (0.48)	SIZING	START	0.203 (0.008)	1.14 (0.045)	0.178	1379 (200.0)		78 (-320)	LN ₂	5680 CYCLES TO BREAK- THROUGH
				STOP	0.203 (.008)	1.14 (0.045)	0.178					
			PROOFING	START	0.203 (0.008)	1.14 (0.045)	0.178	1234 (179.0)		295 (72)	AIR	
				STOP	0.203 (0.008)	1.14 (0.045)	0.178					
			CYCLING	START	0.203 (0.008)	1.14 (0.045)	0.178	690 (100.0)		-1.0		
				STOP	0.711 (0.028)	1.96 (0.077)	0.364					
ICTC -3	0.71 (0.028)	11.9 (0.47)	SIZING	START	0.203 (0.008)	1.17 (0.046)	0.174	1442 (209.2)		78 (-320)	LN ₂	6104 CYCLES TO BREAK- THROUGH
				STOP	0.203 (0.008)	1.17 (0.046)	0.174					
			PROOFING	START	0.203 (0.008)	1.17 (0.046)	0.174	1234 (179.0)		295 (72)	AIR	
				STOP	0.203 (0.008)	1.17 (0.046)	0.174					
			CYCLING	START	0.203 (0.008)	1.17 (0.046)	0.174	690 (100.0)		-0.5		
				STOP	0.711 (0.028)	1.73 (0.063)	0.412					
ICTC -4	0.71 (0.028)	11.9 (0.47)	SIZING	START	0.203 (0.008)	1.07 (0.042)	0.190	1442 (209.2)		78 (-320)	LN ₂	18,483 CYCLES TO BREAK - THROUGH
				STOP	0.203 (0.008)	1.07 (0.042)	0.190					
			PROOFING	START	0.203 (0.008)	1.07 (0.042)	0.190	1234 (179.0)		295 (72)	AIR	
				STOP	0.203 (0.008)	1.07 (0.042)	0.190					
			CYCLING	START	0.203 (0.008)	1.07 (0.042)	0.190	690 (100.0)		0		
				STOP	0.711 (0.028)	1.96 (0.077)	0.364					

Table 20: Continued



SPECIMEN NUMBER	THICKNESS, t mm (Inch)	WIDTH, W mm (Inch)	TEST PARAMETERS DURING:		CRACK DEPTH, a mm (Inch)	CRACK LENGTH, $2c$ mm (Inch)	CRACK SHAPE $a/2c$	Max STRESS, σ_{Max} MN/m ² (Ksi)	STRESS RATIO, $\sigma_{Min}/\sigma_{Max}$	TEMPERATURE, T K (°F)	ENVIRONMENT	REMARKS
ICTC -5	0.69 (0.027)	11.9 (0.47)	SIZING	START	0.203 (0.008)	1.07 (0.042)	0.190	1442 (209.2)		78 (-320)	LN ₂	4243 CYCLES TO BREAK - THROUGH
				STOP	0.203 (0.008)	1.07 (0.042)	0.190					
			PROOFING	START	0.203 (0.008)	1.07 (0.042)	0.190	1234 (179.0)		295 (72)	AIR	
				STOP	0.203 (0.008)	1.07 (0.042)	0.190					
			CYCLING	START	0.203 (0.008)	1.07 (0.042)	0.190	690 (100.0)		-1.0		
				STOP	0.686 (0.027)	1.98 (0.078)	0.346					
ICTC -6	0.69 (0.027)	11.9 (0.47)	SIZING	START	0.178 (0.007)	1.02 (0.040)	0.175	1442 (209.0)		78 (-320)	LN ₂	6361 CYCLES TO BREAK - THROUGH
				STOP	0.178 (0.007)	1.02 (0.040)	0.175					
			PROOFING	START	0.178 (0.007)	1.02 (0.040)	0.175	1234 (179.0)		295 (72)	AIR	
				STOP	0.178 (0.007)	1.02 (0.040)	0.175					
			CYCLING	START	0.178 (0.007)	1.02 (0.040)	0.175	690 (100.0)		-0.5		
				STOP	0.686 (0.027)	2.16 (0.085)	0.318					

Table 21: UNIAXIAL CYCLIC TESTS OF 2.54 mm (0.100 INCH) CRYOSTRETCHED 301 STAINLESS STEEL BM

SPECIMEN NUMBER	THICKNESS, t mm (inch)	WIDTH, W mm (inch)	TEST PARAMETERS DURING:		CRACK DEPTH, a mm (inch)	CRACK LENGTH, 2c mm (inch)	CRACK SHAPE a/2c	Max STRESS, σ_{Max} MN/m ² (Ksi)	STRESS RATIO, $\sigma_{Min}/\sigma_{Max}$	TEMPERATURE, T K (°F)	ENVIRONMENT	REMARKS
2CTC -1	2.44 (0.096)	32.5 (1.28)	SIZING	START	0.330 (0.013)	2.03 (0.080)	0.163	1442 (209.2)		78 (-320)	LN ₂	5982 CYCLES TO BREAK - THROUGH
				STOP	0.330 (0.013)	2.03 (0.080)	0.163					
			PROOFING	START	0.330 (0.013)	2.03 (0.080)	0.163	1234 (179.0)		295 (72)	AIR	
				STOP	0.330 (0.013)	2.03 (0.080)	0.163					
			CYCLING	START	0.330 (0.013)	2.03 (0.080)	0.163	690 (100.0)		-1.0		
				STOP	2.438 (0.076)	6.81 (0.268)	0.358					
2 CTC -3	2.36 (0.093)	32.0 (1.26)	SIZING	START	0.356 (0.014)	1.63 (0.064)	0.219	1442 (209.2)		78 (-320)	LN ₂	10,202 CYCLES TO BREAK - THROUGH
				STOP	0.356 (0.014)	1.63 (0.064)	0.219					
			PROOFING	START	0.356 (0.014)	1.63 (0.064)	0.219	1234 (179.0)		295 (72)	AIR	
				STOP	0.356 (0.014)	1.63 (0.064)	0.219					
			CYCLING	START	0.356 (0.014)	1.63 (0.064)	0.219	690 (100.0)		-0.5		
				STOP	2.362 (0.093)	6.20 (0.244)	0.381					
2 CTC -4	2.44 (0.096)	32.5 (1.28)	SIZING	START	0.305 (0.012)	1.70 (0.067)	0.179	1442 (209.2)		78 (-320)	LN ₂	8627 CYCLES TO BREAK - THROUGH
				STOP	0.305 (0.012)	1.70 (0.067)	0.179					
			PROOFING	START	0.305 (0.012)	1.70 (0.067)	0.179	1234 (179.0)		295 (72)	AIR	
				STOP	0.305 (0.012)	1.70 (0.067)	0.179					
			CYCLING	START	0.305 (0.012)	1.70 (0.067)	0.179	690 (100.0)		-1.0		
				STOP	2.438 (0.096)	6.22 (0.245)	0.392					

Table 21: Continued

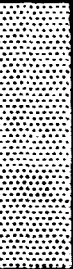

SPECIMEN NUMBER	THICKNESS, t mm (Inch)	WIDTH, w mm (Inch)	TEST PARAMETERS DURING:		CRACK DEPTH, a mm (Inch)	CRACK LENGTH, $2c$ mm (Inch)	CRACK SHAPE $a/2c$	Max STRESS, σ_{Max} MN/m ² (Ksi)	STRESS RATIO, $\sigma_{Min}/\sigma_{Max}$	TEMPERATURE, T K (°F)	ENVIRONMENT	REMARKS	
2 CTC -5	2.46 (0.097)	32.8 (1.29)	SIZING	START	0.279 (0.011)	1.57 (0.062)	0.177	1442 (209.2)		78 (-320)	LN ₂	16,942 CYCLES TO BREAK- THROUGH	
				STOP	0.279 (0.011)	1.57 (0.062)	0.177						
			PROOFING	START	0.279 (0.011)	1.57 (0.062)	0.177	1234 (179.0)		295 (72)	AIR		
				STOP	0.279 (0.011)	1.57 (0.062)	0.177						
			CYCLING	START	0.279 (0.011)	1.57 (0.062)	0.177	690 (100.0)					0
				STOP	2.464 (0.097)	5.64 (0.222)	0.437						
2 CTC -6	2.44 (0.096)	32.5 (1.28)	SIZING	START	0.279 (0.011)	1.52 (0.060)	0.183	1442 (209.2)		78 (-320)	LN ₂	10,866 CYCLES TO BREAK- THROUGH	
				STOP	0.711 (0.028)	1.52 (0.060)	0.467						
			PROOFING	START	0.711 (0.028)	1.52 (0.060)	0.467	1234 (179.0)		295 (72)	AIR		
				STOP	0.711 (0.028)	1.52 (0.060)	0.467						
			CYCLING	START	0.711 (0.028)	1.52 (0.060)	0.467	690 (100.0)					0
				STOP	2.438 (0.096)	5.51 (0.217)	0.442						

Table 22: UNIAXIAL CYCLIC TESTS OF 2219-T62 ALUMINUM WITHOUT SIZING CYCLE

SPECIMEN NUMBER	THICKNESS, t mm (inch)	WIDTH, W mm (inch)	TEST PARAMETERS DURING:	CRACK DEPTH, a mm (inch)	CRACK LENGTH, 2c mm (inch)	CRACK SHAPE a/2c	Max STRESS, σ_{Max} MN/m ² (Ksi)	STRESS RATIO, $\sigma_{Min}/\sigma_{Max}$	TEMPERATURE, T K (°F)	ENVIRONMENT	REMARK		
IATC -17	2.36 (0.093)	63.5 (2.50)	CYCLING	START	0.889 (0.035)	4.39 (0.173)	0.202	249 (36.1)	-0.8	295 (72)	AIR	328 CYCLES TO BREAKTHROUGH	
				STOP	2.362 (0.093)	7.54 (0.297)						0.313	
IATC -18	2.31 (0.091)	63.5 (2.50)	CYCLING	START	0.889 (0.035)	4.37 (0.172)	0.203	249 (36.1)	-0.8				352 CYCLES TO BREAKTHROUGH
				STOP	2.311 (0.091)	7.93 (0.312)						0.292	
IAM -4	2.31 (0.091)	63.5 (2.50)	CYCLING	START	1.092 (0.043)	4.50 (0.177)	0.243	249 (36.1)	0				1587 CYCLES TO BREAKTHROUGH
				STOP	2.311 (0.091)	6.65 (0.262)						0.347	
IAM -5	2.29 (0.090)	63.5 (2.50)	CYCLING	START	0.991 (0.039)	4.57 (0.180)	0.217	249 (36.1)	0				1832 CYCLES TO BREAKTHROUGH
				STOP	2.286 (0.090)	6.27 (0.247)						0.364	
2AX -3	4.57 (0.180)	69.9 (2.75)	CYCLING	START	1.880 (0.074)	8.33 (0.328)	0.226	249 (36.1)	0				1507 CYCLES TO BREAKTHROUGH
				STOP	4.572 (0.180)	12.65 (0.498)						0.361	
2AX -4	4.57 (0.180)	69.9 (2.75)	CYCLING	START	1.803 (0.071)	8.28 (0.326)	0.218	249 (36.1)	0				1898 CYCLES TO BREAKTHROUGH
				STOP	4.572 (0.180)	13.26 (0.522)						0.344	
2AX -5	4.55 (0.179)	69.9 (2.75)	CYCLING	START	1.727 (0.068)	8.20 (0.323)	0.211	249 (36.1)	-0.8		240 CYCLES TO BREAKTHROUGH		
				STOP	4.547 (0.179)	13.46 (0.530)				0.338			
2AX -6	4.55 (0.179)	69.9 (2.75)	CYCLING	START	1.676 (0.066)	8.13 (0.320)	0.206	249 (36.1)	-0.8		605 CYCLES TO BREAKTHROUGH		
				STOP	4.547 (0.179)	13.59 (0.535)				0.335			
2AX -8	4.57 (0.180)	69.9 (2.75)	CYCLING	START	1.676 (0.066)	11.43 (0.450)	0.147	249 (36.1)	0		2238 CYCLES TO BREAKTHROUGH		
				STOP	4.572 (0.180)	14.68 (0.578)				0.311			

ORIGINAL PAGE IS
OF POOR QUALITY

Table 22: Continued

SPECIMEN NUMBER	THICKNESS, t mm (Inch)	WIDTH, W mm (Inch)	TEST PARAMETERS DURING:		CRACK DEPTH, a mm (Inch)	CRACK LENGTH, $2c$ mm (Inch)	CRACK SHAPE $a/2c$	Max STRESS, σ_{Max} MN/m ² (Ksi)	STRESS RATIO, $\sigma_{Min}/\sigma_{Max}$	TEMPERATURE, T K (°F)	ENVIRONMENT	REMARKS
3AX -15	7.72 (0.304)	127.0 (5.00)	CYCLING	START	1.727 (0.068)	8.89 (0.350)	0.194	249 (36.1)	0	295 (72)	AIR	5685 CYCLES TO BREAKTHROUGH
				STOP	7.722 (0.304)	24.13 (0.950)	0.320					
3AX -16	7.70 (0.303)	127.3 (5.01)	CYCLING	START	1.676 (0.066)	8.97 (0.353)	0.187	249 (36.1)	0			5244 CYCLES TO BREAKTHROUGH
				STOP	7.696 (0.303)	23.24 (0.915)	0.331					
3AX -17	7.47 (0.294)	127.0 (5.00)	CYCLING	START	1.727 (0.068)	8.94 (0.352)	0.193	249 (36.1)	-1.0			1648 CYCLES TO BREAKTHROUGH
				STOP	7.468 (0.294)	23.88 (0.940)	0.312					
3AX -18	7.52 (0.296)	127.0 (5.00)	CYCLING	START	1.651 (0.065)	8.89 (0.350)	0.186	249 (36.1)	-1.0			1581 CYCLES TO BREAKTHROUGH
				STOP	7.518 (0.296)	23.75 (0.935)	0.317					

TABLE 23: ILLUSTRATION OF NUMERIC INTEGRATION PROCEDURE TO DETERMINE CYCLIC LIFE.

a	Δa	$a/2c$	σ_o	σ_o/σ_s	Q	a/t	M_{km}	K	K_{av}	da/dN	ΔN
$a_i > a_i$ \vdots	Δa_{ij} \vdots	$a/2c_i$ $a/2c_i$ \vdots $a/2c_f$	σ_o \vdots	σ_o/σ_s \vdots	Q_i Q_i \vdots Q_f	a/t_i a/t_i \vdots 1.0	M_{km_i} M_{km_i} \vdots M_{km_f}	$K_i > K_i$ \vdots K_f	K_{ij} \vdots	$(da/dN)_{ij}$ \vdots	ΔN_{ij} \vdots

$$\sum N =$$

APPENDIX A: DESIGN AND STRESS ANALYSIS OF SPHERICAL CAP SPECIMENS

Four different spherical cap specimen configurations were utilized in this experimental program to determine the influence of a 1 to 1 biaxial stress field on the static fracture stress/ flaw size relationship. These specimens were pressurized internally to develop membrane stresses and were designed primarily around the following requirements:

- (1) Uniform stresses in the vicinity of the apex (where the surface flaw would be located) when pressurized up to 90% of the ultimate strength of the material at the apex.
- (2) No failure at the spherical shell to flange transition when pressurized up to 90% of the ultimate strength of the material at the apex.
- (3) Minimize the effects of the radius of curvature on the fracture results.

The radii for these spherical cap specimens were selected so that the static fracture results were > 90% of flat specimen results. Folias (Ref. A1) has shown that a significant reduction in failure stress can result in a curved panel containing a through crack. This analysis by Folias is applicable only to the linear elastic case and does not really apply to failures occurring in the plastic stress region investigated in this program, but in lieu of any other available analysis the one by Folias was used. Since these specimens had a surface crack rather than a through crack, an effective or equivalent through crack was arrived at so the Folias analysis could be applied. It was assumed that a surface crack (shape equal to 0.20) which just penetrates the thickness has an equivalent through crack area equal to the semi-elliptical surface crack area, or that

$$2c_e = \frac{\pi}{4} (2c) \quad (A-1)$$

where: $2c_e$ = equivalent through crack length
 $2c$ = surface crack length

The relationship between spherically curved and flat panel failure stresses by Follas is expressed by the equation shown below for $\lambda < \text{unity}$.

$$\frac{\sigma_{\text{CURVED PANEL}}}{\sigma_{\text{FLAT PANEL}}} = \frac{1}{(1 + 0.49 \lambda^2)^{1/2}} \quad (\text{A-2})$$

where: σ = stress

$$\lambda^4 = \frac{12(1 - \mu^2)c_e^4}{r^2 t^2}$$

r = radius

t = thickness

μ = Poisson's ratio

For the curved specimens investigated, λ was assumed less than unity and the relationship between the surface crack parameter $\frac{2c}{rt}$ and the failure stresses is presented in Figure A1. If the crack parameter is maintained below about 0.87, the failure stress in a curved panel will be greater than 90% of the flat panel failure stress. This was the basis for the spherical cap radii selections. It should be mentioned that the hoop overwrapped cylindrical tanks, as well as the non-overwrapped all-metal tanks tested in this experimental program, also met this requirement for maximum permissible crack parameter.

The extent of the spherical segment was selected at 120° for ease of fabrication with an apex cap of constant thickness over an arc of 60° ; both selections were based on the desire to have a relatively uniform stress field in the vicinity of the apex. To establish the membrane stresses throughout the spherical cap, a computer shell analysis was run for each configuration. This structural analysis program, BOSOR 3 (Reference A2), performs an elastic stress analysis. The meridional and hoop stresses on the

inside and outside surfaces for the various spherical cap specimens are presented in Figures A2, A3, A4 and A5. These graphs are shown for internal pressures that cause stresses at the apex of about 276 MN/m^2 (40 ksi) and 690 MN/m^2 (100 ksi) for the aluminum and Inconel materials, respectively; both just below the material yield strength.

Uniformity of stresses in the test area was limited to $\pm 10\%$ of the apex stress ($pr/2t$) over an arc length equal to a minimum of 4 times the anticipated crack length. This requirement was arrived at based on the work done by Masters (A3) which established an acceptable width-to-crack length ratio ($W/2c$) of about 5 for finite width uniaxial specimens.

To further evaluate the uniformity of stresses in the vicinity of the cap apex, strain gages were applied to a checkout specimen (configuration 1AB), which did not contain a surface crack and which was then pressurized until the uniaxial ultimate strength of the material was reached at the apex. At various pressure increments the various strain gage values were recorded. The highest pressure at which strain values were recorded with the structure acting elastically was 6.9 kN/m^2 (1000 psi) whereas the specimen was ultimately pressurized to 1600 psi, well into the plastic strain region. The measured stresses due to the 6.9 kN/m^2 (1000 psi) loading are presented in Figure A2 along with the analytical results at the same pressure. The back-to-back strain gages at the apex did not indicate any bending (all gages showed the same amount of strain at a given pressure loading) and the stress at this point is equal biaxial tension defined by the equation:

$$\sigma_x = \sigma_y = \frac{Pr}{2t} \quad (\text{A-3})$$

where: p = internal pressure

t = apex thickness

subscripts x and y denote x and y orientations.

Using the general elastic stress/strain relationships presented below, the modulus of elasticity was calculated to be 91.0 GN/m^2 ($13.2 \times 10^6 \text{ psi}$) based on the strain data obtained at the specimen apex.

$$\epsilon_x = \frac{1}{E} (\sigma_x - \mu \sigma_y) \quad (\text{A-4})$$

$$\epsilon_y = \frac{1}{E} (\sigma_y - \mu \sigma_x) \quad (\text{A-5})$$

where: ϵ = elastic strain

E = modulus of elasticity

This value of modulus of elasticity is higher than that recorded for the uniaxial specimens which had an average value of 73.1 GN/m^2 ($10.6 \times 10^6 \text{ psi}$). This same phenomenon was also observed for the aluminum cylinder tests reported in the Interim Report.

The elastic stresses at locations away from the apex of the bulge specimen were determined using Equations A-4 and A-5 and the measured elastic strains. The value of the modulus of elasticity used to determine these stresses was 91.0 GN/m^2 ($13.2 \times 10^6 \text{ psi}$); the value determined at the apex. Values of modulus of elasticity can vary 10 to 20% in controlled tensile tests and therefore the experimentally determined stresses might also show this kind of variation. Taking this into account, reasonably good agreement is obtained between the experimentally and analytically determined stresses presented in Figure A2. In some cases the experimental values exceed the analytical ones and in other cases the opposite was true.

The experimentally determined stresses at 6.9 kN/m^2 (1000 psi) are replotted in Figure A6 versus arc length from the apex along with the plastic stresses calculated at the maximum pressure attained; 11.0 kN/m^2 (1600 psi). The plastic stresses at 11.0 kN/m^2 (1600 psi) were determined by applying the deformation theory for plastic flow (Ref. A4) as outlined below in the following paragraphs.

The three principal plastic strains were determined from equations:

$$\epsilon'_x = \epsilon_x - \epsilon_{Ex} \quad (A-6)$$

$$\epsilon'_y = \epsilon_y - \epsilon_{Ey} \quad (A-7)$$

$$\epsilon'_z = -\epsilon'_x - \epsilon'_y \quad (A-8)$$

where: ϵ' = plastic strain portion
 ϵ_E = elastic strain portion
 ϵ = total strain

subscripts x, y and z denote x, y and z orientations.

The effective strain ($\bar{\epsilon}$) was then determined from the expression

$$\bar{\epsilon} = \sqrt{2/3(\epsilon'^2_x + \epsilon'^2_y + \epsilon'^2_z)} \quad (A-9)$$

where for equal biaxial tension $\epsilon'_x = \epsilon'_y$. The result is shown below

$$\bar{\epsilon} = 2 \epsilon'_x \quad (A-10)$$

The effective stress ($\bar{\sigma}$) was determined from the expression

$$\bar{\sigma} = \frac{1}{\sqrt{2}} \sqrt{(\sigma_x - \sigma_y)^2 + (\sigma_y - \sigma_z)^2 + (\sigma_z - \sigma_x)^2} \quad (A-11)$$

where for the equal biaxial tension state ($\sigma_x = \sigma_y$) existing at the specimen apex and $\sigma_z = 0$ reduces to:

$$\bar{\sigma} = \sigma_x = \frac{Pr}{2t} \quad (A-12)$$

The plot of effective stress and strain is shown in Figure A7. Using the effective strain based on Equation A-9, the effective stress was then determined at the location in question using Figure A7. The relationship between the plastic strain and stresses can be expressed as follows:

$$\epsilon'_x = \frac{2k}{3} [\sigma_x - 0.5(\sigma_y - \sigma_z)] \quad (A-13)$$

$$\epsilon'_y = \frac{2k}{3} [\sigma_y - 0.5(\sigma_z - \sigma_x)] \quad (A-14)$$

$$\epsilon'_z = \frac{2k}{3} [\sigma_z - 0.5(\sigma_x - \sigma_y)] \quad (A-15)$$

where k is a measure of the plastic modulus of the material.

Using Equations A-13 and A-14, the unknown k can be eliminated and the relationship between σ_x and σ_y is obtained as expressed below:

$$\frac{\epsilon'_x}{\epsilon'_y} = \frac{\sigma_x - 0.5\sigma_y}{\sigma_y - 0.5\sigma_x} \quad (A-16)$$

if $\sigma_z = 0$.

Knowing the effective stress value determined previously, the actual stresses are determined using Equations A-11 and A-16. As indicated in Figure A6, the plastic stresses are reasonably uniform within the accuracy of the measured strain values. It is realized that true strains should be used in evaluating the plastic stresses, but since

the engineering and true strains are essentially equal for the strain values obtained in this test, the engineering strains were used in the calculations.

One interesting result of the instrumented pressure test is illustrated in Figure A7; where the effective stress and effective strain are plotted. Along with the effective stress/strain values determined at the specimen apex, the effective stress/strain relationship for a uniaxial specimen from the Interim Report is plotted. This comparison illustrates there is an apparent strengthening of the equal biaxial result over that of the uniaxial result. The deformation theory of plastic flow states that the effective stress/strain relationship is invariant for a material. As discussed earlier, the elastic modulus of elasticity also appeared to increase for a biaxially loaded structure compared to a uniaxially loaded one.

In summary, the spherical cap specimens were designed to provide a uniform 1 to 1 biaxial stress field in the immediate vicinity of where a surface crack would be introduced and at the same time minimize any curvature effects on the static fracture results obtained and this was achieved.

REFERENCES

- A1 E. S. Folias, "On the Theory of Fracture of Curved Sheets,"
Engineering Fracture Mechanics, Vol. 2, No. 2, November 1970.
- A2 D. Bushnell, "Stress, Stability and Vibration of Complex Shells of
Revolution: Analysis and User's Manual for BOSOR 3", SAMSO
TR-69-375, September 1969.
- A3 J. N. Masters, W. D. Bixler and R. W. Finger, "Fracture Char-
acteristics of Structural Aerospace Alloys Containing Deep Surface
Flaws," NASA CR-134587, dated December 1973.
- A4 J. Marin, Engineering Materials Their Mechanical Properties and
Application, May 1957.

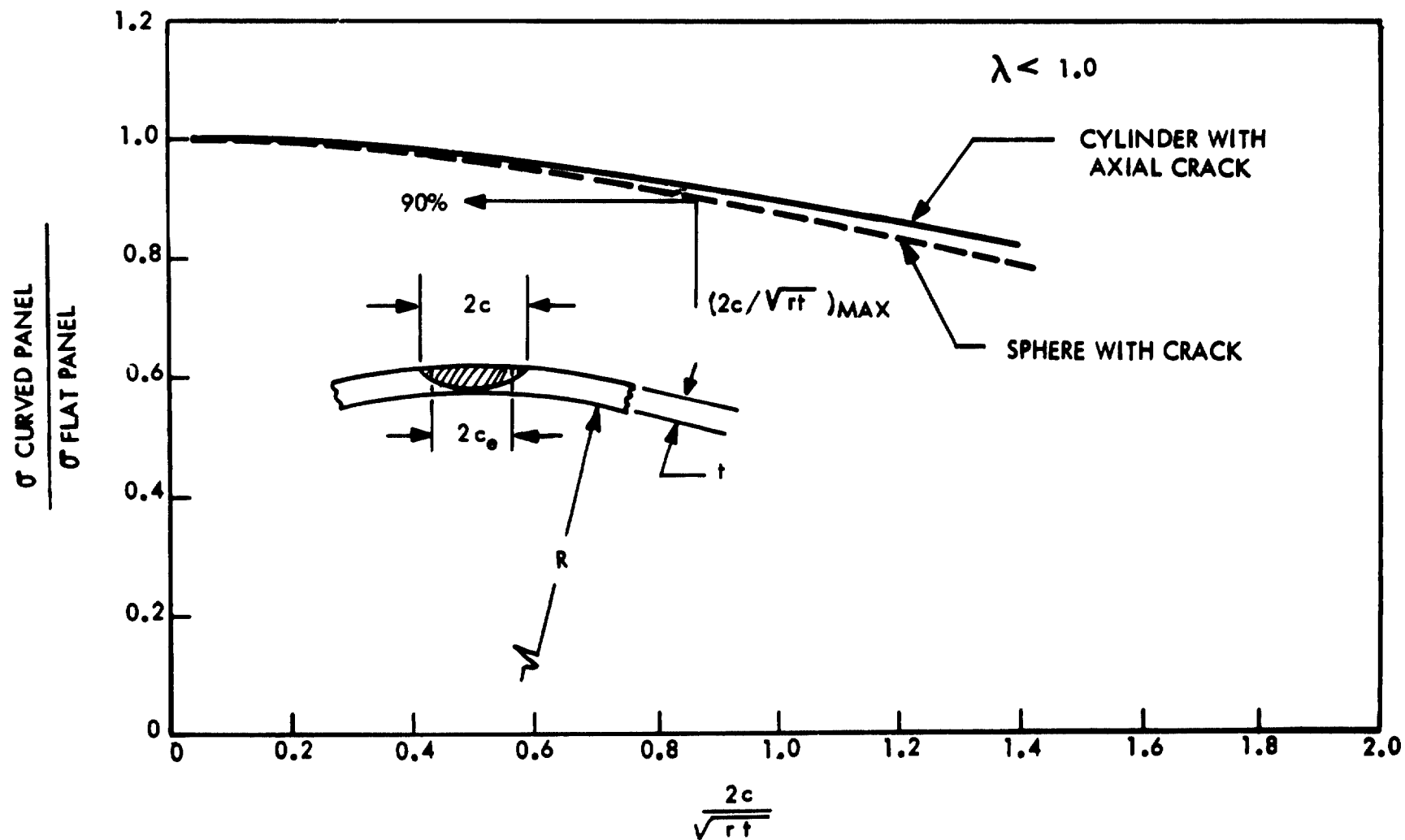


FIGURE A1: ALUMINUM FAILURE STRESS RELATIONSHIP BETWEEN CURVED AND FLAT PANELS CONTAINING A SURFACE FLAW.

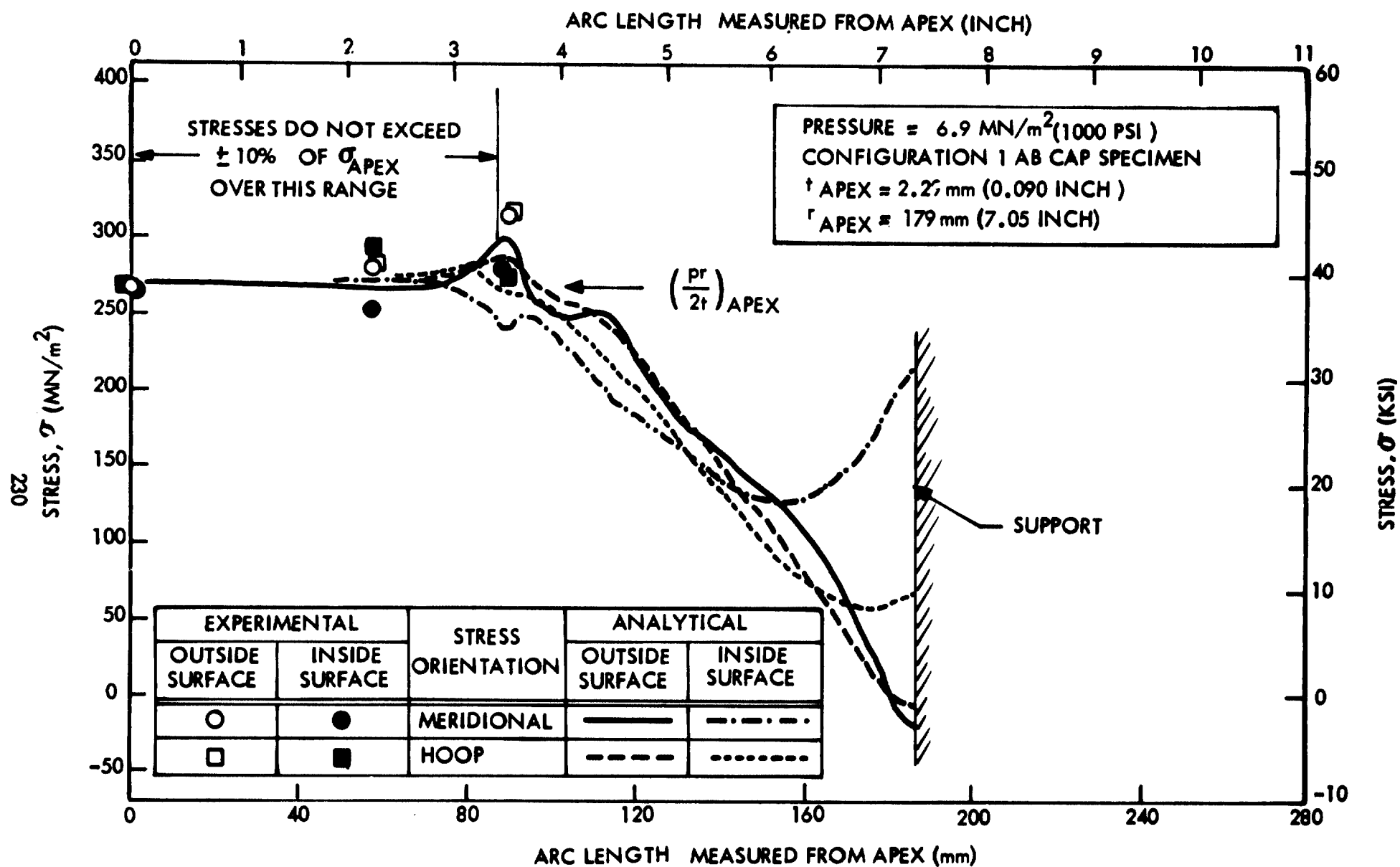


FIGURE A2: COMPARISON OF EXPERIMENTAL AND ANALYTICAL STRESSES FOR 2.29 mm (0.090 INCH) THICK 2219-T62 ALUMINUM CAP SPECIMEN.

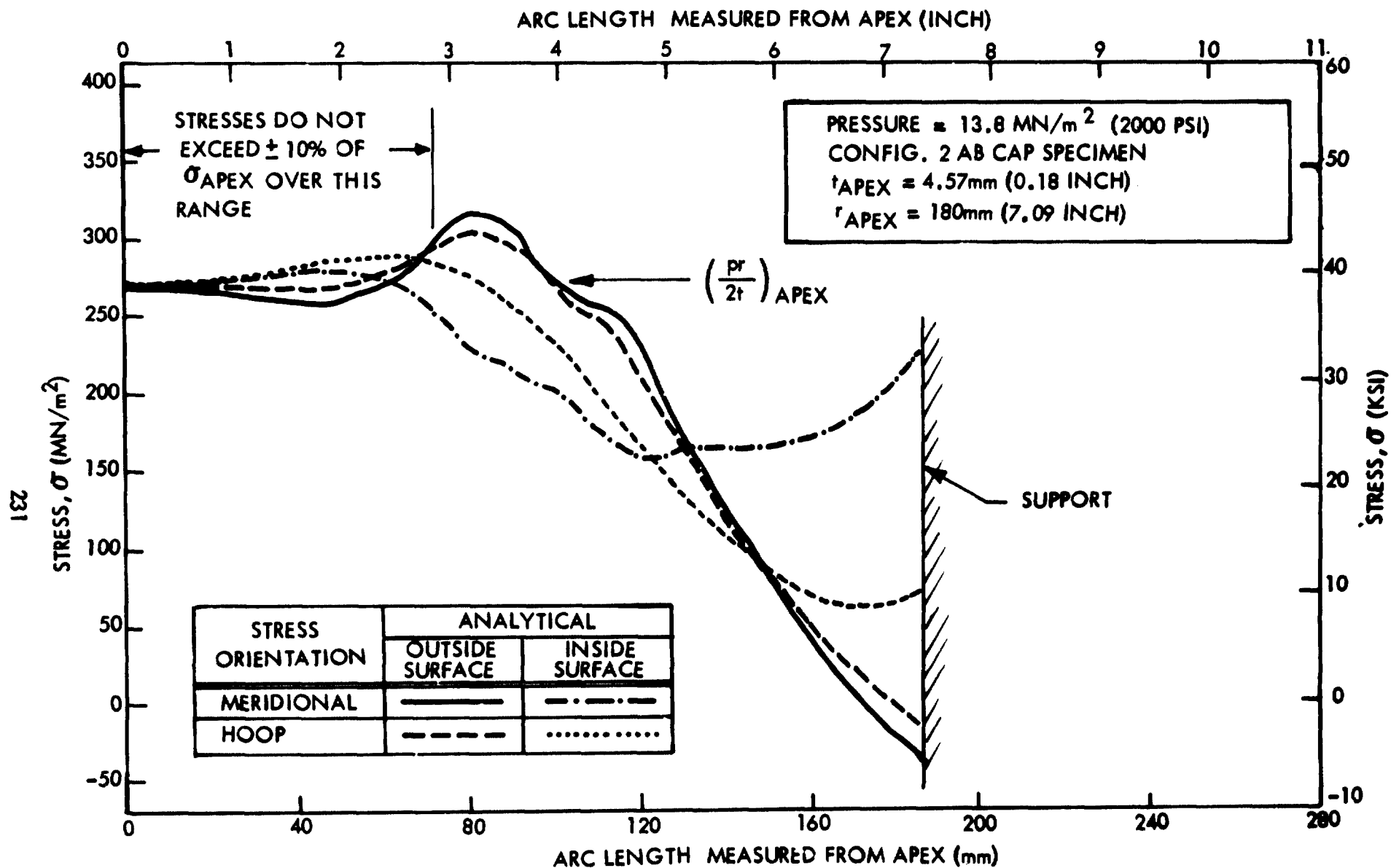


FIGURE A3: ANALYTICAL STRESSES FOR 4.57 mm (0.18 INCH) THICK 2219-T62 ALUMINUM CAP SPECIMEN

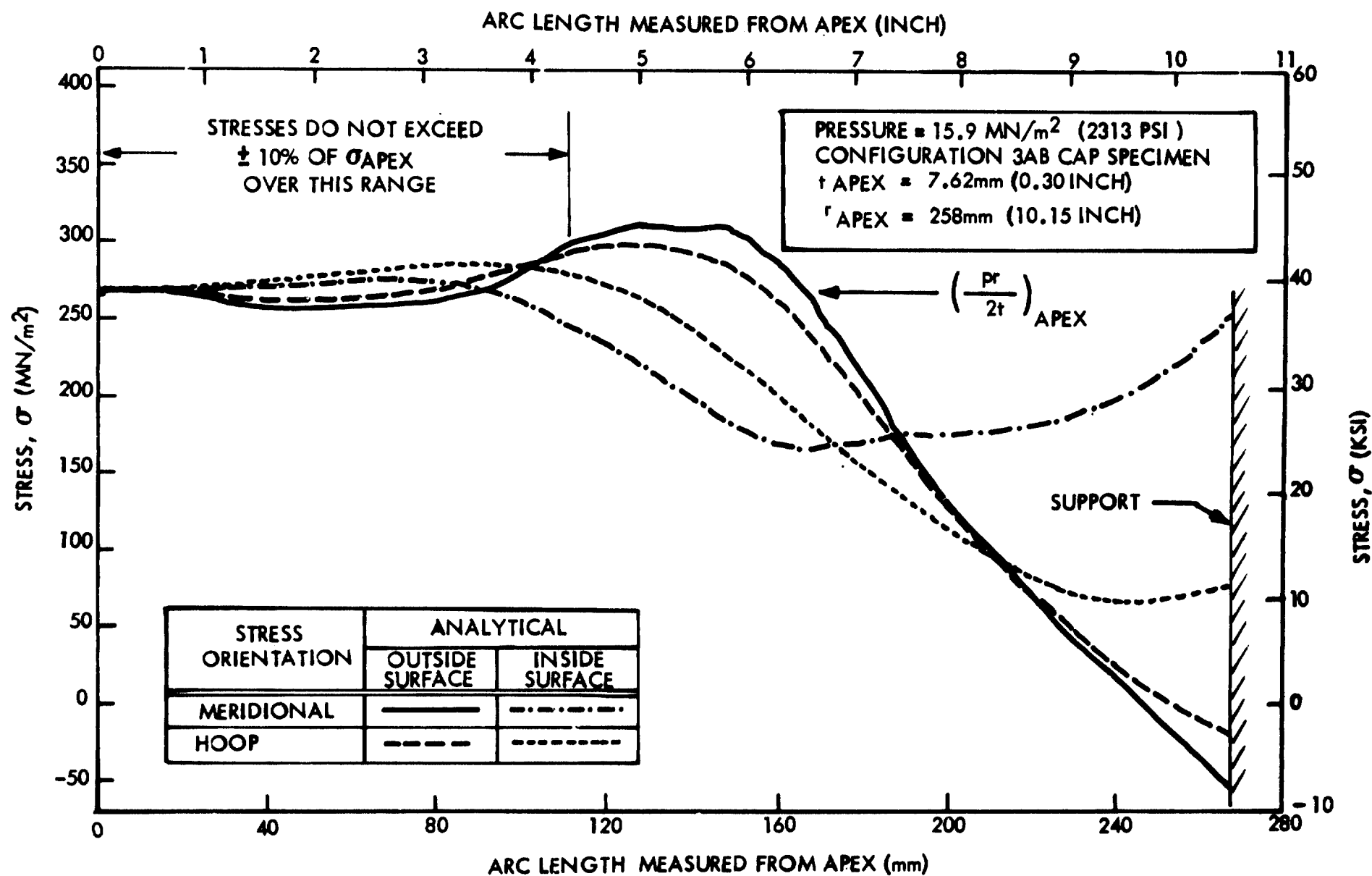


FIGURE A4: ANALYTICAL STRESSES FOR 7.62 mm (0.30 INCH) THICK 2219-T62 ALUMINUM CAP SPECIMEN

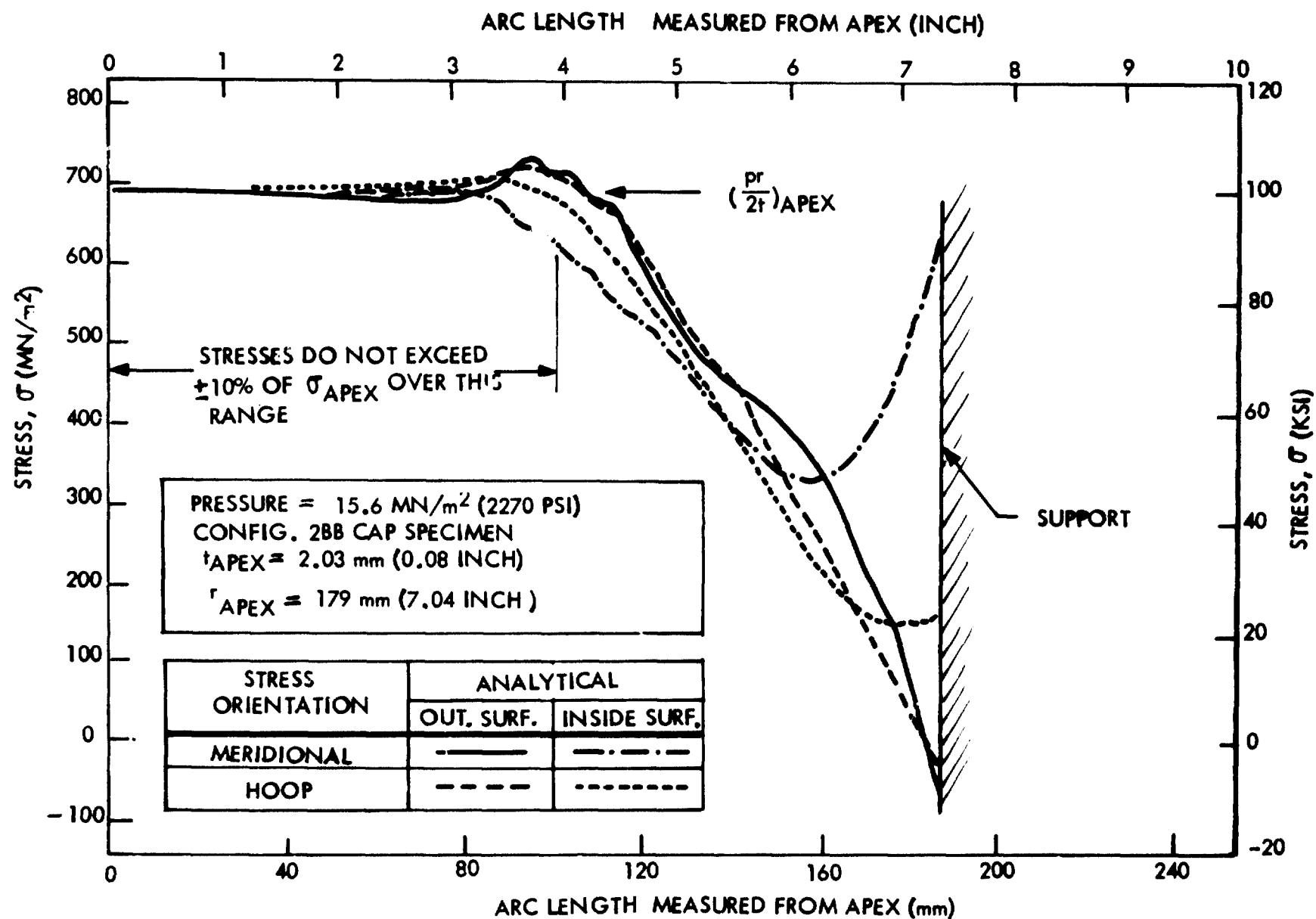


FIGURE A5: ANALYTICAL STRESSES FOR 2.03mm (0.080 INCH) THICK INCONEL X750 STA CAP SPECIMEN

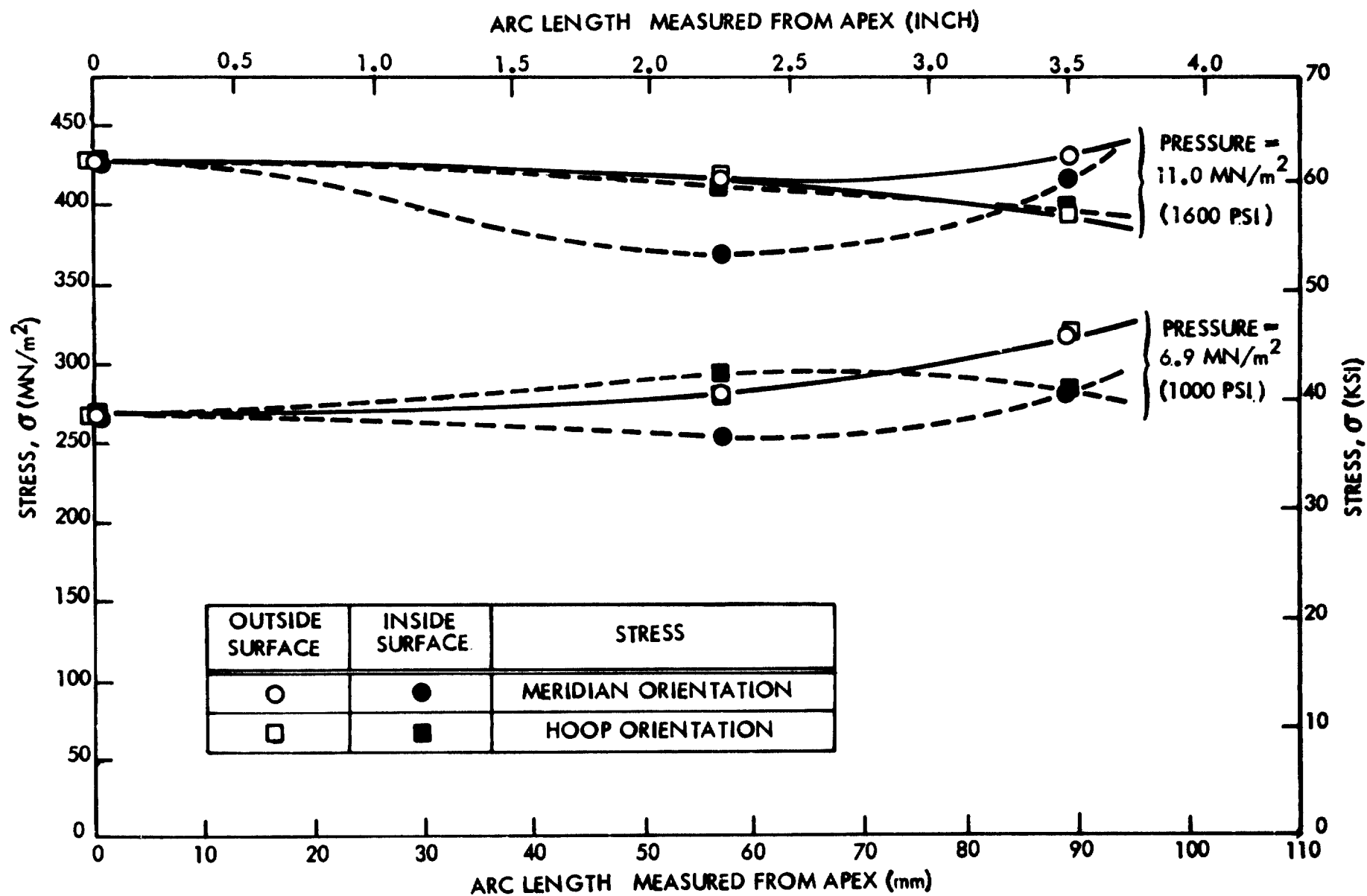


FIGURE A6: STRAIN GAGE RESULTS FOR 2.29 mm (0.090 INCH) THICK 2219-T62 ALUMINUM CAP SPECIMEN

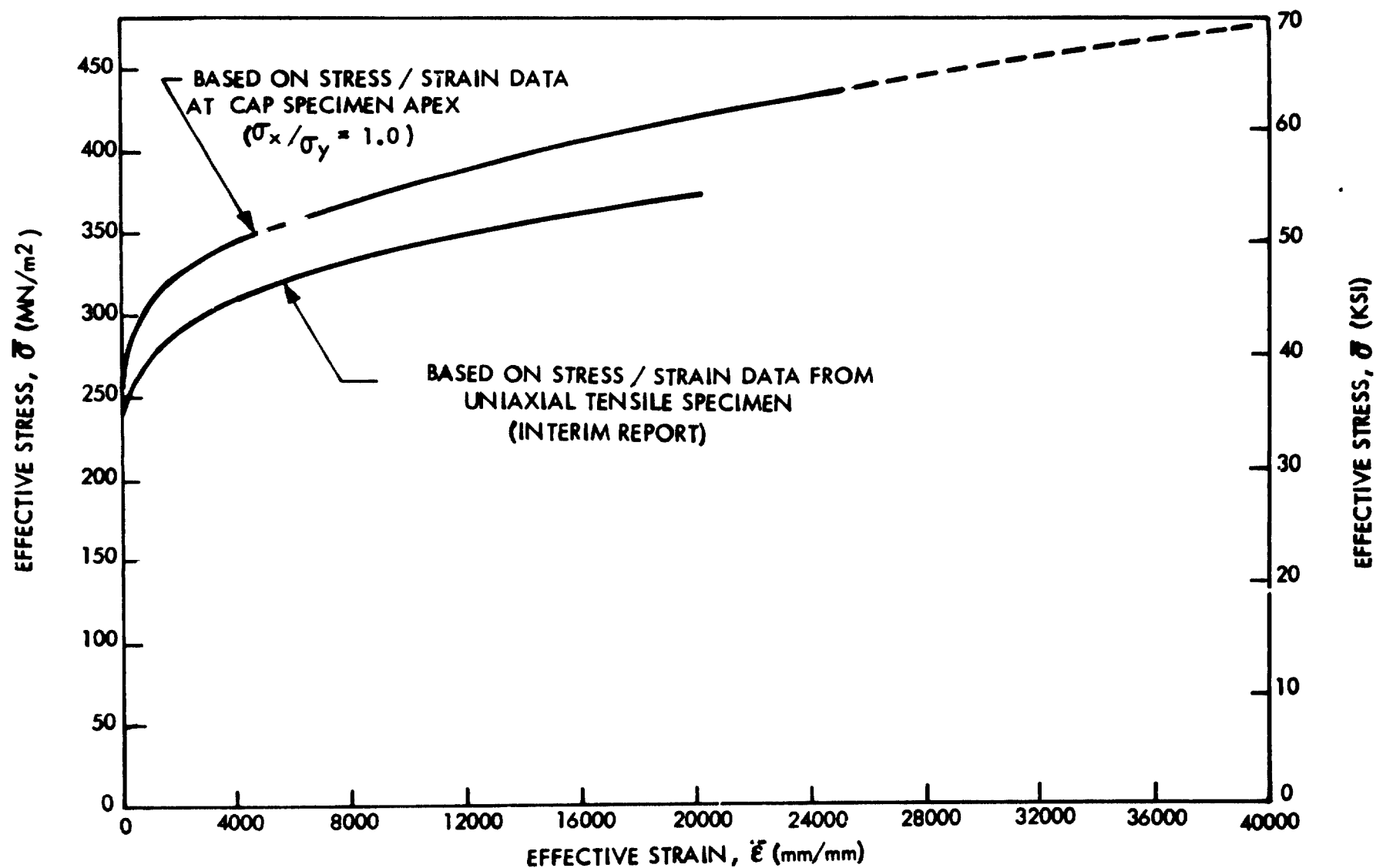


FIGURE A7: EFFECTIVE STRESS VS. EFFECTIVE STRAIN FOR 2.29 mm (0.090 INCH) THICK 2219-T62 ALUMINUM

APPENDIX B: EXAMPLE OF SERVICE LIFE CALCULATION

A detailed example of how to determine the service life of an overwrapped tank with a load sharing liner utilizing the data contained in this report is presented herein. The pertinent parameters established for this example are:

Material	2219-T62 Aluminum Base Metal
Ultimate Strength	431 MN/m ² (62.5 ksi)
Yield Strength	297 MN/m ² (43.1 ksi)
Liner Thickness	4.57 mm (0.180 inch)
Sizing Stress Field	Equal Biaxial (1:1)
Sizing & Operating Temp.	295 K (72° F)
Sizing Stress	345 MN/m ² (50 ksi)
Max. Operating Stress	166 MN/m ² (24 ksi)
Min. Operating Stress	-166 MN/m ² (-24 ksi)

The first step is to calculate the critical crack size screened during sizing from Equation 8:

$$\sigma_s = \sigma_{ult} - S(a/Q)_i^{cr}$$

$$345 \text{ MN/m}^2 = 431 \text{ MN/m}^2 - 47.8 \frac{\text{MN/m}^2}{\text{mm}} (a/Q)_i^{cr} \quad \left(\begin{array}{c} \text{SI} \\ \text{Units} \end{array} \right)$$

$$50 \text{ ksi} = 62.5 \text{ ksi} - 176 \frac{\text{ksi}}{\text{inch}} (a/Q)_i^{cr} \quad \left(\begin{array}{c} \text{US} \\ \text{(Customary)} \\ \text{Units} \end{array} \right)$$

$$(a/Q)_i^{cr} = 1.80 \text{ mm (0.071 inch)}$$

PRECEDING PAGE BLANK NOT FILMED

where the values of σ_s and σ_{ult} are given and S is defined in Figure 45 for the given material, thickness and biaxiality condition. For the example presented herein it is assumed that the initial crack shape $(a/2c)_i$ is 0.1. Other crack shapes (0.3 and 0.5) should be investigated to determine which shape yields the least cyclic life. To determine the critical crack depth screened by the sizing cycle, it is necessary to determine the crack shape parameter (Q) which is a function of $a/2c$ and σ_s/σ_{ys} . Since the sizing stress exceeds the material's yield strength, the σ_s/σ_{ys} ratio is greater than unity. The crack parameter, Q , is undefined at σ/σ_{ys} ratios greater than unity and therefore it will be assumed that σ_s/σ_{ys} is unity and Q determined from Figure 16:

$$Q_i = 0.89$$

The critical crack depth (a_i^{cr}) is then:

$$\begin{aligned} a_i^{cr} &= (a/Q)_i^{cr} Q_i \\ &= 1.80 \text{ mm (0.071 inch)} 0.89 \\ a_i^{cr} &= 1.60 \text{ mm (0.063 inch)} \end{aligned}$$

The critical crack length is:

$$\begin{aligned} 2c_i^{cr} &= 10 a_i^{cr} \\ 2c_i^{cr} &= 16.0 \text{ mm (0.63 inch)} \end{aligned}$$

This crack depth is considerably less than the liner thickness of 4.57 mm (0.180 inch) which indicates that the sizing cycle does screen a crack.

Once the critical crack depth that is screened by the sizing cycle is established, the next step is to determine how many operational pressure cycles the pressure

vessel can withstand without leaking or failing catastrophically. This involves a numeric integration procedure where the crack growth potential (liner thickness minus the crack depth screened by the sizing cycle) is divided into a number of increments and the operational cycles required to grow each increment is calculated. It is first necessary to establish the manner in which the crack shape changes as the crack grows. As pointed out in Paragraph 7.3, the crack shape approaches a steady state value when cycled regardless of the initial crack shape. For the 2219-T62 aluminum, this value is 0.35. If this crack shape was assumed when the crack penetrated the thickness, the crack length would be 13.1 mm (0.514 inch). This is less than the initial value of 16.0 mm (0.630 inch) and, therefore it will be assumed that the crack length does not change while crack depth growth takes place. Table B1 illustrates the numeric integration to determine the operating cycles necessary to cause liner leakage. The stress intensity values (K) are calculated using Equation 6:

$$K_{\max} = 1.1 \sigma_{\max} \left(\frac{\pi a}{Q} \right)^{1/2} M_{km}$$

The numeric integration shown in Table B1 is based on a $\sigma_{\min} / \sigma_{\max}$ (R) ratio of zero so that the result can be compared directly with the parametric life analysis presented in Paragraph 7.5. The cyclic crack growth rates (da/dN) are calculated for each increment of crack growth using Equation 7 with B = 1 (R = 0 condition):

$$\frac{da}{dN} = C B K_{av}^n$$

where K_{av} is the average stress intensity for the increment and the empirical constants for the given material, thickness and temperature are obtained from Figure 70 as presented below:

$$\begin{aligned} n &= 3.38 \\ C &= 23 \times 10^{-9} \frac{\text{mm}}{(\text{MN/m}^{3/2})^n} \quad \left(\begin{array}{l} \text{SI} \\ \text{Units} \end{array} \right) \end{aligned}$$

$$= 1.23 \times 10^{-9} \frac{\text{inch}}{(\text{ksi} \sqrt{\text{in}})^n} \quad \begin{matrix} \text{US} \\ \text{(Customary)} \\ \text{Units} \end{matrix}$$

As Table B1 indicates, the cycles to grow the crack from its initial size to the point of penetrating the thickness is 6515 cycles. From Figure 96 for the same conditions, a cyclic life of 5700 cycles is obtained. The result from Figure 96 is slightly conservative to cover all the conditions presented.

To obtain the service life for the given R ratio of -1.0, it is necessary to determine the appropriate value of the parameter B in the cyclic crack growth rate equation. From Figure 81 for an R = -1.0 and a σ_{\max} of 166 MN/m² (24 ksi), the value of B is 1.9. Therefore, the cyclic crack growth rates are 1.9 times faster at an R = -1.0 than at an R = 0 and the service life based on Equation 13 is:

$$\frac{6515 \text{ Cycles}}{1.9} = 3429 \text{ Cycles}$$

Under the stated operating conditions, the service life of the liner is 3429 cycles based on an assumed initial crack shape of 0.1. As indicated by Figure 98, if an initial crack shape of 0.5 was assumed, the service life at an R = 0 is 1300 cycles which is considerably less than the 5700 cycles arrived at when assuming an initial crack shape of 0.1. Thus, a complete assessment of a liner must include assuming various initial crack shapes and calculating the service life. In addition, the weld metal as well as the base metal should be investigated. The cyclic lives determined do not account for any cyclic crack growth rate data scatter. As suggested in Paragraph 7.3, the cyclic life calculated above should be reduced by a factor of 2 in arriving at a guaranteed life.

One additional check should be made to verify that the liner indeed leaks rather than fails catastrophically. From Table B1, the stress intensity value at crack breakthrough is $24.8 \text{ MN/m}^{3/2}$ ($22.6 \text{ ksi } \sqrt{\text{in}}$). This is less than an apparent toughness of about $55.0 \text{ MN/m}^{3/2}$ ($50.0 \text{ ksi } \sqrt{\text{in}}$), the value at which catastrophic failure is assumed to result, and therefore leakage does occur prior to catastrophic failure.

TABLE B1: CYCLIC LIFE CALCULATION FOR EXAMPLE (R = 0)

a mm (INCH)	Δa mm (INCH)	a/2c	σ_o MN/m ² (KSI)	σ_o/σ_s	Q (FIG. 16)	a/t	M _{km} (FIG. 17)	K MN/m ^{3/2} (KSI $\sqrt{\text{IN}}$)	K _{AV} MN/m ^{3/2} (KSI $\sqrt{\text{IN}}$)	da/dN X 10 ⁻⁶ mm/CYCLE (INCH/ CYCLE)	ΔN (CYCLES)
1.60 (0.063)	0.30 (0.012)	0.100	166 (24)	0.48	1.053	0.350	1.073	13.50 (12.28)	14.28 (12.99)	181 (7.14)	1681
(0.075)	0.30 (0.012)	0.119			1.090	0.417	1.116	15.06 (13.70)	15.78 (14.36)	255 (10.03)	1196
2.21 (0.087)	0.30 (0.012)	0.138			1.130	0.483	1.156	16.50 (15.01)	17.25 (15.70)	344 (13.55)	886
2.51 (0.099)	0.30 (0.012)	0.157			1.170	0.550	1.203	18.00 (16.38)	18.74 (17.05)	455 (17.91)	670
2.82 (0.111)	0.30 (0.012)	0.176			1.215	0.617	1.252	19.46 (17.71)	20.18 (18.36)	584 (23.00)	522
3.12 (0.123)	0.30 (0.012)	0.195			1.260	0.683	1.300	20.89 (19.01)	21.51 (19.57)	725 (28.54)	420
3.43 (0.135)	0.30 (0.012)	0.214			1.310	0.750	1.340	22.12 (20.13)	22.66 (20.62)	865 (34.06)	352
3.73 (0.147)	0.30 (0.012)	0.233			1.365	0.817	1.374	23.19 (21.10)	23.56 (21.44)	987 (38.86)	309
4.04 (0.159)	0.30 (0.012)	0.252			1.420	0.883	1.390	23.93 (21.77)	24.23 (22.05)	1085 (42.72)	281
4.34 (0.171)	0.30 (0.012)	0.271			1.480	0.950	1.403	24.53 (22.32)	24.68 (22.46)	1155 (45.46)	198
4.57 (0.180)	0.23 (0.009)	0.286			1.530	1.000	1.408	24.84 (22.60)			

 $\Sigma \Delta N = 6515 \text{ CYCLES}$

APPENDIX C SYMBOLS

A	=	Failure loci empirical constant
a	=	Semi-elliptical crack depth
a/2c	=	Crack shape
a/Q	=	Crack size
a/t	=	Fraction of crack depth
B	=	Cyclic crack growth rate empirical constant to account for R ratio effects
BM	=	Base metal
C	=	Cyclic crack growth rate empirical constant
c	=	One-half semi-elliptical crack length
COD	=	Crack opening displacement
D	=	Diameter
da/dN	=	Cyclic crack growth rate
E	=	Modulus of elasticity
GOL	=	Growth on loading
K	=	Stress intensity
K_{IE}	=	Engineering fracture toughness
k	=	Plastic constant
L	=	Length
m	=	Failure loci empirical constant
M_{km}	=	Deep flaw magnification factor
MOF	=	Mode of failure
N	=	Cycles
n	=	Cyclic crack growth rate empirical constant
OW	=	Overwrapped
p	=	Tank pressure
Q	=	Crack shape parameter
R	=	Minimum to maximum stress ratio
r	=	Radius
RT	=	Room temperature

S	=	Failure loci empirical constant
T	=	Temperature
t	=	Thickness
W	=	Width
WM	=	Weld Metal

α	=	Crack opening displacement constant
Δ	=	Change or difference
δ	=	Crack opening displacement
ϵ	=	Total strain
$\bar{\epsilon}$	=	Effective Strain
ϵ'	=	Plastic strain
λ	=	Flawed shell parameter
μ	=	Poisson's ratio
σ	=	Stress
$\bar{\sigma}$	=	Effective stress
ϕ	=	Crack shape parameter

SUBSCRIPTS

av	=	Average	ps	=	Prestress
cr	=	Critical	s	=	Sizing
c	=	Critical	ult	=	Ultimate
e	=	Equivalent	x	=	Direction parallel to crack plane
f	=	Final	y	=	Direction perpendicular to crack plane
i	=	Initial			
j	=	Adjacent	ys	=	Yield strength
$max.$	=	Maximum			
$min.$	=	Minimum			
o	=	Operating			